Title
Chemical Tools for Imaging Glycans in Living Systems

Author
Chang, Pamela

Publication Date
2010

Chemical Tools for Imaging Glycans in Living Systems

by

Pamela Vivian Chang

A dissertation submitted in partial satisfaction of the

requirements for the degree

Doctor of Philosophy

in

Chemistry

in the

Graduate Division

of the

University of California, Berkeley

Committee in charge:

Professor Carolyn R. Bertozzi, Chair
Professor Christopher J. Chang
Professor Matthew D. Welch

Spring 2010

Chemical Tools for Imaging Glycans in Living Systems

By Pamela Vivian Chang

Abstract

Chemical Tools for Imaging Glycans in Living Systems

by

Pamela Vivian Chang

Doctor of Philosophy in Chemistry

University of California, Berkeley

Professor Carolyn R. Bertozzi, Chair

Glycans are important mediators of many biological processes, including cell-cell adhesion and communication as well as development, inflammation, and cancer cell metastasis. The composition and expression of these biomolecules are known to change during these physiological processes, and, accordingly, there has been much interest in profiling and imaging glycans *in vivo*. While proteins can be visualized using fluorescent proteins such as GFP, glycans are challenging targets for imaging because they are not genetically encoded. We have developed a two-step method to equip glycans with reporter tags for isolation and visualization from living systems known as the chemical reporter strategy. In our approach, an unnatural sugar, which bears a small reactive functional group known as a chemical reporter, is metabolically incorporated into cell-surface glycans. These reporters can then be detected via a covalent, bioorthogonal reaction such as the Staudinger ligation or Cu-free click chemistry by delivery of exogenous phosphine or cyclooctyne probes, respectively. If an affinity tag or imaging agent is appended to the probe, this method allows for the enrichment and visualization of the labeled glycoconjugates.

This thesis describes the development of new chemical tools for profiling and imaging glycans and their extension to living systems. Chapter 1 provides an overview of recent advances in imaging technologies, including the chemical reporter strategy, for visualizing non-proteinaceous biomolecules such as glycans, lipids, nucleic acids, and small molecule metabolites. Chapter 2 describes the application of Cu-free click chemistry using a panel of cyclooctyne probes to glycan labeling in mice. Chapter 3 describes the synthesis of phosphine and cyclooctyne imaging probes and the evaluation of their ability to image glycans *in vivo*. Chapter 4 outlines the development of a new chemical reporter for detecting the monosaccharide sialic acid and its application to the labeling of murine glycoconjugates. Finally, Chapter 5 presents a novel strategy for cell-selective labeling of glycans using a caged metabolic precursor.

This dissertation is dedicated to my family,
Mou-Hsiung, Yuen-man, Dennis and Jeff

Chemical Tools for Imaging Glycans in Living Systems

Table of Contents

Chapter 2. Copper-free click chemistry in living animals

Chapter 3. Imaging glycans using the chemical reporter strategy

Chapter 4. Development of new chemical reporters of sialic acid biosynthesis

List of Figures

List of Tables

List of Schemes

Acknowledgements

Graduate school has been an incredible experience, and I have so many people to thank for making these past 5.5 years wonderful. First and foremost, I would like to thank my advisor, Carolyn Bertozzi, for being such an amazing mentor. No matter how busy Carolyn is, she makes time for everyone. I remember when I was preparing my oral presentation for my second-year GRS, I needed help with the introductory slides. I had already asked several older students in the lab for their suggestions but no one had any good ideas, so I decided to knock on Carolyn's door to ask for help. Carolyn could see that I was really stressed out about the talk (I strongly dislike public speaking!), so she sat down with me, made me a few slides, and then talked me through them. This is just one example of how supportive Carolyn is, and since then, she has only given more. I am truly grateful for the hours that she has dedicated to giving me advice and editing my papers. Carolyn is also an amazing teacher. From her, I have learned how to give a good talk, write a polished paper, and navigate the scientific political landscape. Finally, Carolyn is a brilliant scientist who is incredibly creative and her ability to think outside of the box is truly remarkable. Over the years, she has inspired me to think big and critically, and for that I am truly grateful.

When I first joined the Bertozzi lab, there were a number of older graduate students in the group who served as invaluable resources. Jenn Prescher, whom I ended up collaborating with on a number of projects, was always a source of positivity when research was not going well. JP was also great at thinking about the big picture, and she taught me how to put my projects into perspective. Nick Agard made daily rounds when I was a first-year and always had good suggestions when my synthetic work had hit a road block. I also valued Nick's creativity and insightful suggestions. Scott Laughlin seemed like he didn't care, but I know that he actually did; and I thank him for teaching me how to do many things, whether it be how to fix my samples for microscopy or how to do a Western blot. When I joined the group, Matt Hangauer was the only one brave enough to stick it out on Team Staudinger Ligation and served as a great sounding board for my phosphine syntheses. I also enjoyed pestering Jason Rush, who was very well read, for synthetic advice as well.

I have to thank Jeremy Baskin, who I've known since my days as an undergraduate at MIT. Jeremy and I were the same year and both decided to go to UC Berkeley for graduate school. I'm glad that he did because he and I have become even better friends than we were before. He has been an invaluable scientific sounding board and incredibly supportive friend over the past several years.

I would also like to thank Isaac Miller and Ellen Sletten for vital help with animal experiments. Having two sets of hands during these very time-sensitive experiments was crucial for the execution of the *in vivo* cyclooctyne study. I also collaborated with a couple of postdocs in the lab on animal experiments—Penny Drake, who honed my skills with tail vein injections, and Peng Wu, who has become a good friend. I did not overlap very long with Danielle Dube, but I thank her for being a cheery, supportive labmate and for leaving me with a good project idea. Anderson Lo was a great undergrad to mentor. He must be the nicest guy that I know, and I enjoyed working with him for 1.5 years. Brian Smart is also one of the nicest guys that I know, and he has been extremely helpful by running my samples on the mass spec. I'd also like to thank Mike Boyce and Wenqing Shui, who have also been very generous with their time. Kimberly Beatty is a recent addition to the group, whom I've enjoyed getting to know over the past couple of years, and I thank her for editing the first chapter of this thesis.

810 has been my home for all of my years in the Bertozzi lab, and it has always been a fun place to work. It all began with the crazy antics of Brian Carlson and Ed Ballister, who were both incredibly witty and entertaining. I also enjoyed getting to know Sarah Gilmore. Though she was a year ahead of me, we applied for postdocs and finished up at about the same time and it was nice to have someone to talk to who was going through a similar experience. In the middle of my graduate career, Kanna Palaniappan and Kim Sogi joined our room, and I thank them for their good sense of humor and general cheeriness.

I am also thankful for the friends that I have made over the years. Stavroula Hatzios has been an extremely supportive friend whom I've always been able to count on. I've enjoyed our excursions to the pool or gym and our conversations over a huge sundae at Fenton's. Phung Gip has also been an incredibly supportive friend who, in addition to Jeremy, helped me get over my initial fear of public speaking. Outside of the lab, Melanie Chiu has been an awesome friend. She is an incredibly giving person, and I've always admired her passion for life and for living life to the fullest.

I'd also like to thank my previous mentor at MIT, Steve Lippard, for all of his support over the past 8.5 years. As the chair of my preliminary exam and member of my thesis committee, Chris Chang has also been incredibly supportive during my tenure in graduate school. We actually overlapped in the Lippard lab, and it has been awesome to watch him transition from being a postdoc to being a highly successful professor at UC Berkeley. I am also grateful for my undergraduate research mentor at MIT, Christiana Zhang, who taught me the skills of organic synthesis, and both JoAnne Stubbe, my biochemistry professor at MIT, and Carolyn's Dad Bill Bertozzi, a MIT physics professor, for their support and encouragement as well.

Last, but not least, I'd like to thank my family—Mom, Dad, Dennis, and Jeff—for their constant love and support over the years.

Chapter 1: Imaging beyond the proteome

Introduction

Molecular imaging is a powerful tool that has enabled the visualization of biomolecules as they function in their native habitat (1). The ability to monitor biological events at the subcellular level has shed light on many physiological processes, including protein trafficking, protein localization, and protein-protein interactions (2). Arguably, the most widely used tool in molecular imaging is the green fluorescent protein (GFP). The discovery and development of GFP by Shimomura, Chalfie, and Tsien, who were rewarded the 2008 Nobel Prize in Chemistry for their efforts, has enabled the tagging and imaging of many proteins of interest (3).

Though imaging of target proteins using fluorescent protein fusions has revolutionized many areas of biology, extension of this strategy to other components of the cell that are not genetically encoded such as glycans, lipids, and nucleic acids has remained challenging. While proteins comprise the largest fraction of the cell, non-proteinaceous biomolecules also play important roles in cell biology (4). Thus, the ability to directly visualize all the components of the cell would allow for a more comprehensive understanding of cellular biochemistry. Here, we discuss the development of emerging technologies that enable imaging beyond the proteome, namely protein post-translational modifications such as glycosylation, phosphorylation, methylation, and lipidation, as well as lipids, glycans, nucleic acids, small molecule metabolites, and inorganic ions.

Fluorescent proteins

Traditionally, GFP has been genetically fused to the gene that encodes the protein of interest in order to produce a chimeric protein that contains the fluorescent protein at its N- or C-terminus (5). Although this strategy is routinely used to image proteins, several groups have applied fluorescent proteins to image lipids, signaling molecules, and post-translational modifications in the cell. Through protein-small molecule interactions, certain proteins can faithfully report on the location of non-proteinaceous biomolecules in the cell such as phosphoinositides.

GFP-tagged binding domains for imaging phosphoinositides

Phosphoinositides, phosphorylated derivatives of the lipid phosphatidylinositol, are important regulators of cellular homeostasis and many signal transduction pathways (6). These lipids are predominantly found in the inner leaflet of the plasma membrane and on the cytosolic face of organelle membranes and are responsible for recruiting a wide variety of proteins. Fluorescent protein fusions to the phosphoinositide-binding domains of these recruited proteins have been used to study phosphoinositide dynamics in live cells using fluorescence microscopy (7, 8).

Förster resonance energy transfer (FRET)-based sensors of signaling molecules

In addition to their contributions toward developing the fluorescent protein toolkit, Tsien and co-workers have also developed a FRET-based reporter system for imaging secondary messengers (3). They were initially interested in visualizing cyclic adenosine 3',5'-monophosphate (cAMP), a small molecule that is involved in intracellular signal transduction. Their first FRET reporter consisted of fluorescein-labeled catalytic subunits of cAMP-dependent protein kinase (PKA) and rhodamine-labeled regulatory subunits of PKA (9). Upon binding of cAMP, the regulatory subunit of PKA dissociates from the catalytic subunit, thus causing a loss in FRET between the two labels. Despite the utility of this probe, Tsien hoped to replace the small molecule organic fluorophores with fluorescent proteins in order to enable imaging of other proteins through genetic fusion (3). Using mutagenesis, they were able to develop GFP with enhanced fluorescence and fluorescent proteins of different colors. Their group discovered that the yellow fluorescent protein (YFP) is a good FRET acceptor for the cyan fluorescent protein (CFP). Following this development, Pozzan and co-workers teamed up with the Tsien laboratory to replace the two fluorophores with CFP and YFP (10). In their work, they demonstrated that this fluorescent protein FRET-based reporter can be used to image cAMP in stimulated rat cardiac myocytes (11). More recently, Dyachok *et al*. have developed a FRET-based sensor to measure cAMP dynamics in pancreatic beta cells using ratiometric evanescent wave microscopy (12, 13). For a comprehensive review of live-cell imaging of cAMP dynamics, see (14).

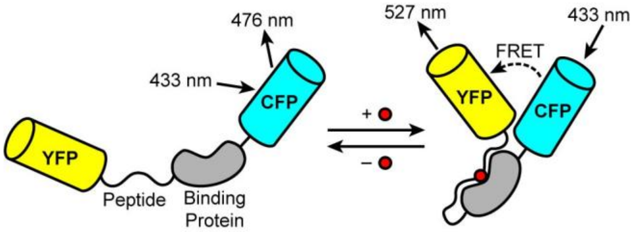

Analyte or PTM (●)	Peptide	Binding Protein	References
Calcium	M13	Calmodulin	16-19
Glutamate	YbeJ^a		26-27
Phosphorylation	Kinase substrate peptide	Phosphoaminoacid binding domains	33-46
Histone methylation	N-terminal region of the histone protein H3	Chromodomains	47
β-O-GlcNAc	Casein kinase II substrate peptide	GafD	50

^{a}YbeJ is a bacterial glutamate-binding protein that undergoes significant conformational change after binding glutamate

Figure 1-1. Genetically-encoded fluorescent protein-based FRET reporters of small molecules and post-translational modifications. PTM = post-translational modification.

Tsien and co-workers also developed fluorescent protein FRET-based sensors of Ca^{2+}, one of the most important secondary messengers in cell biology (15). Dubbed ‘cameleons,’ these indicators consisted of fusions between CFP, the Ca^{2+}-binding protein calmodulin (CaM), the CaM-binding peptide M13, and YFP (Figure 1-1) (16). Increased levels of Ca^{2+} causes CaM to bind to M13, thus changing the distance between the two fluorescent proteins and causing an increase in FRET. More recently, an improved CaM-based FRET indicator was used to detect single action potentials in neurons from brain slices and *in vivo*, a feat which was not possible with previously existing Ca^{2+} sensors (17, 18). The success of these probes, however, is limited by both sensitivity and impaired targeting efficiency due to the large size of the chimeric probe (19). Thus, alternative fluorescent protein-based Ca^{2+} sensors have been developed. One class of second-generation probes, named 'camgaroos,' is based on a single YFP which is pH sensitive (20). Another second-generation Ca^{2+} sensor, named 'pericam' because it is a circularly permutated version of YFP, enables ratiometric measurements, or the simultaneous recording of two distinct fluorescent signals that can allow for quantitative readouts (21). Imoto and co-workers have developed a high-affinity Ca^{2+} probe composed of a single GFP fused to CaM and M13 known as GCaMP (22). Others have developed an improved GCaMP sensor known as GCaMP2, which has been used to image Ca^{2+} in the murine heart (23) and to measure synaptic activity in zebrafish (24). GCaMP3, a more recent improvement to GCaMP2, is brighter and has a greater dynamic range as well as a higher affinity for Ca^{2+} (25).

Fluorescent protein-based FRET reporters for sensing glutamate were also developed by Tsien and co-workers and Frommer and co-workers. Glutamate is the major excitatory neurotransmitter in the brain, and monitoring its levels could provide insight into many neurological processes. Okumoto *et al*. have developed a FRET-based sensor consisting of CFP fused to both a clamshell-shaped bacterial glutamate periplasmic binding protein (YbeJ) and YFP (Figure 1-1) (26). Hires *et al*. have improved this sensor by optimizing the linker sequences and glutamate affinities to enhance its signal-to-noise ratio (27, 28).

A genetically-encoded fluorescent indicator of intracellular H_2O_2 was developed by Lukyanov and co-workers (29). H_2O_2 is a reactive oxygen species (ROS) that is speculated to be involved in paracrine signaling (30). Their design consisted of a fusion of a bacterial H_2O_2-sensitive transcription factor (OxyR) to a circularly permutated YFP. Cysteine oxidation of the OxyR portion induces a conformational change that changes the emission profile of the fluorescent protein. This probe has been used to image peroxide production during wound healing in zebrafish (31).

FRET-based sensors of protein post-translational modifications

Post-translational modifications of proteins are important regulators of protein function (32). Genetically-encoded FRET probes based on the initial design pioneered by Tsien and co-workers have been constructed for monitoring post-translational modifications such as phosphorylation, methylation, and glycosylation (Figure 1-1) (33).

Protein phosphorylation by protein kinases is key for the activation of numerous signal transduction pathways (34). The first FRET-based probes for phosphorylation, which sense protein kinase A and protein tyrosine kinase activities, were developed by Matsuda and co-workers and Tsien and co-workers (35, 36). These sensors consisted of CFP and YFP fused to a consensus substrate for the relevant kinase and a binding domain (36-38). Improved versions of these sensors with better specificity and reversibility have enabled visualization of protein phosphorylation by the tyrosine kinase SrcA during cell mechanotransduction as well as monitoring of protein kinase A activity during insulin signaling (39, 40). A number of groups have developed similarly designed FRET-based sensors of kinase activity. These include probes for Akt/protein kinase B (41, 42) and protein kinase C (43). For detailed reviews, see (33) and (35). More recently, Kapoor and co-workers have examined the dynamics of protein phosphorylation by aurora B kinase, a key mitotic regulator, using FRET-based sensors in live cells (44). There have also been reports of genetically-encoded sensors with enhanced sensitivity and optimized signal-to-noise ratios for fluorescence lifetime imaging (45, 46).

Ting and co-workers have developed CFP/YFP reporters of histone phosphorylation and methylation, which are important modifications that regulate transcription of nearby genes (47-49). Similarly, Mahal and co-workers have developed a FRET-based sensor of protein O-GlcNAcylation, a reversible form of glycosylation of intracellular proteins akin to phosphorylation (50, 51). Development of this probe has allowed for dynamic monitoring of O-GlcNAc modifications in live cells.

Small molecule sensors

Small molecule indicators can be more desirable then genetically-encoded ones in some circumstances because they often exhibit greater dynamic ranges and increased sensitivity (52). They also tend to exhibit faster response kinetics. However, unlike genetically-encoded sensors, with few exceptions they cannot be localized or specifically targeted to a particular organelle in the cell by fusion to the protein of interest (15).

Small molecule fluorophores have been developed for sensing metal ions such as calcium, zinc, copper, and iron. Metal ions are interesting targets for imaging because they play critical roles in cell biology (53). The design of small molecule sensors for metal ions is challenging because the probe must be selective for the specified metal over other biologically abundant cations, including those that exist at much higher cellular concentrations, such as Na^+, K^+, and Mg^{2+}. Thus, in order to create metal-selective probes, knowledge of the principles of coordination chemistry is critical in their design.

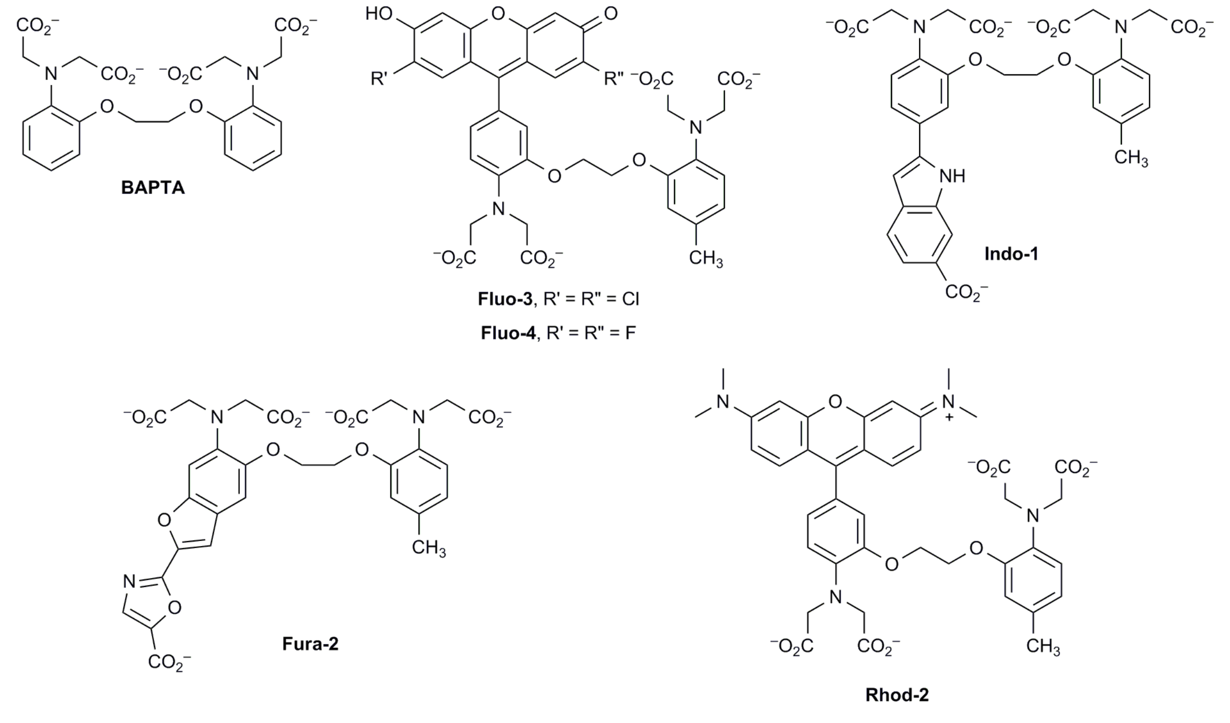

Figure 1-2. Small molecule fluorescent Ca^{2+} sensors.

Fluorescent Ca^{2+} indicators

The first small molecule fluorescent Ca^{2+} sensor was developed by Tsien (54). In this pioneering work, he replaced the two methylene groups of a well-known Ca^{2+} chelator with two benzene rings that enable the molecule to function as a chromophore (BAPTA, Figure 1-2). Since then, many low- and high-affinity dyes for Ca^{2+}-sensing have been developed that emit UV and visible light. Some of these probes include fluorescein derivatives developed by Molecular Probes (Eugene, OR) such as Fluo-4 (Figure 1-2), a brighter, more photostable derivative of Fluo-3 (Figure 1-2), which was developed by Tsien and co-workers (52). Indo-1 and Fura-2 are ratiometric dyes that are widely considered the standard for quantitative intracellular Ca^{2+} measurements (Figure 1-2) (55). Red-shifted Ca^{2+} indicators based on the rhodamine scaffold, including Rhod-2, have also been developed to minimize autofluorescence from biological samples (Figure 1-2) (55, 56). Tour *et al*. have combined the concept of a small molecule sensor of Ca^{2+} and the localization that the tetracysteine motif and FlAsH/ReAsH reagents provide by developing a biarsenical Ca^{2+} indicator to probe Ca^{2+} levels around specific proteins (57).

Small molecule Zn^{2+} indicators

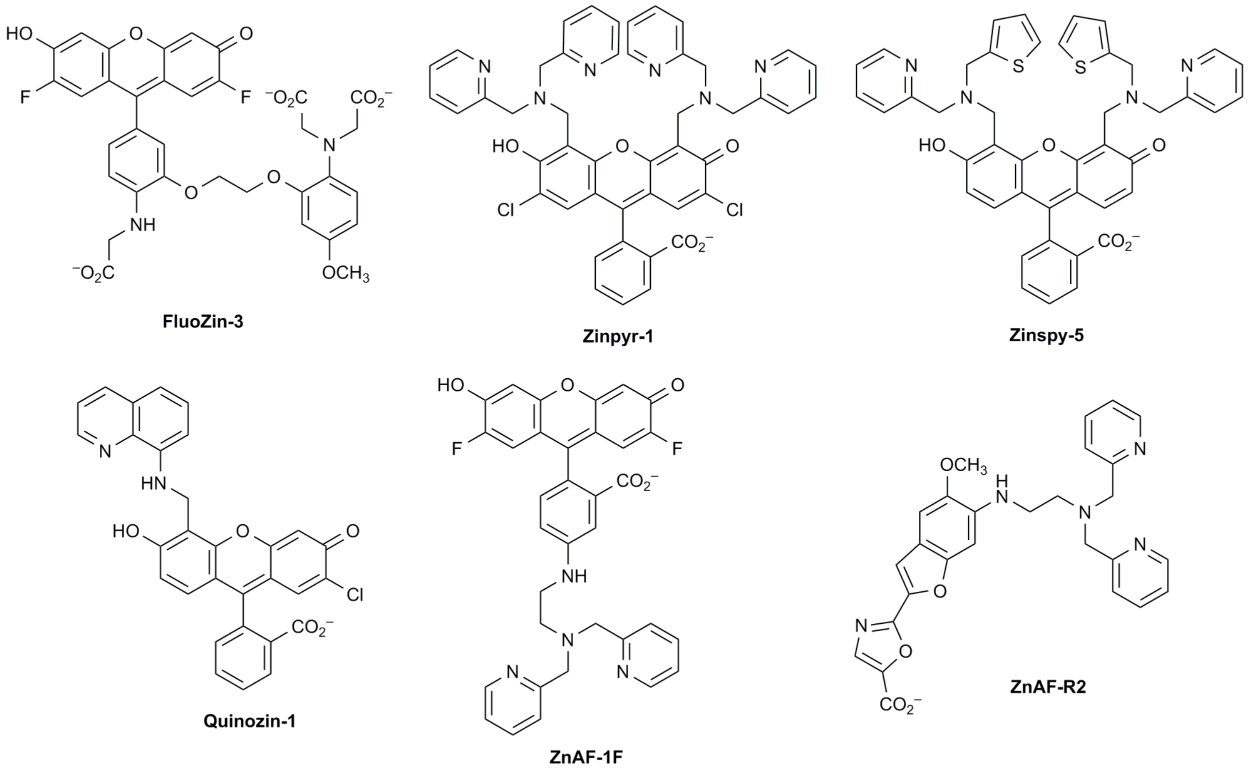

Figure 1-3. Small molecule fluorescent Zn^{2+} sensors.

In the past century, Zn^{2+} has emerged as an important regulator of protein function and signaling (58-60). It has also been implicated in the pathophysiology of several neurodegenerative disorders, including Alzheimer's disease (61). Thus, the ability to image Zn^{2+}

using small molecule sensors could elucidate the roles of zinc homeostasis in relation to disease progression.

Several groups have developed a number of Zn^{2+} sensors that were inspired by analogous probes for Ca^{2+} detection. Gee *et al*. have removed a single acetate arm from the Ca^{2+} chelator of Fluo-3 to create FluoZin-3, which maintains high affinity for Zn^{2+} (Figure 1-3) (62). Lippard and co-workers have developed several classes of fluorescein-based sensors for Zn^{2+} that are modified with a Zn^{2+} chelator on the xanthene core. These include the Zinpyr (63-67), Zinspy (68), and Quinozin (69) series of probes (Figure 1-3). Nagano and co-workers have developed fluorescein-based Zn^{2+} sensors that are functionalized at the phenyl ring of the fluorophore-scaffold (70). These include the ZnAF series (Figure 1-3). In addition to fluorescein-based reagents, BODIPY (71), cyanine (72, 73), and coumarin probes (74, 75) for sensing Zn^{2+} in biological systems have also been developed.

Several ratiometric sensors of Zn^{2+} that capitalize on different mechanisms have been synthesized for quantitative measurements of Zn^{2+} concentrations *in vivo*. FuraZin and IndoZin are ratiometric Zn^{2+} sensors derived from the Ca^{2+} probes Fura and Indo, which operate via an internal charge transfer mechanism (76). Nagano and co-workers have also developed ratiometric Zn^{2+} sensors ZnAF-R1 and -R2, which are based on the Fura scaffold (Figure 1-3) (77). Taki *et al*. have developed ratiometric sensors known as the Zinbo series that exploit excited-state intramolecular proton transfer processes in benzoxazole scaffolds (78). Lippard and co-workers have also developed ratiometric Zn^{2+}-sensors that rely on a two-fluorophore system in which ester-mediated hydrolysis liberates coumarin as an internal standard (79). In addition to fluorescent sensors, Zn^{2+} sensors that rely on alternative imaging modalities such as magnetic resonance imaging (MRI) have been developed (80-82).

Small molecule Cu^{+} and Fe^{2+}/Fe^{3+} indicators

Oxidative stress is thought to cause neuronal cell damage that can eventually lead to pathologies such as Alzheimer’s disease, Parkinson’s disease, and amyotrophic lateral sclerosis (83). Redox-active metals such as Cu^{+} and Fe^{2+} have been implicated in causing oxidative stress by producing ROS such as H_2O_2, superoxide anion ($O_2^{-}\cdot$), and hydroxyl radicals ($\cdot OH$) (84). Therefore, there has been much interest in imaging not only the ROS themselves but the metal ions as well.

Fluorescence detection of copper using small molecule sensors is difficult because Cu^{+} is the major copper species within the reducing environment of the cytosol; however, this ion can readily disproportionate to Cu^{2+} and Cu^{0}. In addition, both Cu^{+} and Cu^{2+} are capable of quenching the fluorescence (58). Currently, there are only two reports of fluorescent Cu^{+} sensors that have been successfully used for visualizing Cu^{+} in live cells. Yang *et al*. have developed a sensor known as CTAP-1 (Figure 1-4A), which comprises a pyrazoline dye platform appended to an azatetrathiacrown receptor for metal coordination (85). Chang and co-workers have developed a Cu^{+} indicator known as CS1 (Figure 1-4A) that combines a BODIPY dye and a thioether metal chelator (86, 87). Chang and co-workers have also developed a MRI-based sensor for copper (88, 89).

Like copper, the major forms of iron in the cell, Fe^{2+} and Fe^{3+}, also exhibit significant quenching capabilities, and designing fluorogenic sensors of iron is difficult as well. Thus, all of the sensors for detecting Fe^{2+}/Fe^{3+} in cellular systems are turn-off probes. For example, calcein (Figure 1-4B) is a commercially available fluorophore that uses a metal chelator for turn-off Fe^{2+}

detection (55). Phen Green SK (Figure 1-4B) is another commercial probe that can detect both Fe^{2+} and Fe^{3+} (55). One drawback of these probes, however, is that they are only partially selective for iron and can detect other metal ions as well (90). The most specific sensors for Fe^{3+} rely on receptors derived from siderophores, which are small, high-affinity iron chelating compounds secreted by bacteria, that can be conjugated directly onto fluorophores (55, 91, 92). A few turn-on sensors for Fe^{3+} have been reported; however, their utility for imaging in cells has not yet been established (93, 94).

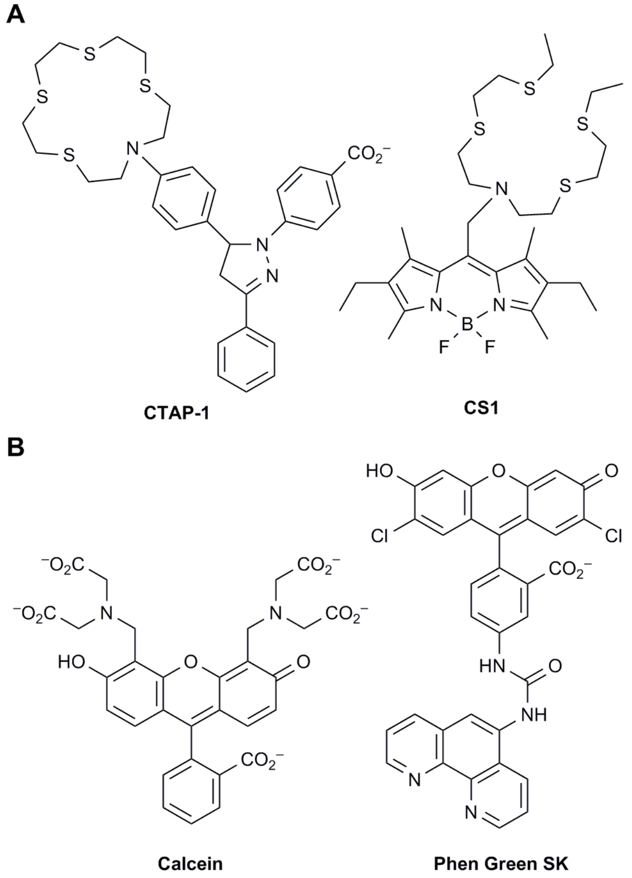

Figure 1-4. Small molecule fluorescent Cu^+ and Fe^{2+}/Fe^{3+} sensors.

Small molecule ROS and RNS indicators

As discussed above, there is mounting evidence that ROS are linked to several neurodegenerative diseases (83). Reactive nitrogen species (RNS) are also thought to cause neuropathological disorders (95). More recently, ROS and RNS have also been implicated as signaling molecules during normal physiological processes (30, 96). The canonical ROS and RNS involved in these processes are H_2O_2 and NO, respectively. Due to space limitation, herein we will discuss only small molecule fluorescence indicators of H_2O_2 and NO. For more in-depth reviews on sensors for other ROS and RNS as well as metal-based fluorogenic probes for NO, see (97), (98), (99), and (100).

The traditional indicators for sensing H_2O_2 include dihydrofluorescein (101) (DHFC, Figure 5A) or dihydrorhodamine (102) (Figure 1-5A); however, these dyes suffer from autooxidation by the excitation light as well as reactivity with other ROS (103, 104). Chang *et al*. have recently developed boronate-based fluorescent probes for sensing H_2O_2, which include their first generation probe Peroxy-fluor-1 (PF1, Figure 1-5A) (105). In the presence of H_2O_2, the boronic esters are chemoselectively deprotected to yield a fluorescent molecule. This concept has also been applied to blue- and red-shifted analogs, Peroxyxanthone-1 (PX1) and Peroxyresorufin-1 (PR1) (106). Second-generation probes that are more sensitive and are capable of detecting H_2O_2 at physiologically relevant concentrations have also been developed. These include Peroxycrimson-1 (PC1) and Peroxygreen-1 (PG1) (Figure 1-5A) (107). FRET-based ratiometric probes for sensing H_2O_2 have been developed as well (108).

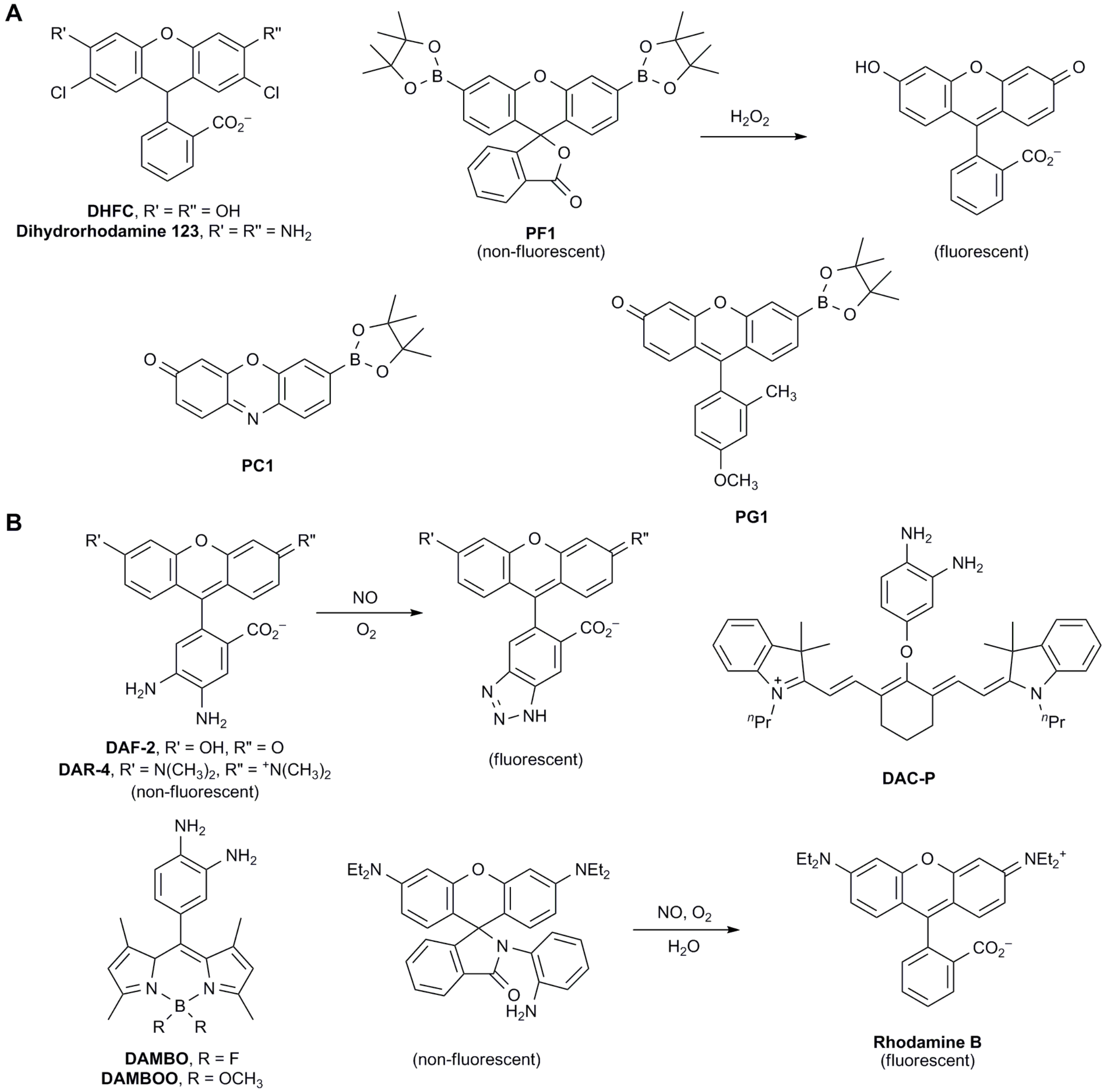

Figure 1-5. Small molecule fluorescent ROS/RNS sensors. (A) Fluorogenic H_2O_2 probes. (B) Fluorogenic NO probes.

Most sensors for NO utilize an *o*-phenylenediamine scaffold that is oxidized to the corresponding aryl triazole in the presence of NO and air (Figure 1-5B) (96). In this design, the electron-rich diamine quenches the fluorescence of the dye by photoinduced electron transfer. Reaction with NO and O_2 generates an electron-poor triazole that triggers the fluorescence turn-on of the dye. Nagano and co-workers have developed a wide variety of probes based on this design that contain fluorescein (109), rhodamine (110), BODIPY (111, 112), and cyanine (113) (Figure 1-5B). This group has also developed fluorescent sensors of NO that have increased sensitivity due to longer intracellular retention times (114). Recently, a variation of the *o*-phenylenediamine scaffold was developed which is based on a quenched rhodamine B spirolactam (Figure 1-5B) (115).

Chemical reporter strategy

For biomolecules such as glycans, lipids, certain protein post-translational modifications, and nucleic acids, detection via genetically-encoded reporters such as fluorescent proteins or small-molecule sensors is not possible. Thus, alternative strategies have been developed.

Lectins and antibodies for imaging glycans

Glycans are interesting targets for imaging because they play key roles in many dynamic biological processes. For example, cell-surface glycans are known to mediate cell-cell adhesion and communication as well as host-pathogen interactions (116). Other examples include embryonic development (117), leukocyte homing (118), and cancer cell metastasis (119). Traditionally, glycans have been detected using antibodies or carbohydrate-binding proteins known as lectins (120). Though lectins have been widely used for the detection and enrichment of glycoconjugates (121, 122), these glycan-binding proteins generally have low affinities for their targets and require multivalency for high-avidity binding (123). Other drawbacks include toxicity and tissue impermeability (124). For these reasons, lectins have limited capabilities for *in vivo* imaging; however, they have been used routinely for imaging glycans *ex vivo* on cultured cells and on tissue samples (125, 126).

Like lectins, antibodies have limited use for *in vivo* imaging, though there is one report of glycan-specific imaging in mice. In this study, Licha *et al*. imaged a peripheral lymph node endothelial glycan termed sulfoadhesin using the MECA-79 antibody (127). Though there are a number of monoclonal antibodies against distinct epitopes, it is difficult to generate antibodies against certain epitopes because the synthesis of many glycan structures can be very cumbersome (128). Thus, applications of antibodies toward *in vivo* imaging are also limited. Furthermore, antibodies also suffer from poor tissue access (129).

Bioorthogonal chemical reporter strategy for imaging glycans

Though lectins and antibodies have been used to image glycans, they are not ideal for imaging dynamic changes in the glycome, the ensemble of glycans displayed on the cell surface. We have developed a complementary approach for imaging the glycome that enables the visualization of glycan dynamics *in vivo* (130). Our method is a two-step strategy in which the first step involves the metabolic incorporation of an unnatural monosaccharide into an organism's glycome (131). This substrate analog contains a reactive group known as a "chemical reporter.” In the second step, the chemical reporter is labeled with an imaging probe via a chemoselective reaction (132).

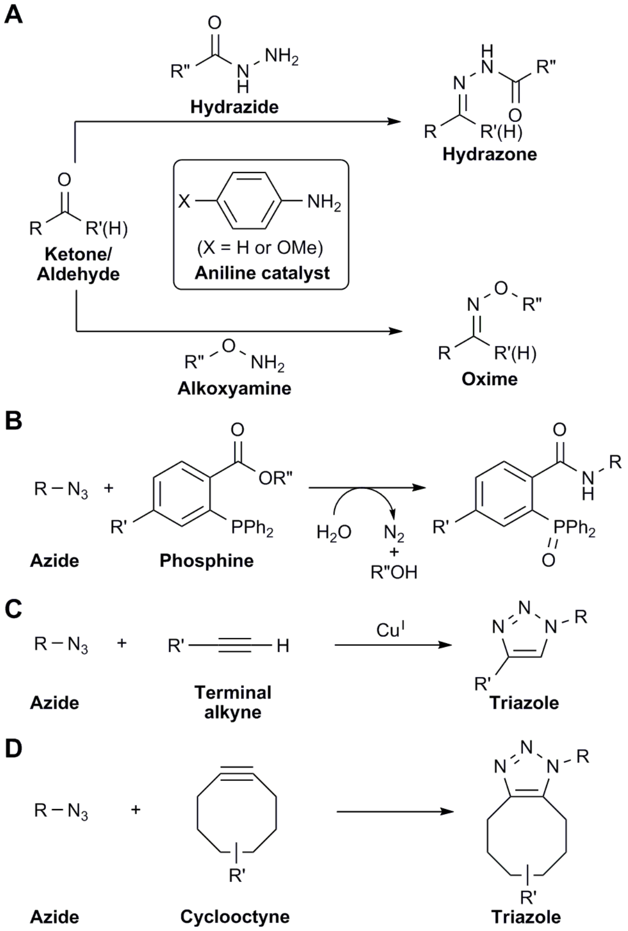

Figure 1-6. Bioorthogonal chemical reactions. (A) Ketone and aldehyde condensation with hydrazides or alkoxyamines. (B) Staudinger ligation between azides and triarylphosphines. (C) Copper-catalyzed azide-alkyne 1,3-dipolar cycloaddition (CuAAC). (D) Cu-free click chemistry.

The requirements for such a chemical reaction are quite rigorous. First, the chemical reporter and its reaction partner must react in a physiological environment (pH 6-8, 37 °C), while simultaneously remaining inert to all of the surrounding functionality in the biological milieu. This task is challenging because there are many nucleophilic and electrophilic functional groups found in cells and living organisms. Second, the reaction must not produce any toxic byproducts or cause harm to the biological sample. Finally, the reporter and its complementary probe must have good bioavailability and form a stable bond. Chemical reactions that meet this collection of criteria are known as “bioorthogonal” (132).

Currently, only a handful of reactions possess the quality of bioorthogonality. These reactions include the condensation of ketones and aldehydes with hydrazide or alkoxyamine probes, the Staudinger ligation of triarylphosphines and azides, and Cu-free click chemistry between cyclooctynes and azides (Figures 1-6A-B, D). These reactions have been used to label not only proteins but glycans and lipids as well.

Ketones and aldehydes are not truly bioorthogonal because keto and aldehydic metabolites are abundant within cells and in biological fluids. In addition, the pH optima of hydrazone and oxime formation with hydrazide and alkoxyamine groups is 3-5, which precludes their use *in vivo* (133). Ketones and aldehydes have been utilized to label proteins and glycans on cell surfaces and in the extracellular environment. These mild electrophiles can form reversible Schiff bases with primary amines such as lysine side chains; however, in water, the equilibrium favors the carbonyl. In contrast, the formation of hydrazones and oximes using hydrazide and aminooxy groups, respectively, are favored in physiological conditions and are quite stable (Figure 1-6A). Dawson and co-workers have greatly accelerated both oxime and hydrazone formation via the use of a nucleophilic aniline catalyst (134, 135).

We have recognized the utility of ketones and aldehydes as chemical reporters and have used them to label glycans (136). In this work, Mahal *et al*. reported that an unnatural keto analog of *N*-acetylmannosamine (ManNAc), *N*-levulinoylmannosamine (ManLev), can be metabolized by mammalian cells to the corresponding keto sialic acid (SiaLev) and incorporated within cell-surface glycans (Figure 1-7A-B) (136). Sadamoto *et al*. have introduced ketones into bacterial cell walls and labeled the chemical reporters with a hydrazide-fluorophore probe (137).

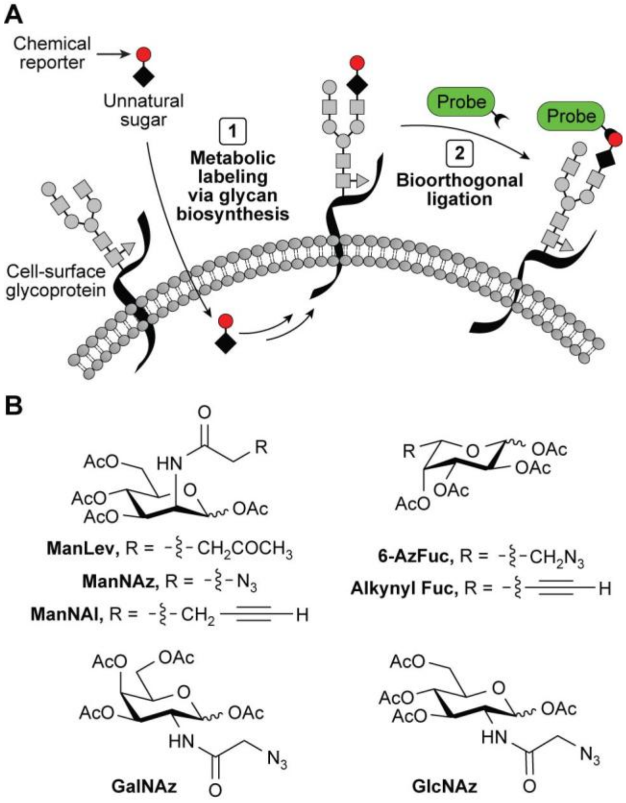

Figure 1-7. Bioorthogonal chemical reporter strategy. (A) Metabolic labeling of cell-surface glycans. (B) Unnatural keto, azido, and alkynyl monosaccharides utilized for metabolic labeling.

More recently, the azide has emerged as the chemical reporter of choice. This functional group is unique in that it is truly bioorthogonal to the biological milieu. Only one naturally occurring azido-metabolite, which was isolated from unialgal cultures, has been reported to date (138). Moreover, azides can undergo highly selective reactions such as the Staudinger ligation with triarylphosphines, the copper-catalyzed azide-alkyne 1,3-dipolar cycloaddition (CuAAC), and Cu-free click chemistry with strained alkynes (Figure 1-6B-D) (139).

The Staudinger ligation is based on the classic Staudinger reduction, which was developed by Hermann Staudinger in 1919. In this work, Staudinger reported that azides react with triarylphosphines under mild conditions to yield aza-ylide intermediates (140). In the presence of water or an appropriate electrophile, this intermediate can be hydrolyzed or trapped to yield an amine and the corresponding phosphine oxide (141). We modified the classic Staudinger reaction by introducing an electrophilic trap onto the phosphine (142). Termed the Staudinger ligation, this reaction ultimately results in the formation of a covalent amide bond between the azide and phosphine along with oxidation of the phosphine (Figure 1-6B). This reaction also proceeds at physiological pH with no apparent toxicity to live cells and whole organisms (143).

We have shown that an azide-containing analog of ManNAc, termed *N*-azidoacetylmannosamine (ManNAz), can also be metabolically incorporated into cell-surface glycans as the corresponding azido sialic acid (SiaNAz) (Figure 1-7) (142). The Staudinger ligation has been used to image these labeled glycans on live cells using phosphine fluorophore conjugates (144) as well as fluorogenic phosphines (145). Furthermore, we have shown that this reaction can be used to label glycans within living animals (143, 146).

Paulson and co-workers have shown that natural sialic acids can be oxidized to the corresponding aldehyde using sodium periodate and then subsequently imaged using oxime chemistry with alkoxyamine probes (147). In addition to sialic acid-containing glycans, other sectors of the glycome can be metabolically labeled using azido analogs of *N*-acetylgalactosamine (mucin-type O-linked glycans), *N*-acetylglucosamine (β-O-GlcNAcylated proteins), and fucose (fucosylated glycans) (Figure 1-7B) (148-151).

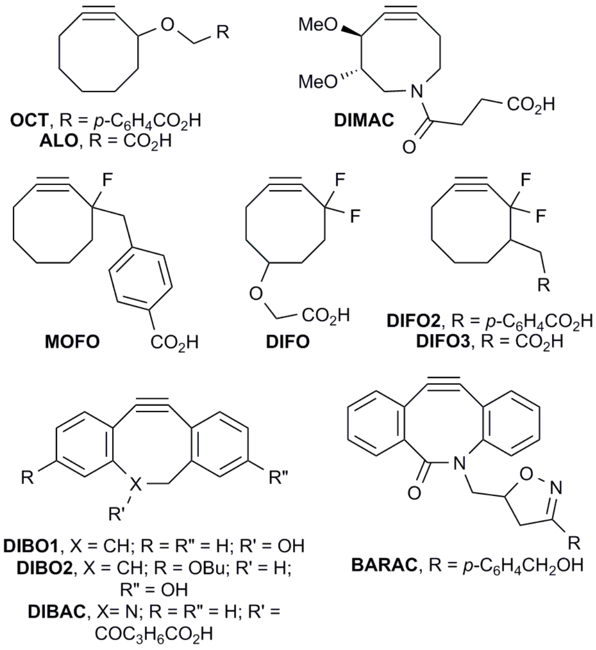

Figure 1-8. Cyclooctyne reagents for Cu-free click chemistry.

Azides can also be exploited as 1,3-dipoles in a [3+2] cycloaddition with alkynes to form triazole products (Figure 1-6C) (139). Sharpless and co-workers and Meldal and co-workers independently showed that the normally sluggish reaction between azides and acetylenes can be greatly accelerated by the addition of a copper catalyst (152, 153). The copper-catalyzed azide-alkyne 1,3-dipolar cycloaddition (CuAAC) is one of the most popular reactions from a family of "click reactions," defined by their highly selective and modular approach to forming chemical bonds (154). CuAAC is much faster than the Staudinger ligation; however, the necessary copper catalyst is cytotoxic (131). CuAAC has been used for imaging glycans using alkynyl ManNAc analogs as well as azido and alkynyl fucose analogs in fixed cells (Figure 1-7B) (151, 155, 156).

We have eliminated the need for a toxic copper catalyst by activation of the alkyne via an alternative mechanism—ring strain. This reaction is accordingly known as Cu-free click chemistry. Agard *et al*. first demonstrated this concept using a cyclooctyne reagent (OCT) whose kinetics were on par with the phosphine reagents utilized in the Staudinger ligation (Figures 1-6D and 1-8) (157). In order to accelerate the strain-promoted cycloaddition, Baskin *et al*. introduced fluorine atoms in an attempt to lower the LUMO energy of the alkyne (MOFO, DIFO, DIFO2, and DIFO3; Figure 1-8) (158, 159). Several theoretical studies have been published to explain the enhanced reactivity of these fluorinated cyclooctynes (160, 161). This reaction has been used to image glycans on live cells (158), the nematode *C. elegans* (162), and zebrafish embryos (163). We have also shown that Cu-free click chemistry can be used to label glycans within mice (164). Second-generation cyclooctynes have been developed including more water-soluble probes (ALO and DIMAC, Figure 1-8) (159, 165) as well as faster reagents based on a dibenzocyclooctynyl scaffold (DIBO1-2, DIBAC, and BARAC; Figure 1-8) (166-168).

Bioorthogonal chemical reporter strategy for imaging lipids

As secondary metabolites and protein post-translational modifications, lipids, like glycans, are not amenable to imaging via genetically-encoded reporters. Lipids are attractive targets for imaging because they play important roles in cellular processes such as signal transduction and membrane fusion. In addition, lipidation of proteins regulates the signaling properties, subcellular localization, trafficking, and activity of many proteins (169). One approach to imaging lipids in live cells has been the application of the bioorthogonal chemical reporter strategy (170).

Phospholipids are the major constituents of cell membranes. Those containing the head group choline are important structural components of membranes and play critical roles in cell signaling (171). Despite the crucial roles of these lipids, little is known about their localization and trafficking (172). Thus, Jao *et al*. have utilized the chemical reporter strategy in order to image their dynamics in cells and tissues. In order to achieve this goal, they synthesized a choline analog that contains a terminal alkyne moiety, which can be detected by using CuAAC (Figure 1-9). Using this technology, they were able to examine the kinetics of phospholipid turnover and the distribution of the lipids in cells and in mice (172). Similarly, Schultz and co-workers have shown that phosphatidic acid analogs that contain either terminal alkynes or cyclooctynes within the lipid tail can be used to image these lipids in cells (Figure 1-9) (173).

Lipidation of proteins via fatty-acylation and prenylation has been known to greatly affect the specificity and efficiency of signal transduction as well as protein-protein interactions (169). Several groups have applied the bioorthogonal chemical reporter strategy to image these protein post-translational modifications. Zhao and co-workers have used azido analogs of farnesylated proteins in order to profile proteins that are post-translationally modified (Figure 1-9) (174). Hang and co-workers and Berthiaume and co-workers have demonstrated that fatty-acylation of eukaryotic proteins by attachment of *S*-palmitoyl groups and *N*-myristoyl to cysteine and *N*-terminal glycine residues, respectively, can be imaged or profiled by employing azido and alkynyl analogs of these lipids and the Staudinger ligation or CuAAC (Figure 1-9) (175-179).

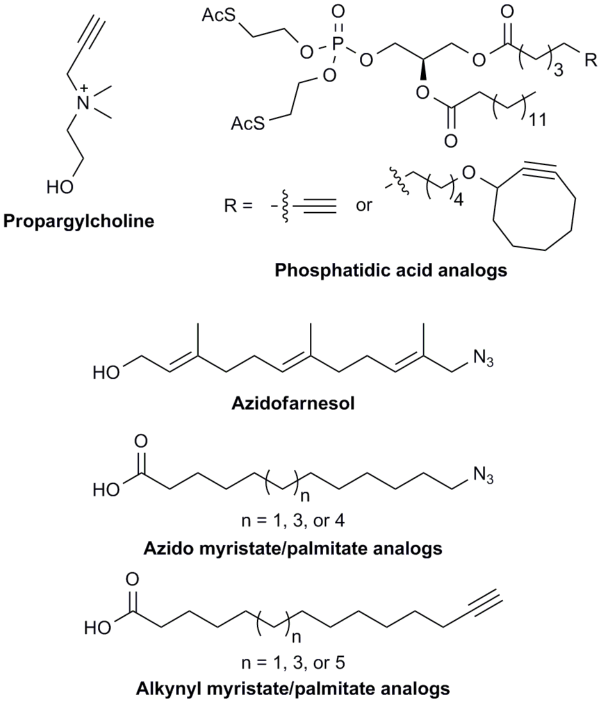

Figure 1-9. Chemical reporters for profiling and visualizing lipids in living systems.

Bioorthogonal chemical reporter strategy for imaging nucleic acids

Nucleic acids are traditionally detected by *in situ* hybridization techniques as well as metabolic incorporation of nucleotide analogs that are either radiolabeled or detected via antibodies. Hybridization approaches include molecular beacons, which have been used for visualizing both DNA and RNA (180, 181). Development of these fluorescent oligonucleotide probes requires the incorporation of fluorescent nucleotides, which can be synthesized using different chemistries (182). For example, Ju and co-workers have synthesized fluorescent oligonucleotides via both CuAAC and the Staudinger ligation for the purposes of DNA sequencing using fluorescence detection (183, 184). Excess fluorophore conjugates of oligonucleotide probes must be washed away to eliminate background signal, so fluorogenic approaches are highly sought after as well. Toward this end, Cai *et al*. have developed a fluorogenic peptide nucleic acid-based probe that is activated by the Staudinger ligation upon DNA hybridization (185).

Other techniques include metabolic incorporation of deoxynucleoside analogs such as [^{3}H]thymidine ([^{3}H]T) and 5-bromo-2'-deoxyuridine (BrdU) (Figure 1-10). [^{3}H]T and BrdU are detected by autoradiography and immunohistochemistry, respectively. Though these analogs have been useful for probing DNA synthesis, both of these techniques are not ideal.

Autoradiography can be cumbersome, and BrdU immunostaining can compromise the integrity of the tissue samples (186). Mitchison and co-workers have synthesized an alkynyl analog of thymidine, 5-ethynyl-2'-deoxyuridine (EdU, Figure 1-10), which is readily incorporated into DNA during DNA replication (187). This chemical reporter can then be detected with CuAAC and has enabled visualization of DNA synthesis in cells and on tissue sections from mice. In addition, this methodology does not cause degradation of the biological samples. More recently, an alkynyl analog of uridine, 5-ethynyluridine (EU, Figure 1-10) has been used to image RNA synthesis *in vivo* using an analogous strategy (188).

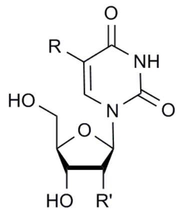

	R	R'
[^{3}H]T	$C(^3H)_3$	H
BrdU	Br	H
EdU	≡—H	H
EU	≡—H	OH

Figure 1-10. Metabolic labels for nucleic acids.

Label-free imaging methods

Imaging mass spectrometry

All of the technologies discussed thus far require labels or contrast agents in order to image the biological molecules of interest. Imaging mass spectrometry (IMS) is an emerging label-free technique that allows for the visualization of endogenous proteins, lipids, and small molecules (189). IMS can be used to create 2D and 3D images of the proteomic or small molecule content of cells or tissues by combining the measurement capability of mass spectrometers with a surface sampling process (190). Currently, two main ionization methods are used to generate images. These techniques include matrix-assisted laser desorption ionization (MALDI) and secondary ion mass spectrometry (SIMS) IMS. Though IMS has been used for imaging both proteins and other biological molecules, for the purposes of this Chapter, we will focus exclusively on imaging small molecules.

Of the two IMS techniques, MALDI IMS has seen more widespread use for analyzing biological samples due to its large mass-to-charge ratio (m/z) range (up to 100,000), which is useful for analyzing proteomes (191). Imaging with MALDI mass spectrometry, however, is only capable of achieving resolutions of about 20 μm, while SIMS can achieve better than 100 nm with specialized instruments (192). On the other hand, SIMS has been documented to detect molecules of masses up to only 1 kDa (190). While many groups have taken advantage of these imaging technologies, a number of laboratories continue to pursue the development of new and improved methodologies, including those that can achieve ionization under ambient conditions (193, 194).

For analysis by MALDI IMS, biological samples are prepared in a similar manner to protein or peptide samples. Typically, a thin cryosection of tissue is covered with an organic matrix. The sample is then scanned by the mass spectrometer, and spectra are collected over a predefined area. The resulting data set contains an array of spectra including different signals of measured mass and intensity. The intensity of the signal or combinations of signals can then be plotted to generate an image over the sample surface (195). This technique has been used to image many different molecules, including phospholipids (195). As discussed above, these lipids are involved in cell signaling pathways and have been implicated in diseases such as lipid storage disorders as well as Alzheimer's disease and Down syndrome (196). McLean *et al*., Jackson *et al*., and Rujoi *et al*. have used MALDI IMS to visualize phospholipids in rat brains and mammalian lens tissue (197-199). Lipid distribution maps have also been obtained in colon cancer tissues as well as tissue samples from patients with Fabry's disease (200, 201). In addition to lipids, Dorrestein and co-workers have applied MALDI IMS to imaging secondary metabolites produced by marine cyanobacteria and sponges (202) as well as in *Bacillus subtilis* and *Streptomyces coelicolor* (203).

SIMS relies on an accelerated primary ion beam to ionize the sample by bombarding the surface to generate secondary ions, which are then detected by a mass spectrometer (192). Based on instrument design, there are two different approaches to SIMS. The first method, time-of-flight (TOF) SIMS, uses a primary ion beam that is pulsed, and the resulting secondary ions are detected by a TOF mass spectrometer. The second approach, termed dynamic SIMS, uses a continuous primary ion beam, and preselected ions are detected by a magnetic sector mass spectrometer. SIMS has not been widely adopted for analyzing biological samples because of its poor sensitivity and spatial resolution, though specialized instruments are being developed to address these issues (*vide infra*) (192). It is also challenging to identify the molecules due to extensive fragmentation of the ionic species. TOF-SIMS, however, has been used to image lipids in cells and tissues (204-206). TOF-SIMS has also been used to image highly curved membranes during Tetrahymena mating (207). In this study, Ostrowski *et al*. discovered that the fusion region contains elevated amounts of 2-aminoethylphosphonolipid, a high-curvature lipid.

In the last decade, advancements in instrumentation have greatly improved the utility of SIMS for imaging biological samples. These developments include nanoSIMS, which allows image resolution of a few tens of nanometers (192). This technique has been applied in tracer studies examining ^{13}C-labeled free fatty acid transport across cell membranes (208). Boxer and co-workers have used nanoSIMS to image lipid domains within supported lipid bilayers with a lateral resolution of 100 nm (209). NanoSIMS has also been used to demonstrate that deep-sea anaerobic methane-oxidizing archaea fix nitrogen and cyanide and share the products with sulfate-reducing bacterial symbionts (210). Lechene *et al*. have developed multiple-isotope imaging mass spectrometry (MIMS), in which multiple isotopes are detected simultaneously, enabling both imaging and quantification of labeled molecules within subcellular compartments (211). Other technical advances include cluster time-of-flight (TOF)-SIMS, which has been shown to improve the yield of secondary ions produced (212). This technique utilizes heavier primary ions that have improved efficiency for production of secondary ions, thus allowing easier identification of biomolecules. Many groups have demonstrated that cluster TOF-SIMS imaging can be used to image lipids in rodent brains and tissues (213-217). Finally, Heeren and co-workers have developed matrix-enhanced SIMS (ME-SIMS), which combines the high spatial resolution of SIMS with the sample preparation of MALDI IMS (218). Like cluster TOF-SIMS, ME-SIMS also increases the molecular ion yield.

Raman and coherent anti-Stokes Raman scattering (CARS) microscopy

Raman and coherent anti-Stokes Raman scattering (CARS) microscopy rely on optical signals for imaging biological specimens (219). Both of these techniques have been used to image proteins, lipids, and nucleic acids. Xie and co-workers have recently demonstrated that stimulated emission can also be used as a contrast mechanism for microscopy (220). They have used this technique to image chromoproteins, small molecule drug distributions *in vivo*, as well as hemoglobin. For the purposes of this Chapter, we will focus exclusively on Raman and CARS applications of imaging small molecules.

Raman microscopy relies on a phenomenon known as Raman scattering. This effect occurs when the wavelength of scattered light shifts slightly from the original wavelength of light due to excitation of the light-scattering molecules to a vibrationally excited state (219). Because the shift in wavelength depends strongly on the molecule's structure and chemical environment, the resulting spectra can be used to identify specific molecules in the sample. In Raman microscopy, spectra are obtained from each position in the sample to construct a 2D or 3D image of molecular distribution based on signal intensities. This imaging technique has been used to visualize nucleic acids (221, 222) and lipid bodies (223) in live cells. Raman microscopy has also been used to discern malignant tissue from healthy tissue for cancer diagnostic purposes (224-226). More recently, Xie and co-workers have greatly improved the sensitivity of Raman microscopy by developing a new technique known as stimulated Raman scattering (SRS) microscopy (227). They have used SRS imaging to visualize lipids in live cells and tissues from mice.

Raman microscopy, however, suffers from several limitations (228). First, the Raman effect is very weak, and consequently, data acquisition times are long. Second, the creation of images requires high powered lasers and long integration times per pixel, impeding video-rate microscopy. Much stronger vibrational signals can be obtained using CARS microscopy. In CARS, light beams with two different optical frequencies interact with the sample. A strong CARS signal is produced when the difference of the two frequencies matches the vibrational frequency of the molecules. Because CARS is orders of magnitude more sensitive than Raman microscopy, it enables video-rate vibrational imaging. The Reintjes group was the first to use CARS as a contrast mechanism for microsopy (229). The technique was popularized by Xie and co-workers almost two decades later when they developed a greatly improved method that allowed for higher sensitivity, higher spatial resolution, and three-dimensional sectioning capabilities (230).

Since then, CARS has been used extensively for many *in vitro* and *in vivo* imaging applications. Wurpel *et al*. and Potma *et al*. have used CARS to image lipid vesicles and lipids on supported bilayers (231, 232). Xie and co-workers have also used CARS to image lipids in live cells (233-235). Others have imaged lipids in infection models (236, 237), mouse brains (238), and whole organisms such as *C. elegans* (239). Improvements to CARS include video-rate microscopy applications of imaging lipids in the skin of live mice (240) as well as frequency modulation CARS, which significantly increases the detection sensitivity of CARS by decreasing the non-resonant background (241).

Non-optical imaging methods

Non-optical imaging modalities that exploit other wavelengths of the electromagnetic spectrum, including gamma rays and radiowaves, are used regularly in the clinic. These include positron emission tomography, single photon emission computed tomography, MRI, and magnetic resonance spectroscopic imaging.

Positron emission tomography (PET) imaging

Positron emission tomography (PET) imaging is used clinically to diagnose cancer and to monitor disease progression and response to therapy (242). PET detects gamma rays produced by a radioactive isotope tracer that is injected into the patient. The radioactive tracer emits positrons from its nucleus (243). A single positron eventually collides with a nearby electron, and the two particles annihilate each other to produce energy in the form of two gamma rays, which are emitted 180 degrees apart. These gamma rays are then detected by a camera. Commonly used PET isotopes include ^{15}O, ^{13}N, ^{11}C, and ^{18}F (1). Other less commonly used ones include ^{14}O, ^{64}Cu, ^{62}Cu, ^{124}I, ^{76}Br, ^{82}Rb, and ^{68}Ga. Most of these isotopes are produced in a cyclotron, and some can be produced in a generator. Many of these isotopes also have short half-lives, e.g., the half-life of ^{18}F is 110 minutes.

An ^{18}F-labelled analog of glucose, 2-[^{18}F]fluoro-2-deoxy-D-glucose (FDG), is the most widely used tracer for oncological PET imaging (244). This glucose analog is transported into cells by glucose transporters and then phosphorylated by hexokinase to form FDG-6-phosphate. Because FDG-6-phosphate is not a substrate for downstream glycolytic enzymes, this compound rapidly accumulates in cells that have increased hexokinase activity and levels of glucose transporters, which include tumor cells. This preferential uptake allows for the routine clinical detection of tumors over surrounding tissue in human patients.

In basic research, PET imaging has also been used for monitoring cell proliferation ([^{11}C]thymidine and 3'-deoxy-3'-[^{18}F]fluorothymidine) (245, 246), bone metastasis ([^{18}F]fluoride) (247, 248), perfusion (^{15}O-labeled water) (249), as well as hypoxia ([^{18}F]fluoromisonidazole) (250). In addition, the use of ^{11}C- and ^{18}F-labeled choline has recently gained attention for applications in prostate cancer imaging (251-253).

Single photon emission computed tomography (SPECT) imaging

Single photon emission computed tomography (SPECT) detects photons from gamma-emitting isotopes, such as ^{99m}Tc, ^{111}In, ^{123}I, and ^{131}I (1). These nuclides are relatively inexpensive, and their longer half-lives obviates the need for a cyclotron. The emitted gamma rays are detected by cameras that rotate around the subject to create a 3D tomographic image. Compared to PET imaging, SPECT has similar spatial resolution but is 10-fold less sensitive (1). Like PET, there have been advances in the imaging of molecular targets, though SPECT has not yet been used clinically. Some examples of imaging applications in mice include imaging apoptosis via ^{99m}Tc-labeled annexin V, which binds phosphatidylserine (254), as well as mRNA via ^{111}In-labeled oligodeoxynucleotides (255).

MRI and magnetic resonance spectroscopic imaging (MRSI)

Like PET, magnetic resonance imaging (MRI) has been used clinically to diagnose cancer (1). In MRI, the relaxation of unpaired nuclear spins, or magnetic dipoles, from organic molecules or water is detected after the subject is pulsed with radiowaves in the presence of a strong magnetic field. In the MRI scanner, a strong magnet that produces the magnetic field causes these magnetic dipoles to align themselves with the field. Following the pulse, the dipoles return to their baseline orientation, which is detected by a radiofrequency coil. A scanner determines the rate of relaxation, and this measurement is converted into an MR signal. MRI contrast relies on the fact that dipoles in different physicochemical environments will have different relaxation times and generate different signals. Clinically, MRI can detect tumors based on contrast provided by differences in relaxation time of the protons in the tumor compared to surrounding tissue.

Within the last two decades, the concept of using magnetic resonance spectroscopy for clinical imaging has emerged. Magnetic resonance spectroscopic imaging (MRSI) is a relatively new method that allows for the visualization of small molecule metabolites in cells and tissues. Proton MRSI has been applied to characterizing the metabolic profiles of brain tumors in the hopes of distinguishing diseased from healthy tissue (256). Many groups have shown that levels of *N*-acetylaspartate decrease while those of choline-containing compounds increase in the tumor relative to normal brain (257-261). Heesters *et al*. have also shown that lactate is present in high-grade gliomas and unspecified astrocytomas but absent in most low-grade gliomas (262). Other groups have shown that lipid levels are also higher in brain tumors (263, 264). A number of studies have tried to correlate relative ratios of the different metabolites in order to classify tumor tissue; however, no criteria that clearly separate all tumor types have been developed (265). In addition to brain tumors, MRSI has also been used to profile similar metabolites in prostate and breast cancers (266, 267).

In the last decade, many groups have begun to use hyperpolarized molecules to increase the enhancement of the MR signal (268). Hyperpolarization is achieved by placing the sample in a high magnetic field and keeping it at very low temperatures until the hyperpolarized state is achieved (268). The increase in the relative number of nuclei aligned with the magnetic field greatly improves the signal-to-noise ratio when acquiring the spectrum. Because of its increased sensitivity, this method also allows for the detection of nuclei other than hydrogen in which the NMR-active nucleus has a lower natural abundance. The most commonly used isotope is ^{13}C, although in principle, other nuclei such as ^{15}N (269) or ^{3}He could be used as well (270). Hyperpolarized ^{129}Xe biosensors have also been developed and are reviewed elsewhere (270, 271).

Currently, all applications of hyperpolarized MRSI *in vivo* use ^{13}C-labeled small molecules (268). The first angiographic image of hyperpolarized ^{13}C-labeled pyruvate was reported by Golman *et al*.(272). Pyruvate is a key molecule in primary metabolism in mammalian cells (268). Subsequently, a number of studies using ^{13}C-labeled pyruvate have emerged. The first example of tumor imaging *in vivo* using this technique was reported by Golman *et al*. (273). In their work, they showed that the tumor tissue contained higher levels of lactate and lower levels of alanine. ^{13}C-labeled pyruvate has also been used to image prostate cancer in a transgenic adenocarcinoma of mouse prostate (TRAMP) mouse model (274). Kurhanewicz and co-workers have used hyperpolarized ^{13}C-labeled pyruvate to examine other metabolic products including lactate and alanine in the same TRAMP model (275). Nelson *et al*. have extended this technology to higher organisms by injecting ^{13}C-labeled pyruvate into dogs to image increased levels of lactate in prostate tumor tissues (276). Another study has shown that the levels of lactate in tumors decrease following tumor therapy (277). Other applications of MRSI also exist. For instance, numerous groups have examined cardiac metabolism using ^{13}C-labeled pyruvate (268). More recently, Gallagher *et al*. have shown that MRSI can be used to image changes in pH *in vivo* using hyperpolarized ^{13}C-labeled bicarbonate (278).

Conclusions

Imaging has revolutionized our understanding of basic processes in cell biology as well as disease development and progression. For example, macroscopic imaging modalities such as X-ray imaging and MRI have greatly advanced our understanding of human anatomy and physiology. In the past few decades, microscopic imaging techniques such as fluorescence imaging have enabled the visualization of molecular events in cellular systems and model organisms. Despite these significant advances, many challenges remain for the future. The translation of imaging technologies to use *in vivo* has been slower than anticipated. Ultimately, it is hoped that the application of these new tools in living systems will shed light on fundamental biological processes and aid in disease diagnosis and treatment.

References

1. Massoud TF, Gambhir SS (2003) Molecular imaging in living subjects: Seeing fundamental biological processes in a new light. *Genes Dev* 17:545-580.

2. Gaietta G, *et al.* (2002) Multicolor and electron microscopic imaging of connexin trafficking. *Science* 296:503-507.

3. Tsien RY (2009) Constructing and exploiting the fluorescent protein paintbox (Nobel Lecture). *Angew Chem Int Ed Engl* 48:5612-5626.

4. Alberts B, *et al.* (2008) *Molecular Biology of the Cell* (Garland Science, New York).

5. Zhang J, Campbell RE, Ting AY, Tsien RY (2002) Creating new fluorescent probes for cell biology. *Nat Rev Mol Cell Biol* 3:906-918.

6. Martin TF (1998) Phosphoinositide lipids as signaling molecules: Common themes for signal transduction, cytoskeletal regulation, and membrane trafficking. *Annu Rev Cell Dev Biol* 14:231-264.

7. Halet G (2005) Imaging phosphoinositide dynamics using GFP-tagged protein domains. *Biol Cell* 97:501-518.

8. Varnai P, Balla T (2006) Live cell imaging of phosphoinositide dynamics with fluorescent protein domains. *Biochim Biophys Acta* 1761:957-967.

9. Adams SR, Harootunian AT, Buechler YJ, Taylor SS, Tsien RY (1991) Fluorescence ratio imaging of cyclic AMP in single cells. *Nature* 349:694-697.

10. Zaccolo M, *et al.* (2000) A genetically encoded, fluorescent indicator for cyclic AMP in living cells. *Nat Cell Biol* 2:25-29.

11. Zaccolo M, Pozzan T (2002) Discrete microdomains with high concentration of cAMP in stimulated rat neonatal cardiac myocytes. *Science* 295:1711-1715.

12. Dyachok O, Isakov Y, Sagetorp J, Tengholm A (2006) Oscillations of cyclic AMP in hormone-stimulated insulin-secreting beta-cells. *Nature* 439:349-352.

13. Dipilato LM, Zhang J (2009) Fluorescent protein-based biosensors: Resolving spatiotemporal dynamics of signaling. *Curr Opin Chem Biol* in press.

14. Willoughby D, Cooper DM (2008) Live-cell imaging of cAMP dynamics. *Nat Methods* 5:29-36.

15. McCombs JE, Palmer AE (2008) Measuring calcium dynamics in living cells with genetically encodable calcium indicators. *Methods* 46:152-159.

16. Miyawaki A, *et al.* (1997) Fluorescent indicators for Ca^{2+} based on green fluorescent proteins and calmodulin. *Nature* 388:882-887.

17. Wallace DJ, *et al.* (2008) Single-spike detection in vitro and in vivo with a genetic Ca^{2+} sensor. *Nat Methods* 5:797-804.

18. Palmer AE, Tsien RY (2006) Measuring calcium signaling using genetically targetable fluorescent indicators. *Nat Protoc* 1:1057-1065.

19. Rudolf R, Mongillo M, Rizzuto R, Pozzan T (2003) Looking forward to seeing calcium. *Nat Rev Mol Cell Biol* 4:579-586.

20. Baird GS, Zacharias DA, Tsien RY (1999) Circular permutation and receptor insertion within green fluorescent proteins. *Proc Natl Acad Sci USA* 96:11241-11246.

21. Nagai T, Yamada S, Tominaga T, Ichikawa M, Miyawaki A (2004) Expanded dynamic range of fluorescent indicators for Ca^{2+} by circularly permuted yellow fluorescent proteins. *Proc Natl Acad Sci USA* 101:10554-10559.

22. Nakai J, Ohkura M, Imoto K (2001) A high signal-to-noise Ca^{2+} probe composed of a single green fluorescent protein. *Nat Biotechnol* 19:137-141.

23. Tallini YN, *et al.* (2006) Imaging cellular signals in the heart in vivo: Cardiac expression of the high-signal Ca^{2+} indicator GCaMP2. *Proc Natl Acad Sci USA* 103:4753-4758.

24. Dreosti E, Odermatt B, Dorostkar MM, Lagnado L (2009) A genetically encoded reporter of synaptic activity in vivo. *Nat Methods* 6:883-889.

25. Tian L, *et al.* (2009) Imaging neural activity in worms, flies and mice with improved GCaMP calcium indicators. *Nat Methods* 6:875-881.

26. Okumoto S, *et al.* (2005) Detection of glutamate release from neurons by genetically encoded surface-displayed FRET nanosensors. *Proc Natl Acad Sci USA* 102:8740-8745.

27. Hires SA, Zhu Y, Tsien RY (2008) Optical measurement of synaptic glutamate spillover and reuptake by linker optimized glutamate-sensitive fluorescent reporters. *Proc Natl Acad Sci USA* 105:4411-4416.

28. Tsien RY (2005) Building and breeding molecules to spy on cells and tumors. *FEBS Lett* 579:927-932.

29. Belousov VV, *et al.* (2006) Genetically encoded fluorescent indicator for intracellular hydrogen peroxide. *Nat Methods* 3:281-286.

30. Rhee SG, *et al.* (2005) Intracellular messenger function of hydrogen peroxide and its regulation by peroxiredoxins. *Curr Opin Cell Biol* 17:183-189.

31. Niethammer P, Grabher C, Look AT, Mitchison TJ (2009) A tissue-scale gradient of hydrogen peroxide mediates rapid wound detection in zebrafish. *Nature* 459:996-999.

32. Wold F (1981) In vivo chemical modification of proteins (post-translational modification). *Annu Rev Biochem* 50:783-814.

33. Aye-Han NN, Ni Q, Zhang J (2009) Fluorescent biosensors for real-time tracking of post-translational modification dynamics. *Curr Opin Chem Biol* 13:392-397.

34. Tarrant MK, Cole PA (2009) The chemical biology of protein phosphorylation. *Annu Rev Biochem* 78:797-825.

35. Zhang J, Allen MD (2007) FRET-based biosensors for protein kinases: Illuminating the kinome. *Mol Biosyst* 3:759-765.

36. Kurokawa K, *et al.* (2001) A pair of fluorescent resonance energy transfer-based probes for tyrosine phosphorylation of the CrkII adaptor protein in vivo. *J Biol Chem* 276:31305-31310.

37. Zhang J, Ma Y, Taylor SS, Tsien RY (2001) Genetically encoded reporters of protein kinase A activity reveal impact of substrate tethering. *Proc Natl Acad Sci USA* 98:14997-15002.

38. Ting AY, Kain KH, Klemke RL, Tsien RY (2001) Genetically encoded fluorescent reporters of protein tyrosine kinase activities in living cells. *Proc Natl Acad Sci USA* 98:15003-15008.

39. Wang Y, *et al.* (2005) Visualizing the mechanical activation of Src. *Nature* 434:1040-1045.

40. Zhang J, Hupfeld CJ, Taylor SS, Olefsky JM, Tsien RY (2005) Insulin disrupts beta-adrenergic signalling to protein kinase A in adipocytes. *Nature* 437:569-573.

41. Sasaki K, Sato M, Umezawa Y (2003) Fluorescent indicators for Akt/protein kinase B and dynamics of Akt activity visualized in living cells. *J Biol Chem* 278:30945-30951.

42. Kunkel MT, Ni Q, Tsien RY, Zhang J, Newton AC (2005) Spatio-temporal dynamics of protein kinase B/Akt signaling revealed by a genetically encoded fluorescent reporter. *J Biol Chem* 280:5581-5587.

43. Violin JD, Zhang J, Tsien RY, Newton AC (2003) A genetically encoded fluorescent reporter reveals oscillatory phosphorylation by protein kinase C. *J Cell Biol* 161:899-909.

44. Fuller BG, *et al.* (2008) Midzone activation of aurora B in anaphase produces an intracellular phosphorylation gradient. *Nature* 453:1132-1136.

45. Ouyang M, Sun J, Chien S, Wang Y (2008) Determination of hierarchical relationship of Src and Rac at subcellular locations with FRET biosensors. *Proc Natl Acad Sci USA* 105:14353-14358.

46. Harvey CD, *et al.* (2008) A genetically encoded fluorescent sensor of ERK activity. *Proc Natl Acad Sci USA* 105:19264-19269.

47. Lin CW, Jao CY, Ting AY (2004) Genetically encoded fluorescent reporters of histone methylation in living cells. *J Am Chem Soc* 126:5982-5983.

48. Lin CW, Ting AY (2004) A genetically encoded fluorescent reporter of histone phosphorylation in living cells. *Angew Chem Int Ed Engl* 43:2940-2943.

49. Felsenfeld G, Groudine M (2003) Controlling the double helix. *Nature* 421:448-453.

50. Carrillo LD, Krishnamoorthy L, Mahal LK (2006) A cellular FRET-based sensor for beta-O-GlcNAc, a dynamic carbohydrate modification involved in signaling. *J Am Chem Soc* 128:14768-14769.

51. Hart GW, Housley MP, Slawson C (2007) Cycling of O-linked beta-N-acetylglucosamine on nucleocytoplasmic proteins. *Nature* 446:1017-1022.

52. Paredes RM, Etzler JC, Watts LT, Zheng W, Lechleiter JD (2008) Chemical calcium indicators. *Methods* 46:143-151.

53. Lippard SJ, Berg JM (1994) *Principles of Bioinorganic Chemistry* (University Science Books, Mill Valley).

54. Tsien RY (1980) New calcium indicators and buffers with high selectivity against magnesium and protons: Design, synthesis, and properties of prototype structures. *Biochemistry* 19:2396-2404.

55. Haugland RP (2005) *The Handbook: A Guide to Fluorescent Probes and Labeling Technologies* (Molecule Probes, Inc., Eugene, OR).

56. Minta A, Kao JP, Tsien RY (1989) Fluorescent indicators for cytosolic calcium based on rhodamine and fluorescein chromophores. *J Biol Chem* 264:8171-8178.

57. Tour O, *et al.* (2007) Calcium Green FlAsH as a genetically targeted small-molecule calcium indicator. *Nat Chem Biol* 3:423-431.

58. Que EL, Domaille DW, Chang CJ (2008) Metals in neurobiology: Probing their chemistry and biology with molecular imaging. *Chem Rev* 108:1517-1549.

59. Domaille DW, Que EL, Chang CJ (2008) Synthetic fluorescent sensors for studying the cell biology of metals. *Nat Chem Biol* 4:168-175.

60. Frederickson C (2003) Imaging zinc: Old and new tools. *Sci STKE* 2003:1-4.

61. Frederickson CJ, Koh JY, Bush AI (2005) The neurobiology of zinc in health and disease. *Nat Rev Neurosci* 6:449-462.

62. Gee KR, Zhou ZL, Qian WJ, Kennedy R (2002) Detection and imaging of zinc secretion from pancreatic beta-cells using a new fluorescent zinc indicator. *J Am Chem Soc* 124:776-778.

63. Chang CJ, *et al.* (2004) Bright fluorescent chemosensor platforms for imaging endogenous pools of neuronal zinc. *Chem Biol* 11:203-210.

64. Woodroofe CC, Masalha R, Barnes KR, Frederickson CJ, Lippard SJ (2004) Membrane-permeable and -impermeable sensors of the Zinpyr family and their application to imaging of hippocampal zinc in vivo. *Chem Biol* 11:1659-1666.

65. Burdette SC, Frederickson CJ, Bu W, Lippard SJ (2003) ZP4, an improved neuronal Zn^{2+} sensor of the Zinpyr family. *J Am Chem Soc* 125:1778-1787.

66. Burdette SC, Walkup GK, Spingler B, Tsien RY, Lippard SJ (2001) Fluorescent sensors for Zn(2+) based on a fluorescein platform: Synthesis, properties and intracellular distribution. *J Am Chem Soc* 123:7831-7841.

67. Walkup GK, Burdette SC, Lippard SJ, Tsien RY (2000) A new cell-permeable fluorescent probe for Zn^{2+}. *J Am Chem Soc* 122:5644-5645.

68. Nolan EM, *et al.* (2006) Zinspy sensors with enhanced dynamic range for imaging neuronal cell zinc uptake and mobilization. *J Am Chem Soc* 128:15517-15528.

69. Nolan EM, *et al.* (2005) QZ1 and QZ2: Rapid, reversible quinoline-derivatized fluoresceins for sensing biological Zn(II). *J Am Chem Soc* 127:16812-16823.

70. Hirano T, Kikuchi K, Urano Y, Higuchi T, Nagano T (2000) Highly zinc-selective fluorescent sensor molecules suitable for biological applications. *J Am Chem Soc* 122:12399-12400.

71. Wu Y, *et al.* (2005) Boron dipyrromethene fluorophore based fluorescence sensor for the selective imaging of Zn(II) in living cells. *Org Biomol Chem* 3:1387-1392.

72. Tang B, *et al.* (2006) Highly sensitive and selective near-infrared fluorescent probe for zinc and its application to macrophage cells. *Chem Commun* 3609-3611.

73. Kiyose K, Kojima H, Urano Y, Nagano T (2006) Development of a ratiometric fluorescent zinc ion probe in near-infrared region, based on tricarbocyanine chromophore. *J Am Chem Soc* 128:6548-6549.

74. Lim NC, *et al.* (2005) Coumarin-based chemosensors for zinc(II): Toward the determination of the design algorithm for CHEF-type and ratiometric probes. *Inorg Chem* 44:2018-2030.

75. Lim NC, Bruckner C (2004) DPA-substituted coumarins as chemosensors for zinc(II): Modulation of the chemosensory characteristics by variation of the position of the chelate on the coumarin. *Chem Commun* 1094-1095.

76. Gee KR, Zhou ZL, Ton-That D, Sensi SL, Weiss JH (2002) Measuring zinc in living cells. A new generation of sensitive and selective fluorescent probes. *Cell Calcium* 31:245-251.

77. Maruyama S, Kikuchi K, Hirano T, Urano Y, Nagano T (2002) A novel, cell-permeable, fluorescent probe for ratiometric imaging of zinc ion. *J Am Chem Soc* 124:10650-10651.

78. Taki M, Wolford JL, O'Halloran TV (2004) Emission ratiometric imaging of intracellular zinc: Design of a benzoxazole fluorescent sensor and its application in two-photon microscopy. *J Am Chem Soc* 126:712-713.

79. Woodroofe CC, Lippard SJ (2003) A novel two-fluorophore approach to ratiometric sensing of Zn^{2+}. *J Am Chem Soc* 125:11458-11459.

80. Zhang XA, Lovejoy KS, Jasanoff A, Lippard SJ (2007) Water-soluble porphyrins as a dual-function molecular imaging platform for MRI and fluorescence zinc sensing. *Proc Natl Acad Sci USA* 104:10780-10785.

81. Hanaoka K, *et al.* (2002) Design and synthesis of a novel magnetic resonance imaging contrast agent for selective sensing of zinc ion. *Chem Biol* 9:1027-1032.

82. Hanaoka K, Kikuchi K, Urano Y, Nagano T (2001) Selective sensing of zinc ions with a novel magnetic resonance imaging contrast agent. *J Chem Soc-Perkin Trans 2* 1840-1843.

83. Barnham KJ, Masters CL, Bush AI (2004) Neurodegenerative diseases and oxidative stress. *Nat Rev Drug Discov* 3:205-214.

84. Halliwell B, Gutteridge J (1999) *Free Radicals in Biology and Medicine* (Oxford University Press, Oxford).

85. Yang L, *et al.* (2005) Imaging of the intracellular topography of copper with a fluorescent sensor and by synchrotron x-ray fluorescence microscopy. *Proc Natl Acad Sci USA* 102:11179-11184.

86. Zeng L, Miller EW, Pralle A, Isacoff EY, Chang CJ (2006) A selective turn-on fluorescent sensor for imaging copper in living cells. *J Am Chem Soc* 128:10-11.

87. Miller EW, Zeng L, Domaille DW, Chang CJ (2006) Preparation and use of Coppersensor-1, a synthetic fluorophore for live-cell copper imaging. *Nat Protoc* 1:824-827.

88. Que EL, *et al.* (2009) Copper-responsive magnetic resonance imaging contrast agents. *J Am Chem Soc* 131:8527-8536.

89. Que EL, Chang CJ (2006) A smart magnetic resonance contrast agent for selective copper sensing. *J Am Chem Soc* 128:15942-15943.

90. Petrat F, Rauen U, de Groot H (1999) Determination of the chelatable iron pool of isolated rat hepatocytes by digital fluorescence microscopy using the fluorescent probe, Phen Green SK. *Hepatology* 29:1171-1179.

91. Ma Y, Luo W, Camplo M, Liu Z, Hider RC (2005) Novel iron-specific fluorescent probes. *Bioorg Med Chem Lett* 15:3450-3452.

92. Lytton SD, Mester B, Libman J, Shanzer A, Cabantchik ZI (1992) Monitoring of iron(III) removal from biological sources using a fluorescent siderophore. *Anal Biochem* 205:326-333.

93. Xiang Y, Tong A (2006) A new rhodamine-based chemosensor exhibiting selective Fe(III)-amplified fluorescence. *Org Lett* 8:1549-1552.

94. Xiang Y, Tong A, Jin P, Ju Y (2006) New fluorescent rhodamine hydrazone chemosensor for Cu(II) with high selectivity and sensitivity. *Org Lett* 8:2863-2866.

95. Ignarro LJ (2000) *Nitric Oxide Biology and Pathobiology* (Academic Press, San Diego).

96. Miller EW, Chang CJ (2007) Fluorescent probes for nitric oxide and hydrogen peroxide in cell signaling. *Curr Opin Chem Biol* 11:620-625.

97. McQuade LE, Lippard SJ (2009) Fluorescent probes to investigate nitric oxide and other reactive nitrogen species in biology. *Curr Opin Chem Biol* in press.

98. Gomes A, Fernandes E, Lima JL (2006) Use of fluorescence probes for detection of reactive nitrogen species: A review. *J Fluoresc* 16:119-139.

99. Soh N (2006) Recent advances in fluorescent probes for the detection of reactive oxygen species. *Anal Bioanal Chem* 386:532-543.

100. Lim MH, Lippard SJ (2007) Metal-based turn-on fluorescent probes for sensing nitric oxide. *Acc Chem Res* 40:41-51.

101. LeBel CP, Ischiropoulos H, Bondy SC (1992) Evaluation of the probe 2',7'-dichlorofluorescein as an indicator of reactive oxygen species formation and oxidative stress. *Chem Res Toxicol* 5:227-231.

102. Henderson LM, Chappell JB (1993) Dihydrorhodamine 123: A fluorescent probe for superoxide generation? *Eur J Biochem* 217:973-980.

103. Marchesi E, Rota C, Fann YC, Chignell CF, Mason RP (1999) Photoreduction of the fluorescent dye 2'-7'-dichlorofluorescein: A spin trapping and direct electron spin resonance study with implications for oxidative stress measurements. *Free Radic Biol Med* 26:148-161.

104. Afzal M, *et al.* (2003) Method to overcome photoreaction, a serious drawback to the use of dichlorofluorescein in evaluation of reactive oxygen species. *Biochem Biophys Res Commun* 304:619-624.

105. Chang MC, Pralle A, Isacoff EY, Chang CJ (2004) A selective, cell-permeable optical probe for hydrogen peroxide in living cells. *J Am Chem Soc* 126:15392-15393.

106. Miller EW, Albers AE, Pralle A, Isacoff EY, Chang CJ (2005) Boronate-based fluorescent probes for imaging cellular hydrogen peroxide. *J Am Chem Soc* 127:16652-16659.

107. Miller EW, Tulyathan O, Isacoff EY, Chang CJ (2007) Molecular imaging of hydrogen peroxide produced for cell signaling. *Nat Chem Biol* 3:263-267.

108. Albers AE, Okreglak VS, Chang CJ (2006) A FRET-based approach to ratiometric fluorescence detection of hydrogen peroxide. *J Am Chem Soc* 128:9640-9641.

109. Kojima H, *et al.* (1998) Detection and imaging of nitric oxide with novel fluorescent indicators: Diaminofluoresceins. *Anal Chem* 70:2446-2453.

110. Kojima H, *et al.* (2001) Bioimaging of nitric oxide with fluorescent indicators based on the rhodamine chromophore. *Anal Chem* 73:1967-1973.

111. Gabe Y, Ueno T, Urano Y, Kojima H, Nagano T (2006) Tunable design strategy for fluorescence probes based on 4-substituted BODIPY chromophore: Improvement of highly sensitive fluorescence probe for nitric oxide. *Anal Bioanal Chem* 386:621-626.

112. Gabe Y, Urano Y, Kikuchi K, Kojima H, Nagano T (2004) Highly sensitive fluorescence probes for nitric oxide based on boron dipyrromethene chromophore-rational design of potentially useful bioimaging fluorescence probe. *J Am Chem Soc* 126:3357-3367.

113. Sasaki E, *et al.* (2005) Highly sensitive near-infrared fluorescent probes for nitric oxide and their application to isolated organs. *J Am Chem Soc* 127:3684-3685.

114. Izumi S, Urano Y, Hanaoka K, Terai T, Nagano T (2009) A simple and effective strategy to increase the sensitivity of fluorescence probes in living cells. *J Am Chem Soc* 131:10189-10200.

115. Zheng H, Shang GQ, Yang SY, Gao X, Xu JG (2008) Fluorogenic and chromogenic rhodamine spirolactam based probe for nitric oxide by spiro ring opening reaction. *Org Lett* 10:2357-2360.

116. Varki A, *et al.* (2008) *Essentials of Glycobiology* (Cold Spring Harbor Laboratory Press, New York).

117. Haltiwanger RS, Lowe JB (2004) Role of glycosylation in development. *Annu Rev Biochem* 73:491-537.

118. Rosen SD (2004) Ligands for L-selectin: Homing, inflammation, and beyond. *Annu Rev Immunol* 22:129-156.

119. Fuster MM, Esko JD (2005) The sweet and sour of cancer: Glycans as novel therapeutic targets. *Nat Rev Cancer* 5:526-542.

120. Sharon N (2007) Lectins: Carbohydrate-specific reagents and biological recognition molecules. *J Biol Chem* 282:2753-2764.

121. Pilobello KT, Mahal LK (2007) Lectin microarrays for glycoprotein analysis. *Methods Mol Biol* 385:193-203.

122. Hirabayashi J (2004) Lectin-based structural glycomics: Glycoproteomics and glycan profiling. *Glycoconj J* 21:35-40.

123. Kiessling LL, Pohl NL (1996) Strength in numbers: Non-natural polyvalent carbohydrate derivatives. *Chem Biol* 3:71-77.

124. Ohba H, Bakalova R (2003) Relationships between degree of binding, cytotoxicity and cytoagglutinating activity of plant-derived agglutinins in normal lymphocytes and cultured leukemic cell lines. *Cancer Chemother Pharmacol* 51:451-458.

125. Carlsson S, Carlsson MC, Leffler H (2007) Intracellular sorting of galectin-8 based on carbohydrate fine specificity. *Glycobiology* 17:906-912.

126. Paessens LC, Garcia-Vallejo JJ, Fernandes RJ, van Kooyk Y (2007) The glycosylation of thymic microenvironments. A microscopic study using plant lectins. *Immunol Lett* 110:65-73.

127. Licha K, *et al.* (2005) Optical molecular imaging of lymph nodes using a targeted vascular contrast agent. *J Biomed Opt* 10:41205.

128. Hang HC, Bertozzi CR (2001) Chemoselective approaches to glycoprotein assembly. *Acc Chem Res* 34:727-736.

129. Dvorak HF, Nagy JA, Dvorak AM (1991) Structure of solid tumors and their vasculature: Implications for therapy with monoclonal antibodies. *Cancer Cells* 3:77-85.

130. Laughlin ST, Bertozzi CR (2009) Imaging the glycome. *Proc Natl Acad Sci USA* 106:12-17.

131. Sletten EM, Bertozzi CR (2009) Bioorthogonal chemistry: Fishing for selectivity in a sea of functionality. *Angew Chem Int Ed Engl* 48:6974-6998.

132. Prescher JA, Bertozzi CR (2005) Chemistry in living systems. *Nat Chem Biol* 1:13-21.

133. Jencks WP (1959) Studies on the mechanism of oxime and semicarbazone formation. *J Am Chem Soc* 81:475-481.

134. Dirksen A, Dirksen S, Hackeng TM, Dawson PE (2006) Nucleophilic catalysis of hydrazone formation and transimination: Implications for dynamic covalent chemistry. *J Am Chem Soc* 128:15602-15603.

135. Dirksen A, Hackeng TM, Dawson PE (2006) Nucleophilic catalysis of oxime ligation. *Angew Chem Int Ed Engl* 45:7581-7584.

136. Mahal LK, Yarema KJ, Bertozzi CR (1997) Engineering chemical reactivity on cell surfaces through oligosaccharide biosynthesis. *Science* 276:1125-1128.

137. Sadamoto R, *et al.* (2004) Control of bacteria adhesion by cell-wall engineering. *J Am Chem Soc* 126:3755-3761.

138. Griffin RJ (1994) The medicinal chemistry of the azido group. *Prog Med Chem* 31:121-232.

139. Baskin JM, Bertozzi CR (2007) Bioorthogonal click chemistry: Covalent labeling in living systems. *QSAR Comb Sci* 26:1211-1219.

140. Staudinger H, Meyer J (1919) Uber neue organische phosphoverbindungen III. Phosphinmethlenderivate und phosphinimine. *Helv Chim Acta* 2:635-646.

141. Gololobov YG, Kasukhin LF (1992) Recent advances in the Staudinger ligation. *Tetrahedron* 48:1353-1406.

142. Saxon E, Bertozzi CR (2000) Cell surface engineering by a modified Staudinger reaction. *Science* 287:2007-2010.

143. Prescher JA, Dube DH, Bertozzi CR (2004) Chemical remodelling of cell surfaces in living animals. *Nature* 430:873-877.

144. Chang PV, Prescher JA, Hangauer MJ, Bertozzi CR (2007) Imaging cell surface glycans with bioorthogonal chemical reporters. *J Am Chem Soc* 129:8400-8401.

145. Hangauer MJ, Bertozzi CR (2008) A FRET-based fluorogenic phosphine for live-cell imaging with the Staudinger ligation. *Angew Chem Int Ed Engl* 47:2394-2397.

146. Dube DH, Prescher JA, Quang CN, Bertozzi CR (2006) Probing mucin-type O-linked glycosylation in living animals. *Proc Natl Acad Sci USA* 103:4819-4824.

147. Zeng Y, Ramya TN, Dirksen A, Dawson PE, Paulson JC (2009) High-efficiency labeling of sialylated glycoproteins on living cells. *Nat Methods* 6:207-209.

148. Hang HC, Yu C, Kato DL, Bertozzi CR (2003) A metabolic labeling approach toward proteomic analysis of mucin-type O-linked glycosylation. *Proc Natl Acad Sci USA* 100:14846-14851.

149. Vocadlo DJ, Hang HC, Kim EJ, Hanover JA, Bertozzi CR (2003) A chemical approach for identifying O-GlcNAc-modified proteins in cells. *Proc Natl Acad Sci USA* 100:9116-9121.

150. Rabuka D, Hubbard SC, Laughlin ST, Argade SP, Bertozzi CR (2006) A chemical reporter strategy to probe glycoprotein fucosylation. *J Am Chem Soc* 128:12078-12079.

151. Sawa M, *et al.* (2006) Glycoproteomic probes for fluorescent imaging of fucosylated glycans in vivo. *Proc Natl Acad Sci USA* 103:12371-12376.

152. Rostovtsev VV, Green LG, Fokin VV, Sharpless KB (2002) A stepwise Huisgen cycloaddition process: Copper(I)-catalyzed regioselective "ligation" of azides and terminal alkynes. *Angew Chem Int Ed Engl* 41:2596-2599.

153. Tornoe CW, Christensen C, Meldal M (2002) Peptidotriazoles on solid phase: [1,2,3]-Triazoles by regiospecific copper(I)-catalyzed 1,3-dipolar cycloadditions of terminal alkynes to azides. *J Org Chem* 67:3057-3064.

154. Kolb HC, Finn MG, Sharpless KB (2001) Click chemistry: Diverse chemical function from a few good reactions. *Angew Chem Int Ed Engl* 40:2004-2021.

155. Chang PV, *et al.* (2009) Metabolic labeling of sialic acids in living animals with alkynyl sugars. *Angew Chem Int Ed Engl* 48:4030-4033.

156. Hsu TL, *et al.* (2007) Alkynyl sugar analogs for the labeling and visualization of glycoconjugates in cells. *Proc Natl Acad Sci USA* 104:2614-2619.

157. Agard NJ, Prescher JA, Bertozzi CR (2004) A strain-promoted [3 + 2] azide-alkyne cycloaddition for covalent modification of biomolecules in living systems. *J Am Chem Soc* 126:15046-15047.

158. Baskin JM, *et al.* (2007) Copper-free click chemistry for dynamic in vivo imaging. *Proc Natl Acad Sci USA* 104:16793-16797.

159. Agard NJ, Baskin JM, Prescher JA, Lo A, Bertozzi CR (2006) A comparative study of bioorthogonal reactions with azides. *ACS Chem Biol* 1:644-648.

160. Schoenebeck F, Ess DH, Jones GO, Houk KN (2009) Reactivity and regioselectivity in 1,3-dipolar cycloadditions of azides to strained alkynes and alkenes: A computational study. *J Am Chem Soc* 131:8121-8133.

161. Ess DH, Jones GO, Houk KN (2008) Transition states of strain-promoted metal-free click chemistry: 1,3-Dipolar cycloadditions of phenyl azide and cyclooctynes. *Org Lett* 10:1633-1636.

162. Laughlin ST, Bertozzi CR (2009) In vivo imaging of Caenorhabditis elegans glycans. *ACS Chem Biol* 4:1068-1072.

163. Laughlin ST, Baskin JM, Amacher SL, Bertozzi CR (2008) In vivo imaging of membrane-associated glycans in developing zebrafish. *Science* 320:664-667.

164. Chang PV, *et al.* (2010) Copper-free click chemistry in living animals. *Proc Natl Acad Sci USA* in press.

165. Sletten EM, Bertozzi CR (2008) A hydrophilic azacyclooctyne for Cu-free click chemistry. *Org Lett* 10:3097-3099.

166. Poloukhtine AA, Mbua NE, Wolfert MA, Boons GJ, Popik VV (2009) Selective labeling of living cells by a photo-triggered click reaction. *J Am Chem Soc* 131:15769-15776.

167. Ning X, Guo J, Wolfert MA, Boons GJ (2008) Visualizing metabolically labeled glycoconjugates of living cells by copper-free and fast Huisgen cycloadditions. *Angew Chem Int Ed Engl* 47:2253-2255.

168. Debets MF, *et al.* (2010) Aza-dibenzocyclooctynes for fast and efficient enzyme PEGylation via copper-free (3+2) cycloaddition. *Chem Commun* 46:97-99.

169. Resh MD (2006) Trafficking and signaling by fatty-acylated and prenylated proteins. *Nat Chem Biol* 2:584-590.

170. Charron G, Wilson J, Hang HC (2009) Chemical tools for understanding protein lipidation in eukaryotes. *Curr Opin Chem Biol* 13:382-391.

171. Vance JE, Vance DE (2004) Phospholipid biosynthesis in mammalian cells. *Biochem Cell Biol* 82:113-128.

172. Jao CY, Roth M, Welti R, Salic A (2009) Metabolic labeling and direct imaging of choline phospholipids in vivo. *Proc Natl Acad Sci USA* 106:15332-15337.

173. Neef AB, Schultz C (2009) Selective fluorescence labeling of lipids in living cells. *Angew Chem Int Ed Engl* 48:1498-1500.

174. Kho Y, *et al.* (2004) A tagging-via-substrate technology for detection and proteomics of farnesylated proteins. *Proc Natl Acad Sci USA* 101:12479-12484.

175. Charron G, *et al.* (2009) Robust fluorescent detection of protein fatty-acylation with chemical reporters. *J Am Chem Soc* 131:4967-4975.

176. Hang HC, *et al.* (2007) Chemical probes for the rapid detection of fatty-acylated proteins in mammalian cells. *J Am Chem Soc* 129:2744-2745.

177. Martin DD, *et al.* (2008) Rapid detection, discovery, and identification of post-translationally myristoylated proteins during apoptosis using a bio-orthogonal azidomyristate analog. *FASEB J* 22:797-806.

178. Kostiuk MA, *et al.* (2008) Identification of palmitoylated mitochondrial proteins using a bio-orthogonal azido-palmitate analogue. *FASEB J* 22:721-732.

179. Yap MC, *et al.* (2009) Rapid and selective detection of fatty acylated proteins using {omega}-alkynyl-fatty acids and click chemistry. *J Lipid Res* in press.

180. Dirks RW, Tanke HJ (2006) Advances in fluorescent tracking of nucleic acids in living cells. *Biotechniques* 40:489-496.

181. Bao G, Rhee WJ, Tsourkas A (2009) Fluorescent probes for live-cell RNA detection. *Annu Rev Biomed Eng* 11:25-47.

182. Gramlich PM, Wirges CT, Manetto A, Carell T (2008) Postsynthetic DNA modification through the copper-catalyzed azide-alkyne cycloaddition reaction. *Angew Chem Int Ed Engl* 47:8350-8358.

183. Wang CC, Seo TS, Li Z, Ruparel H, Ju J (2003) Site-specific fluorescent labeling of DNA using Staudinger ligation. *Bioconjug Chem* 14:697-701.

184. Seo TS, Li Z, Ruparel H, Ju J (2003) Click chemistry to construct fluorescent oligonucleotides for DNA sequencing. *J Org Chem* 68:609-612.

185. Cai J, Li X, Yue X, Taylor JS (2004) Nucleic acid-triggered fluorescent probe activation by the Staudinger reaction. *J Am Chem Soc* 126:16324-16325.

186. Rakic P (2002) Neurogenesis in adult primate neocortex: An evaluation of the evidence. *Nat Rev Neurosci* 3:65-71.

187. Salic A, Mitchison TJ (2008) A chemical method for fast and sensitive detection of DNA synthesis in vivo. *Proc Natl Acad Sci USA* 105:2415-2420.

188. Jao CY, Salic A (2008) Exploring RNA transcription and turnover in vivo by using click chemistry. *Proc Natl Acad Sci USA* 105:15779-15784.

189. Cornett DS, Reyzer ML, Chaurand P, Caprioli RM (2007) MALDI imaging mass spectrometry: Molecular snapshots of biochemical systems. *Nat Methods* 4:828-833.

190. McDonnell LA, Heeren RM (2007) Imaging mass spectrometry. *Mass Spectrom Rev* 26:606-643.

191. Heeren RMA, *et al.* (2006) Why don't biologists use SIMS? A critical evaluation of imaging MS. *App Surf Sci* 252:6827-6835.

192. Boxer SG, Kraft ML, Weber PK (2009) Advances in imaging secondary ion mass spectrometry for biological samples. *Annu Rev Biophys* 38:53-74.

193. Cooks RG, Ouyang Z, Takats Z, Wiseman JM (2006) Detection technologies. Ambient mass spectrometry. *Science* 311:1566-1570.

194. Takats Z, Wiseman JM, Gologan B, Cooks RG (2004) Mass spectrometry sampling under ambient conditions with desorption electrospray ionization. *Science* 306:471-473.

195. Francese S, *et al.* (2009) MALDI mass spectrometry imaging, from its origins up to today: The state of the art. *Comb Chem High Throughput Screen* 12:156-174.

196. Woods AS, Jackson SN (2006) Brain tissue lipidomics: Direct probing using matrix-assisted laser desorption/ionization mass spectrometry. *AAPS J* 8:E391-395.

197. McLean JA, Ridenour WB, Caprioli RM (2007) Profiling and imaging of tissues by imaging ion mobility-mass spectrometry. *J Mass Spectrom* 42:1099-1105.

198. Jackson SN, *et al.* (2005) Direct tissue analysis of phospholipids in rat brain using MALDI-TOFMS and MALDI-ion mobility-TOFMS. *J Am Soc Mass Spectrom* 16:133-138.

199. Rujoi M, Estrada R, Yappert MC (2004) In situ MALDI-TOF MS regional analysis of neutral phospholipids in lens tissue. *Anal Chem* 76:1657-1663.

200. Shimma S, *et al.* (2007) MALDI-based imaging mass spectrometry revealed abnormal distribution of phospholipids in colon cancer liver metastasis. *J Chromatogr B Analyt Technol Biomed Life Sci* 855:98-103.

201. Touboul D, *et al.* (2007) MALDI-TOF and cluster-TOF-SIMS imaging of Fabry disease biomarkers. *Int J Mass Spectrom* 260:158-165.

202. Esquenazi E, *et al.* (2008) Visualizing the spatial distribution of secondary metabolites produced by marine cyanobacteria and sponges via MALDI-TOF imaging. *Mol Biosyst* 4:562-570.

203. Yang YL, Xu Y, Straight P, Dorrestein PC (2009) Translating metabolic exchange with imaging mass spectrometry. *Nat Chem Biol* 5:885-887.

204. Fletcher JS (2009) Cellular imaging with secondary ion mass spectrometry. *Analyst* 134:2204-2215.

205. Johansson B (2006) ToF-SIMS imaging of lipids in cell membranes. *Surf Interface Anal* 38:1401-1412.

206. Nygren H, Malmberg P, Kriegeskotte C, Arlinghaus HF (2004) Bioimaging TOF-SIMS: Localization of cholesterol in rat kidney sections. *FEBS Lett* 566:291-293.

207. Ostrowski SG, Van Bell CT, Winograd N, Ewing AG (2004) Mass spectrometric imaging of highly curved membranes during Tetrahymena mating. *Science* 305:71-73.

208. Kleinfeld AM, Kampf JP, Lechene C (2004) Transport of 13C-oleate in adipocytes measured using multi imaging mass spectrometry. *J Am Soc Mass Spectrom* 15:1572-1580.

209. Kraft ML, Weber PK, Longo ML, Hutcheon ID, Boxer SG (2006) Phase separation of lipid membranes analyzed with high-resolution secondary ion mass spectrometry. *Science* 313:1948-1951.

210. Dekas AE, Poretsky RS, Orphan VJ (2009) Deep-sea archaea fix and share nitrogen in methane-consuming microbial consortia. *Science* 326:422-426.

211. Lechene C, *et al.* (2006) High-resolution quantitative imaging of mammalian and bacterial cells using stable isotope mass spectrometry. *J Biol* 5:20.

212. Mas S, Perez R, Martinez-Pinna R, Egido J, Vivanco F (2008) Cluster TOF-SIMS imaging: A new light for in situ metabolomics? *Proteomics* 8:3735-3745.

213. Malmberg P, *et al.* (2007) Localization of lipids in the aortic wall with imaging TOF-SIMS. *Biochim Biophys Acta* 1771:185-195.

214. Amaya KR, Monroe EB, Sweedler JV, Clayton DF (2007) Lipid imaging in the zebra finch brain with secondary ion mass spectrometry. *Int J Mass Spectrom* 260:121-127.

215. Nygren H, Borner K, Hagenhoff B, Malmberg P, Mansson JE (2005) Localization of cholesterol, phosphocholine and galactosylceramide in rat cerebellar cortex with imaging TOF-SIMS equipped with a bismuth cluster ion source. *Biochim Biophys Acta* 1737:102-110.

216. Touboul D, Brunelle A, Halgand F, De La Porte S, Laprevote O (2005) Lipid imaging by gold cluster time-of-flight secondary ion mass spectrometry: Application to Duchenne muscular dystrophy. *J Lipid Res* 46:1388-1395.

217. Sjovall P, Lausmaa J, Johansson B (2004) Mass spectrometric imaging of lipids in brain tissue. *Anal Chem* 76:4271-4278.

218. McDonnell LA, *et al.* (2005) Subcellular imaging mass spectrometry of brain tissue. *J Mass Spectrom* 40:160-168.

219. Fujita K, Smith NI (2008) Label-free molecular imaging of living cells. *Mol Cells* 26:530-535.

220. Min W, *et al.* (2009) Imaging chromophores with undetectable fluorescence by stimulated emission microscopy. *Nature* 461:1105-1109.

221. Uzunbajakava N, *et al.* (2003) Nonresonant confocal Raman imaging of DNA and protein distribution in apoptotic cells. *Biophys J* 84:3968-3981.

222. Puppels GJ, *et al.* (1990) Studying single living cells and chromosomes by confocal Raman microspectroscopy. *Nature* 347:301-303.

223. van Manen HJ, Kraan YM, Roos D, Otto C (2005) Single-cell Raman and fluorescence microscopy reveal the association of lipid bodies with phagosomes in leukocytes. *Proc Natl Acad Sci USA* 102:10159-10164.

224. Huang Z, *et al.* (2003) Near-infrared Raman spectroscopy for optical diagnosis of lung cancer. *Int J Cancer* 107:1047-1052.

225. Shafer-Peltier KE, *et al.* (2002) Raman microspectroscopic model of human breast tissue: Implications for breast cancer diagnosis in vivo. *J Raman Spectrosc* 33:552-563.

226. Nijssen A, *et al.* (2002) Discriminating basal cell carcinoma from its surrounding tissue by Raman spectroscopy. *J Invest Dermatol* 119:64-69.

227. Freudiger CW, *et al.* (2008) Label-free biomedical imaging with high sensitivity by stimulated Raman scattering microscopy. *Science* 322:1857-1861.

228. Evans CL, Xie XS (2008) Coherent anti-Stokes Raman scattering microscopy: Chemical imaging for biology and medicine. *Annu Rev Anal Chem* 1:883-909.

229. Duncan MD, Reintjes J, Manuccia TJ (1982) Scanning coherent anti-Stokes Raman microscope. *Opt Lett* 7:350-352.

230. Zumbusch A, Holtom GR, Xie XS (1999) Three-dimensional vibrational imaging by coherent anti-Stokes Raman scattering. *Phys Rev Lett* 82:4142-4145.

231. Wurpel GW, Rinia HA, Muller M (2005) Imaging orientational order and lipid density in multilamellar vesicles with multiplex CARS microscopy. *J Microsc* 218:37-45.

232. Potma EO, Evans C, Xie XS, Jones RJ, Ye J (2003) Picosecond-pulse amplification with an external passive optical cavity. *Opt Lett* 28:1835-1837.

233. Xie XS, Yu J, Yang WY (2006) Living cells as test tubes. *Science* 312:228-230.

234. Nan X, Potma EO, Xie XS (2006) Nonperturbative chemical imaging of organelle transport in living cells with coherent anti-stokes Raman scattering microscopy. *Biophys J* 91:728-735.

235. Nan X, Cheng JX, Xie XS (2003) Vibrational imaging of lipid droplets in live fibroblast cells with coherent anti-Stokes Raman scattering microscopy. *J Lipid Res* 44:2202-2208.

236. Nan X, Tonary AM, Stolow A, Xie XS, Pezacki JP (2006) Intracellular imaging of HCV RNA and cellular lipids by using simultaneous two-photon fluorescence and coherent anti-Stokes Raman scattering microscopies. *Chembiochem* 7:1895-1897.

237. Rakic B, *et al.* (2006) Peroxisome proliferator-activated receptor alpha antagonism inhibits hepatitis C virus replication. *Chem Biol* 13:23-30.

238. Evans CL, *et al.* (2007) Chemically-selective imaging of brain structures with CARS microscopy. *Opt Express* 15:12076-12087.

239. Hellerer T, *et al.* (2007) Monitoring of lipid storage in Caenorhabditis elegans using coherent anti-Stokes Raman scattering (CARS) microscopy. *Proc Natl Acad Sci USA* 104:14658-14663.

240. Evans CL, *et al.* (2005) Chemical imaging of tissue in vivo with video-rate coherent anti-Stokes Raman scattering microscopy. *Proc Natl Acad Sci USA* 102:16807-16812.

241. Ganikhanov F, Evans CL, Saar BG, Xie XS (2006) High-sensitivity vibrational imaging with frequency modulation coherent anti-Stokes Raman scattering (FM CARS) microscopy. *Opt Lett* 31:1872-1874.

242. Willmann JK, van Bruggen N, Dinkelborg LM, Gambhir SS (2008) Molecular imaging in drug development. *Nat Rev Drug Discov* 7:591-607.

243. Weissleder R, Pittet MJ (2008) Imaging in the era of molecular oncology. *Nature* 452:580-589.

244. Gambhir SS (2002) Molecular imaging of cancer with positron emission tomography. *Nat Rev Cancer* 2:683-693.

245. Krohn KA, Mankoff DA, Eary JF (2001) Imaging cellular proliferation as a measure of response to therapy. *J Clin Pharmacol* Suppl:96S-103S.

246. Shields AF, *et al.* (1998) Imaging proliferation in vivo with [F-18]FLT and positron emission tomography. *Nat Med* 4:1334-1336.

247. Blake GM, Park-Holohan SJ, Cook GJ, Fogelman I (2001) Quantitative studies of bone with the use of 18F-fluoride and 99mTc-methylene diphosphonate. *Semin Nucl Med* 31:28-49.

248. Ohta M, *et al.* (2001) Whole body PET for the evaluation of bony metastases in patients with breast cancer: Comparison with 99Tcm-MDP bone scintigraphy. *Nucl Med Commun* 22:875-879.

249. Bacharach SL, Libutti SK, Carrasquillo JA (2000) Measuring tumor blood flow with H(2)(15)O: practical considerations. *Nucl Med Biol* 27:671-676.

250. Koh WJ, *et al.* (1995) Evaluation of oxygenation status during fractionated radiotherapy in human nonsmall cell lung cancers using [F-18]fluoromisonidazole positron emission tomography. *Int J Radiat Oncol Biol Phys* 33:391-398.

251. Hara T, Kosaka N, Kishi H (1998) PET imaging of prostate cancer using carbon-11-choline. *J Nucl Med* 39:990-995.

252. Kotzerke J, *et al.* (2000) Experience with carbon-11 choline positron emission tomography in prostate carcinoma. *Eur J Nucl Med* 27:1415-1419.

253. Price DT, *et al.* (2002) Comparison of [18 F]fluorocholine and [18 F]fluorodeoxyglucose for positron emission tomography of androgen dependent and androgen independent prostate cancer. *J Urol* 168:273-280.

254. Blankenberg FG, *et al.* (1998) In vivo detection and imaging of phosphatidylserine expression during programmed cell death. *Proc Natl Acad Sci USA* 95:6349-6354.

255. Dewanjee MK, *et al.* (1994) Noninvasive imaging of c-myc oncogene messenger RNA with indium-111-antisense probes in a mammary tumor-bearing mouse model. *J Nucl Med* 35:1054-1063.

256. Nelson SJ (2003) Multivoxel magnetic resonance spectroscopy of brain tumors. *Mol Cancer Ther* 2:497-507.

257. Chang L, *et al.* (1995) Localized in vivo 1H magnetic resonance spectroscopy and in vitro analyses of heterogeneous brain tumors. *J Neuroimaging* 5:157-163.

258. McBride DQ, *et al.* (1995) Analysis of brain tumors using 1H magnetic resonance spectroscopy. *Surg Neurol* 44:137-144.

259. Usenius JP, *et al.* (1994) Quantitative metabolite patterns of human brain tumors: Detection by 1H NMR spectroscopy in vivo and in vitro. *J Comput Assist Tomogr* 18:705-713.

260. Usenius JP, Vainio P, Hernesniemi J, Kauppinen RA (1994) Choline-containing compounds in human astrocytomas studied by 1H NMR spectroscopy in vivo and in vitro. *J Neurochem* 63:1538-1543.

261. Shimizu H, *et al.* (1996) Noninvasive evaluation of malignancy of brain tumors with proton MR spectroscopy. *AJNR Am J Neuroradiol* 17:737-747.

262. Heesters MA, Kamman RL, Mooyaart EL, Go KG (1993) Localized proton spectroscopy of inoperable brain gliomas. Response to radiation therapy. *J Neurooncol* 17:27-35.

263. Somorjai RL, *et al.* (1996) Classification of 1H MR spectra of human brain neoplasms: The influence of preprocessing and computerized consensus diagnosis on classification accuracy. *J Magn Reson Imaging* 6:437-444.

264. Preul MC, *et al.* (1996) Accurate, noninvasive diagnosis of human brain tumors by using proton magnetic resonance spectroscopy. *Nat Med* 2:323-325.

265. Callot V, *et al.* (2008) (1)H MR spectroscopy of human brain tumours: A practical approach. *Eur J Radiol* 67:268-274.

266. Kurhanewicz J, Swanson MG, Nelson SJ, Vigneron DB (2002) Combined magnetic resonance imaging and spectroscopic imaging approach to molecular imaging of prostate cancer. *J Magn Reson Imaging* 16:451-463.

267. Stanwell P, Mountford C (2007) In vivo proton MR spectroscopy of the breast. *Radiographics* 27 Suppl 1:S253-266.

268. Viale A, Aime S (2009) Current concepts on hyperpolarized molecules in MRI. *Curr Opin Chem Biol* in press.

269. Gabellieri C, *et al.* (2008) Therapeutic target metabolism observed using hyperpolarized 15N choline. *J Am Chem Soc* 130:4598-4599.

270. Taratula O, Dmochowski IJ (2009) Functionalized (129)Xe contrast agents for magnetic resonance imaging. *Curr Opin Chem Biol* in press.

271. Schroder L, Lowery TJ, Hilty C, Wemmer DE, Pines A (2006) Molecular imaging using a targeted magnetic resonance hyperpolarized biosensor. *Science* 314:446-449.

272. Golman K, *et al.* (2001) Parahydrogen-induced polarization in imaging: Subsecond (13)C angiography. *Magn Reson Med* 46:1-5.

273. Golman K, Zandt RI, Lerche M, Pehrson R, Ardenkjaer-Larsen JH (2006) Metabolic imaging by hyperpolarized 13C magnetic resonance imaging for in vivo tumor diagnosis. *Cancer Res* 66:10855-10860.

274. Chen AP, *et al.* (2007) Hyperpolarized C-13 spectroscopic imaging of the TRAMP mouse at 3T-initial experience. *Magn Reson Med* 58:1099-1106.

275. Albers MJ, *et al.* (2008) Hyperpolarized 13C lactate, pyruvate, and alanine: Noninvasive biomarkers for prostate cancer detection and grading. *Cancer Res* 68:8607-8615.

276. Nelson SJ, *et al.* (2008) DNP-hyperpolarized C-13 magnetic resonance metabolic imaging for cancer applications. *Appl Magn Reson* 34:533-544.

277. Day SE, *et al.* (2007) Detecting tumor response to treatment using hyperpolarized 13C magnetic resonance imaging and spectroscopy. *Nat Med* 13:1382-1387.

278. Gallagher FA, *et al.* (2008) Magnetic resonance imaging of pH in vivo using hyperpolarized 13C-labelled bicarbonate. *Nature* 453:940-943.

Chapter 2: Copper-free click chemistry in living animals[a]

Introduction

The laboratory mouse is widely regarded as the model organism of choice for studying human pathology because of extensive documentation relating the similarities between human and mouse anatomy, physiology, cell biology, as well as their genomes (1). Several studies using mouse models have related human disease conditions to altered glycosylation (2). For example, reduced glycosylation of glucose transporter-2 has been shown to impair glucose transport and insulin secretion, producing a condition in mice that is similar to type 2 diabetes in humans (3). Mouse models have also revealed that dysfunctional protein O-GlcNAcylation may contribute to the pathology of Alzheimer's disease (4).

Driven by such observations, researchers are increasingly interested in probing glycosylation, and more generally, carbohydrate metabolism, in mouse models. Toward this goal, Reutter and co-workers demonstrated that unnatural analogs of *N*-acetyl mannosamine that are modified at the *N*-acyl position can be used to probe terminal sialic acid residues within rodents (5). As a means to monitor changes in glycosylation associated with the onset of disease, this approach was later extended to include metabolic labeling with unnatural sugars followed by chemical tagging with probes for fluorescence imaging or affinity capture (6). The unnatural sugar must be outfitted with a bioorthogonal functional group, also termed a “chemical reporter”, that possesses unique reactivity with a second functional group installed on the probe reagent (7). The azide is well-suited as a chemical reporter because it adds a small structural perturbation to the underlying sugar, is essentially inert to the cellular environment, and has multiple modes of reactivity (8). The Staudinger ligation, which capitalizes on the electrophilic character of the azide, chemoselectively forms an amide bond between azides and triarylphosphines (9). This reaction has been employed to tag azidosugar-labeled glycoconjugates on cultured cells and in live mice (10, 11).

Despite the utility of the Staudinger ligation, the phosphine reagents have certain liabilities. They are susceptible to oxidation by molecular oxygen, for example, which limits their shelf-life and may also provide a pathway for rapid liver metabolism (12). Moreover, the Staudinger ligation has a relatively sluggish reaction rate, compromising its ability to monitor rapid biological processes *in vivo* (9). In the context of mouse models, rapid kinetics are important so that the reaction can occur on a faster time scale than metabolic clearance of the probe.

For these reasons, we developed an alternative bioorthogonal reaction modeled on the Huisgen 1,3-dipolar cycloaddition of azides and alkynes, which forms triazole products (13). Our modifications to the classic reaction included situation of the alkyne within a strained cyclooctyne ring (14) as well as the addition of propargylic fluorine atoms (15, 16), two features that significantly accelerated the reaction rate. Another strategy for accelerating the reaction of azides and terminal alkynes involves the use of a Cu catalyst (17, 18) in a reaction widely referred to as “click chemistry;” however, the toxicity of the metal precludes its use in the presence of live cells or organisms. Because cyclooctyne reagents react with azides at rates approaching that of the metal-catalyzed transformation, we refer to these cycloadditions with the term “Cu-free click chemistry.” Various cyclooctyne reagents have recently been used to probe

---

[a] Jennifer A. Prescher, Jeremy M. Baskin, Ellen M. Sletten, Isaac A. Miller, Nicholas J. Agard, and Anderson Lo contributed to the work presented in this chapter.

glycans on cultured cells (16, 19) and in developing zebrafish (20), as well as protein and phospholipid dynamics in live cells (21, 22).

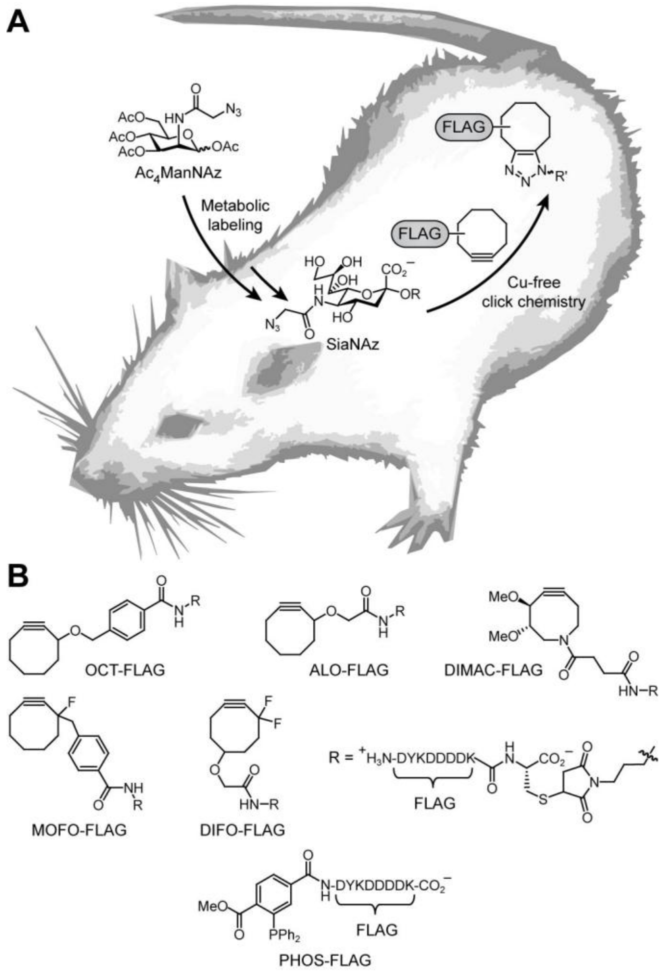

Figure 2-1. Cu-free click chemistry in mice. (A) Mice were injected with $Ac_4ManNAz$ once daily for 1 wk to allow for metabolic labeling of glycans with SiaNAz. The mice were then injected with a cyclooctyne-FLAG conjugate for *in vivo* covalent labeling of azido glycans. (B) Panel of FLAG conjugates used in this study.

In this Chapter, we evaluate Cu-free click chemistry for its performance in mice with the goal of identifying new reagents that are suitable for bioorthogonal ligations *in vivo*. We delivered azides to cell-surface sialoglycoconjugates by injecting mice with the metabolic precursor peracetylated *N*-azidoacetylmannosamine ($Ac_4ManNAz$) (Figure 2-1A) (11, 23). We then labeled glycoconjugates bearing the corresponding azido sialic acid, SiaNAz, by covalent reaction *in vivo* with a panel of cyclooctyne-FLAG peptide conjugates (Figure 2-1B). The labeled biomolecules were probed by *ex vivo* analysis of cells and tissue lysates. The relative amounts of ligation products observed with different cyclooctynes suggest that both intrinsic reaction kinetics and other properties such as solubility and tissue access govern the efficiency of Cu-free click chemistry in mice. More broadly, Cu-free click chemistry appears to possess the requisite bioorthogonality to achieve specific biomolecule labeling in this important model organism.

Results and discussion

Evaluation of cyclooctyne reagents on cultured cells

Prior to *in vivo* studies, we noted that our first-generation cyclooctyne, OCT (14), has considerable hydrophobicity (LogS[b] = -5.49) (24, 25) and, accordingly, poor water solubility, a property that might compromise its bioavailability. We therefore synthesized an aryl-less cyclooctyne (ALO) lacking the hydrophobic phenyl ring in its linker (15) as well as a highly water-soluble dimethoxy azacyclooctyne (DIMAC) (26). DIMAC possesses a nitrogen atom within the strained ring system to interrupt the hydrophobic surface area as well as two methoxy groups to enhance the compound's polarity. We calculated LogS values for ALO and DIMAC of -4.22 and -3.35, respectively (24, 25).

To improve the intrinsic reactivity of the cyclooctynes with azides, we previously introduced fluorine atoms at the propargylic position, generating a monofluorinated cyclooctyne (MOFO) (15) and a difluorinated cyclooctyne (DIFO) (16). Recent theoretical studies have attributed the enhanced reactivity of the fluorinated cyclooctynes in cycloadditions with azides to changes in distortion and interaction energies in the transition state of the reaction (27, 28). The relative second-order rate constants of ALO, OCT, DIMAC, MOFO and DIFO are approximately 1, 2, 3, 4 and 75, respectively, in model reactions (14-16, 26). On this relative scale, the phosphine probe is comparable to OCT.

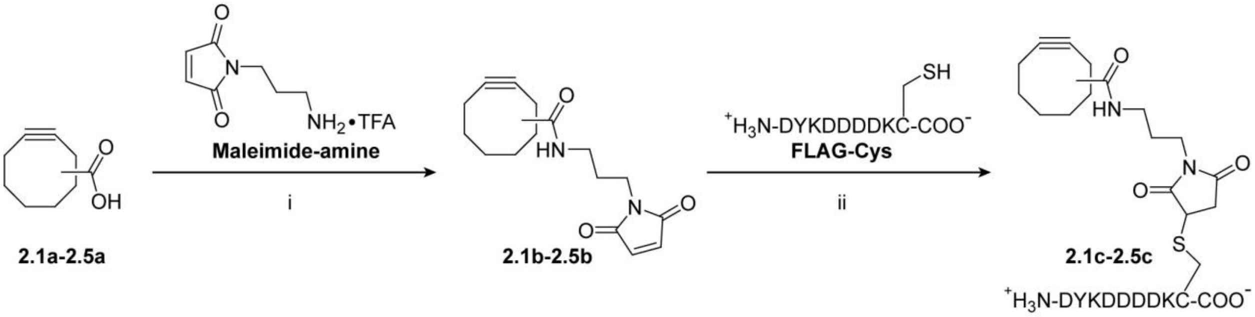

Scheme 2-1. Synthesis of the panel of cyclooctyne-FLAG conjugates. i) **2.1b**: 1. Pfp-TFA, anhydrous pyridine, 4 h. 2. Maleimide-amine (16), TEA, CH_2Cl_2, 24 h, 48%. **2.2b** and **2.3b**: Maleimide-amine, DIPEA, HATU, MeCN, 2 h, 79% and 94%, respectively. **2.4b**: Maleimide-amine, TEA, HATU, HOBt, CH_2Cl_2, 15 min, 65%. **2.5b**: Synthesized as previously reported (16). ii) **2.1c-2.5c**: FLAG-Cys, DMF/H_2O, 12 h; **2.1c**: 51%, **2.2c**: 43%, **2.3c**: 56%, **2.4c**: 27%, **2.5c**: 49% (16).

To facilitate detection of the ligation products, we conjugated a water-soluble FLAG peptide epitope tag (DYKDDDDK) to the cyclooctynes (Figure 2-1B, synthesis described in

---

[b] LogS values were calculated for the Michael addition adducts of methanethiol and the corresponding cyclooctyne maleimide derivatives using the LogS software developed by Tetko *et al*. (http://www.vcclab.org/lab/alogps/). More negative values indicate poorer water solubility.

Scheme 2-1). This was achieved by introducing a cysteine residue at the C-terminus of the FLAG peptide sequence, which was then coupled to a cyclooctyne-maleimide derivative (Scheme 2-2).

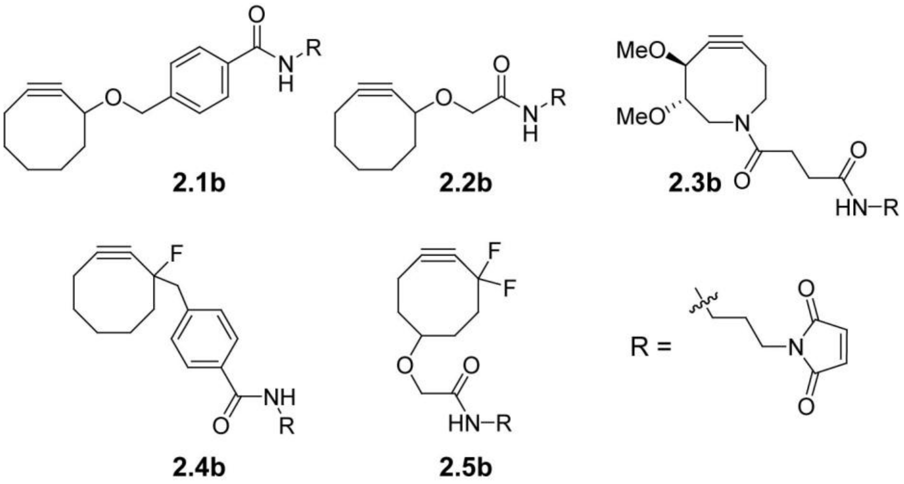

Scheme 2-2. Panel of cyclooctyne maleimide derivatives.

We next tested the ability of the cyclooctyne-FLAG reagents to label SiaNAz residues within glycoconjugates on cultured cells. Jurkat T cells were incubated with or without Ac_4ManNAz for three days. The cells were then treated with a cyclooctyne-FLAG probe or, as a positive control, with a previously described phosphine-FLAG peptide conjugate (PHOS-FLAG, Figure 2-1B) (29). The cells were analyzed by flow cytometry using a fluorescein isothiocyanate (FITC)-labeled anti-FLAG antibody (FITC-anti-FLAG) (Figure 2-2A). All reagents labeled the cells in an azide-dependent manner, with DIFO-FLAG generating the strongest signal. Thus, on cultured cells, the rank order of labeling efficiencies matched that of the reagents' intrinsic reactivities.

Comparison of cyclooctyne and phosphine probes in vivo

After confirming the reactivity of the panel of cyclooctynes on cultured cells, we tested whether the cyclooctyne-FLAG conjugates can react with cell-surface SiaNAz residues *in vivo*. B6D2F1 mice were administered Ac_4ManNAz (300 mg/kg in 70% aqueous DMSO) or vehicle once daily for seven days in accord with our previous studies of ManNAz metabolism *in vivo* (11). On day eight, the mice were injected intraperitoneally (IP) with a cyclooctyne-FLAG reagent. After three hours, the mice were euthanized, and the splenocytes were isolated and analyzed for the presence of cycloadducts by flow cytometry. Splenocytes were chosen for analysis based on our previous studies demonstrating the high incorporation levels of SiaNAz into these cells (11).

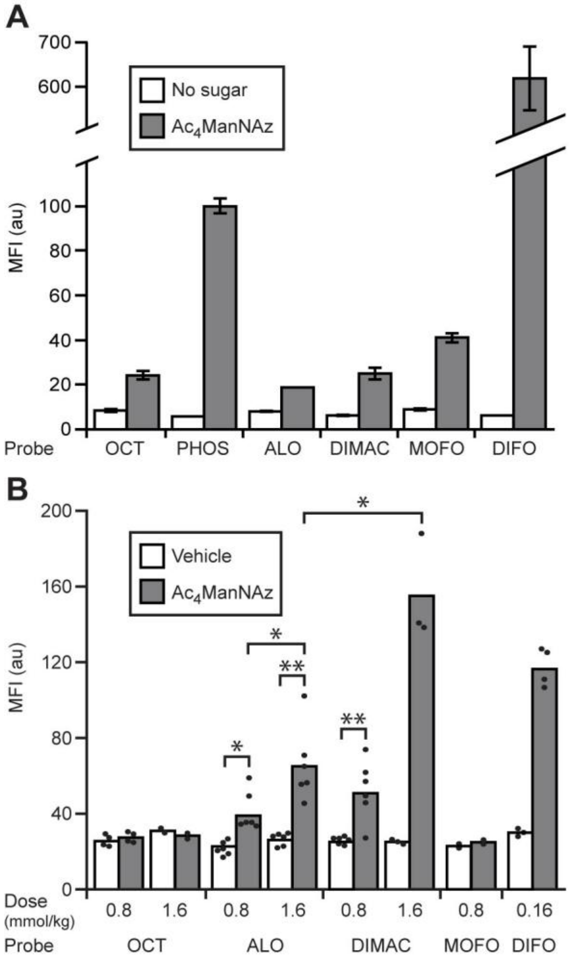

Figure 2-2. Chemical tagging of azido glycans *in vitro* and *in vivo* with cyclooctyne probes. (A) Jurkat cells were incubated with (gray bars) or without (white bars) $Ac_4ManNAz$ (25 μM) for 3 d. The cells were then labeled with a FLAG conjugate (250 μM of OCT-FLAG (OCT), PHOS-FLAG (PHOS), ALO-FLAG (ALO), DIMAC-FLAG (DIMAC), MOFO-FLAG (MOFO), or DIFO-FLAG (DIFO)) for 1 h at rt. The cells were stained with FITC-conjugated anti-FLAG antibody (FITC-anti-FLAG) and then analyzed by flow cytometry. Error bars represent the standard deviation from the average MFI of three replicate samples. (B) Mice were injected with either $Ac_4ManNAz$ (300 mg/kg, IP, gray bars) or vehicle (70% DMSO, white bars) once daily for 7 d. On day 8, the mice were injected IP with various doses (as indicated) of either OCT-FLAG (OCT), ALO-FLAG (ALO), DIMAC-FLAG (DIMAC), MOFO-FLAG (MOFO), or DIFO-FLAG (DIFO). After 3 h, the mice were euthanized, and splenocytes were isolated, labeled with FITC-anti-FLAG, and analyzed by flow cytometry. Each point represents the average MFI value of three replicate samples from an individual mouse. Each bar represents the average MFI value of splenocytes isolated from separate mice (n = 3-11). Mean fluorescence intensity (MFI) is in arbitrary units (au). For all *in vivo* experiments, *ex vivo* reactions of isolated splenocytes with FLAG conjugates verified the presence of cell-surface azides for all of these probes (Figure 2-3). * $P < 0.02$; ** $P < 0.008$.

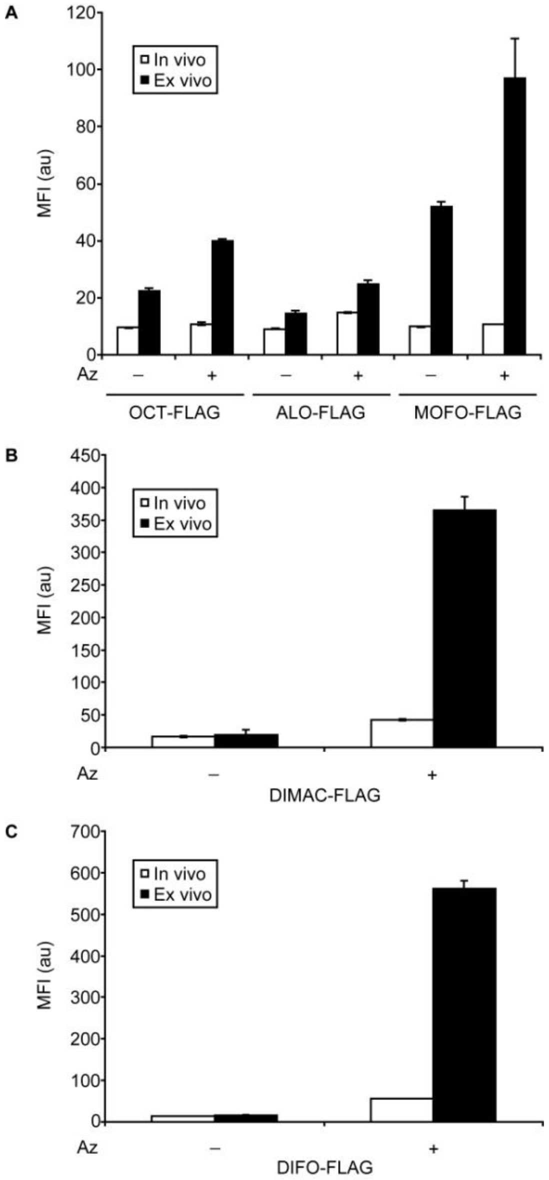

Figure 2-3. Comparison of *in vivo* and subsequent *ex vivo* reactions on isolated splenocytes. After 3 h of *in vivo* ligation, splenocytes from mice treated with $Ac_4ManNAz$ (300 mg/kg, IP, + Az) or vehicle (70% DMSO, – Az) once daily for 7 d and a FLAG conjugate on day 8 were isolated. The presence of cell-surface FLAG epitopes on a portion of the splenocytes from mice injected with (A) OCT-FLAG (0.8 mmol/kg), ALO-FLAG (0.8 mmol/kg), or MOFO-FLAG (0.8 mmol/kg), (B) DIMAC-FLAG (0.8 mmol/kg), and (C) DIFO-FLAG (0.16 mmol/kg) was probed via flow cytometry analysis using FITC-anti-FLAG (white bars). Another portion of the splenocytes was reacted *ex vivo* with additional probe-FLAG conjugate (250 µM) for 1 h at rt (black bars), followed by staining with FITC-anti-FLAG and analysis by flow cytometry. (A) OCT-FLAG, ALO-FLAG, MOFO-FLAG were used as probes for both the *in vivo* and respective *ex vivo* reactions; (B) DIMAC-FLAG was used as a probe for the *in vivo* reaction, and PHOS-FLAG was used for the subsequent *ex vivo* reaction; (C) DIFO-FLAG was used as a probe for the *in vivo* reaction, and PHOS-FLAG was used for the subsequent *ex vivo* reaction.

Interestingly, despite the ability of OCT-FLAG to label azides on cultured cells, splenocytes isolated from mice treated with $Ac_4ManNAz$ and OCT-FLAG (0.8 mmol/kg or 1.6 mmol/kg) did not show any detectable labeling *in vivo* (Figure 2-2B). Subjecting the splenocytes to an additional reaction with the same OCT-FLAG probe *ex vivo* verified the presence of unreacted cell-surface azides (Figure 2-3A). The lack of splenocyte labeling by OCT-FLAG could reflect poor access to organs after IP injection, perhaps due to limited absorption from the peritoneal cavity into the blood stream. Therefore, we examined serum glycoproteins for the presence of cycloadducts by Western blotting with an anti-FLAG antibody (Figure 2-4A). No detectable signal was observed, suggesting that OCT-FLAG may not have entered the blood stream after IP administration. Alternatively, the compound may be sequestered by nonspecific interactions with serum components or cleared from the blood stream on a time scale that is faster than the rate of the covalent reaction.

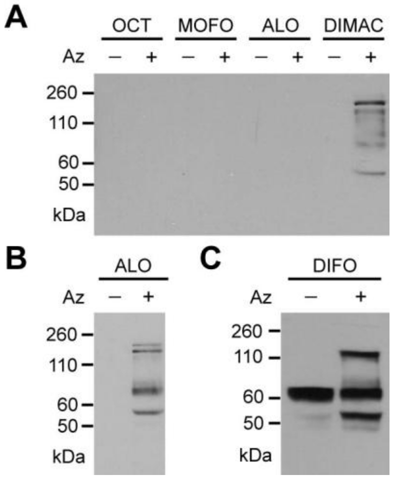

Figure 2-4. Chemical tagging of serum glycoproteins *in vivo* using Cu-free click chemistry. Mice were injected with either $Ac_4ManNAz$ (300 mg/kg, IP, + Az) or vehicle (70% DMSO, – Az) once daily for 7 d. On day 8, the mice were injected IP with various doses of a cyclooctyne-FLAG probe. Serum was collected and analyzed by Western blot with a horseradish peroxidase-anti-FLAG antibody conjugate (HRP-anti-FLAG). (A) Samples from mice injected with 0.8 mmol/kg OCT-FLAG (OCT), MOFO-FLAG (MOFO), ALO-FLAG (ALO), DIMAC-FLAG (DIMAC); blot was exposed for 3 s. (B) Same blot as (A) exposed for 30 s, showing serum glycoproteins labeled with ALO-FLAG. (C) Samples from mice injected with 0.16 mmol/kg DIFO-FLAG; exposed for 2 s.

Splenocytes from mice treated with $Ac_4ManNAz$ and either ALO-FLAG or DIMAC-FLAG (both tested at doses of 0.8 mmol/kg and 1.6 mmol/kg) displayed a significant increase in fluorescence relative to those from vehicle mice, indicating that Cu-free click chemistry proceeds *in vivo* (Figure 2-2B). These probes do not possess significantly faster intrinsic kinetics than OCT, yet they react to a greater extent on splenocytes, suggesting that their physical properties contribute to their *in vivo* reactivities.

MOFO-FLAG and DIFO-FLAG are more intrinsically reactive than OCT but also less soluble in 70% DMSO, thus mandating the use of lower doses (0.8 mmol/kg and 0.16 mmol/kg, respectively) in the *in vivo* experiment. Splenocytes isolated from mice treated with both $Ac_4ManNAz$ and MOFO-FLAG did not show any significant labeling *in vivo* (Figure 2-2B). We also examined serum glycoproteins for chemical modification with MOFO-FLAG; however, no labeling was observed (Figure 2-4A). By contrast, DIFO-FLAG produced significant splenocyte labeling *in vivo* compared to vehicle-treated mice, even at a dose that was 10-fold lower than the highest dose tested for other cyclooctynes (Figure 2-2B). The intrinsic kinetic advantage enjoyed by DIFO *in vitro* is thus reiterated *in vivo*, despite its poor solubility properties. We conclude from this comparative study that physical properties as well as inherent reactivities can both contribute to the efficiency of splenocyte labeling in mice.

Encouraged by these results, we sought to compare *in vivo* Cu-free click chemistry using the best two reagents, DIMAC-FLAG and DIFO-FLAG, with the Staudinger ligation using PHOS-FLAG. In these experiments, mice were injected with either $Ac_4ManNAz$ or vehicle and then either DIMAC-FLAG, DIFO-FLAG, or PHOS-FLAG at the same dose. As shown in Figure 2-5, at the same concentrations, PHOS-FLAG produced more reaction products on splenocytes than either DIMAC- or DIFO-FLAG, despite the fact that the phosphine's *in vitro* reaction efficiency is comparable to DIMAC's and 10-fold lower than DIFO's (Figure 2-2A).

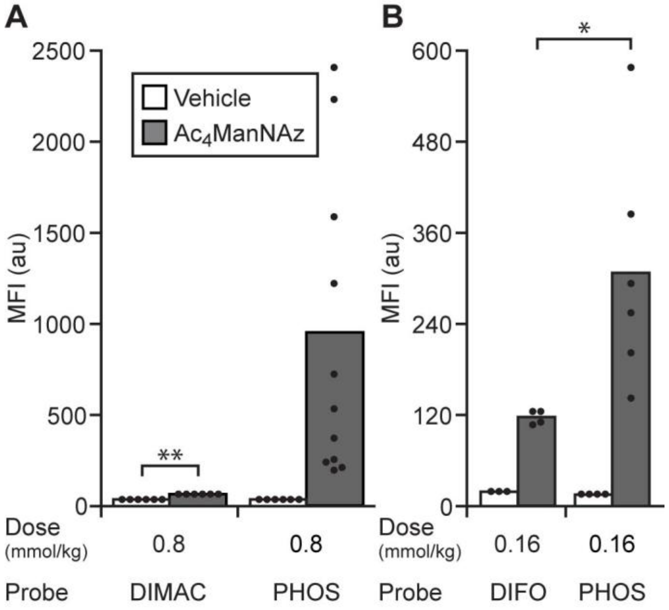

Figure 2-5. Comparison of Cu-free click chemistry and the Staudinger ligation for labeling splenocyte cell-surface azides *in vivo*. Mice were injected with $Ac_4ManNAz$ (300 mg/kg, IP, gray bars) or vehicle (70% DMSO, white bars) once daily for 7 d. On day 8, the mice were injected with either (A) DIMAC-FLAG (DIMAC, 0.8 mmol/kg, IP), (B) DIFO-FLAG (DIFO, 0.16 mmol/kg, IP), or PHOS-FLAG (PHOS) at the same dose. Three hours post-injection of the FLAG conjugates, the mice were euthanized, and the splenocytes were harvested, labeled with FITC-anti-FLAG, and analyzed by flow cytometry. Each point represents the average MFI value of three replicate samples from an individual mouse. Each bar represents the average MFI value of splenocytes isolated from separate mice (n = 3-11). * $P < 0.02$; ** $P < 0.008$.

These results may reflect differences in tissue access for the various reagents, a possibility that we addressed by Western blot analysis of serum and tissue lysates from mice treated with $Ac_4ManNAz$ or vehicle, followed by probe-FLAG conjugates. We observed detectable labeling of serum glycoproteins with all of the cyclooctynes except OCT-FLAG and

MOFO-FLAG as discussed above (Figure 2-4). Thus, ALO-, DIMAC- and DIFO-FLAG have some degree of access to the vasculature. From our panel of three isolated organs, we observed labeling with ALO-FLAG only in the intestines (Figure 2-6A, overnight exposure). With DIMAC- and DIFO-FLAG, labeling was observed in all of the organs harvested, with the strongest labeling in the intestines, followed by the heart and liver (Figure 2-6B and C, 5-min and 1-h exposure, respectively). The relative intensity of glycoprotein labeling in the intestines may reflect this organ's proximity to the IP injection site. For comparative purposes we also probed the same organs for the presence of Staudinger ligation products derived from injected PHOS-FLAG. Again, we observed glycoprotein labeling in all of the organs harvested, with the strongest signal in samples from the intestines, followed by the heart and liver (Figure 2-6D, 10-s exposure). Thus, PHOS-FLAG appears to access the same organs as DIMAC- and DIFO-FLAG.

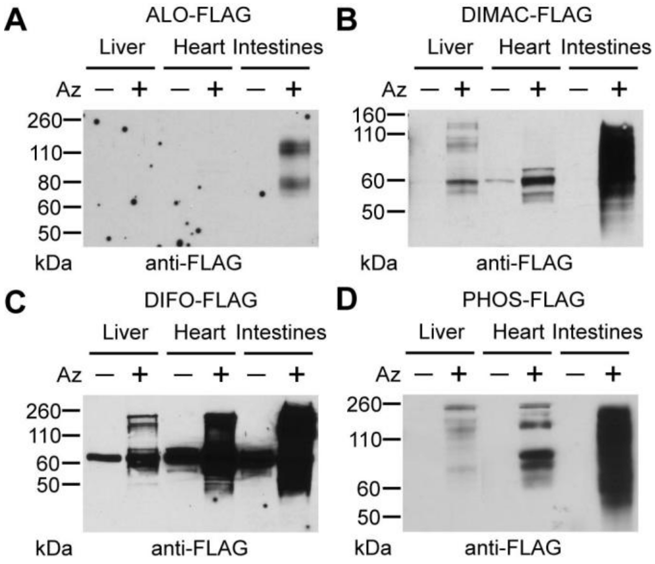

Figure 2-6. Cu-free click chemistry and Staudinger ligation products are observed in a variety of tissues *in vivo*. Mice were injected with $Ac_4ManNAz$ (300 mg/kg, IP, + Az) or vehicle (70% DMSO, – Az) once daily for 7 d. On day 8, the mice were injected with either (A) ALO-FLAG (0.8 mmol/kg, IP), blot was exposed overnight; (B) DIMAC-FLAG (0.8 mmol/kg, IP), blot was exposed for 5 min; (C) DIFO-FLAG (0.16 mmol/kg, IP), blot was exposed for 1 h; or (D) PHOS-FLAG (0.8 mmol/kg, IP), blot was exposed for 10 s. Three hours post-injection of the FLAG conjugates, the mice were euthanized, and organs (liver, heart, intestines) were harvested and homogenized. The organ lysates were analyzed by Western blot probing with HRP-anti-FLAG. Each lane represents organ lysate from a single representative mouse.

DIFO-FLAG binds mouse serum albumin (MSA) with high affinity

We noted that the Western blots of organ lysates (Figure 2-6C) and serum (Figure 2-4C) from mice treated with vehicle followed by DIFO-FLAG showed a strongly-labeled band with an apparent molecular weight around 65 kDa. A similar band, though much more faint, was observed in the Western blot of heart lysates from mice treated with vehicle followed by DIMAC-FLAG (Figure 2-6B). Thus, DIFO-FLAG and, to a lesser extent, DIMAC-FLAG seem to bind a ubiquitous species in an azide-independent manner. Mouse serum albumin (MSA), with a molecular weight of 68 kDa, was the most obvious candidate (30). MSA is the most abundant serum protein and is known for its role as a carrier protein for small hydrophobic molecules (31).

We tested the MSA-binding activity of DIFO-FLAG by immunoprecipitation of liver lysates derived from $Ac_4ManNAz$ or vehicle-treated mice using an anti-FLAG antibody or isotype control. Western blots of the captured glycoproteins probed using either an anti-FLAG (Figure 2-7A) or anti-MSA (Figure 2-7B) antibody confirmed that the species labeled with DIFO-FLAG in an azide-independent manner was indeed MSA. We also immunoprecipitated MSA from liver lysate samples from the same mice using an anti-MSA antibody or isotype control. Western blots of the captured proteins were probed using either an anti-FLAG (Figure 2-7C) or anti-MSA antibody (Figure 2-7D) to verify that MSA was indeed modified by the FLAG epitope. It should be noted that the Western blots in Figure 7 reflect samples that were exposed to both 1 M urea and β-mercaptoethanol and were boiled for 10 min before being run on a reducing, denaturing gel. The persistence of MSA labeling after these treatments suggests that the interaction might be covalent. MSA has two free cysteine residues that are subject to covalent modification by other metabolites (32). It is possible that nonspecific binding to the DIFO core, a highly hydrophobic moiety, facilitates covalent interactions with cysteine or other nucleophilic residues.

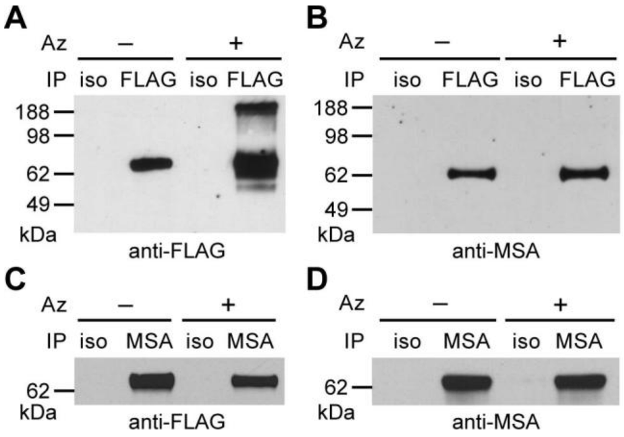

Figure 2-7. DIFO-FLAG binds mouse serum albumin (MSA). Liver lysates from mice injected with $Ac_4ManNAz$ (300 mg/kg, IP, + Az) or vehicle (70% DMSO, – Az) once daily for 7 d, followed by one bolus of DIFO-FLAG (0.16 mmol/kg, IP) on day 8, were immunoprecipitated with (A-B) an anti-FLAG antibody (FLAG) or an isotype control (iso), or (C-D) an anti-MSA antibody (MSA) or an isotype control (iso). The samples were analyzed by Western blot probing for (A and C) FLAG or (B and D) MSA.

Conclusions

Cu-free click chemistry has been previously used to monitor azidosugars (16, 33), proteins bearing azido amino acids (34, 35), lipids (22), and site-specifically labeled proteins (21) in live cells. In this paper, we have demonstrated that Cu-free click chemistry using a variety of cyclooctyne probes can be employed to label azidosugars in the physiologically relevant context of a mouse. Cyclooctynes thereby join the ranks of a privileged few reagents that possess the requisite bioorthogonality to find their covalent reaction partners in animals. Most of these reagents, however, require non-covalent complexation with an enzyme target to deliver a covalent warhead to a nucleophilic residue nearby (36, 37). Only the Staudinger ligation and Cu-free click chemistry reagents possess sufficient bioorthogonality for direct covalent labeling of their targets *in vivo*. The ability to perform these chemical reactions in living animals could enable therapeutic targeting or molecular imaging of changes in metabolism in mouse models of human disease.

Among the cyclooctynes tested, DIFO-FLAG, which possesses the best intrinsic reactivity with azides, was the most efficient reagent for labeling serum or tissue-resident glycoproteins. DIMAC- and ALO-FLAG also afforded detectable labeling, though at lower levels. Their advantage over OCT- and MOFO-FLAG may reflect their superior water solubility. It should be noted, however, that PHOS-FLAG, a reagent with lower inherent reactivity than DIFO, gave the most robust labeling of splenocytes after the three-hour *in vivo* reaction. DIFO's bioavailability may be compromised by significant binding to serum albumin. Thus, optimization of bioorthogonal reagents for *in vivo* applications may require consideration of both their intrinsic reactivities as well as their pharmacokinetic properties.

Analysis of the detailed biodistributions and serum residence times of the above reagents will be an interesting extension of this work. Moreover, pathways of metabolic clearance will be important to characterize in the design of optimal bioorthogonal reagents. Literature precedents suggest that phosphines (12) and terminal alkynes (38) can be metabolized in the liver by cytochrome P450 enzymes. Internal alkynes also may be oxidized by P450 enzymes, though their routes of metabolism are less well characterized (39). The metabolism of cyclooctynes has not been explored, offering another interesting future direction.

Materials and methods

General

All chemical reagents were of analytical grade, obtained from commercial suppliers, and used without further purification unless otherwise noted. With the exception of reactions performed in aqueous media, all reaction vessels were flame-dried prior to use. Reactions were performed in a N_2 atmosphere, except in the case of reactions performed in aqueous media, and liquid reagents were added with a syringe unless otherwise noted. Tetrahydrofuran (THF) was distilled under N_2 from Na/benzophenone immediately prior to use, and CH_2Cl_2 was distilled from CaH_2 immediately prior to use. Anhydrous pyridine and DMF were purchased from Acros Organics (Morris Plains, NJ). Chromatography was carried out with Merck 60 230–400 mesh silica gel. Reactions and chromatography fractions were analyzed with Analtech 250 micron silica gel G plates and visualized by staining with ceric ammonium molybdate or by absorbance of UV light at 254 nm. When an R_f is reported for a compound, the solvent that was used was the chromatography solvent unless otherwise noted. Organic extracts were dried over $MgSO_4$, and solvents were removed with a rotary evaporator at reduced pressure (20 torr), unless otherwise noted. IR spectra were of thin films on NaCl plates. Unless otherwise noted, ^1H, ^{13}C, and ^{19}F NMR spectra were obtained with 300 MHz, 400 MHz, 500 MHz, or 600 MHz Bruker spectrometers. Chemical shifts are reported in δ ppm referenced to the solvent peak for ^1H and ^{13}C and relative to $CFCl_3$ for ^{19}F. Coupling constants (*J*) are reported in Hz. Low- and high-resolution fast atom bombardment (FAB) and electrospray ionization (ESI) mass spectra were obtained at the UC Berkeley Mass Spectrometry Facility, and elemental analyses were obtained at the UC Berkeley Micro-Mass Facility. Melting points were determined using a Mel-Temp 3.0 melting point apparatus and are uncorrected. Reversed-phase HPLC was performed using a Rainin Instruments Dynamax SD-200 system equipped with a Varian UV-Vis detector (model 345) and a Microsorb C18 analytical column (4.6 x 250 mm) at a flow rate of 1 mL/min, a semipreparative column (10 x 250 mm) at a flow rate of 4 mL/min, or a preparative column (21.4 x 250 mm) at a flow rate of 20 mL/min. HPLC samples were filtered with a Pall Life Sciences Acrodisc CR 13 mm syringe filter equipped with a 0.2 μm PTFE membrane prior to injection. $Ac_4ManNAz$ (29), PHOS-FLAG (29), OCT (14), ALO (15), MOFO (15), DIMAC (26), DIFO-maleimide (16) and DIFO-FLAG (16) were synthesized according to previously published procedures.

Dulbecco's phosphate-buffered saline pH 7.4 (PBS), anti-FLAG M2-peroxidase (HRP-anti-FLAG), and fluorescein isothiocyanate (FITC)-anti-FLAG were purchased from Sigma. RPMI-1640 media was obtained from Invitrogen Life Technologies, Inc., and fetal bovine serum (FBS) was obtained from HyClone Laboratories. Flow cytometry analysis was performed on a BD FACSCalibur flow cytometer using a 488 nm argon laser. At least 10^4 live cells were analyzed for each sample. Cell viability was ascertained by gating the samples on the basis of forward scatter (to sort by size) and side scatter (to sort by granularity). The average fluorescence intensity was calculated from each of three replicate experiments to obtain a mean value in arbitrary units. The data points are representative of at least three separate experiments. SDS-PAGE was performed on pre-cast 12% polyacrylamide gels (Bio-Rad) and Western blots were developed using a SuperSignal West Pico Chemiluminescent Detection Kit (Pierce).

Chemical synthesis

Synthesis of cyclooctyne-FLAG conjugates

We initially attempted to attach the cyclooctyne via its carboxylic acid directly onto the N-terminus of a Wang resin-bound FLAG peptide. However, this route was unsuccessful due to decomposition of the strained alkyne in the presence of the strongly acidic cleavage cocktail, consistent with observations from Wolfbeis and co-workers (40). Thus, we opted to introduce a cysteine residue at the C-terminus of the FLAG peptide sequence, which was then coupled to a cyclooctyne-maleimide compound (Schemes 2-1 and 2-2).

OCT-maleimide (2.1b). Pentafluorophenyl trifluoroacetate (Pfp-TFA) (343 μL, 2.00 mmol) was added to OCT (14) (**2.1a**, 258 mg, 1.00 mmol) in anhydrous pyridine (8.0 mL). The reaction was stirred for 4 h, diluted with CH_2Cl_2 (250 mL), and washed with 1 M HCl (3 x 250 mL) and a sat. $NaHCO_3$ solution (2 x 250 mL). The organic layer was dried over $MgSO_4$, filtered, and concentrated. The crude ester was dissolved in dry CH_2Cl_2 (5 mL). Maleimide-amine (16) (693 mg, 4.50 mmol) was added, followed by triethylamine (1.26 mL, 9.00 mmol). The reaction was stirred for 24 h and then concentrated. The crude product was purified by silica gel chromatography (3:2 petroleum ether/EtOAc to 2:3 petroleum ether/EtOAc) to give the desired product as a white solid (0.190 g, 48%). ^{1}H NMR ($CDCl_3$, 300 MHz): δ 1.24-2.30 (m, 12H), 3.38 (app q, 2H, *J* = 6.0 Hz), 3.64 (app t, 2H, *J* = 6.0), 4.21 (m, 1H), 4.43 (app d, 1H, *J* = 12.0), 4.71 (app d, 1H, *J* = 12.0), 6.73 (s, 2H), 7.02 (m, 1H), 7.41 (d, 2H, *J* = 8.1 Hz), 7.80 (d, 2H, *J* = 8.1 Hz). ^{13}C NMR ($CDCl_3$, 75 MHz): δ 21.1, 26.6, 28.4, 30.0, 34.6, 35.0, 36.5, 42.6, 70.7, 72.3, 92.8, 100.9, 127.3, 128.1, 133.5, 134.6, 142.4, 167.8, 171.5. FAB-HRMS: Calcd. for $C_{23}H_{27}N_2O_4^+$ $[M+H]^+$: 395.1971, found: 395.1976.

ALO-maleimide (2.2b). ALO (15) (**2.2a**, 15 mg, 0.080 mmol) was dissolved in MeCN (1.5 mL) and cooled to 0 °C. *N*,*N*-Diisopropylethylamine (0.07 mL, 0.4 mmol) was added, followed by maleimide-amine (35 mg, 0.13 mmol) and HATU (36 mg, 0.095 mmol). The mixture was warmed to rt and allowed to react for 2 h, at which point the reaction was evaporated to dryness. The crude product was purified by silica gel chromatography with a 12:1 toluene/acetone solvent system to yield the desired product (20 mg, 79%, R_f = 0.6 in 1:1 toluene/acetone). ^{1}H NMR (600 MHz, MeOD): δ 1.36-1.42 (m, 1H), 1.52-1.62 (m, 2H), 1.67 (quin, 2H, *J* = 6.8 Hz), 1.72-1.79 (m, 2H), 1.80-1.86 (m, 1H), 1.94-1.98 (m, 1H), 2.03-2.09 (m, 2H), 2.12-2.17 (m, 1H), 3.12 (q, 2H, *J* = 6.6 Hz), 3.44 (td, 2H, *J* = 6.7, 1.3 Hz), 3.76 (d, 1H, *J* = 15.2 Hz), 3.88 (d, 1H, *J* = 15.2 Hz), 4.20-4.22 (m, 1H), 6.72 (s, 2H). ^{13}C NMR (150 MHz, MeOD): δ 21.4, 27.6, 29.5, 31.0, 35.6, 36.1, 37.2, 43.3, 69.1, 74.5, 92.6, 102.4, 135.6, 172.7, 172.8. ESI-HRMS: Calcd. for $C_{17}H_{22}O_4N_2Na^+$ $[M+Na]^+$: 341.1472, found: 341.1466.

DIMAC-maleimide (2.3b). DIMAC (26) (**2.3a**, 0.100 g, 0.372 mmol,) was dissolved in MeCN (8 mL) and cooled to 0 °C. *N*,*N*-Diisopropylethylamine (0.33 mL, 1.9 mmol) was added, followed by maleimide-amine (158 mg, 0.589 mmol) and HATU (162 mg, 0.427 mmol). The mixture was warmed to rt and allowed to react for 4 h, at which point the reaction was evaporated to dryness. The crude product was purified by silica gel chromatography using a toluene/acetone solvent system (5:1 to 3:1 to 1:1) to yield the desired product (141 mg, 94%, R_f = 0.2 in 1:1 toluene/acetone) as a 10:1 mixture of rotamers (designated rotH). ^{1}H NMR (600

MHz, D_2O): δ 1.78 (quin, 2H, *J* = 6.8 Hz, 2rotH), 2.21-2.25 (m, 1 rotH), 2.32 (dt, 1H, *J* = 16.8, 3.2 Hz), 2.50-2.60 (m, 2H, 2rotH), 2.62-2.69 (1H, 1rotH), 2.73-2.82 (2H, 1rotH), 2.84-2.92 (m, 1rotH), 3.02 (dd, 1H, *J* = 14.3, 9.0 Hz), 3.05-3.08 (m, 1rotH), 3.12-3.21 (m, 2H, 3rotH), 3.28-3.34 (m, 4H), 3.36 (s, 3rotH), 3.51-3.56 (m, 5H, 3rotH), 3.69 (t, 1H, *J* = 8.8 Hz), 3.67-3.73 (m, 2rotH), 3.82 (t, 1rotH, *J* = 8.4 Hz), 4.00 (d, 1rotH, *J* = 15.9 Hz), 4.05 (d, 1H, *J* = 14.2 Hz), 4.16 (dd, 1H, *J* = 14.9, 5.5 Hz), 4.20 (dt, 1H, *J* = 8.6, 2.5 Hz), 4.22-4.24 (m, 1rotH), 4.35 (dt, 1rotH, *J* = 7.9, 2.3 Hz), 6.83 (s, 2H, 2rotH). ^{13}C NMR (150 MHz, D_2O, no rotamer peaks tabulated): δ 20.8, 27.1, 28.4, 30.9, 35.1, 36.7, 52.1, 54.3, 56.7, 58.1, 76.2, 84.4, 90.8, 99.0, 134.4, 173.2, 174.75, 174.77. ESI-HRMS: Calcd. for $C_{20}H_{27}O_6N_3Na^+$ $[M+Na]^+$: 428.1792, found 428.1785.

MOFO-maleimide (2.4b). Triethylamine (0.508 ml, 3.65 mmol) was added to a solution of MOFO (15) (**2.4a**, 0.200 g, 0.768 mmol), maleimide-amine (0.235 g, 0.875 mmol), HATU (0.305 g, 0.802 mmol), and 1-hydroxybenzotriazole (HOBt, 0.123 g, 0.802 mmol) in CH_2Cl_2 (3 mL) at rt. The reaction was stirred for 15 min, quenched with H_2O (10 mL), and diluted with CH_2Cl_2 (50 mL). The organic layer was washed with 1 N HCl (3 x 50 mL), sat. $NaHCO_3$ (3 x 50 mL), and brine (2 x 25 mL) and dried over $MgSO_4$. Chromatography of the crude product (2:1 to 1:1 hexanes/EtOAc) yielded the desired product as a white solid (0.198 g, 65%, R_f = 0.30 in 1:1 hexanes/EtOAc), mp 122.0-124.0 °C (dec). IR: 3413, 2931, 2854, 2222, 1705, 1640 cm^{-1}. ^1H NMR ($CDCl_3$, 400 MHz): δ 1.39 (m, 1H), 1.74 (m, 2H), 1.81-2.06 (m, 6H), 2.14-2.32 (m, 3H), 3.05 (d, 1H, *J* = 2.8 Hz), 3.09 (s, 1H), 3.40 (q, 2H, *J* = 6.4 Hz), 3.67 (t, 2H, *J* = 6.0 Hz), 6.75 (s, 2H), 6.93 (m, 1H), 7.41 (d, 2H, *J* = 8.0 Hz), 7.81 (d, 2H, *J* = 8.0 Hz). ^{13}C NMR ($CDCl_3$, 100 MHz): δ 20.5, 26.0, 28.1, 29.4, 34.0, 34.8, 36.2, 44.6 (d, *J* = 25.0 Hz), 47.8 (d, *J* = 24.0 Hz), 90.7 (d, *J* = 32.0 Hz), 95.3 (d, *J* = 174.0 Hz), 104.5 (d, *J* = 10.0 Hz), 126.7, 130.5, 132.9, 134.2, 139.6, 167.1, 171.1. ^{19}F NMR ($CDCl_3$, 376 MHz): δ -139.0 (m). FAB-HRMS: Calcd. for $C_{23}H_{26}N_2O_3F^+$ $[M+H]^+$: 397.1927, found: 397.1920.

General procedure for synthesis of cyclooctyne-FLAG peptide conjugates

Cysteine-modified FLAG peptide (FLAG-Cys, H_2N-DYKDDDDKC-CO_2H) was synthesized on Fmoc-Cys(Trt) Wang resin (100-200 mesh) using standard Fmoc solid-phase peptide synthesis with N^α-Fmoc protected amino acids and DIC/HOBt ester activation in NMP. A five-fold excess of amino acid was used for the coupling steps, which involved gentle rotation for 30 min and was repeated once for each amino acid. Fmoc removal was achieved with 20% piperidine in NMP (1 x 30 min). The peptide was cleaved for 3 h using a solution of trifluoroacetic acid:triisopropylsilane:water (95:2.5:2.5) and precipitated with ether. The crude product was dried and used without further purification. Cyclooctyne-FLAG conjugates were synthesized using standard thiol-maleimide coupling chemistry. Briefly, the cyclooctyne-maleimide derivatives were dissolved in anhydrous DMF and added to a solution of FLAG-Cys (1.5-2.2 eq) in an equal amount of water. If necessary, additional DMF was added to the reaction mixture to solubilize the reactants. The resulting solutions were stirred overnight, concentrated, and filtered prior to purification by reversed-phase HPLC. Gradients used are listed below. Solvent A is ddH_2O + 0.1% TFA, and solvent B is MeCN + 0.1% TFA. The appropriate fractions were pooled and lyophilized to provide the conjugates as fluffy white powders.

OCT-FLAG (**2.1c**): Purified using a gradient of 0-15 %B over 5 min, followed by 15-50 %B over 35 min; 51%. (ESI-HRMS): Calcd. for $C_{67}H_{92}O_{25}N_{13}S^+$ $[M+H]^+$: 1510.6043, found: 1510.6094.

ALO-FLAG (**2.2c**): Purified using a gradient of 5-70 %B over 40 min; 43%. (ESI-HRMS): Calcd. for $C_{61}H_{88}O_{25}N_{13}S^{+}$ $[M+H]^{+}$: 1434.5730, found: 1434.5770.
DIMAC-FLAG (**2.3c**): Purified using a gradient of 0-35 %B over 30 min; 56%. (ESI-HRMS) Calcd. for $C_{64}H_{90}N_{14}O_{27}S^{2-}$ $[M-2H]^{2-}$: 759.2916; found 759.2941.
MOFO-FLAG (**2.4c**): Purified using a gradient of 0-15 %B over 5 min, followed by 15-50 %B over 35 min; 27%. (ESI-HRMS): Calcd. for $C_{67}H_{91}O_{24}N_{13}FS^{+}$ $[M+H]^{+}$: 1512.6014, found: 1512.5999.

Cell culture

Jurkat (human T cell lymphoma) cells and isolated splenocytes were maintained in a 5% CO_2, water-saturated atmosphere and grown in RPMI-1640 media supplemented with 10% FBS, penicillin (100 units/mL), and streptomycin (0.1 mg/mL). Cell densities were maintained between 1×10^{5} and 2×10^{6} cells per mL.

Labeling of cultured cells with FLAG conjugates and flow cytometry analysis

Jurkat cells were incubated for 3 d in untreated medium or medium containing 25 μM Ac_4ManNAz. The cells were then distributed into a 96-well V-bottom tissue culture plate, pelleted (2500 x g for 3 min), and washed with 200 μL (3x) of labeling buffer (PBS containing 1% FBS). Cells were then incubated with a cyclooctyne-FLAG conjugate (**2.1c-2.5c**) or PHOS-FLAG (250 μM) in labeling buffer for 1 h at room temperature. After incubation, the cells were pelleted, washed three times with labeling buffer, and resuspended in the same buffer containing FITC-anti-FLAG (1:900 dilution of the Sigma stock). After a 30-min incubation on ice, the cells were washed once with 200 μL of cold labeling buffer and then diluted to a volume of 400 μL for flow cytometry analysis.

Mice

Wild type B6D2F1 mice (aged 5-8 weeks) were purchased from The Jackson Laboratory or Charles River Laboratories. Animals were handled in accordance with Animal Use Protocol R234-0510B (approved by the Animal Care and Use Committee at the University of California, Berkeley).

Compound administration

B6D2F1 mice were administered Ac_4ManNAz (300 mg/kg in 70% DMSO from a 116 mM stock solution) or vehicle (70% DMSO) intraperitoneally once daily for 7 days. Twenty-four hours after the final Ac_4ManNAz bolus, mice were injected intraperitoneally with either PHOS-FLAG (0.16 mmol/kg or 0.8 mmol/kg in 70% DMSO or water from a 26.7 mM or 133 mM stock solution, respectively), OCT-FLAG (0.8 mmol/kg or 1.6 mmol/kg in 70% DMSO from a 133 mM or 267 mM stock solution, respectively), ALO-FLAG (0.8 mmol/kg or 1.6 mmol/kg in 70% DMSO from a 133 mM or 267 mM stock solution, respectively), DIMAC-FLAG (0.8 mmol/kg and 1.6 mmol/kg in water from a 133 mM or 267 mM stock solution, respectively), MOFO-FLAG (0.8 mmol/kg in 70% DMSO from a 133 mM stock solution), or DIFO-FLAG (0.16 mmol/kg in 70% DMSO from a 26.7 mM stock solution). All doses of azidosugar, vehicle, and

FLAG-conjugates were administered in approximately 150 μL of 70% DMSO or water. Three hours post-injection of the FLAG conjugates, the mice were euthanized, and a panel of organs was harvested.

Splenocyte analysis after Cu-free click chemistry in vivo

Splenocytes from mice treated first with $Ac_4ManNAz$ or vehicle followed by the appropriate FLAG conjugate were isolated and probed for the presence of cell-surface FLAG epitopes using a previously reported protocol (11). Briefly, isolated splenocytes were incubated directly with FITC-anti-FLAG in labeling buffer (PBS + 1% FBS, 1:900 dilution of Sigma stock) for 30 min on ice. The cells were then washed once with labeling buffer and analyzed by flow cytometry.

Labeling of splenocyte cell-surface azides ex vivo

Splenocytes isolated as described above were further reacted *ex vivo* with OCT-FLAG, ALO-FLAG, MOFO-FLAG, or PHOS-FLAG to probe for the presence of unreacted azides. Briefly, splenocytes were incubated with either PHOS-FLAG or one of the cyclooctyne-FLAG conjugates (250 μM) for 1 h at room temperature in labeling buffer. The cells were then rinsed three times with labeling buffer, treated with FITC-anti-FLAG for 30 min on ice, rinsed with labeling buffer once, and analyzed by flow cytometry.

Western blot analysis of serum glycoproteins

Whole blood was collected from anesthetized mice injected first with either $Ac_4ManNAz$ or vehicle and then PHOS-FLAG or a cyclooctyne-FLAG conjugate by cardiac puncture from the closed thorax. The samples were allowed to clot, and the serum was then isolated by removal of the agglutinated red blood cells and leukocytes. The samples were then centrifuged (13,500 x g for 10 min) to remove residual cell debris, and the supernatant was collected and diluted with lysis buffer (150 mM NaCl, 1% NP-40, 20 mM Tris-HCl, 1 mM EDTA, pH 7.4) containing protease inhibitors (Complete, Roche). Protein concentrations were determined using the *DC* protein assay kit (Bio-Rad). The samples (50 μg of protein per lane) were analyzed by Western blot, probing with a horseradish peroxidase-anti-FLAG antibody conjugate (HRP-anti-FLAG) as previously described (11).

Lysis of murine organs and Western blot analysis

Organs (liver, heart, and intestines) harvested from mice injected first with either $Ac_4ManNAz$ or vehicle and then PHOS-FLAG or a cyclooctyne-FLAG conjugate were rinsed with cold PBS and minced. The organs were then transferred into 1.5 mL of lysis buffer (150 mM NaCl, 1% NP-40, 20 mM Tris-HCl, 1 mM EDTA, pH 7.4) containing protease inhibitors (Complete, Roche) and homogenized using a Dounce homogenizer. The lysates were centrifuged (13,500 x g for 10 min) to remove cell debris, and the supernatant was collected. Protein concentrations were determined using the *DC* protein assay kit (Bio-Rad). The samples (100 μg of protein per lane) were analyzed by Western blot, probing with HRP-anti-FLAG as previously described (11).

Immunoprecipitation of FLAG-labeled liver lysates to probe for mouse serum albumin (MSA)

Liver lysate (10 mg of protein) from mice treated with either $Ac_4ManNAz$ or vehicle and subsequently injected with DIFO-FLAG were prepared as described above and incubated with 60 μg of M2 anti-FLAG antibody (Sigma) or isotype control (mouse IgG1 isotype, Sigma) in 10 mL of lysis buffer containing protease inhibitors (Complete, Roche) at 4 ºC with rotation overnight. Ultralink Immobilized Protein A/G (60 μL, Pierce) was added, and the sample was rotated for 2 h at room temperature. At this point, the resin was pelleted by centrifugation (1000 x g for 1 min), and the supernatant was discarded. Wash buffer A (750 μL of 50 mM Tris, 300 mM NaCl, 1% Triton X-100, pH 7.4) was added. The sample was pelleted on a benchtop microfuge, and the supernatant was discarded. A second wash with 750 μL of wash buffer A was performed, followed by two washes of 750 μL each with wash buffer B (50 mM Tris, 1.3 M NaCl, 1% Triton X-100, pH 7.4) and wash buffer C (50 mM Tris, 1.3 M NaCl, 1 M urea, 1% Triton X-100, pH 7.4). The beads were then diluted with 1X SDS gel loading buffer (Bio-Rad) containing β-mercaptoethanol, boiled for 10 min, and analyzed by Western blot, using HRP-anti-FLAG (1:1000 dilution of Sigma stock) to probe for FLAG (1/5 of the total elution) or goat anti-MSA (affinity-purified polyclonal, 1:5000 dilution of Bethyl Laboratories stock), followed by donkey anti-goat-HRP (1:5000 dilution of Santa Cruz Biotechnology stock) to probe for MSA (4/5 of the total elution).

Immunoprecipitation of MSA from liver lysates to probe for the FLAG epitope

MSA was immunoprecipitated as previously described (32). Briefly, liver lysate (10 mg of protein) from mice treated with either $Ac_4ManNAz$ or vehicle and subsequently injected with DIFO-FLAG were prepared as described above. The samples were pre-cleared with Ultralink Immobilized Protein A/G (50 μL, Pierce) by rotation for 1 h at 4 ºC in 10 mL of 50 mM sodium phosphate, pH 7.4 (immunoprecipitation buffer), followed by centrifugation to pellet the beads (3700 x g for 5 min) and collection of the supernatant. In separate tubes, anti-MSA or an isotype control antibody (goat anti-mouse IgG) (15 μg) was bound to a separate sample of Ultralink Immobilized Protein A/G (50 μL) by rotation for 1 h at 4 ºC in 10 mL of immunoprecipitation buffer. The antibody-bound beads were rinsed once with 5 mL of immunoprecipitation buffer, and the pre-cleared lysate was added to the antibody-bound beads and rotated overnight at 4 ºC. Then the beads were pelleted (3700 x g for 5 min), rinsed 3 times with 1 mL of immunoprecipitation buffer, and eluted by boiling for 10 min in 1X SDS gel loading buffer (Bio-Rad). One quarter of the sample was analyzed by Western blot, probing with goat anti-MSA (affinity-purified polyclonal, 1:5000 dilution of Bethyl Laboratories stock) followed by donkey anti-goat-HRP (1:5000 dilution of Santa Cruz Biotechnology stock), and the remainder of the elution was analyzed by Western blot, probing with HRP-anti-FLAG (1:1000 dilution of Sigma stock).

References

1. Peters LL, *et al.* (2007) The mouse as a model for human biology: A resource guide for complex trait analysis. *Nat Rev Genet* 8:58-69.

2. Ohtsubo K, Marth JD (2006) Glycosylation in cellular mechanisms of health and disease. *Cell* 126:855-867.

3. Ohtsubo K, *et al.* (2005) Dietary and genetic control of glucose transporter 2 glycosylation promotes insulin secretion in suppressing diabetes. *Cell* 123:1307-1321.

4. Hart GW, Housley MP, Slawson C (2007) Cycling of O-linked beta-N-acetylglucosamine on nucleocytoplasmic proteins. *Nature* 446:1017-1022.

5. Kayser H, *et al.* (1992) Biosynthesis of a nonphysiological sialic acid in different rat organs, using N-propanoyl-D-hexosamines as precursors. *J Biol Chem* 267:16934-16938.

6. Prescher JA, Bertozzi CR (2006) Chemical technologies for probing glycans. *Cell* 126:851-854.

7. Prescher JA, Bertozzi CR (2005) Chemistry in living systems. *Nat Chem Biol* 1:13-21.

8. Sletten EM, Bertozzi CR (2009) Bioorthogonal chemistry: Fishing for selectivity in a sea of functionality. *Angew Chem Int Ed Engl* 48:6974-6998.

9. Lin FL, Hoyt HM, van Halbeek H, Bergman RG, Bertozzi CR (2005) Mechanistic investigation of the Staudinger ligation. *J Am Chem Soc* 127:2686-2695.

10. Kohn M, Breinbauer R (2004) The Staudinger ligation - A gift to chemical biology. *Angew Chem Int Ed Engl* 43:3106-3116.

11. Prescher JA, Dube DH, Bertozzi CR (2004) Chemical remodelling of cell surfaces in living animals. *Nature* 430:873-877.

12. Wiley RA, Sternson LA, Sasame HA, Gillette JR (1972) Enzymatic oxidation of diphenylmethylphosphine and 3-dimethylaminopropyldiphenylphosphine by rat liver microsomes. *Biochem Pharmacol* 21:3235-3247.

13. Huisgen R (1963) 1.3-Dipolare Cycloadditionen - Ruckschau Und Ausblick. *Angew Chem Int Ed* 75:604-637.

14. Agard NJ, Prescher JA, Bertozzi CR (2004) A strain-promoted [3 + 2] azide-alkyne cycloaddition for covalent modification of biomolecules in living systems. *J Am Chem Soc* 126:15046-15047.

15. Agard NJ, Baskin JM, Prescher JA, Lo A, Bertozzi CR (2006) A comparative study of bioorthogonal reactions with azides. *ACS Chem Biol* 1:644-648.

16. Baskin JM, *et al.* (2007) Copper-free click chemistry for dynamic in vivo imaging. *Proc Natl Acad Sci USA* 104:16793-16797.

17. Rostovtsev VV, Green LG, Fokin VV, Sharpless KB (2002) A stepwise Huisgen cycloaddition process: Copper(I)-catalyzed regioselective "ligation" of azides and terminal alkynes. *Angew Chem Int Ed Engl* 41:2596-2599.

18. Tornoe CW, Christensen C, Meldal M (2002) Peptidotriazoles on solid phase: [1,2,3]-Triazoles by regiospecific copper(I)-catalyzed 1,3-dipolar cycloadditions of terminal alkynes to azides. *J Org Chem* 67:3057-3064.

19. Ning X, Guo J, Wolfert MA, Boons GJ (2008) Visualizing metabolically labeled glycoconjugates of living cells by copper-free and fast Huisgen cycloadditions. *Angew Chem Int Ed Engl* 47:2253-2255.

20. Laughlin ST, Baskin JM, Amacher SL, Bertozzi CR (2008) In vivo imaging of membrane-associated glycans in developing zebrafish. *Science* 320:664-667.

21. Fernandez-Suarez M, *et al.* (2007) Redirecting lipoic acid ligase for cell surface protein labeling with small-molecule probes. *Nat Biotechnol* 25:1483-1487.

22. Neef AB, Schultz C (2009) Selective fluorescence labeling of lipids in living cells. *Angew Chem Int Ed Engl* 48:1498-1500.

23. Laughlin ST, Bertozzi CR (2007) Metabolic labeling of glycans with azido sugars and subsequent glycan-profiling and visualization via Staudinger ligation. *Nat Protoc* 2:2930-2944.

24. Tetko IV, Tanchuk VY, Kasheva TN, Villa AE (2001) Internet software for the calculation of the lipophilicity and aqueous solubility of chemical compounds. *J Chem Inf Comput Sci* 41:246-252.

25. Tetko IV, Tanchuk VY, Kasheva TN, Villa AE (2001) Estimation of aqueous solubility of chemical compounds using E-state indices. *J Chem Inf Comput Sci* 41:1488-1493.

26. Sletten EM, Bertozzi CR (2008) A hydrophilic azacyclooctyne for Cu-free click chemistry. *Org Lett* 10:3097-3099.

27. Ess DH, Jones GO, Houk KN (2008) Transition states of strain-promoted metal-free click chemistry: 1,3-Dipolar cycloadditions of phenyl azide and cyclooctynes. *Org Lett* 10:1633-1636.

28. Bach RD (2009) Ring strain energy in the cyclooctyl system. The effect of strain energy on [3 + 2] cycloaddition reactions with azides. *J Am Chem Soc* 131:5233-5243.

29. Laughlin ST, *et al.* (2006) Metabolic labeling of glycans with azido sugars for visualization and glycoproteomics. *Methods Enzymol* 415:230-250.

30. Mano N, Sato K, Goto J (2006) Specific affinity extraction method for small molecule-binding proteins. *Anal Chem* 78:4668-4675.

31. Peters T (1996) *All About Albumin* (Academic Press, San Diego).

32. Cheng L, *et al.* (2008) Covalent binding of the nitroso metabolite of sulfamethoxazole is important in induction of drug-specific T-cell responses in vivo. *Mol Pharmacol* 73:1769-1775.

33. Poloukhtine AA, Mbua NE, Wolfert MA, Boons GJ, Popik VV (2009) Selective labeling of living cells by a photo-triggered click reaction. *J Am Chem Soc* 131:15769-15776.

34. Link AJ, Vink MK, Tirrell DA (2004) Presentation and detection of azide functionality in bacterial cell surface proteins. *J Am Chem Soc* 126:10598-10602.

35. Link AJ, Tirrell DA (2003) Cell surface labeling of Escherichia coli via copper(I)-catalyzed [3+2] cycloaddition. *J Am Chem Soc* 125:11164-11165.

36. Edgington LE, *et al.* (2009) Noninvasive optical imaging of apoptosis by caspase-targeted activity-based probes. *Nat Med* 15:967-973.

37. Tsukiji S, Miyagawa M, Takaoka Y, Tamura T, Hamachi I (2009) Ligand-directed tosyl chemistry for protein labeling in vivo. *Nat Chem Biol* 5:341-343.

38. Ortiz de Montellano PR (1985) *Bioactivation of Foreign Compounds* (Academic Press, Inc., Orlando).

39. Ortiz de Montellano PR, Kunze KL (1980) Self-catalyzed inactivation of hepatic cytochrome P-450 by ethynyl substrates. *J Biol Chem* 255:5578-5585.

40. Kele P, Mezo G, Achatz D, Wolfbeis OS (2009) Dual labeling of biomolecules by using click chemistry: A sequential approach. *Angew Chem Int Ed Engl* 48:344-347.

Chapter 3: Imaging glycans using the chemical reporter strategy[a]

Introduction

Because clinical diagnostic imaging relies exclusively on gross anatomical changes that occur relatively late in disease progression, the field of molecular imaging has been focused on imaging tissue-specific biomarkers that are associated with the early onset of disease. To date, the field has focused primarily on protein-based markers that are targeted with green fluorescent protein (GFP) fusions or with antibody conjugates, receptor ligands, or enzyme substrates/inhibitors (1, 2). In addition to changes in protein expression, cancer cells have long been known to display glycosylation patterns that are strikingly different from those found on normal cells from the same tissue (3, 4). For example, numerous cancers have been shown to express elevated levels of glycan structures that contain the monosaccharide sialic acid (Figure 3-1) (5, 6). Furthermore, a strong correlation between cell-surface sialic acid levels and metastatic potential has also been observed in several different tumor types (7, 8). Thus, an imaging strategy that targets sialic acid could potentially be used for the noninvasive monitoring of cancer development and progression.

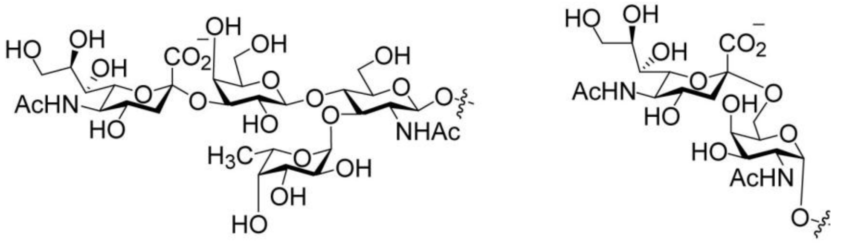

Sialyl Lewis^x Sialyl Tn

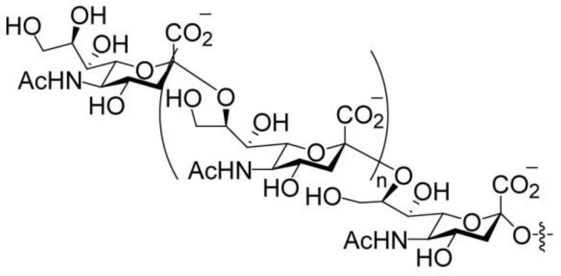

Polysialic acid (n = 20-200)

Figure 3-1. Altered glycosylation patterns are a hallmark of cancer. The epitopes depicted here represent a small subset of sialylated glycans found on malignant cells.

Glycans, unlike proteins, cannot be visualized by fusion to GFP or other genetically encoded tags because glycosylation is a post-translational modification. Therefore, alternative strategies including lectin and antibody conjugates are necessary to image these biomolecules *in vivo*. However, these protein-based reagents have limited tissue access due to their large size and

---

[a] Jennifer A. Prescher, Matthew J. Hangauer, Danielle H. Dube, and Pritha Ray (Stanford University) contributed to the work presented in this chapter.

may be restricted to imaging vascular targets (9, 10). In addition, most lectins are isolated from plants and can be highly cytotoxic. Furthermore, there are relatively few known antibodies against glycans. These reagents also exhibit low affinities for their targets (high micromolar to millimolar) and cannot reveal subtle changes in glycan profiles that can accompany physiological changes.

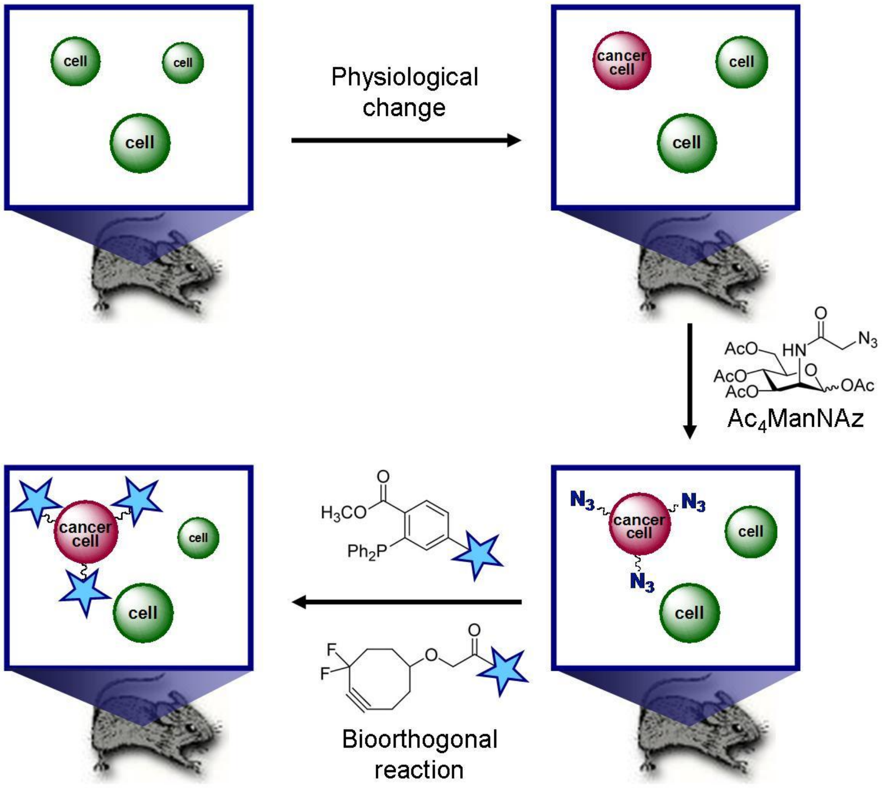

Figure 3-2. A strategy for noninvasive imaging of glycans. Physiological changes such as malignant transformation may be reflected in altered cell-surface glycosylation patterns. For example, cancer cells are known to overexpress sialic acid and are more metabolically active than normal cells. It is possible that greater amounts of Ac_4ManNAz could be metabolized and incorporated onto tumor cell surfaces. Subsequent covalent labeling of the cell-surface azides via Staudinger ligation or Cu-free click chemistry with imaging agents would enable noninvasive detection of the altered tissue.

The bioorthogonal chemical reporter strategy provides an alternative means to visualize glycans within living animals (11). We have previously shown that unnatural sugars can be introduced into cell-surface glycans in mice by the metabolism of precursor analogs (12). The unnatural analogs can be endowed with chemical reporters or functional groups that are capable of chemoselective reaction with exogenous probes. For example, Ac_4ManNAz is converted by cells to SiaNAz *in vivo*, which provides a readout of flux through the sialic acid biosynthetic pathway. Since cancer cells are known to overexpress sialic acids and are more metabolically active than nonmalignant cells, we believe that higher levels of SiaNAz could be incorporated onto tumor cell surfaces compared with healthy cells. The azides can then be covalently tagged with the Staudinger ligation using phosphine imaging agents or Cu-free click chemistry using cyclooctyne reagents. This two step strategy could enable the delivery of diagnostic agents to cell surfaces that are rich in sialic acid, as depicted schematically in Figure 3-2.

This strategy has several advantages over other approaches to glycan visualization. First, the azidosugar, phosphine and cyclooctyne imaging agents are all small molecules that have the potential for broad tissue penetrance. By contrast, antibody conjugates have limited tissue access (9). Second, the targeting event involves a covalent bond at the cell surface rather than a non-covalent association. Thus, unbound imaging probes can be cleared without rapid loss of specific signal. This feature is key to achieving adequate contrast to detect the target for imaging modalities with high sensitivity (2). Third, the approach permits imaging of metabolic flux, a parameter that cannot be monitored by conventional glycan-binding reagents. Lastly, the covalent tagging step involving an exogenous probe is versatile with respect to the imaging modality, so potentially any phosphine- or cyclooctyne-imaging agent conjugate can be utilized.

Interest in fluorescence imaging has grown significantly over the last decade due to its improved sensitivity, recent improvements in instrumentation, and relatively low cost (no cyclotron or superconducting magnet is required, as is the case with positron emission tomography (PET) and magnetic resonance imaging (MRI) (2). In addition, fluorescent dyes have been designed with a wide range of spectral properties, and multiple dyes can be imaged simultaneously and independently. With the advent of near-infrared (NIR) dyes, which have superior tissue penetrance and minimize background autofluorescence, fluorophores have become more popular for imaging in living subjects (13). For these reasons, we have synthesized phosphines and cyclooctynes containing fluorophores for fluorescence imaging.

This Chapter summarizes our work toward developing fluorescent probes for imaging glycans on live cells and in mice. We have synthesized an assortment of phosphine and cyclooctyne probes for fluorescence imaging, and these reagents were employed for glycan-specific imaging in healthy mice. Currently, we are investigating several murine tumor models for robust azidosugar incorporation *in vivo* and plan to employ the optimal reagent for imaging cancer in these models.

Results and discussion

Synthesis and photophysical characterization of fluorescent phosphine and cyclooctyne probes

Our first goal was to develop reagents for direct visualization of azides. Coumarin- and fluorescein-phosphine conjugates have been employed for biochemical detection of azide-labeled proteins and nucleotides (14). Although these reagents could potentially be adapted for cell imaging, NIR probes have emerged as the preferred choice for cellular and whole-animal imaging (2). Thus, we prepared a panel of probes including a Cyanine 5.5 (Cy5.5)-phosphine conjugate (**3.1**) (Figure 3-3), which absorbs and emits NIR light. For comparative purposes, we also synthesized fluorescein-, rhodamine B-, and Alexa Fluor 568-phosphine conjugates (**3.2-3.4**), respectively, as well as a Cy5.5-DIFO conjugate (**3.5**). The photophysical parameters of the probes were similar to those of their parent fluorophores (Figure 3-3). These imaging probes were prepared as described in Scheme 3-1.

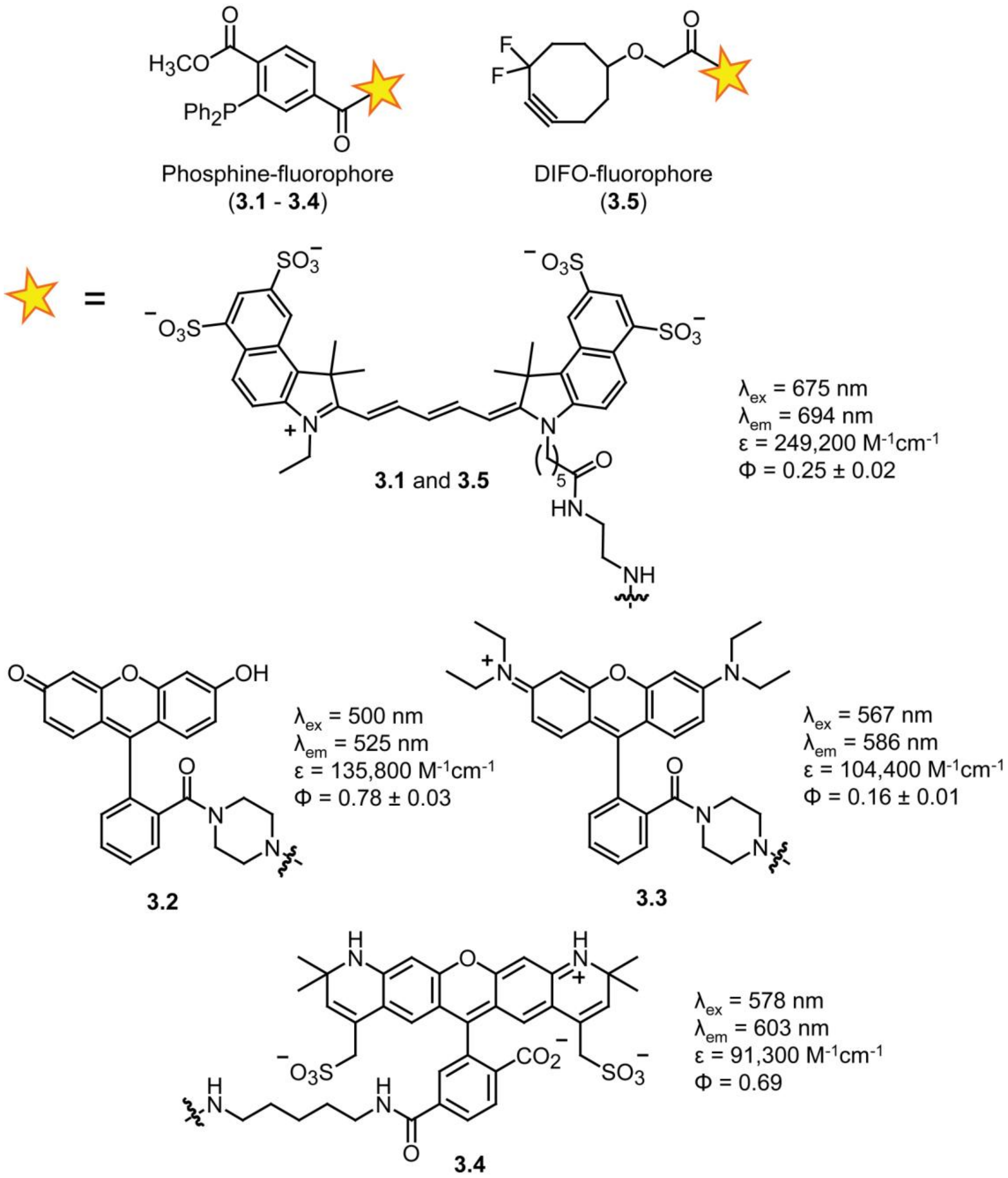

Phosphine-fluorophore
(**3.1** - **3.4**)

DIFO-fluorophore
(**3.5**)

3.1 and **3.5**

λ_{ex} = 675 nm
λ_{em} = 694 nm
ε = 249,200 $M^{-1}cm^{-1}$
Φ = 0.25 ± 0.02

3.2

λ_{ex} = 500 nm
λ_{em} = 525 nm
ε = 135,800 $M^{-1}cm^{-1}$
Φ = 0.78 ± 0.03

3.3

λ_{ex} = 567 nm
λ_{em} = 586 nm
ε = 104,400 $M^{-1}cm^{-1}$
Φ = 0.16 ± 0.01

3.4

λ_{ex} = 578 nm
λ_{em} = 603 nm
ε = 91,300 $M^{-1}cm^{-1}$
Φ = 0.69

Figure 3-3. Phosphine and cyclooctyne probes for glycan-specific imaging.

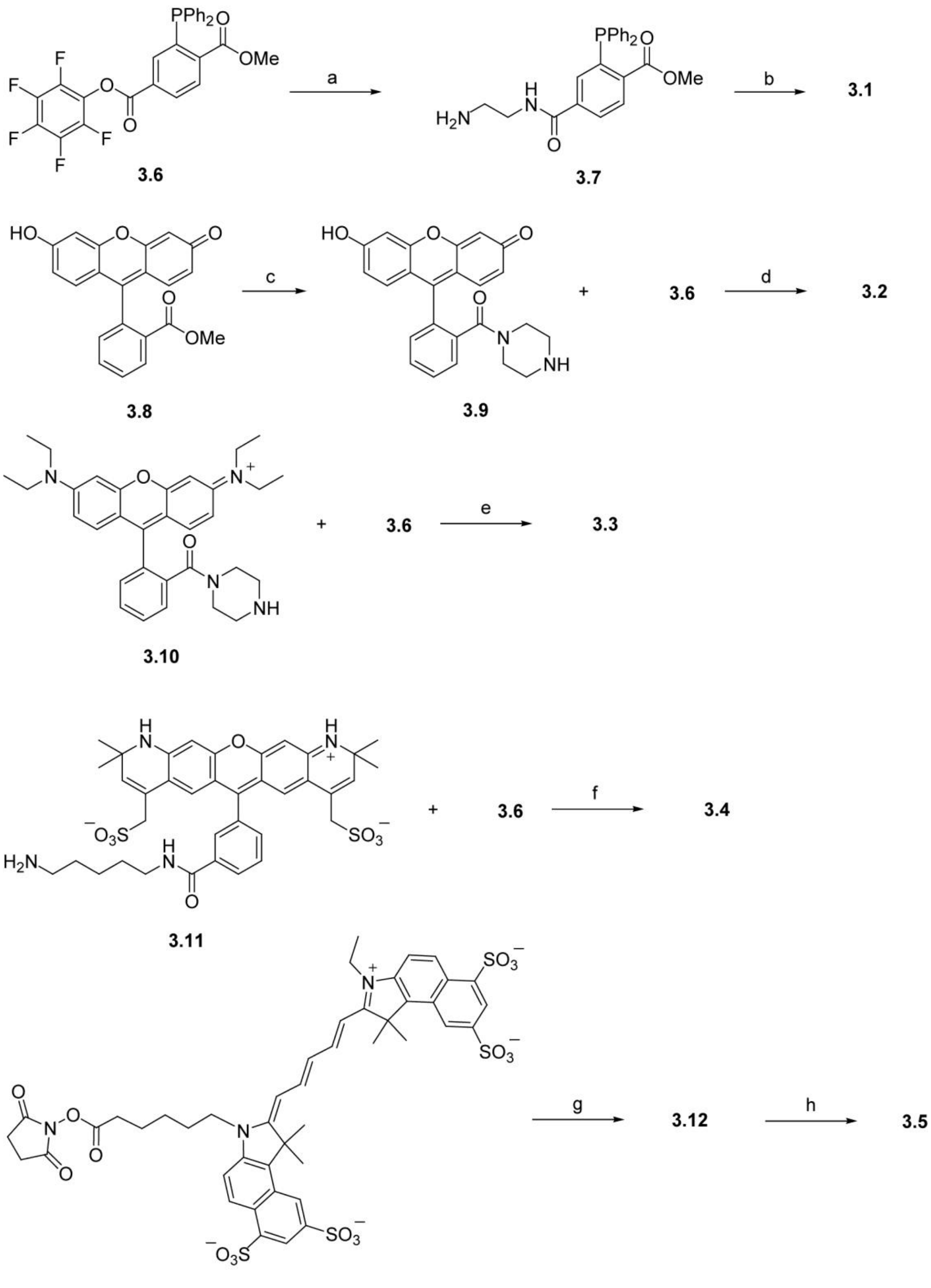

Scheme 3-1. Synthesis of phosphine- and cyclooctyne-imaging probes. (a) Ethylenediamine, DIPEA, CH_2Cl_2, under Ar, 91%; (b) Cy5.5-NHS ester, TEA, DMSO, under Ar, 36%; (c) Trimethyl aluminum (2.0 M in toluene), piperazine, CH_2Cl_2, reflux, 88%; (d) DIPEA, DMF, under Ar, 30%; (e) DIPEA, CH_2Cl_2, under Ar, 75%; (f) DIPEA, DMSO, under Ar, 75%; (g) Ethylenediamine, TEA, DMSO, 24%; (h) DIFO-Pfp ester (15), TEA, DMSO, 69%.

Chemical tagging of azide-containing protein with fluorescent phosphines

To confirm the reactivity of the probes with azide-labeled biomolecules, we incubated **3.1**-**3.3** with recombinant murine dihydrofolate reductase (mDHFR) bearing azido homoalanine in place of native methionine (16). Analysis by gel electrophoresis and in-gel fluorescence imaging showed selective labeling of the azido protein and no detectable labeling of the native protein (Figure 3-4).

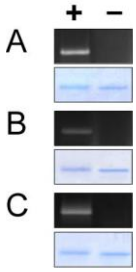

Figure 3-4. Specific labeling of azido-mDHFR with **3.1-3.3**. Purified azido-mDHFR (+) and native mDHFR (–) were incubated overnight at rt in 8 M urea with 10 μM **3.1**-**3.3**, and the samples were analyzed by SDS-PAGE. The extent of Staudinger ligation was determined by fluorescence (top), and total protein content was determined by staining with Coomassie Blue (bottom): (A) **3.1**, (B) **3.2**, and (C) **3.3**.

Imaging cell-surface glycans using the chemical reporter strategy

We next evaluated the fluorescent phosphines in cell imaging experiments. Azides were introduced into Jurkat cell-surface glycans by metabolic labeling of their sialic acids using the precursor $Ac_4ManNAz$. The cells bearing azido sialic acids (SiaNAz) were then reacted with various concentrations of **3.1**-**3.3** (10 μM – 1 mM) and their fluorescence was quantified by flow cytometry. Compounds **3.2** and **3.3** showed high background labeling at all concentrations tested, which obscured any potential azide-specific labeling (Figures 3-5 and 3-6). Although reducing the dye concentration could diminish background labeling, the corresponding decrease in Staudinger ligation rate would also diminish the sensitivity of azide detection.

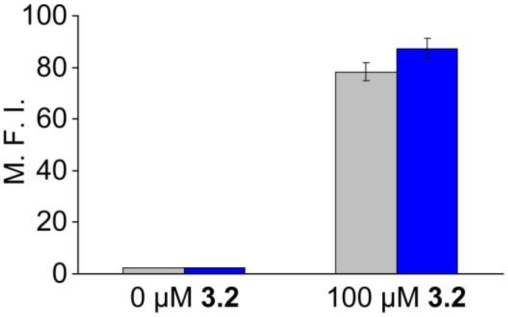

Figure 3-5. Flow cytometry analysis of Jurkat cells labeled with **3.2**. The cells were first incubated in the presence of (blue bars) or absence (gray bars) of $Ac_4ManNAz$ (25 μM) for 3 d and then labeled with **3.2** for 1 h at rt at various concentrations. M.F.I. = mean fluorescence

intensity (arbitrary units). Error bars represent the standard deviation of the mean from three replicate samples.

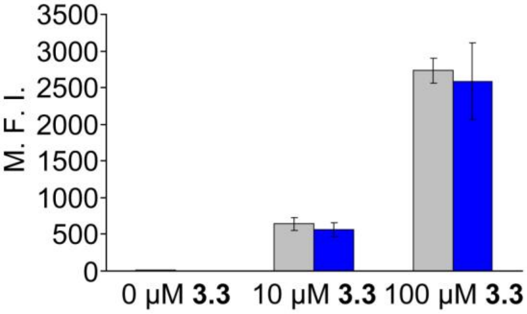

Figure 3-6. Flow cytometry analysis of Jurkat cells labeled with **3.3**. The cells were first incubated in the presence of (blue bars) or absence (gray bars) of Ac$_4$ManNAz (25 µM) for 3 d and then labeled with **3.3** for 1 h at rt at various concentrations. M.F.I. = mean fluorescence intensity (arbitrary units). Error bars represent the standard deviation of the mean from three replicate samples.

Compound **3.1**, however, was superior with respect to background labeling. Even at 10 µM, **3.1** showed detectable fluorescent labeling of SiaNAz-labeled Jurkat cells compared to control cells lacking azides (Figure 3-7). Background labeling remained low at 100 µM **3.1** and only became significant at concentrations approaching 1 mM. We attribute the lower background labeling observed with **3.1** to its higher charge density, and therefore greater solubility, which allows for efficient removal of excess probe during the washes. As a control, we synthesized an oxidized form of **3.1** in which the phosphine was converted to an unreactive phosphine oxide (**3.1-ox**). Incubation of SiaNAz-labeled Jurkat cells with **3.1-ox** revealed labeling that was identical to that of cells lacking azides.

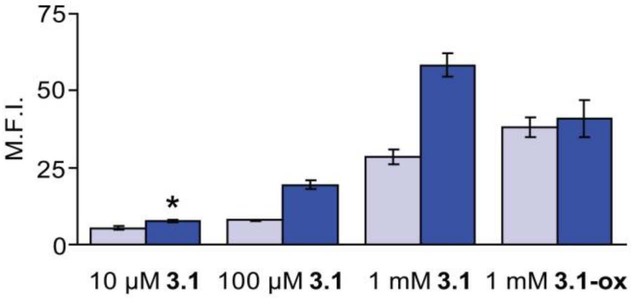

Figure 3-7. Flow cytometry analysis of Jurkat cells labeled with **3.1** or phosphine oxide of **3.1** (**3.1-ox**). The cells were first incubated in the presence of (dark blue bars) or absence (light blue bars) of Ac$_4$ManNAz (25 µM) for 3 d and then labeled with **3.1** or **3.1-ox** for 1 h at rt at various concentrations. M.F.I. = mean fluorescence intensity (arbitrary units). Error bars represent the standard deviation of the mean from three replicate samples. *$P < 0.004$ (t-test; two-tailed distribution).

Having validated **3.1** in flow cytometry experiments, we next employed the compound for cell imaging. Chinese hamster ovary (CHO) cells were grown in the presence or absence of $Ac_4ManNAz$ and then reacted with **3.1** for 2 h at 37 °C. Due to internalization of **3.1**, the cells were fixed and permeabilized and then washed to remove any excess unreacted probe. CHO cells displaying azides showed labeling of the cell surface with **3.1** (Figure 3-8). Colocalization studies suggest that the intracellular punctate staining is due to glycoconjugate recycling to the Golgi complex during incubation with **3.1** (Figure 3-9) (17). By contrast, the cells not treated with azidosugar displayed no significant fluorescence. Similar cell imaging experiments with **3.4** showed significant azide-dependent labeling of the cell surface glycans as well (Figure 3-10A and B). With this fluorescent phosphine, we observed minimal internalization of the probe, so fixation was not necessary and the cells were imaged live. These studies demonstrated that fluorescent phosphines can be used to image glycans on live cells. We also demonstrated that the DIFO-Cy5.5 conjugate (**3.5)** can also label glycans on live cells (Figure 3-10C and D).

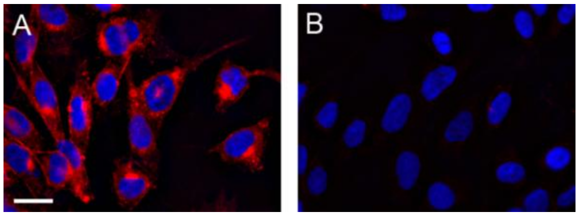

Figure 3-8. Fluorescence microscopy of CHO cells labeled with **3.1**. Cells incubated for 3 d in the (A) presence or (B) absence of $Ac_4ManNAz$ (100 μM) were treated with **3.1** (200 μM) for 2 h at 37 °C. The cells were then fixed and permeabilized with MeOH and stained with DAPI before imaging. Red = Cy5.5 channel. Blue = DAPI channel. Scale bar = 20 μm.

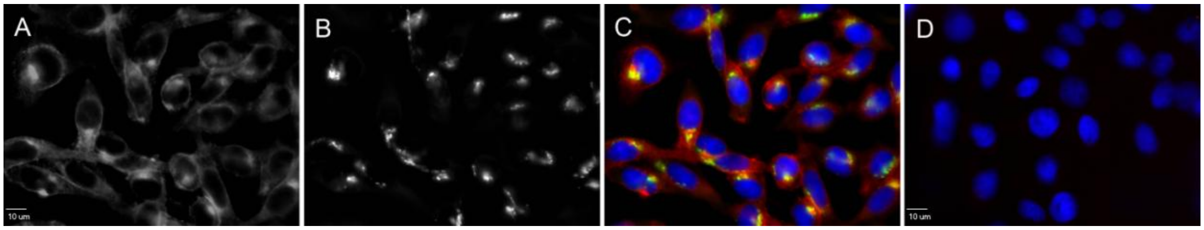

Figure 3-9. Colocalization studies of CHO cells labeled with **3.1**. Cells incubated for 3 d in the (A-C) presence or (D) absence of $Ac_4ManNAz$ (100 μM) were treated with **3.1** (200 μM) for 2 h at 37 °C. The cells were then fixed and permeabilized with MeOH and stained with a primary antibody specific for the Golgi apparatus (rabbit polyclonal anti-Giantin) and a secondary antibody (FITC-conjugated goat anti-rabbit). The cells were stained with DAPI and imaged by fluorescence microscopy. (A) Cy5.5 channel. (B) FITC channel. (C) Cy5.5, FITC, and DAPI channels. (D) Cy5.5 and DAPI channels. Red = Cy5.5 channel. Green = FITC channel. Blue = DAPI channel. Scale bar = 10 μm.

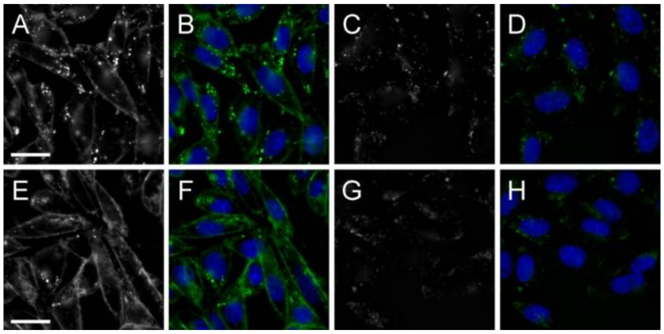

Figure 3-10. Fluorescence microscopy of CHO cells labeled with **3.4** or **3.5**. Cells incubated for 3 d in the (A-B) and (E-F) presence or (C-D) and (G-H) absence of $Ac_4ManNAz$ (100 μM for (A-B) and 50 μM for (E-F)) were treated with (A-D) **3.4** (200 μM) for 2 h at 37 °C or (E-H) **3.5** (10 μM) for 1 h at 37 °C. The cells were washed, stained with Hoescht 33342, and imaged. (A) and (C) Texas Red channel. (B) and (D) Texas Red and DAPI channels. (E) and (G) Cy5.5 channel. (F) and (H) Cy5.5 and DAPI channels. Green = (B) and (D) Texas Red channel; (F) and (H) Cy5.5 channel. Blue = DAPI channel. Scale bar = 20 μm.

The ability to detect multiple chemical reporters would allow for simultaneous monitoring of different glycan subtypes. We explored this possibility by imaging two different sugars on the same cells: sialic acids, which are common terminal components of glycans, and GalNAc residues, which are found in all mucin-type O-linked glycans. Ketone groups were introduced into sialic acids using peracetylated *N*-levulinoylmannosamine ($Ac_4ManLev$) as a metabolic precursor (18), and azides were introduced into GalNAc residues using the salvage pathway substrate peracetylated *N*-azidoacetylgalactosamine ($Ac_4GalNAz$) (19). Jurkat cells were fed the metabolic labels either singly or in combination and then reacted with both **3.1** and biotin hydrazide in one pot, followed by staining with FITC-avidin. As shown in Figure 3-11, cells that were grown in the presence of $Ac_4ManLev$ only (Figure 3-11D) and $Ac_4GalNAz$ only (Figure 3-11A) exhibited an increase in signal over background (Figure 3-11C). Jurkat cells incubated with both metabolic labels showed dual labeling with both dyes (Figure 3-11B). As expected, cells that were incubated with both sugars and reacted with **3.1-ox** and FITC-avidin showed no fluorescence above background (data not shown). Thus, sialic acid and GalNAc residues can be simultaneously visualized on the same cells.

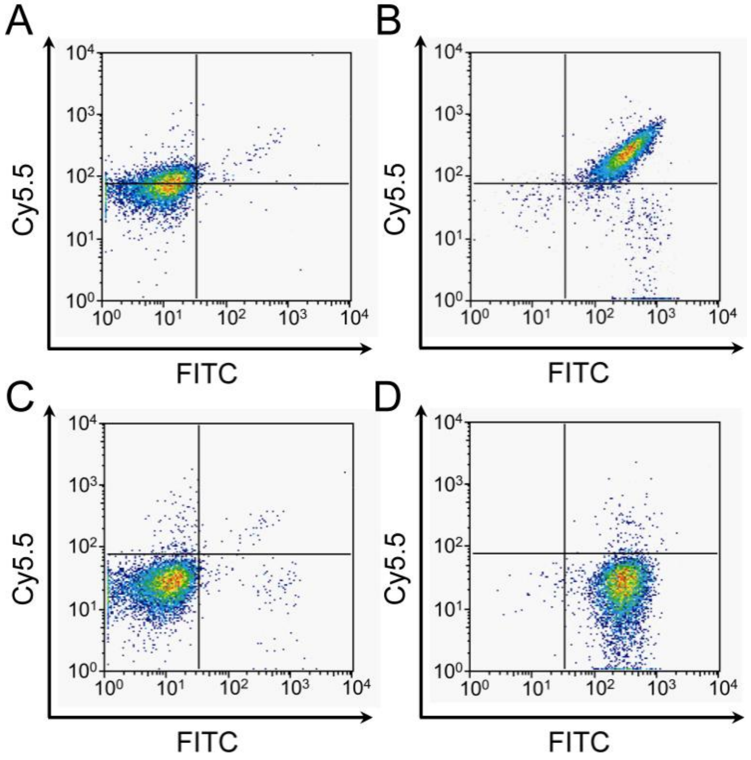

Figure 3-11. Labeling of live cells bearing two bioorthogonal chemical reporters. Jurkat cells were incubated with combinations of Ac_4ManLev (50 µM), Ac_4GalNAz (150 µM), or no sugar for 2 d, followed by labeling with both **3.1** and biotin hydrazide at pH 6.5, followed by FITC-avidin. The fluorescence of each sample was measured by flow cytometry. x-axis: FITC fluorescence; y-axis: Cy5.5 fluorescence. (A) – Ac_4ManLev, + Ac_4GalNAz. (B) + Ac_4ManLev, + Ac_4GalNAz. (C) – Ac_4ManLev, – Ac_4GalNAz. (D) + Ac_4ManLev, – Ac_4GalNAz.

Visualization of glycans in healthy mice using fluorescence imaging

In order to establish proper dosing and imaging parameters, pilot experiments were performed to verify that the fluorescent phosphines can undergo the Staudinger ligation *in vivo*. For these experiments, we tested the most promising imaging agents (**3.1**, **3.3-3.5**) due to their red-shifted emission wavelengths, which are ideal for *in vivo* imaging. Nude mice (nu/nu) were injected with Ac_4ManNAz (300 mg/kg in 70% aqueous DMSO) or vehicle as a control intraperitoneally (IP) once daily for seven days. Twenty-four hours after the final azidosugar injection, the mice received one bolus of **3.1** (2, 10, 20, 50, or 200 µg, intravenously (IV)). The animals were anesthetized and imaged live at various time points using a Xenogen IVIS 200 (in collaboration with Dr. Pritha Ray and Prof. Sanjiv Gambhir, Stanford University) or CRI Maestro optical imaging system. The higher doses resulted in residual unreacted probe, which persisted in both the vehicle- and Ac_4ManNAz-treated mice even after two or four days (50 and 200 µg doses, respectively) post-injection of the phosphine. The superior tissue penetrance of light emitted from **3.1** and low background autofluorescence of NIR dyes necessitate the rapid clearance of unbound probe to achieve azide-specific signal. A smaller injected dose (e.g., 2, 10, or 20 µg) could alleviate the high background fluorescence due to excess, unreacted probe. However, a lower dose would also reduce the total concentration of phosphine reagent administered to the animals and, accordingly, slow the rate of Staudinger ligation. Indeed, no detectable azide-dependent labeling with **3.1** was observed at all of the doses and imaging time points (up to 48 h post-injection of **3.1**) tested. Representative images in which mice were injected with the 20 μg dose of **3.1** are shown in Figure 3-12. Nude mice treated with vehicle or $Ac_4ManNAz$ using the standard dosing regimen were also injected with the DIFO conjugate of the same fluorophore **3.5** (0.2, 2, 10, or 50 μg, IV). Again, no azide-dependent labeling was observed. A representative image is shown in Figure 3-13.

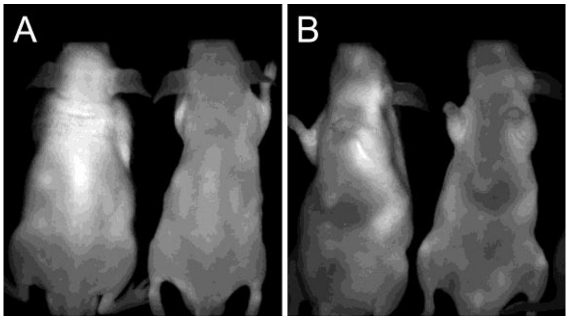

Figure 3-12. Fluorescence imaging of mice with **3.1**. Mice were injected with $Ac_4ManNAz$ (300 mg/kg, IP, right) or vehicle (70% DMSO, IP, left) once daily for 7 d. On day 8, the mice were injected with one bolus of **3.1** (20 μg in ddH_2O, IV via the tail vein). The images shown were acquired 6.5 h post-injection of **3.1**. (A) Dorsal image. (B) Ventral image.

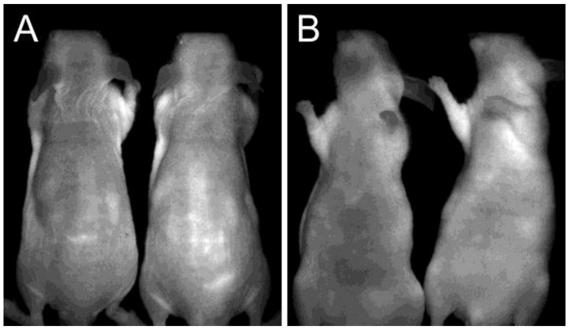

Figure 3-13. Fluorescence imaging of mice with **3.5**. Mice were injected with $Ac_4ManNAz$ (300 mg/kg, IP, right) or vehicle (70% DMSO, IP, left) once daily for 7 d. On day 8, the mice were injected with one bolus of **3.5** (50 μg in ddH_2O, IV via the tail vein). The images shown were acquired 7 h post-injection of **3.5**. (A) Dorsal image. (B) Ventral image.

From these studies, we concluded that red-shifted fluorescent phosphines such as **3.3** and **3.4** that can be injected at higher doses (milligram as opposed to microgram) could be more promising for achieving azide-dependent labeling *in vivo*. In order to test this hypothesis, nude mice were injected with $Ac_4ManNAz$ (300 mg/kg in 70% aqueous DMSO, IP) or vehicle as a control once daily for seven days. Twenty-four hours after the final azidosugar injection, the mice received one bolus of **3.3** or **3.3-ox**, an oxidized version of the probe that serves as a negative control because it cannot undergo the Staudinger ligation (2 mg, IV). Though azide-dependent labeling was demonstrated by a two-fold fluorescent signal increase from the mouse injected with both $Ac_4ManNAz$ and **3.3** as compared to the vehicle control and mouse injected with **3.3-ox** (data not shown) (20), these results could not be reliably replicated due to toxicity of the probe.

Necropsy (in collaboration with Dr. Nina Hahn (OLAC)) of mice injected with **3.3** (2 mg, IV) revealed clotting in and around the heart. These results suggest that the hydrophobic nature of the compound could cause it to precipitate in the blood stream immediately after injection due to its solubility limit. Follow-up toxicity studies were performed to determine a lower dose of **3.3** that would be safe to inject. From the doses tested (0.5 – 2 mg of **3.3**, IV), all of the nude mice survived only at the lowest dose (0.5 mg) while greater than 50% of the mice administered 1-2 mg of **3.3** died shortly after injection of the probe. Toxicity studies using **3.3** were also performed in FVB mice, which unlike nu/nu mice, are not immunodeficient. These mice were able to withstand a greater dose of **3.3** (up to 1 mg). However, when imaging experiments in FVB mice were attempted, injections of the 0.5 or 1 mg doses of **3.3** and **3.3-ox** IV following injections of the azidosugar, which was administered as described previously, were toxic to the FVB mice. Due to the hydrophobic nature of **3.3**, *in vivo* imaging studies were also performed with the more water-soluble Alexa Fluor 568-phosphine conjugate **3.4**. In these experiments, nude mice were injected with either vehicle or $Ac_4ManNAz$ as before, followed by one bolus of **3.4** (2 mg, IV). With this probe, no azide-dependent labeling was observed at all time points up to 48 h post-injection of the phosphine. A representative image is shown in Figure 3-14.

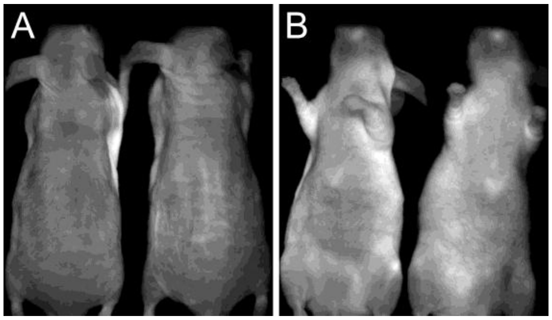

Figure 3-14. Fluorescence imaging of mice with **3.4**. Mice were injected with $Ac_4ManNAz$ (300 mg/kg, IP, right) or vehicle (70% DMSO, IP, left) for 7 d. On day 8, the mice were injected with one bolus of **3.4** (2 mg in ddH_2O, IV via the tail vein). The images shown were acquired 6 h post-injection of **3.4**. (A) Dorsal image. (B) Ventral image.

For all of the probes tested, the mice were sacrificed at multiple imaging time points and organs (liver, heart, kidney, spleen, and intestines) were harvested for *ex vivo* imaging; however, no azide-specific labeling was observed internally as well (data not shown). These studies suggest that direct fluorophore conjugates to the phosphine or DIFO may not be suitable for imaging azide-labeled glycans *in vivo* due to the high background fluorescence caused by excess, uncleared probe.

Design and synthesis of "smart" fluorogenic phosphines for in vivo *imaging*

Due to the high background fluorescence caused by excess, unreacted probe, which can mask azide-dependent labeling, these studies highlighted the need for improved azide-labeling reagents for *in vivo* imaging, especially those that can achieve high signal-to-noise ratios.

Fluorescent probes are unique in that they can be engineered for conditional activation (2). In the context of the Staudinger ligation, activation of fluorescence for phosphine dyes can be achieved by cleavage of the ester bond in the reaction (shown schematically in Figure 3-15A). Using this strategy, these "smart" turn-on phosphine probes become fluorescent only after undergoing the ligation with azides. This approach has been validated using a quenched phosphine that contains the dye fluorescein (21).

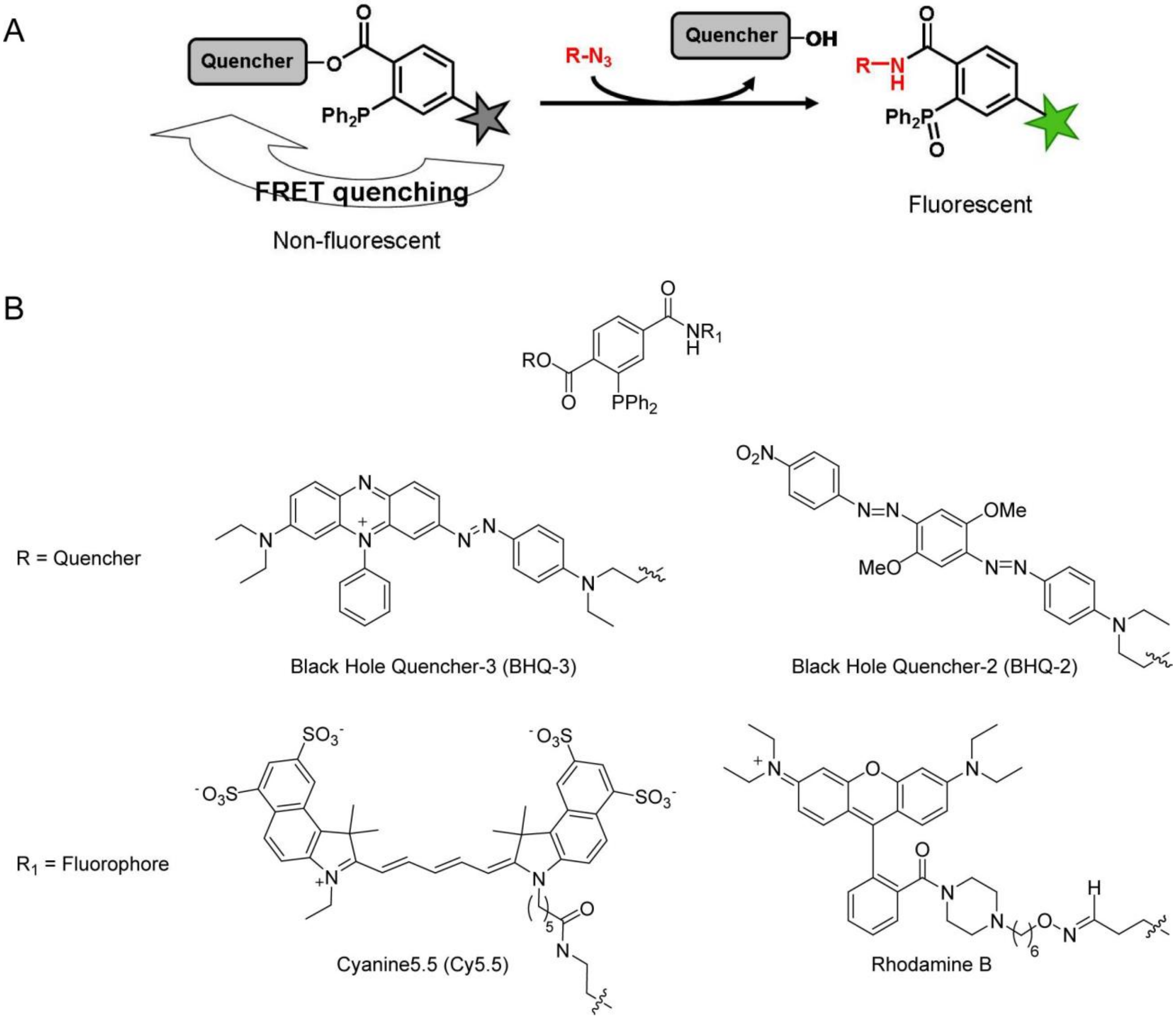

Figure 3-15. Activatable probes for Staudinger ligation. (A) A strategy for phosphine probes that become fluorescent after undergoing the Staudinger ligation. (B) Panel of fluorogenic phosphines.

For *in vivo* imaging, dyes that emit at longer wavelengths and therefore have greater tissue penetrance are more ideal. Toward this end, we attempted to synthesize a quenched phosphine that contains the NIR dye Cy5.5 and its corresponding FRET quencher, Black Hole Quencher-3 (BHQ-3) (22, 23) (Figure 3-15B); however, all synthetic manipulations in order to conjugate this quencher to the phosphine resulted in significant decomposition of BHQ-3. In addition, the quencher was unstable under acidic and basic conditions, and correspondence with a chemist employed at the commercial vendor of BHQ-3 (Biosearch Technologies) indicated that BHQ-3 is only stable in mild aqueous environments and cannot be manipulated using standard organic chemistries (personal communication).

Due to the limited availability of NIR FRET quenchers (24), we thus set out to synthesize a quenched phosphine that contains the red-shifted fluorophore rhodamine B and its corresponding FRET quencher, Black Hole Quencher-2 (BHQ-2) (22, 25) (Figure 3-15B). Because of the incompatibility of amino protecting group chemistry with the phosphine-BHQ2 conjugate, we decided to append the fluorophore to the phosphine via an oxime linkage (Figure 3-15B). Oxime formation with either a commercially available amino-oxy Alexa Fluor 647 (structure not available from Invitrogen) resulted in quantitative oxidation of the phosphine. As an alternative, amino-oxy rhodamine B (26) (Figure 3-15B) was also utilized, however, this final product oxidized rapidly after purification. A model Staudinger ligation of this compound with 2-azidoethanol resulted in decomposition, oxidation of the quenched phosphine, and no detectable ligation product.

Compared to syntheses of other phosphine compounds in our laboratory, these studies suggest that phosphine oxidation is highly dependent on the substituents on the phosphine, i.e., some fluorophores and quenchers result in more rapid oxidation than others. For example, phosphine conjugates containing dyes that emit UV wavelengths of light tend to oxidize more quickly than phosphine conjugates containing red-shifted fluorophores (unpublished observations). In the case of the quenched phosphine containing fluorescein, phosphine oxidation can also be mitigated by appending the quencher on the phosphine before appending the fluorophore (21); however, in the case of red-shifted quenched phosphines, the phosphine still oxidized relatively quickly after the attachment of either amino-oxy fluorophore in the last step. In the future, alternative dyes and quenchers will need to be investigated to find an optimal FRET pair that will minimize phosphine oxidation.

Screen of cancer cell lines for conversion of $Ac_4ManNAz$ to cell-surface SiaNAz

In parallel with imaging experiments in healthy mice, we aimed to select an appropriate model system for assessing whether azidosugar metabolism and the Staudinger ligation could be applied to tumor imaging in mice. First, we screened a panel of cancer cell lines as shown in Figure 3-16 for conversion of $Ac_4ManNAz$ to cell surface SiaNAz. These cell lines represent a variety of cancer types known to possess abnormal patterns of glycosylation compared to their healthy counterparts. Briefly, the cells were grown in media supplemented with 10 μM $Ac_4ManNAz$ or no azidosugar for three days. Cell-surface associated azides were detected by Staudinger ligation with PHOS-FLAG (27) followed by flow cytometry analysis (28). From this initial screen, several human cancer cell lines were identified for their ability to incorporate SiaNAz into their cell-surface glycans. These include the human neuroblastoma SK-N-SH and the prostate cancer cells lines DU145, PC3, and LNCaP. Based on these results, we chose SK-N-SH cells to establish xenografts in nude mice for our initial evaluation of azidosugar incorporation into tumors *in vivo*.

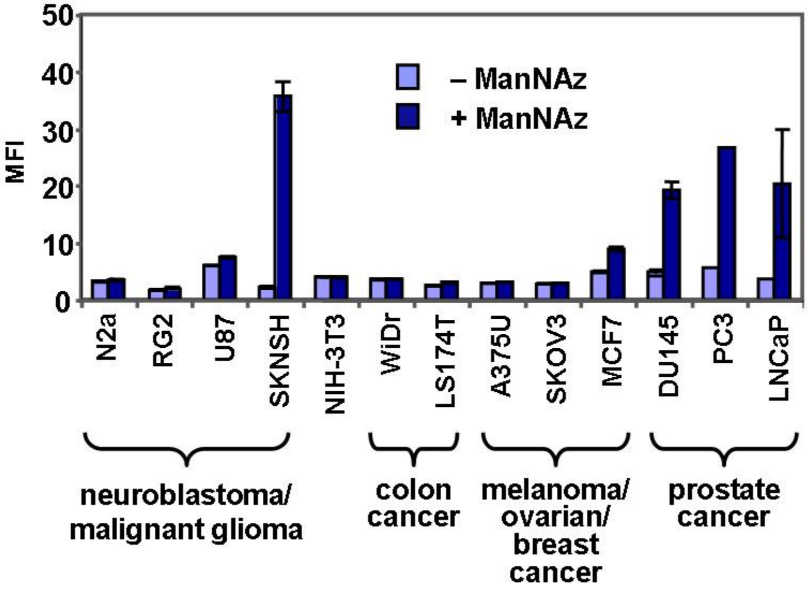

Figure 3-16. Metabolism of $Ac_4ManNAz$ in various mammalian cancer cell lines. Cell lines were treated with no azidosugar (light blue bars) or with 10 μM $Ac_4ManNAz$ (dark blue bars) for 3 d, then probed for the presence of cell-surface SiaNAz residues using PHOS-FLAG, followed by FITC-anti-FLAG. Flow cytometry data are presented above, with the mean fluorescence intensity (MFI) in arbitrary units plotted on the y-axis. Error bars represent the standard deviation of the mean for three replicate labeling reactions.

Evaluation of tumor xenografts for azidosugar metabolism

We first implanted SK-N-SH cells subcutaneously into nude mice. After tumor masses were visible (about 2-3 weeks), we injected the mice with $Ac_4ManNAz$ (300 mg/kg) or vehicle (70% DMSO) IP once daily for seven days. After the final azidosugar injection, the mice were sacrificed 24 h later, and their tumors and spleens were resected. Cancer cells were teased out of the solid tumor mass by collagenase treatment and then probed for azides via Staudinger ligation with PHOS-FLAG. Similar analyses were performed with isolated splenocytes from the same mice. Flow cytometry analysis revealed that tumor cells from $Ac_4ManNAz$-treated mice were labeled with much lower levels of azides than splenocytes (20).

The discrepancy between the SiaNAz-labeling *in vitro* and *in vivo* might be attributed to poor accessibility of $Ac_4ManNAz$ to the tumor tissue in mice. Our previous studies suggest that highly vascularized organs are strongly labeled with $Ac_4ManNAz$ (12). However, in these xenograft model studies, the tumor cells were implanted subcutaneously in poorly vascularized areas relatively far removed from the site of azidosugar injection. Alternatively, the lack of tumor cell labeling *in vivo* might be explained by the slow growth of the cancer cells. The use of more aggressive cancer cell lines with increased metabolism could possibly enhance the degree of azidosugar incorporation.

To test these hypotheses, we investigated an alternate mode of establishing tumors in mice using the leukemic cell line RMA. RMA cells are known to form large subcutaneous tumors in mice and can be used to grow IP tumors as well. We first demonstrated that RMA cells can be labeled with $Ac_4ManNAz$ in culture (20). These cells were then implanted subcutaneously in the flank or in the abdominal cavity of nude mice. Both sets of mice were injected with $Ac_4ManNAz$ or vehicle as described above. On day eight, the mice were sacrificed, and the RMA cells were harvested by collagenase treatment of subcutaneous tumors or IP lavage. Successful isolation of the tumor cells was confirmed by staining with an anti-CD3 antibody to probe for a standard RMA cell marker. The cells were probed for surface-associated azides via Staudinger ligation with PHOS-FLAG, followed by incubation with FITC-anti-FLAG and flow cytometry analysis.

Azidosugar labeling was observed in the IP implanted tumor, while no labeling was observed on tumor cells isolated from the subcutaneous tumor. Interestingly, a concomitant decrease in azidosugar labeling of splenocytes from the mouse bearing the IP tumor was also observed, suggesting that a portion of the azidosugar was metabolized by the tumor cells prior to trafficking to the spleen (20). While preliminary, these data indicate that azidosugar labeling efficiency is strongly influenced by proximity of the tumor tissue to the injection site. Our results also suggest that azidosugar labeling can be increased by intratumoral injection or IV administration of the sugar. Experiments to test these hypotheses, along with an examination of $Ac_4ManNAz$ incorporation into IP implanted SK-N-SH cells, should be instructive.

Conclusions

As fluorescent protein fusions have revolutionized biology by enabling studies of proteins in authentic environments such as cells and living organisms, analogous tools for visualizing glycans could enable the monitoring of glycan expression and dynamics. These processes were previously inaccessible in an imaging context. Here we present chemical tools including chemical reporters and bioorthogonal reagents that can be used to image glycans at the cellular level. Glycan visualization at the organismal level could facilitate the detection of changes in glycosylation associated with development and disease. For example, numerous cancers have been shown to express an elevated level of sialylated glycans. Diagnostic or therapeutic strategies that target cells on the basis of sialic acid could be used for the detection of cancer.

In this Chapter, our initial progress toward imaging sialylated glycans in healthy mice via azidosugar metabolism and bioorthogonal reactions with fluorescent phosphine and cyclooctyne probes was presented. Future directions include the optimization of our imaging agents and their application in a conditional murine tumor model, which more closely mimic spontaneous cancer development in humans than tumor xenografts. In collaboration with Prof. Martin Pomper and Dr. Catherine Foss (Johns Hopkins University), we are also developing phosphine-based imaging agents for single photon emission computed tomography (SPECT). Imaging experiments with a phosphine-[^{125}I]Bolton-Hunter radionuclide probe in healthy mice and in NOD.17 SCID mice, which are known to spontaneously develop a widely disseminated lymphoma (29), are currently underway. Ultimately, we hope our approach using chemical reporters and bioorthogonal reactions may be used to visualize, profile, and identify changes in glycan expression that accompany not only cancer but also other diseases and physiological processes such as inflammation and development.

Materials and methods

General

All chemical reagents were of analytical grade, obtained from commercial suppliers, and used without further purification unless otherwise noted. Ac_4ManNAz (27), Ac_4ManLev (18), Ac_4GalNAz (27), and PHOS-FLAG (27) were synthesized according to previously published procedures. Cyanine 5.5 was purchased as its mono-N-hydroxysuccinimidyl (NHS) ester from GE Healthcare, and Alexa Fluor 568 cadaverine was purchased from Invitrogen. Air-sensitive reactions were performed under Ar using standard Schlenk techniques, and all solvents were degassed by three freeze-pump-thaw cycles. Reversed-phase HPLC was performed using a Rainin Instruments Dynamax SD-200 system equipped with a Varian UV-Vis detector (model 345) and a Microsorb C18 analytical column (4.6 x 250 mm) at a flow rate of 1 mL/min, a semipreparative column (10 x 250 mm) at a flow rate of 4 mL/min, or a preparative column (21.4 x 250 mm) at a flow rate of 20 mL/min. HPLC samples were filtered with a Pall Life Sciences Acrodisc CR 13 mm syringe filter equipped with a 0.2 μm PTFE membrane prior to injection. Flash chromatography was performed using Merck 60 Å 230-400 mesh silica gel. For the purification of phosphine compounds, flash chromatography was performed under Ar. Analytical thin layer chromatography (TLC) was performed on glass-backed Analtech Uniplate GHLF silica gel plates, and compounds were visualized by staining with ceric ammonium molybdate, 5% H_2SO_4 in ethanol, ninhydrin, and/or the absorbance of UV light (λ = 254 nm or 365 nm). Dichloromethane (CH_2Cl_2) and triethylamine (TEA) were dried over CaH_2 and distilled under a N_2 atmosphere prior to use. Anhydrous *N*,*N*-dimethylformamide (DMF), dimethylsulfoxide (DMSO), and *N*,*N*-diisopropylethylamine (DIPEA) were used from commercial sources without further purification.

NMR spectra were acquired using a Bruker AV-500, AVQ-400, or AVB-400 spectrometer. ^1H NMR spectra were obtained at 400 or 500 MHz and ^{13}C NMR spectra were obtained at 100 MHz and are referenced to residual solvent peaks. ^{31}P NMR spectra were obtained at 162 or 202 MHz and are referenced relative to 85% H_3PO_4 in D_2O. IR spectral data were obtained using a Perkin-Elmer 1600 FT-IR spectrometer. Low and high-resolution fast atom bombardment (FAB) and electrospray ionization (ESI) mass spectra were obtained at the UC-Berkeley Mass Spectrometry Laboratory. ESI-FT/MS and MALDI-TOF/MS were performed at the HHMI Mass Spectrometry Laboratory at UC Berkeley. Uncorrected melting points were determined using a Mel-Temp 3.0 melting point apparatus.

Dulbecco's phosphate-buffered saline pH 7.4 (PBS), fluorescein isothiocyanate (FITC)-anti-FLAG, and fluorescein isothiocyanate (FITC)-avidin were purchased from Sigma Aldrich. All mammalian cell culture media were obtained from Invitrogen, and fetal bovine serum (FBS) was obtained from HyClone Laboratories. SDS-PAGE was performed on pre-cast 12% polyacrylamide gels (Bio-Rad).

Flow cytometry analysis was performed on a BD FACSCalibur flow cytometer equipped with a 488 nm argon laser and a 635 He-Ne red diode array laser. At least 10^4 cells were analyzed for each sample. Cell viability was ascertained by gating the samples on the basis of forward scatter (to sort by size) and side scatter (to sort by granularity). The average fluorescence intensity was calculated from each of three replicate samples to obtain a mean value in arbitrary units. The data points are representative of at least three separate experiments. Data were collected in triplicate using at least 10,000 live cells for all data points. Centrifugation of mammalian cells was performed in a Sorvall centrifuge from Kendro Laboratory Products equipped with a SH3000 rotor. A Zeiss Axiovert 200M inverted microscope equipped with a 63 × 1.4 numerical aperture Plan-Apochromat oil immersion lens was used for imaging. A 175 W Xenon lamp housed in a Sutter DG4 illuminator linked to the microscope by an optical fiber assured shuttering and illumination. Image stacks containing 20-40 sections spaced 0.5 μm apart were acquired by using a CoolSNAP HQ charged-coupled device camera (Roper Scientific). SLIDEBOOK software (Intelligent Imaging Innovations) was used to control the microscope and the camera. The image stacks were digitally deconvolved by using the nearest-neighbor algorithm in SLIDEBOOK. *In vivo* imaging was performed using an IVIS 200 or a CRI Maestro fluorescence imaging system.

Synthesis and characterization of new compounds

Phosphine ethylenediamine conjugate (3.7). To a solution of ethylenediamine (411 mg, 6.84 mmol) in CH_2Cl_2 (100 mL) was added DIPEA (1.3 mL, 7.5 mmol). Compound **3.6** (3.3 g, 6.2 mmol) in CH_2Cl_2 was added dropwise over 10 min. The resulting mixture was stirred for 6 h under Ar. The crude reaction mixture was concentrated *in vacuo* and purified by flash chromatography on silica gel (9:1 CH_2Cl_2:MeOH) to give 2.3 g (91%) of a yellow solid. IR (thin film): 3313, 3242, 3064, 3003, 2957, 2917, 2849, 1696, 1630 cm^{-1}. ^{1}H NMR (400 MHz, CD_3OD): δ 3.01 (app t, *J* = 6.0 Hz, 2H), 3.51 (app t, *J* = 6.0 Hz, 2H), 3.69 (s, 3H), 7.24-7.36 (m, 10H), 7.52 (dd, *J* = 1.6, 4.0 Hz, 1H), 7.83 (dd, *J* = 1.6, 8.0 Hz, 1H), 8.04 (dd, *J* = 3.6, 8.4 Hz, 1H); ^{13}C NMR (100 MHz, CD_3OD): δ 40.4, 42.1, 51.2, 126.3, 128.2, 128.3, 128.7, 130.1, 130.2, 133.1, 133.6, 133.8, 136.7, 136.9, 137.1, 137.2, 137.5, 140.8, 141.1, 167.0, 168.3; ^{31}P NMR (162 MHz, CD_3OD): δ -4.06; HRMS (FAB): Calcd for $C_{23}H_{24}N_2O_3P^+$ $[M + H]^+$ 407.1525, found 407.1520.

Cyanine 5.5 phosphine conjugate (3.1). Cyanine 5.5 mono-NHS ester (10.0 mg, 8.90 μmol) was dissolved in DMSO (110 μL). Compound **3.7** (7.23 mg, 17.8 μmol) was added to the solution followed by addition of TEA (75.0 μL, 534 μmol). The reaction mixture was agitated under Ar for 6 h at rt in the dark. The sample was then diluted three-fold with water and purified by reversed-phase HPLC (C18 semipreparative column) using a gradient of 25%-35% CH_3CN + 0.1% TFA over 60 min. The purified product was lyophilized to dryness to yield 4.2 mg of a blue solid (36% yield). mp: 200-202 °C (dec); ^{1}H NMR (500 MHz, 1:1 CD_3OD:$CDCl_3$): δ 1.39 (m, 2H), 1.44 (t, *J* = 7.5 Hz, 3H), 1.64 (m, 2H), 1.78 (m, 2H), 2.00 (s, 12H), 2.16 (m, 2H), 3.31 (m, 2H, under CD_3OD signal), 3.35 (t, *J* = 4.0 Hz, 2H), 3.70 (s, 3H), 4.06 (m, 2H), 4.20 (m, 2H), 7.31-7.38 (m, 8H), 7.54-7.61 (m, 8H), 7.88 (dd, *J* = 1.5, 8.0 Hz, 1H), 8.10 (dd, *J* = 4.0, 8.0 Hz, 1H), 8.19 (m, 2H), 8.56 (s, 1H), 8.59 (s, 1H), 8.73 (s, 1H), 8.75 (s, 1H), 9.05 (d, *J* = 9.0, 1H), 9.08 (d, *J* = 9.0, 1H); ^{31}P NMR (202 MHz, 1:1 CD_3OD:$CDCl_3$): δ -6.58; HRMS (ESI-FT): Calcd for $C_{64}H_{66}N_4O_{16}PS_4^+$ $[M+H]^+$ 1305.302, found 1305.324.

Fluorescein piperazine core (3.9). A 2.0 M solution of trimethyl aluminum in toluene (22 mL, 45 mmol) was added dropwise to a solution of piperazine (7.7 g, 0.090 mol) in 35 mL of CH_2Cl_2. After 4 h, a white precipitate formed. A solution of **3.8** (30) (7.8 g, 23 mmol) in 15 mL CH_2Cl_2 was added dropwise to the heterogeneous solution and gas evolution was observed. After stirring at reflux for 18 h in the dark, the reaction was cooled to rt and 200 mL of MeOH was added. Then, 1 N HCl (500 mL) was added slowly and gas evolution was observed. The heterogeneous solution was stirred in the dark until gas evolution ceased. The reaction mixture was concentrated *in vacuo* and purified by flash chromatography on silica gel (4:1 CH_2Cl_2:MeOH) to yield 7.9 g (88%) of a red-orange solid. R_f = 0.23 (6:1 CH_2Cl_2:MeOH, UV); mp 281-283 °C (dec); ^{1}H NMR (400 MHz, CD_3OD): δ 3.14 (m, 4H), 3.62 (m, 2H), 3.84 (m, 2H), 7.27 (dd, *J* = 2.0, 9.2 Hz, 2H), 7.34-7.37 (m, 2H), 7.61-7.62 (m, 1H), 7.65-7.68 (d, *J* = 9.2 Hz, 2H), 7.84-7.86 (m, 3H); ^{13}C NMR (100 MHz, CD_3OD): δ 39.9, 41.8, 44.4, 45.6, 103.7, 118.4, 121.6, 129.4, 132.0, 132.0, 132.2, 132.4, 134.9, 135.6, 161.1, 166.2, 169.2, 173.3; HRMS (ESI): Calcd for $C_{24}H_{21}N_2O_4^+$ $[M+H]^+$ 401.1501, found 401.1491.

Fluorescein phosphine conjugate (3.2). Compound **3.6** (368 mg, 0.695 mmol) was added to a solution of **3.9** (278 mg, 0.695 mmol) and DIPEA (0.250 mL, 1.44 mmol) in 5 mL of DMF. The reaction was stirred under Ar overnight at rt in the dark. The resulting reaction mixture was concentrated *in vacuo* and purified by flash chromatography on silica gel (20:1 to 4:1 CH_2Cl_2:MeOH) to yield 155 mg (30%) of a bright orange solid. Due to facile phosphine oxidation, the solid was further purified by HPLC (reversed-phase C18 preparative column, 10%-80% CH_3CN over 60 min) prior to use. R_f = 0.82 (10:1 CH_3CN:H_2O, UV); mp 100-102 °C; ^{1}H NMR (400 MHz, CD_3OD): δ 2.99 (m, 4H), 3.47 (m, 4H), 3.66 (s, 3H), 6.82, (m, 1H), 7.14-7.29 (m, 12H), 7.47-7.58 (m, 5H), 7.73-7.82 (m, 4H), 8.04-8.07 (m, 1H); ^{13}C NMR (100 MHz, CD_3OD): δ 41.2, 41.3, 41.6, 46.3, 51.2, 102.2, 116.5, 120.2, 127.2, 127.7, 128.3, 128.4, 128.5, 128.7, 130.1, 130.3, 130.4, 130.7, 130.8, 131.3, 131.4, 132.0, 132.1, 133.1, 133.4, 133.6, 134.8, 135.7, 135.9, 137.0, 137.1, 137.7, 159.2, 162.9, 166.6, 167.7, 169.6, 172.3; ^{31}P NMR (162 MHz, acetone-d_6): δ -4.79; HRMS (MALDI-TOF): Calcd for $C_{45}H_{36}N_2O_7P^+$ $[M+H]^+$ 747.2260, found 747.2270.

Rhodamine phosphine conjugate (3.3). Compound **3.10** (31) (122 mg, 0.223 mmol) was added to a solution of **3.6** (131 mg, 0.245 mmol) in CH_2Cl_2 (10 mL), followed by DIPEA (120 µL, 0.86 mmol). The solution was stirred overnight under Ar in the dark. The reaction solution was concentrated *in vacuo*, and the resulting crude product was purified by flash column chromatography (12:1 CH_2Cl_2:MeOH) to provide 151 mg (75%) of a dark red solid. ^{1}H NMR (400 MHz, CD_3OD): δ 1.18 (t, *J* = 6.8, 12H), 2.92 (br s, 2H), 3.19-3.37 (m, 5H), 3.55-3.62 (m, 10H) 6.74 (br s, 1H), 6.89-7.01 (m, 4H), 7.11-7.30 (m, 12H), 7.36-7.42 (m, 2H), 7.50-7.61 (m, 2H), 7.65-7.72 (m, 2H), 7.95 (dd, *J* = 3.6, 8.0, 1H); ^{13}C NMR (100 MHz, CD_3OD): δ 11.4, 45.5, 51.2, 95.9, 113.4, 114.0, 127.5, 128.4, 128.4, 128.7, 129.9, 130.3, 130.7, 130.7, 131.8, 132.0, 133.4, 133.6, 134.9, 137.1, 137.2, 137.7, 155.5, 155.8, 157.8, 166.6, 168.1, 169.5; ^{31}P NMR (162 MHz, CD_3OD): δ -4.60; HRMS (FAB): Calcd. for $C_{53}H_{54}N_4O_5P^+$ $[M^+]$ 857.3832, found 857.3813.

Alexa Fluor 568 phosphine conjugate (3.4). Alexa Fluor 568 cadaverine (28.0 mg, 34.4 µmol) was dissolved in 2 mL of DMSO. DIPEA (30.0 µL, 0.172 mmol) and **3.6** (37.0 mg, 68.8 µmol) were added, and the solution was stirred overnight under Ar in the dark. The crude was then diluted in ddH_2O (2 mL), filtered, and purified by HPLC (reversed-phase C18 preparative column, 25%-40% CH_3CN + 0.1% TFA over 40 min) to yield 29.0 mg of a bright purple solid (75%). HRMS (ESI): Calcd. for $C_{59}H_{58}O_{13}N_4PS_2^+$ $[M^+]$ 1125.3174, found 1125.3158.

Cyanine 5.5 ethylenediamine conjugate (3.12). Ethylenediamine (35.0 µL, 0.522 mmol) was dissolved in 100 µL DMSO. Triethylamine (75.0 µL, 0.538 mmol) was added, followed by cyanine 5.5-NHS ester (10.0 mg, 8.86 µmol). The reaction was stirred overnight in the dark. The reaction was then diluted with ddH_2O, filtered, and purified by HPLC (reversed-phase C18 preparative column, 0% CH_3CN + 0.1% TFA for 5 min followed by 0%-50% CH_3CN + 0.1% TFA over 60 min) to yield 2.03 mg of a dark blue solid (24%). HRMS (ESI): Calcd. for $C_{43}H_{49}O_{13}N_4S_4^-$ [M^-] 957.2184, found 957.2179.

Cyanine 5.5 DIFO conjugate (3.5). Compound **3.12** (2.03 mg, 2.11 μmol) was dissolved in 50 μL DMSO. Triethylamine (20.0 μL, 125 μmol) was added, followed by DIFO-Pfp ester (15) (4.00 mg, 10.4 μmol) in 50 μL DMSO dropwise with stirring. The resulting mixture was stirred overnight in the dark. The reaction was then diluted with ddH_2O, filtered, and purified by HPLC (reversed-phase C18 preparative column, 0%-60% CH_3CN over 60 min) to yield 1.67 mg of a dark blue solid (69%). HRMS (ESI-FT): Calcd. for $C_{53}H_{60}F_2N_4O_{15}S_4$ [M] 1158.2906, found: 1158.2860.

Photophysical characterization of fluorescent phosphines

Absorption spectra were collected on a Varian Cary-100 UV-Vis spectrophotometer using 1-cm quartz cells or a Molecular Devices UV-Vis spectrophotometric microtiter plate reader. Fluorescence spectra were recorded on a Photon Technology International Quanta Master 4 L-format scanning spectrofluorometer equipped with a LPS-220B 75-W xenon lamp and power supply, A-1010B lamp housing with integrated igniter, switchable 814 photon-counting/analog photomultiplier detection unit, and MD5020 motor driver.

Extinction coefficients were determined by plotting a standard Beer-Lambert plot ($A = cl\varepsilon$). Relative quantum yields were measured according to the methods of Fery-Forgues *et al.* (32). Cyanine 5.5 (33), fluorescein (34), and rhodamine 101 (35) were used as standards for compounds **3.1**, **3.2**, and **3.3**, respectively. Briefly, the sample and standard were weighed on a microbalance and dissolved in PBS, pH 7.4 (**3.1** and **3.3**) or 0.1 N NaOH (**3.2**) at concentrations such that the absorbance value was ~0.4 at the excitation wavelength. The solutions of sample and standard were then diluted ten-fold, and emission spectra were recorded and integrated.

Protein labeling with phosphine probes

Wild-type murine dihydrofolate reductase (mDHFR) and azido mDHFR (16) (400 ng) were labeled with compounds **3.1-3.3** (10 μM final concentration in 20 μL of 8 M urea) for 12 h at rt in the dark. The samples were then diluted with 4X SDS-PAGE loading buffer and heated for 3 min at 95 °C before being loaded onto a polyacrylamide gel (Criterion pre-cast gel, 4-12% Bis-Tris). After electrophoresis, the gel was visualized on a Typhoon 9410 Variable Mode Imager (fluorescence mode) to detect protein labeling and then stained with Coomassie Blue to verify equal protein content.

Cell culture conditions

All media and reagents were obtained from commercial suppliers and used without further purification or alteration unless otherwise noted. Jurkat cells were cultured in RPMI-1640 media (GIBCO) supplemented with 10% FBS, 100 units/mL penicillin and 100 μg/mL streptomycin. Chinese hamster ovary (CHO) cells were cultured in Ham's F-12 media (GIBCO) supplemented with 10% FBS, 100 units/mL penicillin and 100 μg/mL streptomycin. The cells were maintained at 37 ˚C and 5% CO_2 and counted using a Z2 Coulter cell counter.

Cell-surface azide labeling and detection by flow cytometry

Jurkat cells were seeded at a density of 2.0 x 10^5 cells/mL in culture flasks containing 10 mL of media and incubated for 3 d in untreated media or media containing peracetylated *N*-azidoacetylmannosamine ($Ac_4ManNAz$, 25 μM final concentration). After incubation, the cells were transferred to a 96-well V-bottom plate and pelleted by centrifugation at 2536 x g for 3 min. The medium was decanted, and the cells were resuspended in 200 μL of PBS (pH 7.4) containing 1% FBS (FACS buffer). Centrifugation was repeated and cells were washed a second time. After pelleting, the supernatant was decanted, and the cells were resuspended with 100 μL of compounds **3.1-3.3** in FACS buffer (10 μM, 100 μM, and 1 mM final concentrations) and incubated at rt for 1 h in the dark. As a negative control, the cells were also treated with an oxidized version of **3.1** (**3.1-ox**, 1 mM final concentration).

Following the labeling reaction, the samples were maintained at 4 ˚C until analysis in order to slow recycling of the plasma membrane. The cells were pelleted, the supernatant was decanted, and the cells were then resuspended in 200 μL of FACS buffer. This step was repeated six additional times to wash away the excess unreacted probe. The cells were then resuspended in 200 μL of FACS buffer and transferred into an additional 200 μL of FACS buffer for flow cytometry analysis.

Cell labeling and detection by fluorescence microscopy

Cells were seeded on slides mounted with 8 tissue culture wells (Lab-Tek) with either untreated media or media containing $Ac_4ManNAz$ (100 μM final concentration) for 3 d. The cells were labeled with **3.1** (200 μM) for 2 h at 37 ˚C. The cells were washed three times with media and then fixed and permeabilized with cold MeOH (-20 ˚C) for 5 min. The cells were washed with PBS (3 times, 10 min each). The cells were blocked in PBS with 1% BSA for 15 min, followed by the addition of the primary antibody (rabbit polyclonal anti-Giantin, 1:750 dilution, Abcam) diluted in blocking buffer. After incubation at rt for 2 h, the cells were washed three times, blocked for 10 min, and incubated with the secondary antibody (FITC-conjugated goat anti-rabbit, 1:400 dilution, Invitrogen) diluted in blocking buffer for 1 h. After three washes, the cells were mounted with Vectashield containing the nuclear stain DAPI (Vector Laboratories) before imaging.

For imaging experiments using **3.4**, CHO cells were seeded as described above and then labeled with **3.4** (200 μM) for 2 h at 37 ˚C. The cells were washed three times with media and incubated with Hoechst 33342 (1:1000 dilution of 1 mg/mL stock) for 2 min. The cells were washed two times with media and then imaged.

For **3.5**, CHO cells were seeded on slides mounted with 8 tissue culture wells (Lab-Tek) with either untreated media or media containing $Ac_4ManNAz$ (50 μM final concentration) for 3 d. The cells were labeled with **3.5** (10 μM) for 1 h at 37 ˚C. The cells were washed three times with media and incubated with Hoechst 33342 (1:1000 dilution of 1 mg/mL stock) for 2 min. The cells were washed two times with media and then imaged.

Cell-surface azide and ketone labeling and detection by flow cytometry

Jurkat cells were seeded at a density of 2.5 x 10^5 cells/mL in culture flasks containing 10 mL of media and incubated for 2 d in untreated media, media containing peracetylated *N*-azidoacetylgalactosamine (Ac_4GalNAz, 150 μM final concentration), peracetylated *N*-levulinoylmannosamine (Ac_4ManLev, 50 μM final concentration) or both Ac_4GalNAz (150 μM final concentration) and Ac_4ManLev (50 μM final concentration). The cells were then treated with biotin hydrazide (Sigma Aldrich, 1 mM in PBS with 1% FBS, pH 6.5) and compound **3.1** (100 μM final concentration in PBS with 1% FBS, pH 6.5) for 2 h at rt in the dark.

The cells were pelleted, the supernatant was decanted, and the cells were then resuspended in 200 μL of FACS buffer. This step was repeated two additional times. After the final wash, the samples were resuspended FACS buffer containing FITC-avidin (Sigma Aldrich, 5 μg/mL final concentration). The cells were incubated with FITC-avidin for 15 min in the dark, washed three times with FACS buffer, and then resuspended in 200 μL of FACS buffer. The labeling with FITC-avidin and wash steps were repeated once more. After the second labeling, the cells were resuspended in 200 μL of FACS buffer and transferred into 200 μL of additional FACS buffer for flow cytometry analysis.

As a negative control, Jurkat cells treated with both Ac_4GalNAz and Ac_4ManLev were labeled with **3.1-ox** (100 μM final concentration in PBS with 1% FBS, pH 6.5), followed by labeling with FITC-avidin as described above.

It should be noted that the unnatural sugars used in the above experiments show no adverse effects toward cell viability. We have addressed this issue in previous work (19, 36, 37). These published studies have established that concentrations up to 50 μM Ac_4ManLev and Ac_4ManNAz, and up to 200 μM Ac_4GalNAz, are not toxic to a majority of mammalian cells as assessed by exclusion of trypan blue and propidium iodide and confirmed by normal growth of the cells (based on expected doubling times during cell division). We have also quantified the amount of cell surface glycans that are metabolically labeled with Ac_4ManNAz. Our results indicate that 40% of natural sialic acids are replaced with SiaNAz upon Ac_4ManNAz treatment of Jurkat cells, whereas the substitution efficiency of CHO cell sialosides under similar conditions is about 30% (38).

Mice

Nude (nu/nu) and FVB mice (aged 5-8 weeks) were purchased from The Jackson Laboratory or Charles River Laboratories. Animals were handled in accordance with Animal Use Protocols R234-0510B (approved by the Animal Care and Use Committee at the University of California, Berkeley) and #7291-5 (Gambhir laboratory, approved by the Animal Care and Use Committee at Stanford University).

Compound administration

Mice were injected with Ac_4ManNAz (300 mg/kg, IP) or vehicle (70% aqueous DMSO, IP) once daily for 7 d, followed by one bolus of a fluorescent probe (**3.1** or **3.1-ox**: 2, 20, and 200 μg in 200 μL of ddH_2O; **3.3** or **3.3-ox**: 0.5, 1, and 2 mg in 200 μL of ddH_2O; **3.4**: 2 mg in 200 μL of ddH_2O; or **3.5**: 0.2, 2, and 20 μg in 200 μL of ddH_2O) IV via the tail vein 24 h after the final azidosugar injection.

Fluorescence imaging of mice treated with phosphine or cyclooctyne probes

For *in vivo* fluorescence imaging, mice were anesthetized with isoflurane and placed in a light-tight chamber equipped with a halogen light source. Whole body images were acquired at various time points post-injection of the fluorescent probe using the appropriate excitation and emission filters for each fluorophore.

Culturing of cancer cells in the presence of azidosugar

Cancer cell lines were kindly provided by P. Ray and S. Gambhir (Stanford University). Cells were cultured in media (from GIBCO; for SK-N-SH cells, MEM + 10% FBS + 1 mM sodium pyruvate; for RMA cells, RPMI-1640 + 10% FBS) supplemented with 100 units/mL penicillin and 100 µg/mL streptomycin and $Ac_4ManNAz$ (10 µM) or no azidosugar. Cells were plated at a density of 1×10^6 cells/mL and incubated for 3 d in a 5% CO_2, water-saturated incubator at 37 °C.

Implantation of tumor xenografts into immunodeficient mice

SK-N-SH or RMA cells (10×10^6) were grafted onto the dorsal flank of nu/nu mice or directly injected into the peritoneal cavity (IP). Once the subcutaneous tumors were palpable (2-3 weeks), azidosugar administration was begun as described above.

Isolation of tumor cells from matrix

Tumor tissues were minced with a razor blade and digested with collagenase (Sigma; 4 mg/mL, total volume of 200 µL for SK-N-SH tumors) or Blendzyme (Sigma; 2 Wunsch units/mL for RMA tumors) for 1 h at 37 °C. The digest was filtered through a nylon mesh cell strainer (40 µm) and transferred into a 50-mL conical tube. The cells were then rinsed with media twice and transferred into a 96-well plate for subsequent Staudinger ligation with PHOS-FLAG (*vide infra*).

Labeling of cell surfaces ex vivo

The presence of cell-surface azides on cancer cell lines, isolated splenocytes, or tumor xenografts were determined via Staudinger ligation using our previously reported assay (12). Briefly, cultured cells or isolated splenocytes were incubated with PHOS-FLAG (250 µM in FACS buffer) for 1 h at rt, then treated with FITC-anti-FLAG (Sigma, 1:900 dilution in FACS buffer) for 30 min on ice and analyzed by flow cytometry.

References

1. Weissleder R, Pittet MJ (2008) Imaging in the era of molecular oncology. *Nature* 452:580-589.

2. Massoud TF, Gambhir SS (2003) Molecular imaging in living subjects: Seeing fundamental biological processes in a new light. *Genes Dev* 17:545-580.

3. Dube DH, Bertozzi CR (2005) Glycans in cancer and inflammation--Potential for therapeutics and diagnostics. *Nat Rev Drug Discovery* 4:477-488.

4. Fuster MM, Esko JD (2005) The sweet and sour of cancer: Glycans as novel therapeutic targets. *Nat Rev Cancer* 5:526-542.

5. Zhang S, *et al.* (1997) Selection of tumor antigens as targets for immune attack using immunohistochemistry: I. Focus on gangliosides. *Int J Cancer* 73:42-49.

6. Zhang S, *et al.* (1997) Selection of tumor antigens as targets for immune attack using immunohistochemistry: II. Blood group-related antigens. *Int J Cancer* 73:50-56.

7. Varki A, *et al.* (2008) *Essentials of Glycobiology* (Cold Spring Harbor Laboratory Press, New York).

8. Takano R, Muchmore E, Dennis JW (1994) Sialylation and malignant potential in tumour cell glycosylation mutants. *Glycobiology* 4:665-674.

9. Dvorak HF, Nagy JA, Dvorak AM (1991) Structure of solid tumors and their vasculature: Implications for therapy with monoclonal antibodies. *Cancer Cells* 3:77-85.

10. Oh P, *et al.* (2004) Subtractive proteomic mapping of the endothelial surface in lung and solid tumours for tissue-specific therapy. *Nature* 429:629-635.

11. Prescher JA, Bertozzi CR (2005) Chemistry in living systems. *Nat Chem Biol* 1:13-21.

12. Prescher JA, Dube DH, Bertozzi CR (2004) Chemical remodelling of cell surfaces in living animals. *Nature* 430:873-877.

13. Frangioni JV (2003) In vivo near-infrared fluorescence imaging. *Curr Opin Chem Biol* 7:626-634.

14. Wang CC, Seo TS, Li Z, Ruparel H, Ju J (2003) Site-specific fluorescent labeling of DNA using Staudinger ligation. *Bioconjug Chem* 14:697-701.

15. Baskin JM, *et al.* (2007) Copper-free click chemistry for dynamic in vivo imaging. *Proc Natl Acad Sci USA* 104:16793-16797.

16. Kiick KL, Saxon E, Tirrell DA, Bertozzi CR (2002) Incorporation of azides into recombinant proteins for chemoselective modification by the Staudinger ligation. *Proc Natl Acad Sci USA* 99:19-24.

17. Huang KM, Snider MD (1993) Glycoprotein recycling to the galactosyltransferase compartment of the Golgi complex. *J Biol Chem* 268:9302-9310.

18. Mahal LK, Yarema KJ, Bertozzi CR (1997) Engineering chemical reactivity on cell surfaces through oligosaccharide biosynthesis. *Science* 276:1125-1128.

19. Hang HC, Yu C, Kato DL, Bertozzi CR (2003) A metabolic labeling approach toward proteomic analysis of mucin-type O-linked glycosylation. *Proc Natl Acad Sci USA* 100:14846-14851.

20. Prescher JA (2006) Probing glycosylation in living animals with bioorthogonal chemistries. *PhD Dissertation, University of California, Berkeley*.

21. Hangauer MJ, Bertozzi CR (2008) A FRET-based fluorogenic phosphine for live-cell imaging with the Staudinger ligation. *Angew Chem Int Ed Engl* 47:2394-2397.

22. Cook R, Lyttle M, Dick D (2006), ed. USPTO (Biosearch Technologies, Inc., USA).

23. Liu X, *et al.* (2007) Optical antisense imaging of tumor with fluorescent DNA duplexes. *Bioconjug Chem* 18:1905-1911.

24. Pham W, Weissleder R, Tung CH (2002) An azulene dimer as a near-infrared quencher. *Angew Chem Int Ed Engl* 41:3659-3662, 3519.

25. Marras SA, Kramer FR, Tyagi S (2002) Efficiencies of fluorescence resonance energy transfer and contact-mediated quenching in oligonucleotide probes. *Nucleic Acids Res* 30:e122.

26. Gilmore JM, Scheck RA, Esser-Kahn AP, Joshi NS, Francis MB (2006) N-terminal protein modification through a biomimetic transamination reaction. *Angew Chem Int Ed Engl* 45:5307-5311.

27. Laughlin ST, Bertozzi CR (2007) Metabolic labeling of glycans with azido sugars and subsequent glycan-profiling and visualization via Staudinger ligation. *Nat Protoc* 2:2930-2944.

28. Luchansky SJ, *et al.* (2003) Constructing azide-labeled cell surfaces using polysaccharide biosynthetic pathways. *Methods Enzymol* 362:249-272.

29. Prochazka M, Gaskins HR, Shultz LD, Leiter EH (1992) The nonobese diabetic SCID mouse: Model for spontaneous thymomagenesis associated with immunodeficiency. *Proc Natl Acad Sci USA* 89:3290-3294.

30. Adamczyk M, Grote J, Moore JA (1999) Chemoenzymatic synthesis of 3'-O-(carboxyalkyl)fluorescein labels. *Bioconjug Chem* 10:544-547.

31. Nguyen T, Francis MB (2003) Practical synthetic route to functionalized rhodamine dyes. *Org Lett* 5:3245-3248.

32. Fery-Forgues SL, Lavabre D (1999) Are fluorescence quantum yields so tricky to measure? A demonstration using familiar stationery products. *J Chem Ed* 76:1260-1264.

33. Xiao M, Selvin PR (2001) Quantum yields of luminescent lanthanide chelates and far-red dyes measured by resonance energy transfer. *J Am Chem Soc* 123:7067-7073.

34. Brannon J, Magde D (1978) Absolute quantum yield determination by thermal blooming. Fluorescein. *J Phys Chem* 82:705-709.

35. Eaton DF (1988) International Union of Pure and Applied Chemistry Organic Chemistry Division Commission on Photochemistry. Reference materials for fluorescence measurement. *J Photochem Photobiol B* 2:523-531.

36. Jacobs CL*, et al.* (2000) Metabolic labeling of glycoproteins with chemical tags through unnatural sialic acid biosynthesis. *Methods Enzymol* 327:260-275.

37. Saxon E*, et al.* (2002) Investigating cellular metabolism of synthetic azidosugars with the Staudinger ligation. *J Am Chem Soc* 124:14893-14902.

38. Luchansky SJ, Argade S, Hayes BK, Bertozzi CR (2004) Metabolic functionalization of recombinant glycoproteins. *Biochemistry* 43:12358-12366.

Chapter 4: Development of new chemical reporters of sialic acid biosynthesis[a]

Introduction

Sialic acids, a family of monosaccharides widely distributed in higher eukaryotes and certain bacteria, are determinants of many functional glycans that play central roles in numerous physiological and pathological processes (1). For example, the sialic acid-containing epitope Siaα2–6Gal serves as the cellular receptor for human influenza-A and -B viruses during infection (2), and linear homopolymers of sialic acids, known as polysialic acid (PSA), modulate neuronal synapse formation in mammalian development (3). The expression of sialoglycoconjugates, such as sialyl Lewis x, sialyl Tn (STn), and PSA, is also a common feature shared by numerous cancers (4). Interestingly, upregulation of these sialosides is strongly correlated with the transformed phenotype of many cancers (5, 6). For example, STn, a mucin-associated disaccharide, is not normally found in healthy tissues but is expressed by malignant tumors, including those of the pancreas and breast (7, 8). In addition, a strong correlation between the level of cell-surface sialic acids and metastatic potential has been observed in several different tumor types (9). Thus, as cancer cells generally display higher levels of sialic acid than their nonmalignant counterparts, sialylated glycoconjugates, collectively termed the "sialome", constitute attractive targets in the search for novel cancer biomarkers.

A variety of methods including affinity chromatography using sialic acid-specific lectins (10-12) or selective periodate oxidation of sialic acids followed by hydrazide capture (13) has been reported for the enrichment and identification of sialylated glycoproteins from bodily fluids or cell lysates. A complementary method that we have developed involves metabolic labeling of sialylated glycoproteins by treating cells or living animals with peracetylated analogs of *N*-acetylmannosamine (ManNAc) bearing chemical reporter groups such as the azide (i.e., peracetylated *N*-azidoacetylmannosamine, Ac_4ManNAz) (14, 15). Ac_4ManNAz is enzymatically deacetylated in the cytosol and then metabolically converted to the corresponding *N*-azidoacetyl sialic acid (SiaNAz), which is subsequently incorporated into sialoglycoconjugates (14, 16). Once presented on the cell surface, the azide-labeled sialylated glycans can be visualized or captured for glycoproteomic analysis with a variety of reagents (17), including Staudinger ligation phosphines (14), terminal alkynes along with reagents for Cu(I)-catalyzed azide-alkyne cycloaddition (CuAAC) (18, 19), or strained alkynes (20).

This Chapter focuses on the development of new bioorthogonal chemical reporters of the sialic acid biosynthetic pathway. In addition to Ac_4ManNAz, our lab has demonstrated that other azido- and keto-analogs of *N*-acetylmannosamine and sialic acid can be metabolically incorporated into cell-surface glycans *in vivo* (21). However, the efficiency of sialic acid labeling using these unnatural sugars is fairly low *in vivo*. Mouse heart tissue glycoproteins incorporate SiaNAz at up to ~3% of total sialic acid, and the azidosugar is undetectable in some organs that are known to possess sialylated glycoconjugates (15). Previous studies in our lab have shown that the efficiency of sialic acid biosynthesis is very sensitive to the *N*-acyl structure of unnatural ManNAc analogs (22, 23). For instance, analogs with long or branched *N*-acyl chains are poor substrates for the biosynthetic enzymes, while those containing short, linear side chains are better tolerated (23). Thus, we were curious how the alkynyl ManNAc analog reported by Wong and coworkers (24) would fare in live animal metabolic labeling studies compared to ManNAz.

---

[a] Peng Wu and Xing Chen contributed to the work presented in this chapter.

Increasing the efficiency of unnatural sugar metabolism could boost the levels of incorporation *in vivo*, which should improve the enrichment and identification of sialylated glycoproteins using mass spectrometry. The development of better chemical reporters of sialic acid biosynthesis could facilitate the discovery of sialylated cancer biomarkers in murine cancer models.

Results and discussion

Alkynyl analog of ManNAc (Ac₄ManNAl) is converted to SiaNAl and incorporated into cell-surface glycans

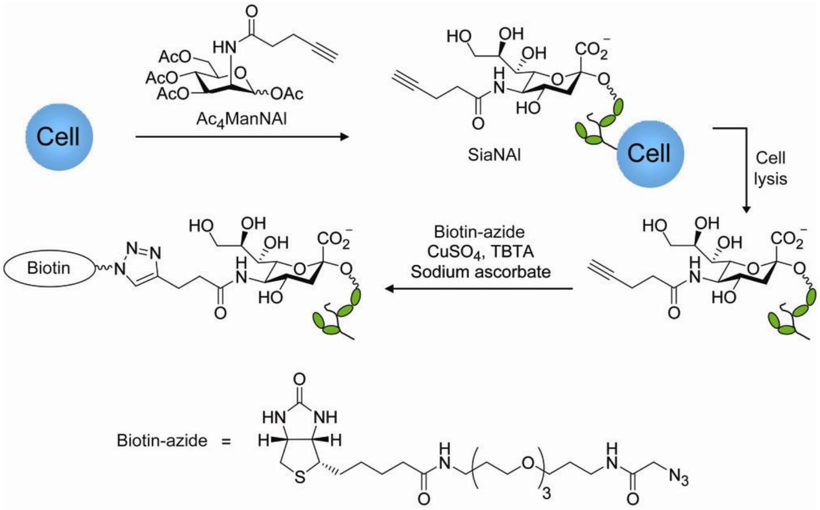

Figure 4-1. Metabolic labeling of cellular glycans with Ac$_4$ManNAl and detection by CuAAC. TBTA = tris[(1-benzyl-1*H*-1,2,3-triazol-4-yl)methyl]amine.

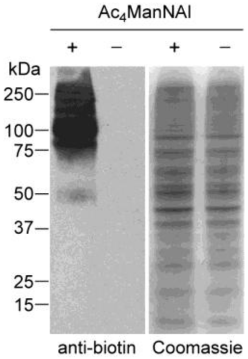

Figure 4-2. Western blot analysis of lysates from Jurkat cells treated with Ac$_4$ManNAl (50 µM) or no sugar. The lysates were reacted with biotin-azide (100 µM) in the presence CuSO$_4$ (1 mM), sodium ascorbate (1 mM), and the tris-triazolyl ligand TBTA (27) (100 µM) for 1 h at rt and analyzed by Western blot using an HRP-conjugated anti-biotin antibody (left panel). Total protein loading was confirmed by Coomassie staining of a duplicate protein gel (right panel).

Toward this goal, we synthesized peracetylated *N*-(4-pentynoyl) mannosamine (Ac$_4$ManNAl, Figure 4-1) and confirmed its metabolic conversion to the corresponding sialic acid (SiaNAl) in cultured cells. Jurkat cells, a human T lymphoma cell line, were cultured with 50 μM Ac_4ManNAl for three days, after which their lysates were reacted with an azido biotin derivative (biotin-azide, Figure 4-1) (25) using standard CuAAC conditions (26). Western blot analysis showed significant glycoprotein labeling in lysates from cells treated with Ac_4ManNAl but no detectable labeling in lysates from untreated cells (Figure 4-2).

Ac_4ManNAl is more efficiently metabolized than Ac_4ManNAz in mammalian cell lines

We confirmed the presence of SiaNAl within these cellular glycans by performing sialic acid compositional analysis using established protocols (28). As shown in Table 4-1, we compared the efficiencies of metabolic conversion of Ac_4ManNAl and Ac_4ManNAz to glycoconjugate-bound SiaNAl and SiaNAz, respectively. Six cell lines were cultured in media supplemented with 50 μM Ac_4ManNAl or Ac_4ManNAz. After 72 hours, the cells were lysed, and the lysates were subjected to sialic acid quantification using a synthetic standard of SiaNAl (**4.1**). In every cell line, metabolic labeling with SiaNAl was substantially more efficient than with SiaNAz. For example, in the human prostate cancer cell line LNCaP, 78% of glycoconjugate-bound sialic acids were substituted with SiaNAl. By contrast, SiaNAz constituted only 51% of LNCaP glycan-associated sialic acids under the same metabolic labeling conditions. Fluorescence microscopy analysis of Ac_4ManNAl-labeled cells after reaction with biotin-azide via CuAAC and staining with FITC-streptavidin confirmed that SiaNAl-modified glycans reside on the cell surface (Figure 4-3).

Cell line	Jurkat	HEK293T	CHO	LNCaP	DU145	PC3
% SiaNAl	74 ± 1	46 ± 2	38 ± 2	78 ± 1	58 ± 2	71 ± 6
% SiaNAz	29 ± 2	27 ± 2	20 ± 4	51 ± 2	40 ± 3	56 ± 21

Table 4-1. Incorporation percentage of SiaNAl vs. SiaNAz *in vitro*. The cells were metabolically labeled with 50 μM Ac_4ManNAl (top row) or Ac_4ManNAz (bottom row) for 3 d and then lysed. Identification and quantification of SiaNAl and SiaNAz was determined by comparison with synthetic standards according to established procedures (28). The error represents the standard deviation from the mean of at least three replicate experiments.

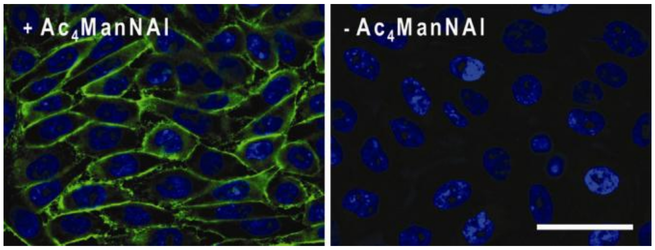

Figure 4-3. Fluorescence micrographs of CHO cells treated with 50 μM Ac_4ManNAl (left) or no sugar (right) for 3 d. The cells were rinsed, fixed with 3% paraformaldehyde, and labeled with biotin-azide (50 μM) in the presence of $CuSO_4$ (100 μM), sodium ascorbate (200 μM), and TBTA (100 μM) for 10 min at rt, followed by secondary labeling with a FITC-streptavidin conjugate. The cells were labeled with DAPI nuclear stain before imaging. (Blue = DAPI channel, Green = FITC channel). Scale bar = 40 μm.

Ac_4ManNAl is metabolized to SiaNAl in laboratory mice

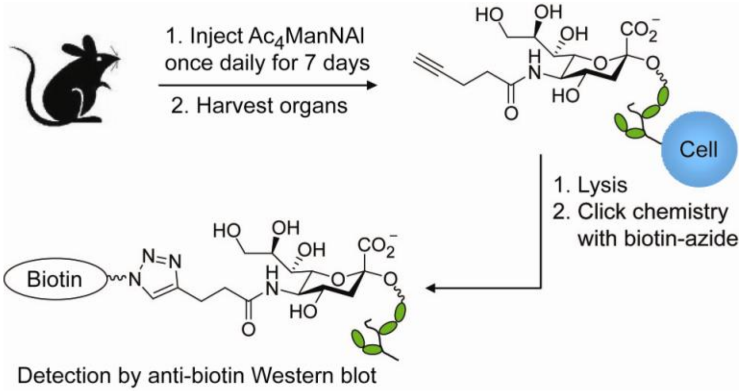

Figure 4-4. Experimental overview for probing Ac_4ManNAl metabolism *in vivo*. Wild-type B6D2F1/J mice were injected with Ac_4ManNAl or vehicle intraperitoneally once daily for seven days. On the eighth day, the organs were collected and homogenized, and organ lysates were probed using CuAAC for the presence of alkyne-bearing glycoproteins by reaction with biotin-azide, followed by Western blot analysis using an HRP-conjugated anti-biotin antibody.

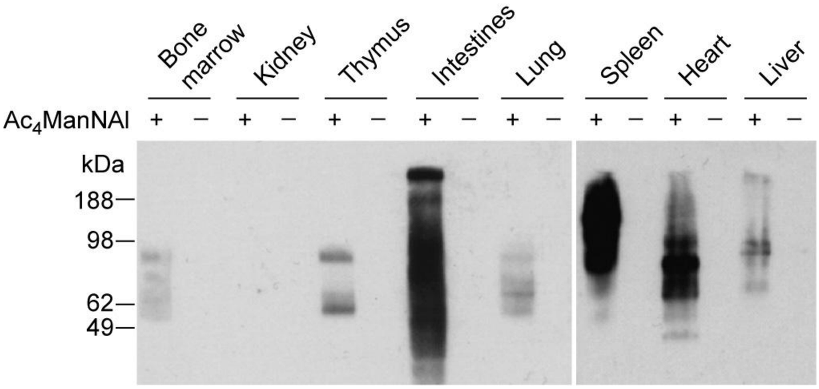

Figure 4-5. Western blot analysis of tissue lysates from B6D2F1/J mice administered Ac_4ManNAl (+) or vehicle (–). Mice were injected with Ac_4ManNAl (300 mg/kg) or vehicle once daily for seven days. On the eighth day, the organs were harvested and homogenized. The lysates were then reacted with biotin-azide (100 μM) in the presence $CuSO_4$ (1 mM), sodium ascorbate (1 mM), and TBTA (100 μM) for 1 h at rt and analyzed by Western blot using an HRP-conjugated anti-biotin antibody. Shown are representative data from three replicate experiments. Total protein loading was confirmed by Coomassie Blue staining of a duplicate protein gel (data not shown).

To determine whether the superior metabolic conversion efficiency of Ac_4ManNAl observed in cell culture is recapitulated *in vivo*, we evaluated its conversion to SiaNAl after administration to laboratory mice. B6D2F1/J mice were injected intraperitoneally with Ac_4ManNAl (300 mg/kg) or vehicle once daily for seven days (Figure 4-4). On the eighth day, the mice were euthanized, and a panel of organs was harvested and homogenized. The presence of glycoprotein-associated alkynes in the soluble fraction of homogenates was probed by

CuAAC with biotin-azide, followed by Western blot analysis. As shown in Figure 4-5, labeling was observed in organ lysates from mice treated with Ac_4ManNAl but not in organ lysates from vehicle-treated mice. Labeled glycoproteins were observed in all of the lysates collected from the bone marrow, thymus, intestines, lung, spleen, heart, liver, and kidney (overexposed blot of kidney sample not shown). These results indicated that Ac_4ManNAl is metabolized *in vivo* and has access to most organs. Furthermore, during this one-week period, no toxic side effects were observed, suggesting that Ac_4ManNAl is well tolerated by the mice.

Ac_4ManNAl is more efficiently metabolized than Ac_4ManNAz in laboratory mice

We then performed comparative *in vivo* metabolism studies of Ac_4ManNAl and Ac_4ManNAz using a similar protocol. The organs were harvested as described above, and the soluble fractions of the organ lysates were reacted with either biotin-azide or a biotin-alkyne derivative (20) using the same CuAAC conditions. Similar to our observations using cultured cells (Table 4-1), Ac_4ManNAl treatment produced stronger labeling in organ lysates than Ac_4ManNAz (Figure 4-6). Based on quantification by densitometry, we estimate that the labeling using ManNAl is at least 25% greater than that using ManNAz (data not shown). However, estimating metabolic incorporation based on these data is difficult because CuAAC displays different reaction kinetics when the limiting reagent is the alkyne compared to the azide (26). Given that the reaction kinetics are faster by approximately 2-3 fold in the latter case, we believe our estimate based on densitometry to be a lower limit.

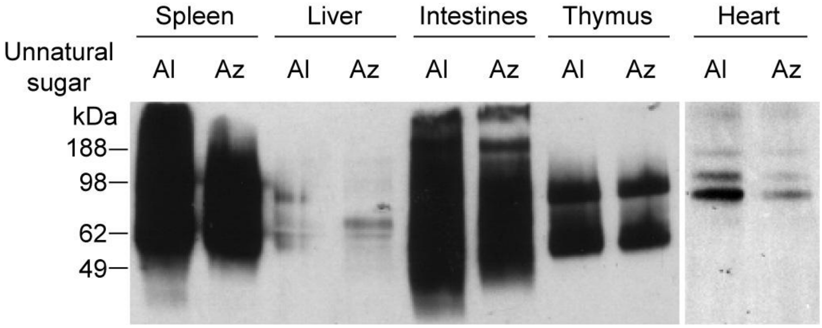

Figure 4-6. Ac_4ManNAl is converted to the corresponding sialic acid more efficiently than Ac_4ManNAz in mouse organs. A panel of organ lysates from mice treated with Ac_4ManNAl (Al) or Ac_4ManNAz (Az) (300 mg/kg) for 7 d were reacted with 100 μM biotin-azide or biotin-alkyne (20), respectively, in the presence $CuSO_4$ (1 mM), sodium ascorbate (1 mM), and TBTA (100 μM) for 1 h at rt and analyzed by Western blot using an HRP-conjugated anti-biotin antibody. Shown are representative data from three replicate experiments. Total protein loading was confirmed by Coomassie Blue staining of a duplicate protein gel (data not shown).

Conclusions

In summary, we have demonstrated that Ac_4ManNAl can metabolically label sialic acids in cultured cells and mice with greater efficiency than Ac_4ManNAz. This metabolic labeling method holds several advantages over previous approaches to sialylated glycoprotein analysis. First, metabolic labeling selects for those glycoproteins that are biosynthesized at high levels, irrespective of their steady-state abundance. Thus, metabolic labeling may reveal novel sialylated biomarkers that are rapidly turned over and therefore missed by steady-state labeling methods. Second, metabolic labeling can be performed in live animals (15), permitting the selective tagging of sialylated glycoconjugates within their native tissue environments.

This alkynyl sugar may therefore be useful in the discovery of sialylated cancer biomarkers using murine cancer models. Moreover, these results underscore the sensitivity of sialic acid biosynthetic enzymes to subtle differences in the *N*-acyl structures of the two ManNAc analogs. Accordingly, further structural modulation of alkynyl and azido ManNAc analogs is worth pursuing in order to further increase metabolic labeling efficiency *in vivo*.

Materials and methods

General

All chemical reagents were obtained from Sigma Aldrich and GFS Chemicals and used without further purification unless otherwise noted. Flash chromatography was performed using Merck 60 Å 230-400 mesh silica gel. Analytical thin layer chromatography (TLC) was performed on glass-backed Analtech Uniplate silica gel plates, and compounds were visualized by staining with phosphomolybdic acid or 10% H_2SO_4 in ethanol. CH_2Cl_2 and THF were dried *in vacuo* over alumina. Anhydrous MeOH and pyridine were purchased from Acros Organics. Organic extracts were dried over Na_2SO_4, and the drying agent was removed by vacuum filtration. Unless otherwise specified, all solvents were removed under reduced pressure using a rotary evaporator. ^1H NMR spectra were obtained at 500 and 600 MHz, and $^{13}C[^1H]$ NMR spectra were obtained at 75 and 125 MHz. Chemical shifts are reported in δ ppm relative to tetramethylsilane, and coupling constants (J) are reported in hertz (Hz). Mass spectra were obtained at the Albert Einstein Laboratory for Macromolecular Analysis and Proteomics. High resolution (HR) FT-ICR MS was performed on a Varian 12.0 T QFT mass spectrometer. Samples were dissolved in 50% methanol/H_2O containing 0.1% formic acid and introduced into the FT-ICR MS using electrospray ionization.

Media, fetal bovine serum (FBS), and Dulbecco’s Phosphate Buffered Saline (PBS) were purchased from Invitrogen (Carlsbad, CA). Cells were counted by hand using a hemocytometer. FITC-conjugated streptavidin, penicillin and streptomycin were purchased from Sigma Aldrich (St. Louis, MO). Detergents, *DC* protein assay kits, and gels for electrophoresis were purchased from Bio-Rad Laboratories (Hercules, CA). Horseradish peroxidase-conjugated anti-biotin antibody (HRP-anti-biotin antibody) was purchased from Jackson ImmunoResearch Laboratories (West Grove, PA). SuperSignal West Pico Chemiluminescent Substrate was obtained from Pierce Biotechnology (Rockford, IL). Protease inhibitor Complete (EDTA-free) was purchased from Roche (Nutley, NJ).

Mice

Wild-type B6D2F1/J mice were purchased from The Jackson Laboratory (Bar Harbor, ME), and the animals were handled in accordance with Animal Use Protocol R234-0609B (approved by the Animal Care and Use Committee at the University of California, Berkeley).

Tissue culture/cell growth conditions

Unless otherwise specified, Jurkat and LNCaP cells were grown in RPMI-1640 media supplemented with 10% FBS, 100 units/mL penicillin and 0.1 mg/mL streptomycin (P/S). HEK 293T cells were grown in Dulbecco’s modified Eagle’s media, supplemented with 10% FBS and P/S. CHO cells were grown in Ham’s F12 media, supplemented with 10% FBS and P/S. DU145 cells were grown in Eagle’s minimal essential media, supplemented with 10% FBS and P/S. PC3 cells were grown in F-12K media, supplemented with 10% FBS and P/S. In all cases, cells were incubated in a 5% CO_2, water-saturated incubator at 37 °C.

Synthesis of SiaNAl

ManNAl (290 mg, 0.0011 mol) (24) was dissolved in 11 mL of 0.050 M potassium phosphate (pH 7.4), followed by addition of sodium pyruvate (1.2 g, 0.011 mol), NaN_3 (final concentration of 1% (w/v)) and NeuAc aldolase (20-25 U, Toyobo, lot no. 85211). The reaction mixture was placed in a shaking incubator at 37 °C for 14 h, after which ^{1}H NMR analysis indicated that the reaction was complete. The reaction mixture was then diluted with 90 mL of H_2O and purified by anion-exchange chromatography using AG1-X2 resin, formate form (Bio-Rad). The product was eluted with a gradient of 1.0 M to 2.5 M formic acid at 1.0 mL/min. Fractions were analyzed for the presence of the desired sialic acid derivative using the periodate-resorcinol method (29). The fractions containing the desired product were combined and concentrated *in vacuo* to give a white solid as exclusively the β-anomer. Yield: 341 mg (89%). ^{1}H NMR (500 MHz, D_2O) δ 1.87 (dd, J = 13.0, 11.5 Hz, 1H), 2.31 (dd, J = 13.0, 5.0 Hz, 1H), 2.39 (br, 1H), 2.49-2.52 (m, 4H), 3.59 (dd, J = 12.0, 6.5 Hz, 1H), 3.66 (dd, J = 9.0, 1.0 Hz, 1H), 3.73-3.76 (m, 1H), 3.83 (dd, J = 12.0, 3.0 Hz, 1H), 3.96 (app t, J = 10.3 Hz, 1H), 4.05-4.10 (m, 2H). ^{13}C NMR (75 MHz, D_2O) δ 14.5, 34.7, 52.0, 63.2, 66.6, 68.3, 70.2, 70.3, 70.4, 83.5, 95.3, 173.4, 175.4. HRMS (ESI): Calcd for $C_{14}H_{22}NO_9$ $[M+H]^+$ 348.1289, found 348.1294.

Preparation of cell lysates and detection of glycoproteins by Western blot analysis

Ac_4ManNAl was maintained as a 50 mM stock solution in filter-sterilized ethanol, which was allowed to evaporate in the cell culture flasks prior to the addition of cells. Cells were seeded at a density of 1.5 x 10^6 cells in 10 mL of media with no alkynyl sugar or 50 μM of Ac_4ManNAl and incubated for three days. The cells were harvested by centrifugation at 2851 × g, and the cell pellets were homogenized in 750 μL of lysis buffer (150 mM NaCl, 1% NP-40, 50 mM Tris-HCl, pH 7.4) containing protease inhibitors (Complete, EDTA-free) by ten freeze-thaw cycles. The insoluble debris was removed by centrifugation at 10,000 × g for 10 min. The soluble protein concentration was determined using the *DC* protein assay kit. Biotin-azide (100 μM from a 50× stock in DMSO) was added to each sample (25 μg protein in 30 μL lysis buffer), followed by freshly prepared sodium ascorbate (1 mM from a 50× stock in water) and TBTA ligand (100 μM from a 40× stock in a 1:4 mixture of DMSO:*t*-butanol). Samples were gently vortexed, and $CuSO_4 \cdot 5H_2O$ (1 mM from a 50× stock in water) was added to each sample, making the total reaction volume 32.5 μL. Samples were vortexed again and allowed to react at rt for 1 h. After adding 8.1 μL of 4× SDS-PAGE loading buffer containing β-mercaptoethanol, the samples were resolved on a Bis-Tris Criterion polyacrylamide gel (12%), transferred to nitrocellulose, and blocked with 5% bovine serum albumin in PBST (Dulbecco's Phosphate Buffered Saline with 0.1% Tween-20) for 1 h at rt. The blocked membrane was incubated for 1 h at rt with an HRP-anti-biotin antibody (1:100,000 dilution) in blocking buffer, washed with PBST (4 x 15 min per wash), and developed using SuperSignal West Pico Chemiluminescent Substrate.

Compound administration and preparation of tissue lysates

Mice (B6D2F1/J) were injected intraperitoneally with Ac_4ManNAl (24), Ac_4ManNAz (17), or vehicle (300 mg/kg in 70% aqueous DMSO) once daily for 7 d. On day 8, the mice were euthanized 24 h post-injection, and the organs were collected, rinsed with cold PBS, and minced.

The organs were then transferred into 1.5 mL of lysis buffer (150 mM NaCl, 1% NP-40, 50 mM Tris-HCl, pH 7.4) containing protease inhibitors (Complete, EDTA-free) and homogenized using a Dounce homogenizer. The cell debris was removed by centrifugation (13,500 × g for 10 min), and the supernatant was collected. Protein concentrations were determined using the *DC* protein assay kit. Click chemistry with biotin-azide or biotin-alkyne probe, SDS-PAGE, and Western blot analysis were performed as described in the previous section.

Fluorescence microscopy

Chinese hamster ovary (CHO) cells were seeded onto glass slides mounted with tissue culture wells (Lab-Tek, Nunc) and incubated with $Ac_4ManNAl$ (50 μM) or no sugar for 3 d. The cells were washed three times with PBS and then fixed with 3% paraformaldehyde in PBS at 4 °C for 20 min. After three washes, cells were treated with biotin-azide (50 μM) in the presence of sodium ascorbate (200 μM), TBTA (100 μM), $CuSO_4 \cdot 5H_2O$ (100 μM) in 200 μL PBS for 10 min at rt. The cells were then washed three times with PBS and blocked in PBS with 1% bovine serum albumin for 20 min, followed by staining with a FITC-streptavidin conjugate (1 μg/mL in PBS). After incubation at rt for 30 min in the dark, the cells were washed three times and then mounted using Vectashield with 4,6-diamidino-2-phenylindole (DAPI, Vector Laboratories). A Zeiss Axiovert 200M inverted microscope equipped with a 63 × 1.4 NA Plan-Apochromat oil immersion lens was employed for imaging. A 175W xenon lamp housed in a Sutter DG4 illuminator linked to the microscope by an optical fiber assured shuttering and illumination. Images were acquired using a CoolSNAP HQ CCD camera (Roper Scientific). Images were deconvolved using the nearest neighbor algorithm in SLIDEBOOK software version 4.2 (Intelligent Imaging Innovations) and are shown as a single z-plane.

Sialic acid identification and quantification as 1,2-diamino-4,5-methylenedioxybenzene (DMB) derivatives by RP-HPLC with fluorescence detection (28)

Lysates from cells treated with 50 μM of $Ac_4ManNAl$, $Ac_4ManNAz$, or no sugar for 3 d were dissolved in a final concentration of 2 M acetic acid and heated to 80 °C for 3 h to release sialic acids. The sialic acids were collected by ultrafiltration through a 3,000 NMWCO ultrafilter and derivatized with 1,2-diamino-4,5-methylenedioxybenzene (DMB). The sialic acid-DMB derivatives were analyzed by reversed phase HPLC coupled with fluorescence detection. Identification and quantification of SiaNAl and SiaNAz was determined by comparison with the synthetic standards of *N*-glycolylneuraminic acid (Neu5Gc), *N*-acetylneuraminic acid (Neu5Ac), SiaNAl, or SiaNAz (30).

References

1. Varki A, *et al.* (2008) *Essentials of Glycobiology* (Cold Spring Harbor Laboratory Press, New York).

2. Olofsson S, Bergstrom T (2005) Glycoconjugate glycans as viral receptors. *Ann Med* 37:154-172.

3. Troy FA, 2nd (1992) Polysialylation: From bacteria to brains. *Glycobiology* 2:5-23.

4. Taylor-Papadimitriou J, Epenetos AA (1994) Exploiting altered glycosylation patterns in cancer: Progress and challenges in diagnosis and therapy. *Trends Biotechnol* 12:227-233.

5. Sell S (1990) Cancer-associated carbohydrates identified by monoclonal antibodies. *Human Pathol* 21:1003-1019.

6. Jorgensen T, *et al.* (1995) Up-regulation of the oligosaccharide sialyl LewisX: A new prognostic parameter in metastatic prostate cancer. *Cancer Res* 55:1817-1819.

7. Itzkowitz S, *et al.* (1991) Expression of Tn, sialosyl Tn, and T antigens in human pancreas. *Gastroenterology* 100:1691-1700.

8. Ogata S, *et al.* (1998) Different modes of sialyl-Tn expression during malignant transformation of human colonic mucosa. *Glycoconj J* 15:29-35.

9. Dube DH, Bertozzi CR (2005) Glycans in cancer and inflammation--Potential for therapeutics and diagnostics. *Nat Rev Drug Discovery* 4:477-488.

10. Zhao J, Simeone DM, Heidt D, Anderson MA, Lubman DM (2006) Comparative serum glycoproteomics using lectin selected sialic acid glycoproteins with mass spectrometric analysis: Application to pancreatic cancer serum. *J Proteome Res* 5:1792-1802.

11. Qui R, Regnier FE (2005) Comparative glycoproteomics of N-linked complex-type glycoforms containing sialic acid in human serum. *Anal Chem* 77:7225-7231.

12. Qui R, Regnier FE (2005) Use of multidimensional lectin affinity chromatography in differential glycoproteomics. *Anal Chem* 77:2802-2809.

13. McDonald CA, Yang JY, Marathe V, Yen TY, Macher BA (2009) Combining results from lectin affinity chromatography and glyco-capture approaches substantially improves the coverage of the glycoproteome. *Mol Cell Proteomics* 8:287-301.

14. Saxon E, Bertozzi CR (2000) Cell surface engineering by a modified Staudinger reaction. *Science* 287:2007-2010.

15. Prescher JA, Dube DH, Bertozzi CR (2004) Chemical remodelling of cell surfaces in living animals. *Nature* 430:873-877.

16. Luchansky SJ, *et al.* (2003) Constructing azide-labeled cell surfaces using polysaccharide biosynthetic pathways. *Methods Enzymol* 362:249-272.

17. Laughlin ST, Bertozzi CR (2007) Metabolic labeling of glycans with azido sugars and subsequent glycan-profiling and visualization via Staudinger ligation. *Nat Protoc* 2:2930-2944.

18. Rostovtsev VV, Green LG, Fokin VV, Sharpless KB (2002) A stepwise Huisgen cycloaddition process: Copper(I)-catalyzed regioselective "ligation" of azides and terminal alkynes. *Angew Chem Int Ed Engl* 41:2596-2599.

19. Tornoe CW, Christensen C, Meldal M (2002) Peptidotriazoles on solid phase: [1,2,3]-Triazoles by regiospecific copper(I)-catalyzed 1,3-dipolar cycloadditions of terminal alkynes to azides. *J Org Chem* 67:3057-3064.

20. Agard NJ, Prescher JA, Bertozzi CR (2004) A strain-promoted [3 + 2] azide-alkyne cycloaddition for covalent modification of biomolecules in living systems. *J Am Chem Soc* 126:15046-15047.

21. Prescher JA (2006) Probing glycosylation in living animals with bioorthogonal chemistries. *PhD Dissertation, University of California, Berkeley*.

22. Keppler OT, Horstkorte R, Pawlita M, Schmidt C, Reutter W (2001) Biochemical engineering of the N-acyl side chain of sialic acid: Biological implications. *Glycobiology* 11:11R-18R.

23. Jacobs CL, *et al.* (2001) Substrate specificity of the sialic acid biosynthetic pathway. *Biochemistry* 40:12864-12874.

24. Hsu TL, *et al.* (2007) Alkynyl sugar analogs for the labeling and visualization of glycoconjugates in cells. *Proc Natl Acad Sci USA* 104:2614-2619.

25. Hang HC, Yu C, Pratt MR, Bertozzi CR (2004) Probing glycosyltransferase activities with the Staudinger ligation. *J Am Chem Soc* 126:6-7.

26. Speers AE, Cravatt BF (2004) Profiling enzyme activities in vivo using click chemistry methods. *Chem Biol* 11:535-546.

27. Chan TR, Hilgraf R, Sharpless KB, Fokin VV (2004) Polytriazoles as copper(I)-stabilizing ligands in catalysis. *Org Lett* 6:2853-2855.

28. Luchansky SJ, Argade S, Hayes BK, Bertozzi CR (2004) Metabolic functionalization of recombinant glycoproteins. *Biochemistry* 43:12358-12366.

29. Jourdian GW, Dean L, Roseman S (1971) The sialic acids. XI. A periodate-resorcinol method for the quantitative estimation of free sialic acids and their glycosides. *J Biol Chem* 246:430-435.

30. Luchansky SJ, Goon S, Bertozzi CR (2004) Expanding the diversity of unnatural cell-surface sialic acids. *Chembiochem* 5:371-374.

Chapter 5: A strategy for the cell-selective delivery of azidosugars[a]

Introduction

Glycans play critical roles in many biological processes including embryonic development (1), inflammation (2), and cancer cell metastasis (3). Because these physiological events are marked by changes in glycan composition and expression, glycans are interesting targets for *in vivo* imaging. We have developed an approach for visualizing and profiling these non-genetically encoded biomolecules known as the bioorthogonal chemical reporter strategy. This two-step method involves the metabolic incorporation of an unnatural sugar bearing a chemical reporter into a specific glycan subtype, followed by a covalent tagging step using a bioorthogonal reaction such as the Staudinger ligation or Cu-free click chemistry (4). This strategy has been used to image glycan dynamics in live cells and living organisms such as *C. elegans* and zebrafish (5, 6). We have also shown that this strategy can be used to tag glycans within mice, resulting in the global labeling of many organs including the liver, heart, kidney, and intestines (7, 8). While these studies have established the chemical reporter strategy as a viable method for imaging or profiling glycans *in vivo*, certain applications, such as tumor imaging, demand the selective labeling of specific cells or tissues *in vivo* (e.g., cancerous versus surrounding tissue). In this Chapter, we describe a strategy for cell-selective metabolic labeling of glycans based on tissue-specific expression of a protease.

Results and discussion

In our approach, we envisioned caging an unnatural analog of the metabolic precursor to the monosaccharide sialic acid that could be precluded from cellular metabolism by virtue of a protecting group. We achieved this feat by attaching a peptide to the 6-hydroxyl group of the unnatural sugar *N*-azidoacetylmannosamine (ManNAz), an analog of *N*-acetylmannosamine and a precursor to sialic acid (Figure 5-1A). In the presence of an extracellular protease that is secreted by the target tissue, the caging group could be cleaved enzymatically to release triacetylated ManNAz (Ac_3ManNAz), which could then be metabolized by cells and incorporated into cell-surface sialic acid residues. These labeled glycans can be detected via Cu-free click chemistry with difluorinated cyclooctyne (DIFO) reagents (Figure 5-1A) (4).

As a model enzyme, we chose the prostate-specific antigen protease (PSA), a serine protease that is secreted at low levels by normal prostatic glandular cells but is highly upregulated by prostate cancer cells (9). Though PSA is used clinically as a biomarker to screen for prostate cancer because its presence can be detected in the blood stream, it is inactive in the serum due to complexation with protease inhibitors (9). Thus, PSA is most active in the tissue of prostate tumors. For these reasons, PSA has been widely used in medicinal chemistry as a means of delivering anticancer agents and imaging reagents to prostate cancer cells and tumors *in vivo* (10-12).

---

[a] Danielle H. Dube contributed to the work presented in this chapter.

Design and synthesis of caged metabolic precursors to sialic acid

Our target compounds consisted of Ac_3ManNAz attached, via a linker at C6, to the hexapeptide Mu-HSSKLY (Mu = morpholino ureidyl), a known PSA substrate that is highly selective for this enzyme over other ubiquitous serine proteases (Figure 5-1B) (12, 13). We chose *p*-aminobenzyl alcohol (PABA) and ethylenediamine (EDA) as linkers due to their ability to release cargo molecules after enzymatic activation of the prodrug and the relative stability of their carbonate and carbamate linkages, respectively (14). Upon cleavage of the peptide, PABA-containing probe **5.1** is designed to release carbon dioxide and an iminoquinone methide intermediate that is subsequently attacked by water (Figure 5-1B) (15). Enzymatic cleavage of EDA-containing probe **5.2** results in expulsion of the linker as a cyclic urea (Figure 5-1B) (16). Compounds **5.1** and **5.2** were synthesized analogously to the route developed by Jones *et al*. as a mixture of anomers (Schemes 5-1 and 5-2) (12).

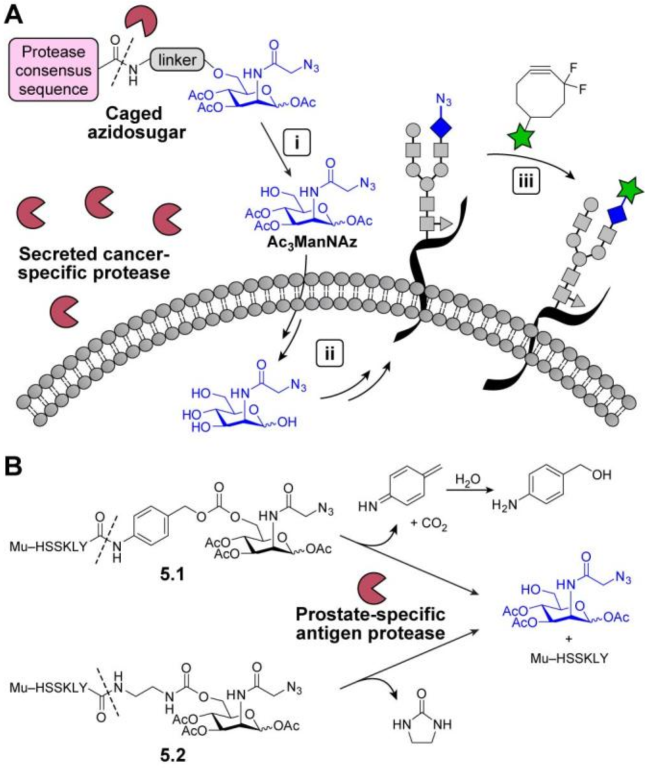

Figure 5-1. A strategy for tissue-specific release of Ac_3ManNAz via enzymatic activation. (A) i. A non-metabolizable caged azidosugar serves as a substrate for a secreted, cancer-specific protease, releasing Ac_3ManNAz. ii. This azidosugar is then metabolized by the cell and incorporated into cell-surface glycans. iii. The azide-labeled glycans are detected via Cu-free click chemistry using difluorinated cyclooctyne reagents. (B) Caged azidosugars used in this study (**5.1** and **5.2**). Cleavage of the indicated peptide bond (dashed lines) by the prostate-specific antigen protease (PSA), results in the release of a linker, the peptide, and Ac_3ManNAz.

Stability studies of caged azidosugars

We first evaluated the hydrolytic stability of **5.1** and **5.2** by incubating these compounds in aqueous buffer for 24 h at 37 °C. Surprisingly, **5.2**, which bears a more stable carbamate linkage, exhibited far greater degradation than carbonate **5.1** (Figure 5-2). Based on these results, we chose to pursue *in vitro* and *in vivo* experiments using **5.1**.

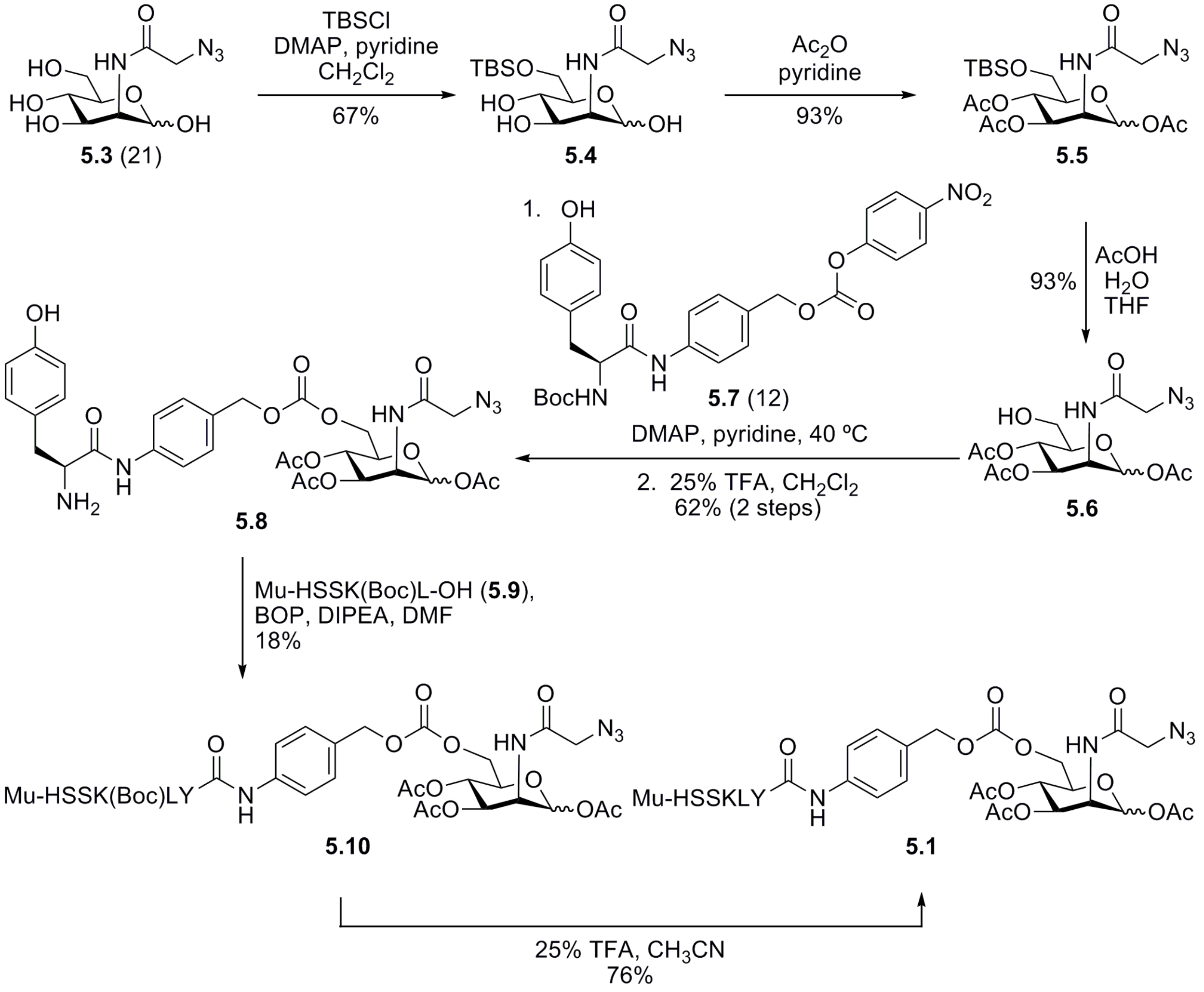

Scheme 5-1. Synthesis of **5.1**.

In vitro *enzymatic uncaging of caged azidosugar* ***5.1*** *using the prostate-specific antigen protease (PSA)*

To confirm that **5.1** can serve as a substrate for PSA, this probe was incubated *in vitro* with active enzyme or, as negative controls, buffer only or heat-killed (HK) enzyme. These enzymatic reactions were analyzed by reversed-phase HPLC and mass spectrometry. Incubation of **5.1** with PSA resulted in release of the peptide (Mu-HSSKLY) and Ac_3ManNAz (Figure 5-3A), while the negative controls exhibited only minor hydrolysis of the starting material to the peptide-linker conjugate (Mu-HSSKLY-PABA) and Ac_3ManNAz (Figure 5-3B and C).

*Selective labeling of cell-surface glycans using caged azidosugar **5.1** and PSA*

Having validated that **5.1** can be enzymatically activated by PSA, we next tested **5.1** for its ability to be uncaged by this enzyme and metabolically incorporated into cell-surface glycans on cultured cells. Chinese hamster ovary (CHO) cells were incubated with **5.1** at various concentrations (0-100 μM) in the presence of PSA (50 μg/mL), no enzyme, or HK PSA for 12 h at 37 °C. The cells were then washed and labeled with a DIFO-biotin conjugate (17), followed by fluorescein isothiocyanate-labeled avidin (FITC-avidin) and analysis by flow cytometry. We observed labeling over background hydrolysis in a concentration-dependent manner, suggesting that the signal is due to enzymatic activation (Figure 5-4A). In contrast, the negative controls exhibited minimal background labeling (Figure 5-4B). We also demonstrated that treatment of CHO cells with **5.1** and increasing amounts of PSA (0-50 μg/mL) resulted in a concentration-dependent signal, thus further supporting that the labeling is due to enzymatic release of Ac_3ManNAz (Figure 5-5). In addition, we verified that **5.1** did not cause any cytotoxicity by incubating CHO cells labeled as above with phycoerythrin-conjugated annexin V, a marker of apoptosis, and analyzing these cells by flow cytometry (Figure 5-6).

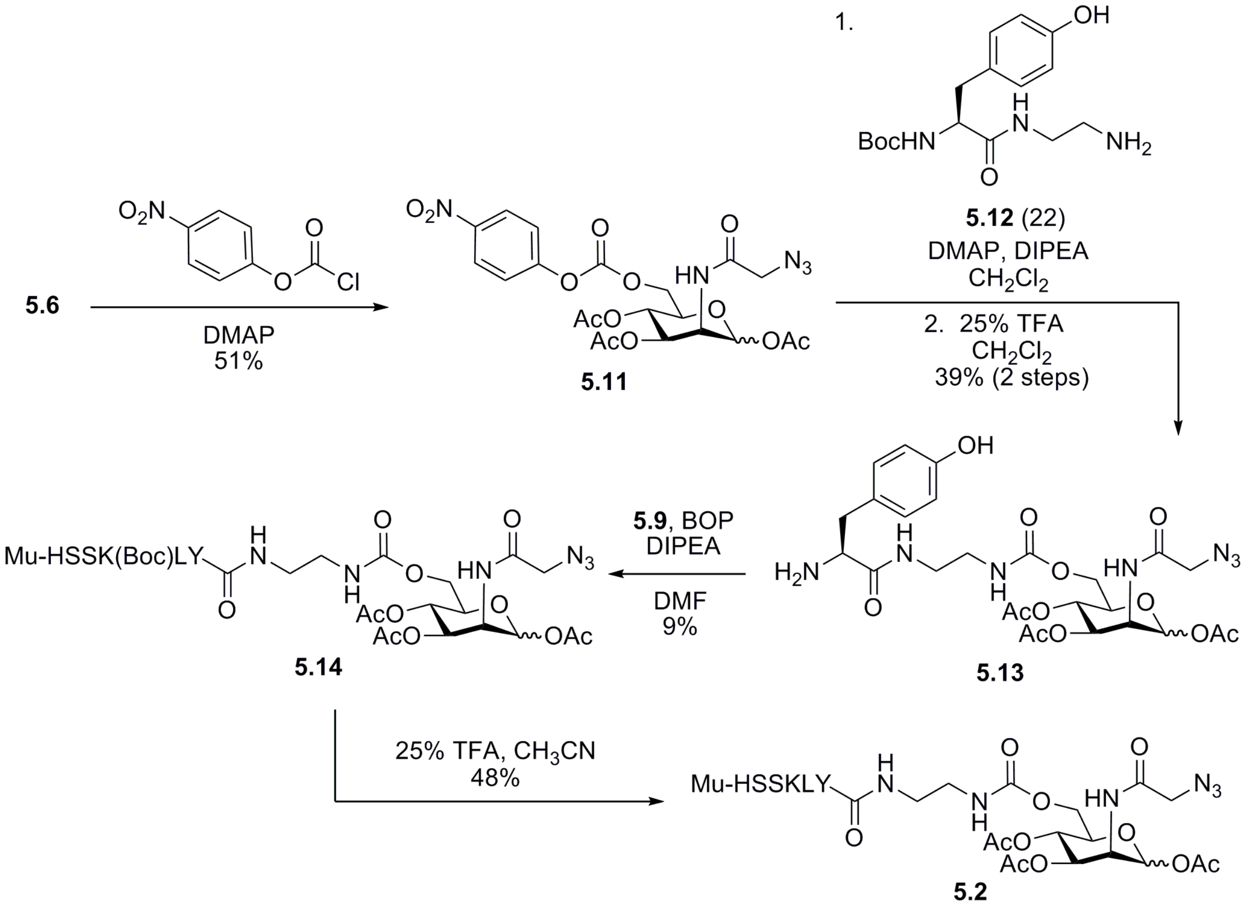

Scheme 5-2. Synthesis of **5.2**.

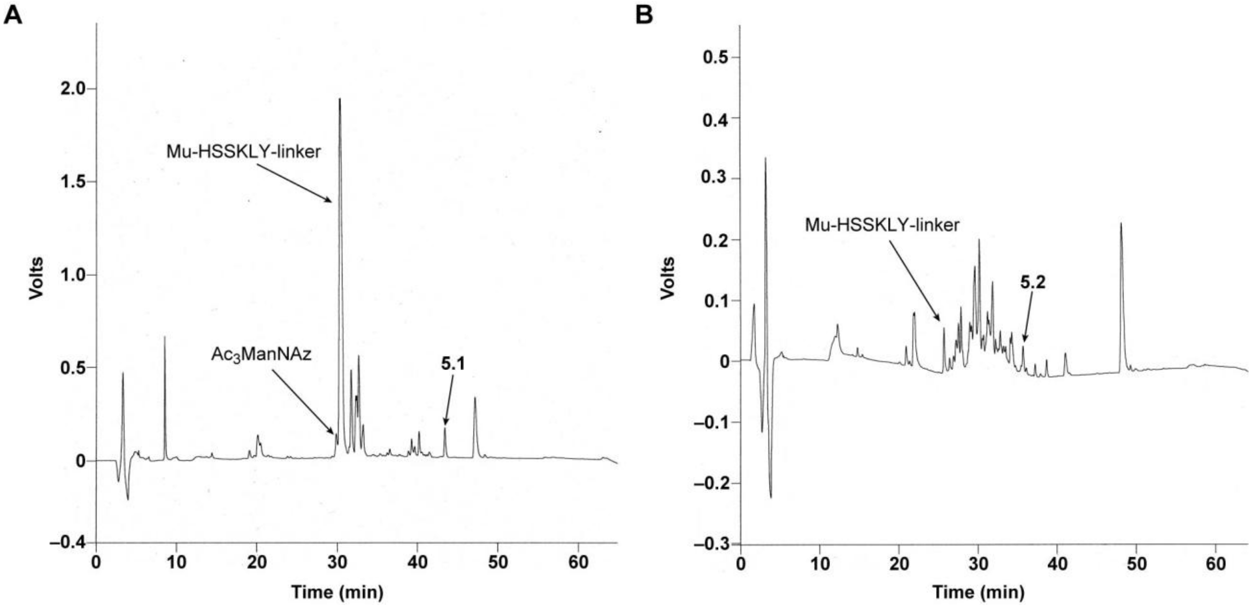

Figure 5-2. Hydrolytic stability test of **5.1** and **5.2**. Compounds **5.1** (A) and **5.2** (B) were incubated in 50 mM Tris, 0.1 M NaCl, pH 7.8, for 24 h at 37 °C. The samples were then analyzed by reversed-phase HPLC.

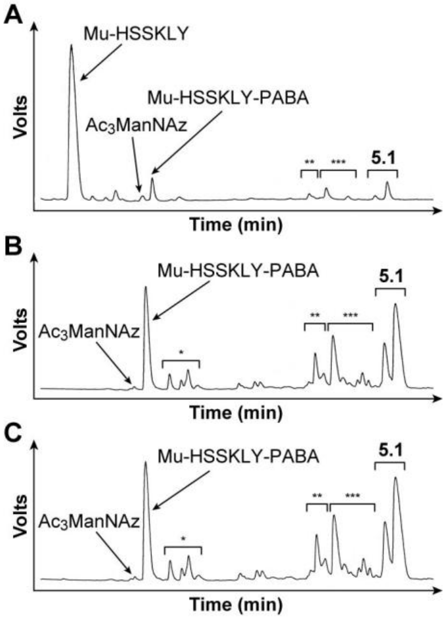

Figure 5-3. Compound **5.1** serves as a substrate for PSA *in vitro*. Shown are HPLC traces of *in vitro* enzymatic reactions of **5.1** (500 μM) in 50 mM Tris, 0.1 M NaCl, pH 7.8, for 6 h with (A) active PSA (50 μg/mL), (B) buffer only, or (C) heat-killed (HK) PSA (50 μg/mL). The identities of the various species based on mass spectrometry are indicated on the traces. *Mono-acetylated Mu-HSSKLY-PABA, **Mono-deacetylated **5.1**, and ***Isomers of **5.1**.

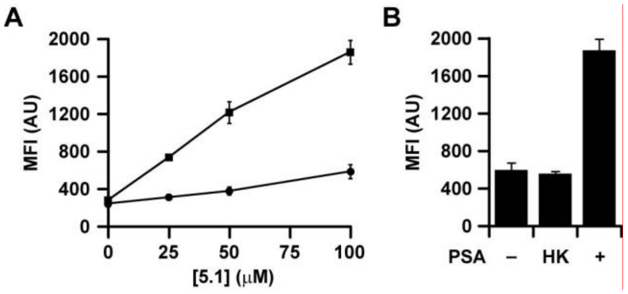

Figure 5-4. Cell-selective metabolic labeling of glycans using **5.1** and PSA. (A) Flow cytometry analysis of CHO cells treated with various concentrations of **5.1** (0-100 μM) and PSA (50 μg/mL, squares) or buffer only (circles). (B) Flow cytometry analysis of CHO cells treated with **5.1** (100 μM) and either buffer only (–), heat-killed (HK) PSA (50 μg/mL), or PSA (+), followed by DIFO-biotin (100 μM) and fluorescein isothiocyanate-conjugated avidin (FITC-avidin). Error bars represent the standard deviation from the mean of three replicate samples. MFI = mean fluorescence intensity in arbitrary units (AU).

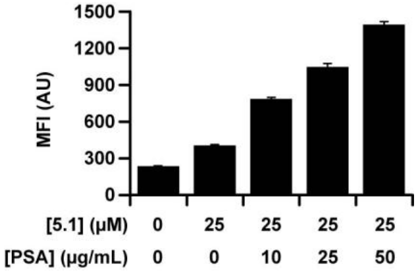

Figure 5-5. Flow cytometry analysis of CHO cells treated with **5.1** and PSA. CHO cells were incubated with or without **5.1** (25 μM) and PSA (0-50 μg/mL) for 12 h at 37 °C. The samples were then labeled with DIFO-biotin (100 μM) for 2 h at 37 °C, followed by FITC-avidin, and analyzed by flow cytometry. MFI = mean fluorescence intensity in arbitrary units (AU). Error bars represent the standard deviation of the average MFI from three replicate samples.

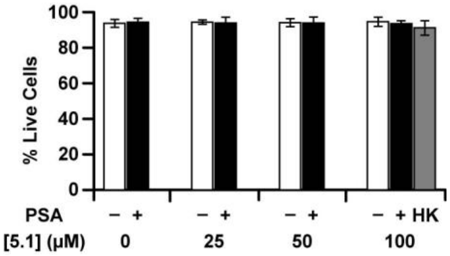

Figure 5-6. Cell viability assay. CHO cells were incubated with **5.1** (0-100 μM) and either PSA (50 μg/mL, +), no enzyme (–), or heat-killed (HK) PSA, for 12 h at 37 °C. The samples were then labeled with DIFO-biotin (100 μM) for 2 h at 37 °C, followed by FITC-avidin and annexin V-phycoerythrin, and analyzed by flow cytometry. Percent live cells represent cells that stain weakly with annexin V. Error bars represent the standard deviation of the average % live cells for three replicate samples.

*Fluorescence microscopy analysis of cells labeled with caged azidosugar **5.1** in the presence of PSA*

Finally, in order to assess whether this strategy can be extended for our long-term goal of *in vivo* imaging of specific tissues, we applied **5.1** for cell imaging by fluorescence microscopy. CHO cells were incubated with **5.1** in the presence of PSA or HK PSA for 12 h at 37 °C. The cells were then washed and labeled with DIFO-biotin, followed by quantum dot-conjugated streptavidin. We observed substantial cell-surface labeling of cells treated with **5.1** and PSA (Figure 5-7A) and minimal cell-surface fluorescence from the negative control, cells treated with **5.1** and HK PSA (Figure 5-7B), confirming that our approach can be used to selectively image cell-surface glycans.

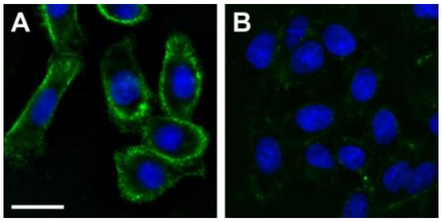

Figure 5-7. Selective imaging of cells using **5.1** in the presence of PSA. Fluorescence microscopy of CHO cells treated with **5.1** (100 μM) and (A) PSA (50 μg/mL) or (B) heat-killed (HK) PSA (50 μg/mL), followed by DIFO-biotin (100 μM) and a quantum-dot 605 streptavidin conjugate. Green = Texas Red channel; Blue = DAPI channel. Scale bar = 20 μm.

Conclusions

In conclusion, we have developed a strategy for targeted labeling of glycans on specific cells or tissues. It should be noted that the concentrations of PSA employed in our studies are physiologically relevant, i.e., they are similar to the levels of PSA secreted by both prostate cancer xenografts in mice as well as prostate tumor tissue obtained from human patients (18). In addition, many cancers, including prostate cancer, are known to express elevated levels of sialic acid compared to surrounding tissue (19, 20). Thus, we hope that our approach can be used to target sialylated tumors *in vivo* for both diagnostic and therapeutic purposes.

Materials and methods

General

All chemical reagents were of analytical grade, obtained from commercial suppliers, and used without further purification unless otherwise noted. Moisture-sensitive reactions were performed in flame-dried flasks under a N_2 atmosphere. Organic extracts were dried over Na_2SO_4, and solvents were removed with a rotary evaporator at reduced pressure (20 torr), unless otherwise noted. Flash chromatography was performed using Silicycle Siliaflash P60 40-63Å 230-400 mesh silica gel. Analytical thin layer chromatography (TLC) was performed on glass-backed Analtech Uniplate GHLF silica gel plates, and compounds were visualized by staining with ceric ammonium molybdate, 5% H_2SO_4 in ethanol, ninhydrin, and/or the absorbance of UV light (λ = 254 nm). Reversed-phase HPLC was performed using a Rainin Instruments Dynamax SD-200 system equipped with a Varian UV-Vis detector (model 345) and a Microsorb C18 analytical column (4.6 x 250 mm) at a flow rate of 1 mL/min, a semipreparative column (10 x 250 mm) at a flow rate of 4 mL/min, or a preparative column (21.4 x 250 mm) at a flow rate of 20 mL/min. HPLC samples were filtered with a Pall Life Sciences Acrodisc CR 13 mm syringe filter equipped with a 0.2 μm PTFE membrane prior to injection. Dichloromethane (CH_2Cl_2) and acetonitrile (CH_3CN) were passed through activated alumina columns under N_2 before use. Pyridine was distilled over CaH_2 under N_2. Anhydrous *N,N*-dimethylformamide (DMF), *N,N*-diisopropylethylamine (DIPEA), triethylamine (TEA), and trifluoroacetic acid (TFA) were used from commercial sources without further purification. DIFO-biotin (17), compounds **5.3** (21), **5.7** (12), and **5.12** (22) were synthesized according to previously published procedures. Boc-tyrosine was purchased from EMD Chemicals (San Diego, CA), and di-Boc-tyrosine was purchased from Advanced Chemtech (Louisville, KY). NMR spectra were acquired using a Bruker DRX-500, AV-500, AVQ-400, or AVB-400 spectrometer. ^{1}H NMR spectra were obtained at 400 or 500 MHz, and ^{13}C NMR spectra were obtained at 75 or 125 MHz and are referenced to residual solvent peaks. Low and high-resolution fast atom bombardment (FAB) and electrospray ionization (ESI) mass spectra were obtained at the UC-Berkeley Mass Spectrometry Laboratory.

Dulbecco's phosphate-buffered saline pH 7.4 (PBS) and fluorescein isothiocyanate-conjugated avidin (FITC-avidin) were purchased from Sigma Aldrich. Ham's F-12 and OptiMEM I media, Hoechst 33342 nuclear stain, and quantum dot 605-streptavidin conjugate were obtained from Invitrogen Life Technologies, Inc. Fetal bovine serum (FBS) was obtained from HyClone Laboratories. Prostate-specific antigen protease (PSA) was purchased from EMD Biosciences. The colorimetric substrate (MeO-Suc-Arg-Pro-Tyr-PNA·TFA) was purchased from MP Biomedicals. Absorbance readings were collected with a Molecular Devices SpectraMax 190 UV-Vis absorbance plate reader. Microcon Ultracel YM-10 centrifugal filter devices were obtained from Millipore. Apoptosis Detection Kit I containing annexin V-phycoerythrin and 10X Binding Buffer was obtained from BD Biosciences. Tissue culture plates were obtained from Corning, and slides mounted with 8-tissue culture wells were obtained from Nunc. Flow cytometry analysis was performed on a BD FACSCalibur flow cytometer equipped with a 488 nm argon laser and 635 nm He-Ne red diode array laser. At least 10^4 live cells were analyzed for each sample. Cell viability was ascertained by gating the samples on the basis of forward scatter (to sort by size) and side scatter (to sort by granularity). The average fluorescence intensity was calculated from three replicate samples to obtain a mean value in arbitrary units. The data points are representative of at least three separate experiments. Fluorescence microscopy was performed on a Zeiss Axiovert 200M inverted microscope equipped with a 63 × 1.4 numerical aperture Plan-Apochromat oil immersion lens was used for imaging. A 175 W Xenon lamp housed in a Sutter DG4 illuminator linked to the microscope by an optical fiber assured shuttering and illumination. Image stacks containing 20-40 sections spaced 0.5 μm apart were acquired by using a CoolSNAP HQ charged-coupled device camera (Roper Scientific). SLIDEBOOK software (Intelligent Imaging Innovations) was used to control the microscope and the camera. The image stacks were digitally deconvolved by using the nearest-neighbor algorithm of SLIDEBOOK.

Synthesis

Compound 5.4. Compound **5.3** (21) (1.20 g, 4.58 mmol) was dissolved in a 1:1 solution of pyridine and CH_2Cl_2 (46 mL). *Tert*-butyldimethylsilyl chloride (1.03 g, 6.87 mmol) and dimethylaminopyridine (30.2 mg, 0.247 mmol) were added. The reaction was stirred for 22 h. The crude product was purified by silica gel chromatography, eluting with 95:5 CH_2Cl_2:CH_3OH to yield 1.15 g (67%) of an off-white solid as a mixture of anomers (3:1 α:β). ^1H NMR of α-anomer (400 MHz, CH_3OD): δ 5.04 (d, 1H, *J* = 1.6), 4.25 (dd, 1H, *J* = 1.6, 4.6), 3.78-4.05 (m, 6H), 3.54 (app t, 1H, *J* = 9.7), 0.94 (s, 9H), 0.11 (app t, 6H, *J* = 2.5). ^{13}C NMR of α-anomer (125 MHz, CH_3OD): δ 169.0, 92.9, 72.3, 68.9, 67.2, 62.7, 53.9, 51.4, 25.0, 17.9. FAB-HRMS: Calcd. for $C_{14}H_{29}N_4O_6Si^+$ $(M+H)^+$ 377.1852, found 377.1848.

Compound 5.5. To a solution of **5.4** (9.20 g, 24.4 mmol) in pyridine (139 mL) was added acetic anhydride (69.3 mL, 0.733 mol). The reaction was stirred for 16 h and concentrated *in vacuo*. The crude product was then purified by silica gel chromatography using a gradient of 2:1 hexanes:ethyl acetate to 1:1 hexanes:ethyl acetate to afford 11.4 g (93%) of a yellow oil as a mixture of anomers (2:3 α:β). ^1H NMR of β-anomer (500 MHz, $CDCl_3$): δ 6.56 (d, 1H, *J* = 9.5), 6.03 (s, 1H), 5.26 (app t, 1H, *J* = 9.9), 5.05 (dd, 1H, *J* = 3.9, 10.0), 4.60 (d, 1H, *J* = 9.6), 4.06 (m, 2H), 3.63-3.85 (m, 3H), 2.00-2.18 (m, 9H), 0.91 (s, 9H), 0.06 (app d, 6H, *J* = 9.1). ^{13}C NMR (125 MHz, $CDCl_3$): δ 170.3, 169.10, 169.05, 168.2, 167.2, 166.6, 91.5, 90.2, 77.2, 77.0, 76.7, 75.7, 72.7, 71.9, 69.3, 64.91, 64.85, 61.1, 61.0, 52.5, 52.3, 49.8, 49.2, 25.61, 25.58, 20.82, 20.77, 20.72, 20.68, 20.6, 18.2, 18.1, -0.06, -5.58, -5.60. FAB-HRMS: Calcd. for $C_{20}H_{34}N_4O_9SiLi^+$ $(M+Li)^+$ 509.2247, found 509.2243.

Compound 5.6. Acetic acid (14 mL) was added to a solution of **5.5** (1.10 g, 2.20 mmol) in a 1:1 solution of THF and H_2O (9.6 mL). The resulting mixture was stirred for 24 h. The reaction was neutralized with sat. $NaHCO_3$, and the crude product was extracted with ethyl acetate (3 x 25 mL). The organic layers were pooled, washed with brine (1 x 75 mL), dried with Na_2SO_4, filtered, and concentrated *in vacuo*. Silica gel chromatography of the crude product, eluting with a gradient of 1:2 hexanes:ethyl acetate to 1:3 hexanes:ethyl acetate, yielded 800 mg (93%) of a white solid as a mixture of anomers (2:1 α:β). ^1H NMR of α-anomer (500 MHz, $CDCl_3$): δ 6.60 (d, 1H, *J* = 9.4), 6.06 (d, 1H, *J* = 1.8), 5.41 (dd, 1H, *J* = 4.4, 10.2), 5.16 (app t, 1H, *J* = 10.2), 4.62-4.65 (m, 1H), 4.04 (m, 2H), 3.59-3.84 (m, 3H), 2.02-2.21 (m, 9H). ^{13}C NMR (125 MHz, $CDCl_3$): δ 170.9, 170.8, 170.2, 170.1, 168.6, 168.5, 167.3, 91.5, 90.3 77.3, 77.0, 76.7, 75.5, 72.5, 72.4, 71.2, 71.1, 68.6, 65.4, 65.3, 60.6, 52.4, 52.3, 52.0, 49.8, 49.3, 20.8, 20.72, 20.68, -0.1. FAB-HRMS: Calcd. for $C_{14}H_{20}N_4O_9Li^+$ $(M+Li)^+$ 395.1396, found 395.1399.

Compound 5.8. Compounds **5.6** (466 mg, 1.20 mmol) and **5.7** (12) (963 mg, 1.75 mmol) were dried by azeotroping with toluene (3 x 10 mL). Pyridine (12 mL) was added, followed by dimethylaminopyridine (214 mg, 1.75 mmol). The resulting mixture was stirred for 18 h at 40 °C. The reaction was concentrated, and the residue was passed through a plug of silica gel using 9:1 toluene:acetone to elute. The crude product was concentrated to afford a white solid that was dissolved in CH_2Cl_2 (3 mL). TFA (1 mL) was added dropwise. The reaction was stirred for 30 min, diluted with toluene (10 mL), and concentrated *in vacuo*. The residual TFA was removed from the crude residue by azeotroping with toluene (3 x 10 mL). The crude product was then dissolved in 1:1 ddH_2O:CH_3CN and purified by reversed-phase HPLC using a C18 column (75:25 ddH_2O:CH_3CN + 0.1 % TFA to 65:35 ddH_2O:CH_3CN + 0.1% TFA over 60 min) to yield 62.2 mg (62%) of a white solid as a mixture of anomers (2:1 α:β). ^{1}H NMR of α-anomer (400 MHz, CH_3OD): δ 7.53 (d, 2H, *J* = 8.4), 7.37 (d, 2H, *J* = 8.4), 7.10 (d, 2H, *J* = 8.4), 6.75 (d, 2H, *J* = 8.4), 5.97 (d, 1H, *J* = 1.6), 5.24-5.31 (m, 2H), 5.13 (s, 2H), 4.60 (m, 1H), 4.34 (dd, 1H, *J* = 5.2, 12.0), 4.10-4.21 (m, 3H), 3.92 (d, 2H, *J* = 3.6), 3.18 (dd, 1H, *J* = 6.8, 14.0), 3.05 (dd, 1H, *J* = 7.6, 14.0), 1.96-2.16 (m, 9H). ^{13}C NMR of α-anomer (75 MHz, CH_3OD): δ 171.8, 171.7, 171.0, 170.1, 168.2, 158.4, 156.4, 139.3, 133.3, 131.8, 130.4, 126.1, 121.4, 117.0, 93.2, 71.6, 70.64, 70.60, 67.4, 67.0, 56.8, 52.5, 50.8, 38.2, 20.82, 20.80, 20.75. ESI-HRMS: Calcd. for $C_{31}H_{37}O_{13}N_6^+$ $(M+H)^+$ 701.2413, found 701.2425.

Compound 5.9. The hexapeptide Mu-HSSK(Boc)L was synthesized on Fmoc-Leu Wang resin (100-200 mesh) using standard Fmoc solid-phase peptide synthesis with N^{α}-Fmoc protected amino acids and DIC/HOBt ester activation in NMP. A five-fold excess of amino acid was used for the coupling steps, which involved gentle rotation for 1 h. Fmoc removal was achieved with 20% piperidine in NMP (1 x 30 min). The peptide was capped at the N-terminus with a five-fold excess of 4-morpholine carbonyl chloride and TEA in NMP. The peptide was cleaved for 4 h using a solution of Reagent K (23) and triisopropylsilane (81.5:5:5:5:2.5:1 TFA:thioanisole:phenol:ddH_2O:ethanedithiol:triisopropylsilane), precipitated with methyl *tert*-butyl ether, and the crude product was dried and used without further purification. The crude peptide (308 mg, 0.450 mmol) was dissolved in DMF (4.4 mL), and TEA (0.0823 mL, 0.541 mmol) was added, followed by di-*tert*-butyldicarbonate (118 mg, 0.541 mmol). The resulting mixture was stirred for 29 h and concentrated *in vacuo*. The crude product was purified by reversed-phase HPLC using a C18 column (80:20 ddH_2O:CH_3CN + 0.1 % TFA to 50:50 ddH_2O:CH_3CN + 0.1% TFA over 40 min) to yield 351 mg (quant.) of a white solid. ESI-HRMS: Calcd. for $C_{34}H_{58}O_{12}N_9^+$ $(M+H)^+$ 784.4199, found 784.4200.

Compound 5.10. Compounds **5.8** (20.5 mg, 0.0293 mmol) and **5.9** (45.9 mg, 0.0586 mmol) were dissolved in DMF (0.29 mL). (Benzotriazol-1-yloxy)tris(dimethylamino)phosphonium hexafluorophosphate (BOP, 28.5 mg, 0.0645 mmol) was added, followed by DIPEA (0.013 mL, 0.0733 mmol), dropwise. The reaction was stirred for 1 h, after which it was concentrated, and the resulting residue was purified by reversed-phase HPLC using a C18 column (65:35 ddH_2O:CH_3CN + 0.1 % TFA to 55:45 ddH_2O:CH_3CN + 0.1% TFA over 60 min) to yield 7.8 mg (18%) of a white solid. ESI-HRMS: Calcd. for $C_{65}H_{92}O_{24}N_{15}^+$ $(M+H)^+$ 1466.6434, found 1466.6481.

Compound 5.1. TFA (0.25 mL) was added dropwise to a solution of **5.10** (10.7 mg, 0.0730 mmol) in CH_3CN (0.75 mL). The resulting mixture was stirred for 2 h, and the reaction was then diluted with toluene (10 mL). The reaction mixture was concentrated *in vacuo,* and residual TFA was removed by azeotroping with toluene (3 x 10 mL). The crude product was purified by reversed-phase HPLC using a C18 column (75:25 ddH$_2$O:CH$_3$CN + 0.1 % TFA to 65:35 ddH$_2$O:CH$_3$CN + 0.1% TFA over 50 min) to yield 7.7 mg (76%) of a white solid. ESI-HRMS: Calcd. for $C_{60}H_{85}O_{22}N_{15}^{2+}$ $[(M + 2H)]^{2+}$ 683.7991, found 683.8005.

Compound 5.11. To a solution of **5.6** (728 mg, 1.87 mmol) in CH$_2$Cl$_2$ (15 mL) was added dimethylaminopyridine (251 mg, 2.06 mmol) and 4-nitrophenylchloroformate (754 mg, 3.75 mmol). After the resulting mixture was stirred overnight at rt, an additional aliquot of 4-nitrophenylchloroformate (75 mg, 0.37 mmol) and DMAP (46 mg, 0.37 mmol) were added. The reaction was stirred for an additional 7 h, after which it was concentrated *in vacuo*. The crude residue was purified by silica gel chromatography with a gradient of 3:1 hexanes:ethyl acetate to 1:1 hexanes:ethyl acetate to provide 523 mg (51%) of a white solid as a mixture of anomers (1:2 α:β). ^{1}H NMR of β-anomer (400 MHz, CDCl$_3$): δ 8.30 (d, 2H, *J* = 8.8), 7.41 (d, 2H, *J* = 9.2), 6.63 (d, 1H, *J* = 9.2), 6.10 (d, 1H, *J* = 1.6), 5.38 (d, 1H, *J* = 4.0), 5.31 (app t, 1H, *J* = 10.0), 4.66 (ddd, 1H, *J* = 2.0, 4.0, 9.6), 4.32-4.49 (m, 2H), 4.10 (m, 2H), 2.03-2.27 (m, 9H). ^{13}C NMR (125 MHz, CDCl$_3$): δ 170.0, 169.8, 168.1, 167.4, 166.9, 155.3, 152.3, 145.5, 125.3, 121.9, 91.2, 90.2, 72.9, 71.2, 70.0, 68.6, 66.2, 66.0, 65.0, 64.8, 52.5, 52.3, 49.2, 20.8, 20.7, 20.6, -0.1. ESI-HRMS: Calcd. for $C_{21}H_{23}O_{13}N_5Na^+$ $(M+Na)^+$ 576.1185, found 576.1176.

Compound 5.13. To a solution of **5.11** (523 mg, 0.945 mmol) and **5.12** (22) (365 mg, 1.13 mmol) in CH$_2$Cl$_2$ (9 mL) was added DIPEA (0.329 mL, 1.89 mmol), followed by dimethylaminopyridine (139 mg, 1.13 mmol). The resulting mixture was stirred for 5 h, and the reaction was concentrated *in vacuo*. The crude residue was run through a plug of silica gel using 3:1 toluene:acetone to elute. The crude product was concentrated and then redissolved in CH$_2$Cl$_2$ (12 mL), and TFA (4 mL) was added. The reaction was stirred for 1 h, diluted in toluene (40 mL), and concentrated. The resulting residue was azeotroped with toluene (3 x 40 mL) to remove any remaining TFA and purified by silica gel chromatography using 98:2 CH$_2$Cl$_2$:CH$_3$OH to 90:10 CH$_2$Cl$_2$:CH$_3$OH as the eluant to yield 0.110 g (39%) of a white solid as a mixture of anomers (4:1 α:β). ^{1}H NMR of α-anomer (500 MHz, CDCl$_3$): δ 7.04 (d, 2H, *J* = 8.0), 6.77 (d, 2H, *J* = 8.0), 5.95 (s, 1H), 5.27 (d, 1H, *J* = 4.0), 5.23 (t, 1H, *J* = 10.0), 4.23 (dd, 1H, *J* = 5.0, 12.0), 4.01-4.08 (m, 1H), 3.85-4.00 (m, 4H), 3.26 (m, 1H), 3.07-3.23 (m, 3H), 2.95-3.06 (m, 2H), 1.96-2.18 (m, 9H). ^{13}C NMR (125 MHz, CDCl$_3$): δ 171.3, 171.1, 170.0, 169.9, 169.8, 169.5, 163.0, 162.7, 157.8, 157.4, 131.1, 125.6, 116.5, 92.6, 91.4, 74.3, 72.0, 71.5, 69.9, 66.4, 63.3, 55.6, 52.3, 52.1, 50.3, 50.2, 50.0, 40.6, 40.0, 37.3, 21.0, 20.93, 20.90, 20.88. ESI-HRMS: Calcd. for $C_{26}H_{36}O_{12}N_7^+$ $(M+H)^+$ 638.2416, found 638.2431.

Compound 5.14. Compounds **5.13** (9.18 mg, 0.0144 mmol) and **5.9** (13.0 mg, 0.0166 mmol) were dissolved in DMF (0.2 mL). BOP (7.96 mg, 0.0180 mmol) was added, followed by DIPEA (0.013 mL, 0.075 mmol), dropwise. The reaction was stirred for 3 h, after which an additional aliquot of **5.9** (6.8 mg, 0.0087 mmol), DIPEA (0.013 mL, 0.075 mmol), and BOP (5.5 mg, 0.012 mmol) were added. The resulting mixture was stirred for an additional 3 h, after which a third portion of **5.9** (13.5 mg, 0.0172 mmol), DIPEA (0.013 mL, 0.075 mmol), and BOP (8.8 mg, 0.020 mmol) were added. The reaction was stirred overnight and concentrated. The resulting crude product was purified by reversed-phase HPLC using a C18 column (70:30 ddH$_2$O:CH$_3$CN

+ 0.1 % TFA to 60:40 ddH_2O:CH_3CN + 0.1% TFA over 60 min) to yield 1.8 mg (9%) of a white solid. ESI-HRMS: Calcd. for $C_{60}H_{91}O_{23}N_{16}^+$ $(M+H)^+$ 1403.6437, found 1403.6457.

Compound 5.2. To a solution of **5.14** (12.9 mg, 0.00919 mmol) in CH_3CN (3 mL) was added TFA (1 mL). The reaction was stirred for 1 h, diluted in toluene (10 mL), and concentrated. The resulting residue was azeotroped with toluene (3 x 10 mL) to remove residual TFA and purified by reversed-phase HPLC using a C18 column (90:10 ddH_2O:CH_3CN + 0.1 % TFA to 50:50 ddH_2O:CH_3CN + 0.1% TFA over 60 min) to yield 5.78 mg (48%) of a white solid. ESI-HRMS: Calcd. for $C_{55}H_{83}O_{21}N_{16}^+$ $(M+H)^+$ 1303.5913, found 1303.5942.

In vitro *stability studies*

Compounds **5.1** and **5.2** (500 μM) were dissolved in 50 mM Tris, 0.1 M NaCl, pH 7.8, and incubated for 24 h at 37 °C. The samples were then analyzed by reversed-phase HPLC using a C18 analytical column (100:0 ddH_2O:CH_3CN + 0.1 % TFA to 60:40 ddH_2O:CH_3CN + 0.1% TFA over 60 min), monitoring at 210 nm, and by mass spectrometry.

PSA activity assay

Activity of PSA and heat-killed (HK) PSA (50 μg/mL) were verified according to a previously established protocol (24) using a colorimetric substrate (MeO-Suc-Arg-Pro-Tyr-PNA·TFA, 500 μM) in 50 mM Tris, 0.1 M NaCl, pH 7.8. The enzymatic reactions were incubated at 37 °C and monitored at 405 nm for release of *p*-nitroanilide every 10 min for 15 h. Buffer only and buffer with substrate were used as negative controls.

In vitro *enzymatic reactions*

Compound **5.1** (500 μM) was incubated with PSA (50 μg/mL), no enzyme, or heat-killed (HK) PSA (50 μg/mL) in 50 mM Tris, 0.1 M NaCl, pH 7.8, for 6 h at 37 °C. The samples were filtered with Microcon Ultracel YM-10 filter devices (10,000 MWCO) by centrifugation (10,621 x g for 20 min) to remove the protein. The cellulose membrane was rinsed (1 x 50 μL ddH_2O), and the sample was centrifuged again (10,621 x g for 10 min). The wash step was repeated twice. The filtrates were then analyzed by reversed-phase HPLC using a C18 analytical column (100:0 ddH_2O:CH_3CN + 0.1 % TFA to 60:40 ddH_2O:CH_3CN + 0.1% TFA over 60 min), monitoring at 210 nm, and by mass spectrometry.

Cell culture

Chinese hamster ovary (CHO) cells were cultured in Ham's F-12 media (GIBCO) supplemented with 10% FBS, 100 units/mL penicillin and 100 μg/mL streptomycin. The cells were maintained at 37 °C and 5% CO_2 in a water-saturated incubator and counted using a hemocytometer. Cell densities were maintained between 1 x 10^5 and 2 x 10^6 cells per mL.

Cell-selective labeling of glycans and cell viability assay

CHO cells were seeded at a density of 167,000 cells per mL in 12-well tissue culture plates containing 1 mL media. After 2 d, the media was aspirated, and the cells were washed with OptiMEM I (3 x 1 mL). The cells were then treated with OptiMEM I (0.4 mL) containing **5.1** (0-100 μM) and either PSA (50 μg/mL), no enzyme, or heat-killed (HK) PSA (50 μg/mL). The cells were incubated for 12 h at 37 °C. Following incubation, the media was removed, and the cells were washed with PBS (3 x 1 mL). The cells were lifted by incubation with 1 mM EDTA (0.65 mL) for 20 min. The cells were then transferred to a 96-well V-bottom plate and pelleted by centrifugation (2536 x g for 3 min). The medium was decanted, and the cells were washed once by resuspension in 0.2 mL of PBS + 1% FBS (FACS buffer), centrifugation (2536 x g for 3 min), and removal of FACS buffer. The cells were then resuspended with DIFO-biotin (17) (100 μM from a 1 mM stock in 12% DMF/PBS) in FACS buffer (0.1 mL) and incubated for 2 h at 37 °C. After the labeling reaction, the cells were washed with FACS buffer (3 x 0.2 mL) and resuspended in 0.1 mL of FACS buffer containing FITC-avidin (1:200 dilution from 1 mg/mL stock). The cells were incubated for 15 min on ice in the dark. The cells were washed once with FACS buffer (0.2 mL), stained with FITC-avidin for a second time, and washed with FACS buffer (1 x 0.2 mL) and then PBS (2 x 0.2 mL). After the second labeling, the cells were resuspended in 1X annexin binding buffer (prepared according to the manufacturer's protocol) containing annexin V-phycoerythrin (0.1 mL) and incubated for 15 min at rt in the dark. Additional 1X binding buffer (0.3 mL) was added, and the samples were analyzed by flow cytometry.

For the experiment shown in Figure 5-5, the analysis was performed as described above with the following modifications: CHO cells were seeded as before but treated with or without **5.1** (25 μM) and various concentrations of PSA (0-50 μg/mL) in OptiMEM I (0.4 mL) for 12 h at 37 °C. The cells were washed and labeled with DIFO-biotin, followed by staining with FITC-avidin as before. Following the second FITC-avidin labeling, the cells were washed with FACS buffer (3 x 0.2 mL) and resuspended in FACS buffer (0.4 mL) for analysis by flow cytometry.

Imaging of cells by fluorescence microscopy

Cells were seeded at a density of 1 x 10^5 cells per mL on slides mounted with eight tissue culture wells in 0.4 mL of media. After 2 d, the cells were washed with OptiMEM I (3 x 0.5 mL) and then treated with **5.1** (100 μM) and either PSA or heat-killed PSA (50 μg/mL) in OptiMEM I (0.2 mL). The cells were incubated for 12 h at 37 °C. The cells were then washed with media (3 x 0.5 mL) and incubated with DIFO-biotin (100 μM) in media (0.125 mL) for 2 h at 37 °C. The cells were washed with FACS buffer (3 x 0.5 mL) and then labeled with a quantum dot 605-streptavidin conjugate (10 nM from 1 μM stock in borate buffer, pH 8.3) in FACS buffer (0.1 mL) for 15 min at rt. The cells were washed with FACS buffer (3 x 0.5 mL) and stained with Hoechst 33342 (0.1 mL of a 1:1000 dilution from a 1 mg/mL DMSO stock) for 2 min in the dark. The cells were washed twice with media (0.5 mL), resuspended in media (0.2 mL), and imaged. The images shown are maximum intensity z-projections of three z-planes, each separated by 0.5 μm, acquired using a 63X objective.

References

1. Haltiwanger RS, Lowe JB (2004) Role of glycosylation in development. *Annu Rev Biochem* 73:491-537.

2. Rosen SD (2004) Ligands for L-selectin: Homing, inflammation, and beyond. *Annu Rev Immunol* 22:129-156.

3. Fuster MM, Esko JD (2005) The sweet and sour of cancer: Glycans as novel therapeutic targets. *Nat Rev Cancer* 5:526-542.

4. Sletten EM, Bertozzi CR (2009) Bioorthogonal chemistry: Fishing for selectivity in a sea of functionality. *Angew Chem Int Ed Engl* 48:6974-6998.

5. Laughlin ST, Bertozzi CR (2009) In vivo imaging of Caenorhabditis elegans glycans. *ACS Chem Biol* 4:1068-1072.

6. Laughlin ST, Baskin JM, Amacher SL, Bertozzi CR (2008) In vivo imaging of membrane-associated glycans in developing zebrafish. *Science* 320:664-667.

7. Chang PV, *et al.* (2010) Copper-free click chemistry in living animals. *Proc Natl Acad Sci USA* in press.

8. Prescher JA, Dube DH, Bertozzi CR (2004) Chemical remodelling of cell surfaces in living animals. *Nature* 430:873-877.

9. Williams SA, Singh P, Isaacs JT, Denmeade SR (2007) Does PSA play a role as a promoting agent during the initiation and/or progression of prostate cancer? *Prostate* 67:312-329.

10. Denmeade SR, *et al.* (1998) Enzymatic activation of a doxorubicin-peptide prodrug by prostate-specific antigen. *Cancer Res* 58:2537-2540.

11. Khan SR, Denmeade SR (2000) In vivo activity of a PSA-activated doxorubicin prodrug against PSA-producing human prostate cancer xenografts. *Prostate* 45:80-83.

12. Jones GB, *et al.* (2006) An image contrast agent selectively activated by prostate specific antigen. *Bioorg Med Chem* 14:418-425.

13. Denmeade SR, *et al.* (1997) Specific and efficient peptide substrates for assaying the proteolytic activity of prostate-specific antigen. *Cancer Res* 57:4924-4930.

14. de Groot FM, Damen EW, Scheeren HW (2001) Anticancer prodrugs for application in monotherapy: Targeting hypoxia, tumor-associated enzymes, and receptors. *Curr Med Chem* 8:1093-1122.

15. Carl PL, Chakravarty PK, Katzenellenbogen JA (1981) A novel connector linkage applicable in prodrug design. *J Med Chem* 24:479-480.

16. Saari WS, Schwering JE, Lyle PA, Smith SJ, Engelhardt EL (1990) Cyclization-activated prodrugs. Basic carbamates of 4-hydroxyanisole. *J Med Chem* 33:97-101.

17. Baskin JM, *et al.* (2007) Copper-free click chemistry for dynamic in vivo imaging. *Proc Natl Acad Sci USA* 104:16793-16797.

18. Denmeade SR, Sokoll LJ, Chan DW, Khan SR, Isaacs JT (2001) Concentration of enzymatically active prostate-specific antigen (PSA) in the extracellular fluid of primary human prostate cancers and human prostate cancer xenograft models. *Prostate* 48:1-6.

19. Zhang S, *et al.* (1997) Selection of tumor antigens as targets for immune attack using immunohistochemistry: I. Focus on gangliosides. *Int J Cancer* 73:42-49.

20. Zhang S, *et al.* (1997) Selection of tumor antigens as targets for immune attack using immunohistochemistry: II. Blood group-related antigens. *Int J Cancer* 73:50-56.

21. Yu H, Yu H, Karpel R, Chen X (2004) Chemoenzymatic synthesis of CMP-sialic acid derivatives by a one-pot two-enzyme system: Comparison of substrate flexibility of three microbial CMP-sialic acid synthetases. *Bioorg Med Chem* 12:6427-6435.

22. Mishchenko EL, *et al.* (2000) Study of the chemical structures of the photo-cross-linking products between Tyr and the 5-azido-2-nitrobenzoyl residue. *J Photochem Photobiol B* 54:16-25.

23. King DS, Fields CG, Fields GB (1990) A cleavage method which minimizes side reactions following Fmoc solid phase peptide synthesis. *Int J Pept Protein Res* 36:255-266.

24. Kurkela R, Herrala A, Henttu P, Nai H, Vihko P (1995) Expression of active, secreted human prostate-specific antigen by recombinant baculovirus-infected insect cells on a pilot-scale. *Nat Biotechnol* 13:1230-1234.

Appendix

^{1}H and ^{13}C NMR spectra

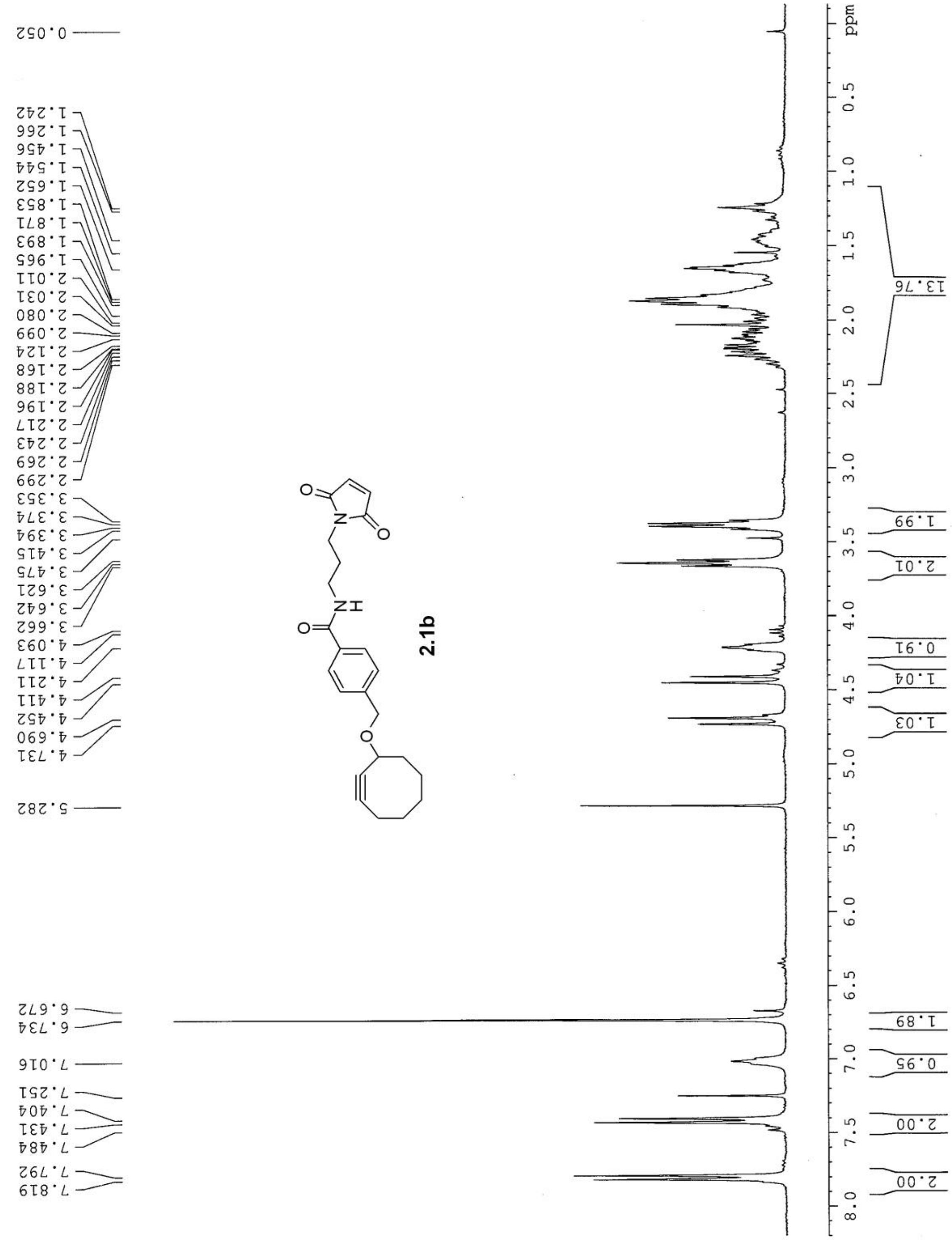

0.052
1.242
1.266
1.456
1.544
1.652
1.853
1.871
1.893
1.965
2.011
2.031
2.080
2.099
2.124
2.168
2.188
2.196
2.217
2.243
2.269
2.299
3.353
3.374
3.394
3.415
3.475
3.621
3.642
3.662
4.093
4.117
4.211
4.411
4.452
4.690
4.731
5.282
6.672
6.734
7.016
7.251
7.404
7.431
7.484
7.792
7.819
13.76
1.99
2.01
0.91
1.04
1.03
1.89
0.95
2.00
2.00
ppm
0.5
1.0
1.5
2.0
2.5
3.0
3.5
4.0
4.5
5.0
5.5
6.0
6.5
7.0
7.5
8.0
O
N
O
H
N
O
O

2.1b

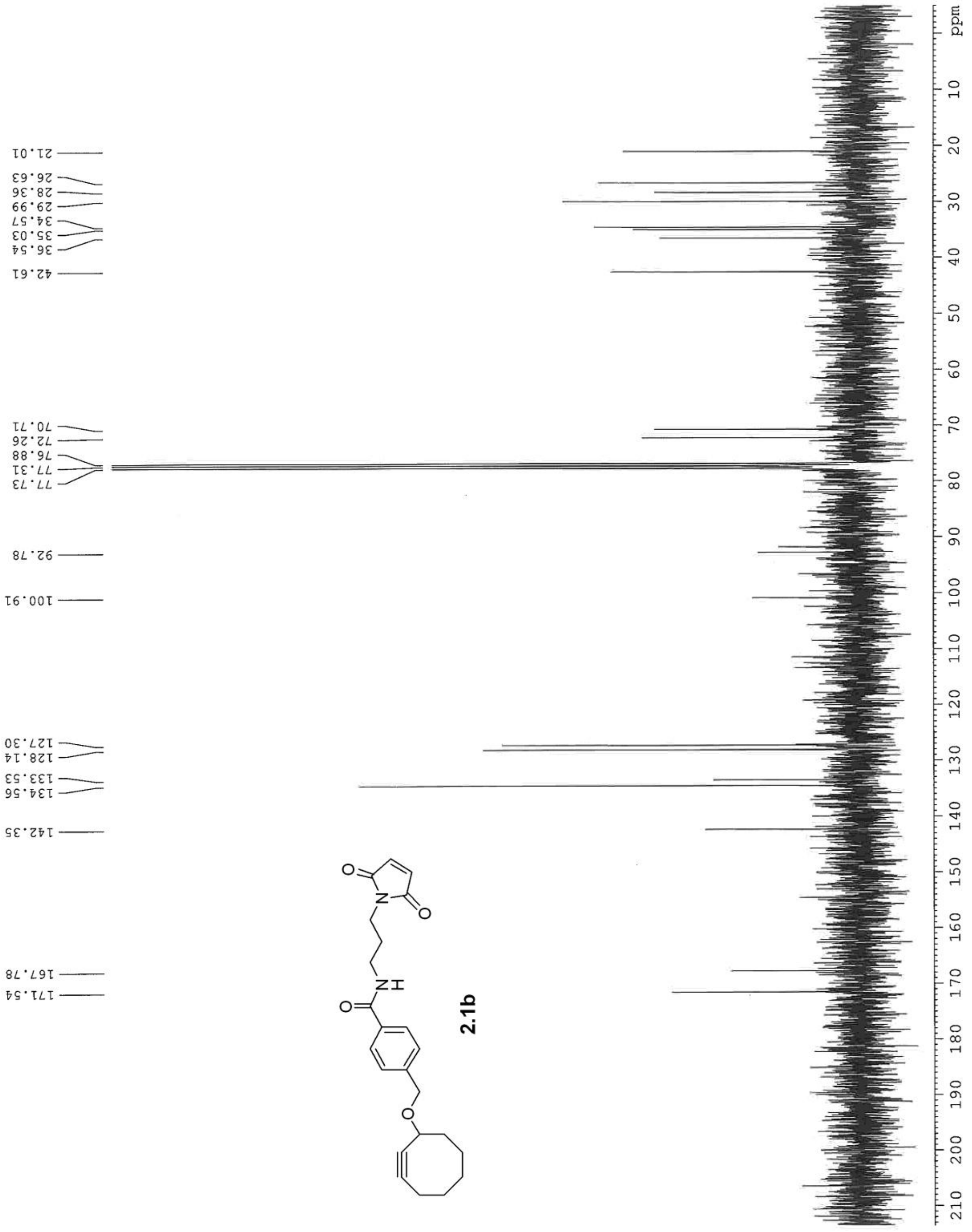
21.01
26.63
28.36
29.99
34.57
35.03
36.54
42.61
70.71
72.26
76.88
77.31
77.73
92.78
100.91
127.30
128.14
133.53
134.56
142.35
167.78
171.54
ppm
10
20
30
40
50
60
70
80
90
100
110
120
130
140
150
160
170
180
190
200
210
O
N
O
N
H
O
O

2.1b

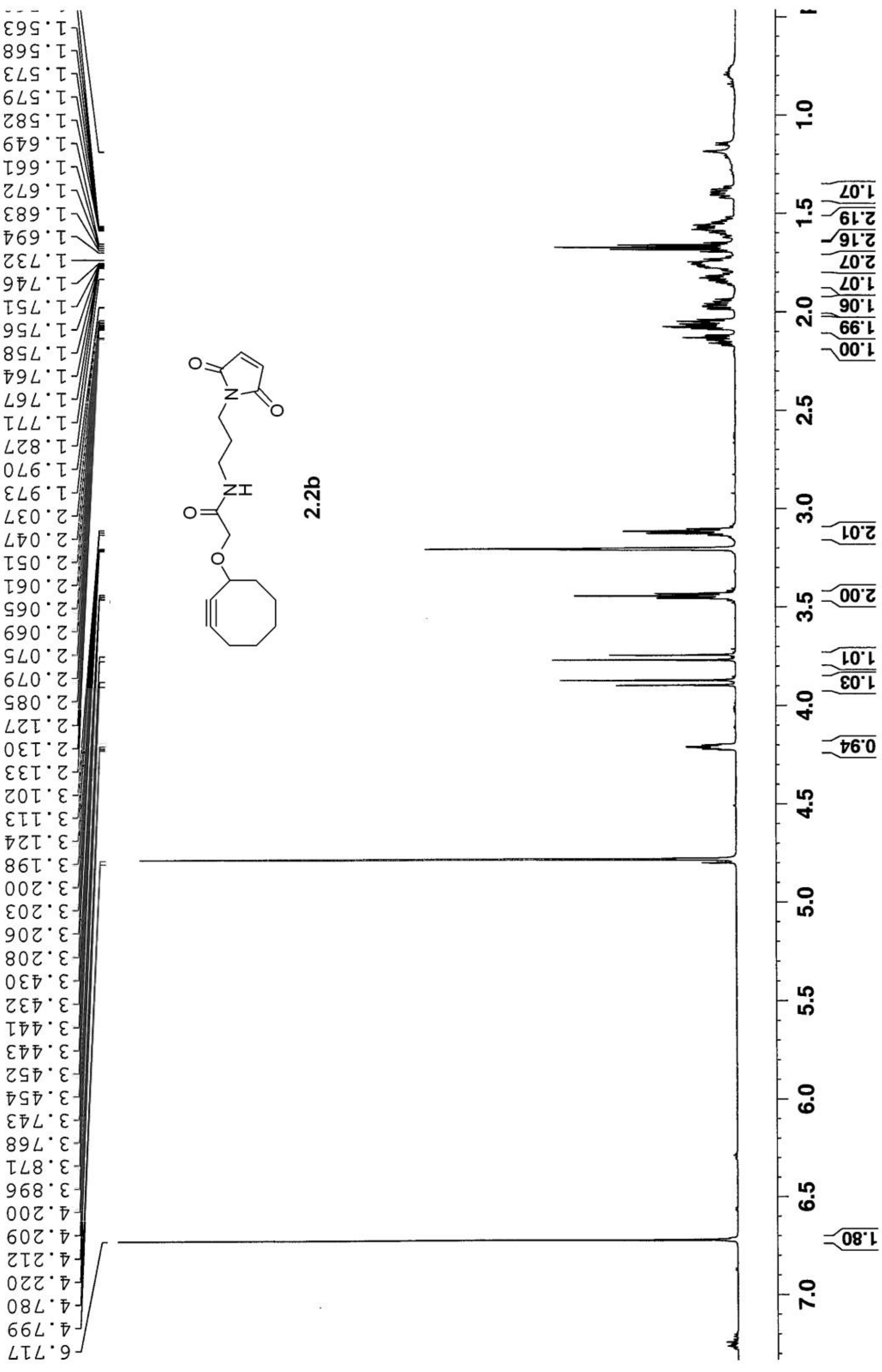
1.563
1.568
1.573
1.579
1.582
1.649
1.661
1.672
1.683
1.694
1.732
1.746
1.751
1.756
1.758
1.764
1.767
1.771
1.827
1.970
1.973
2.037
2.047
2.051
2.061
2.065
2.069
2.075
2.079
2.085
2.127
2.130
2.133
3.102
3.113
3.124
3.198
3.200
3.203
3.206
3.208
3.430
3.432
3.441
3.443
3.452
3.454
3.743
3.768
3.871
3.896
4.200
4.209
4.212
4.220
4.780
4.799
6.717
O
N
H
O
O
O
1.0
1.5
2.0
2.5
3.0
3.5
4.0
4.5
5.0
5.5
6.0
6.5
7.0
1.07
2.19
2.16
2.07
1.07
1.06
1.99
1.00
2.01
2.00
1.01
1.03
0.94
1.80

2.2b

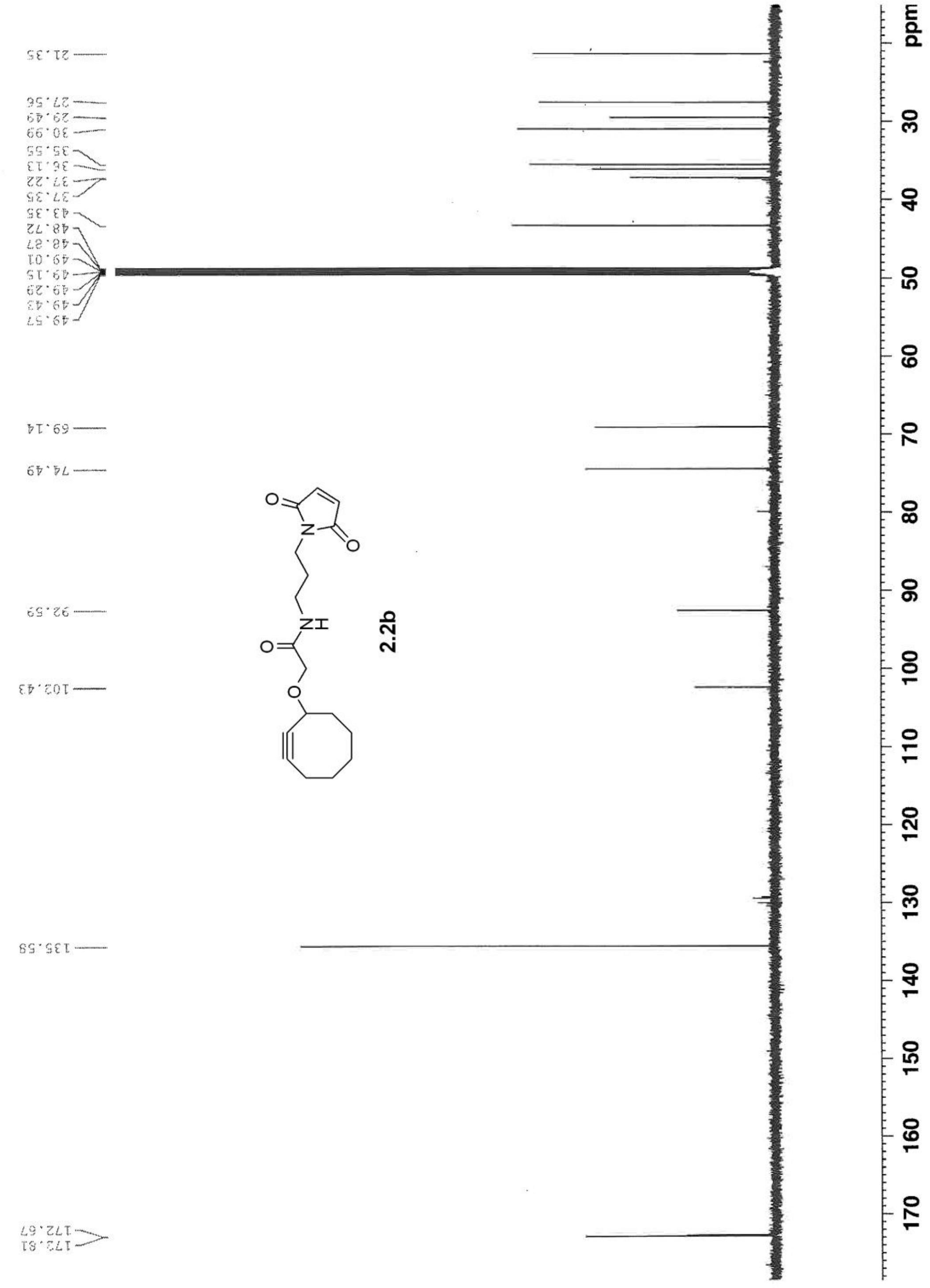
2.2b

21.35
27.56
29.49
30.99
35.55
36.13
37.22
37.35
43.35
48.72
48.87
49.01
49.15
49.29
49.43
49.57
69.14
74.49
92.59
103.43
135.58
172.67
172.81
ppm
30
40
50
60
70
80
90
100
110
120
130
140
150
160
170
O
N
O
H
N
O
O

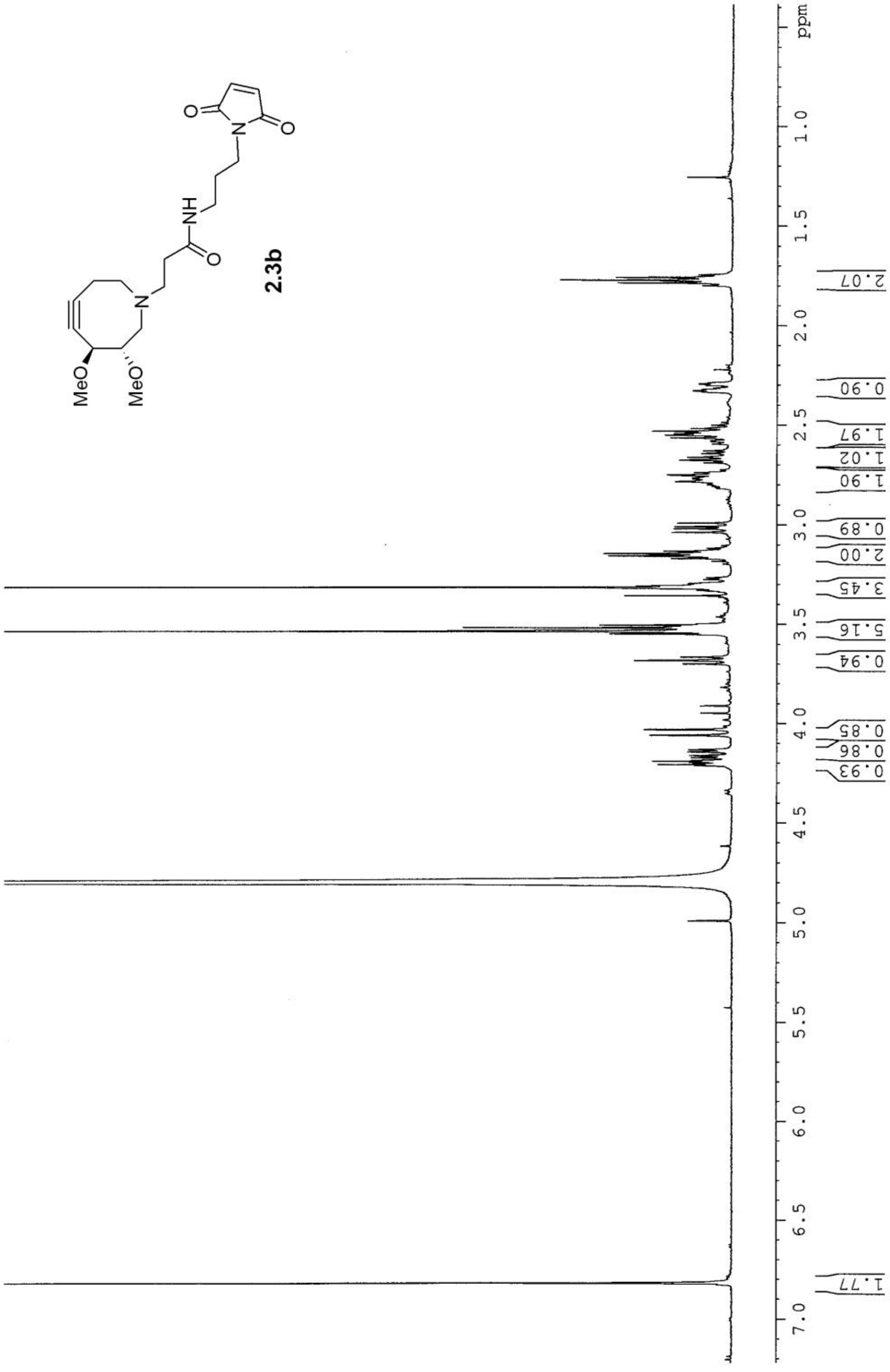
2.3b
MeO
MeO
N
O
NH
N
O
O
ppm
1.0
1.5
2.0
2.5
3.0
3.5
4.0
4.5
5.0
5.5
6.0
6.5
7.0
2.07
0.90
1.97
1.02
1.90
0.89
2.00
3.45
5.16
0.94
0.85
0.86
0.93
1.77

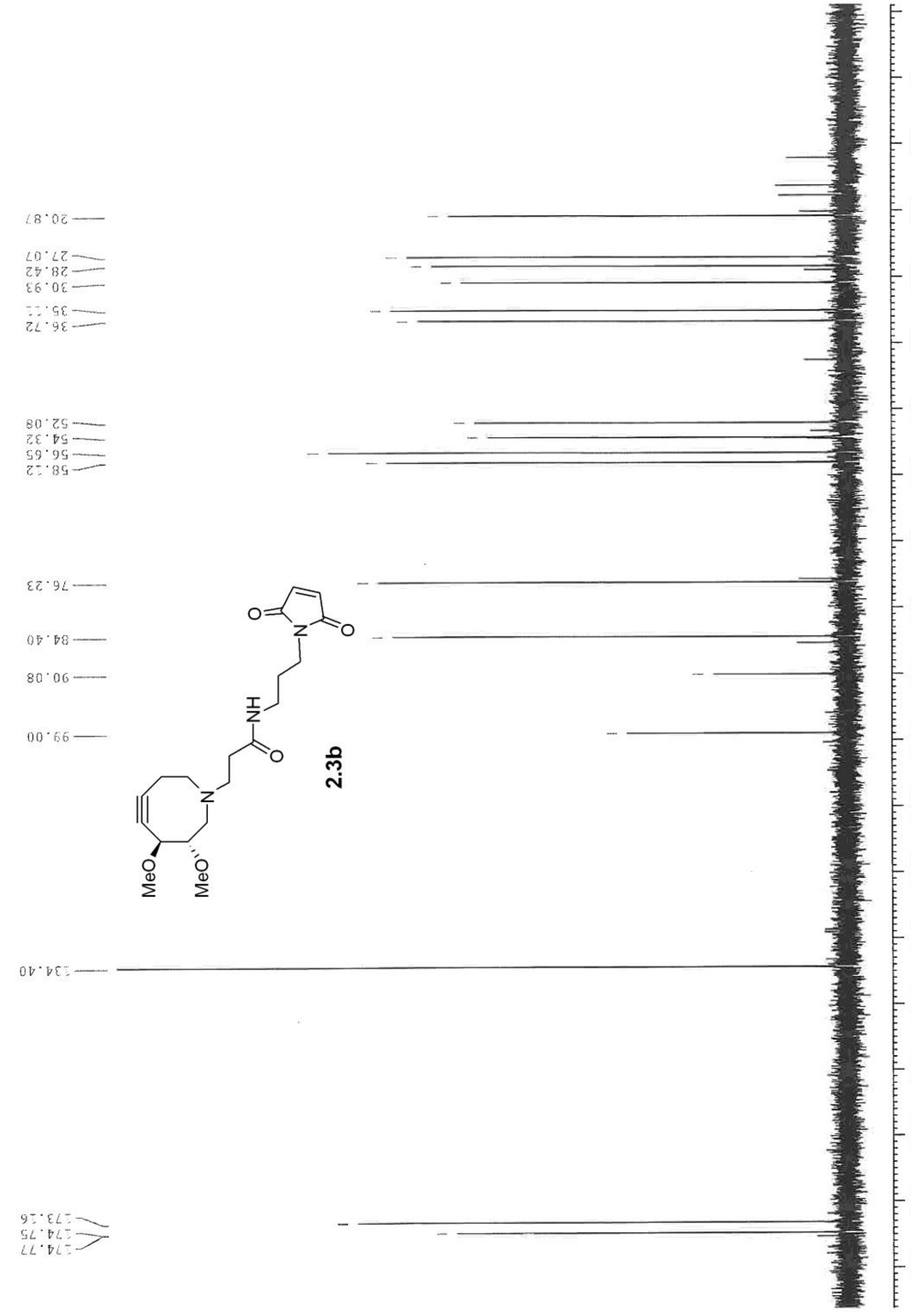
2.3b

20.87
27.07
28.42
30.93
35.11
36.72
52.08
54.32
56.65
58.12
76.23
84.40
90.08
99.00
134.40
173.16
174.75
174.77
MeO
MeO
N
NH
O
N
O
O
0
10
20
30
40
50
60
70
80
90
100
110
120
130
140
150
160
170
180

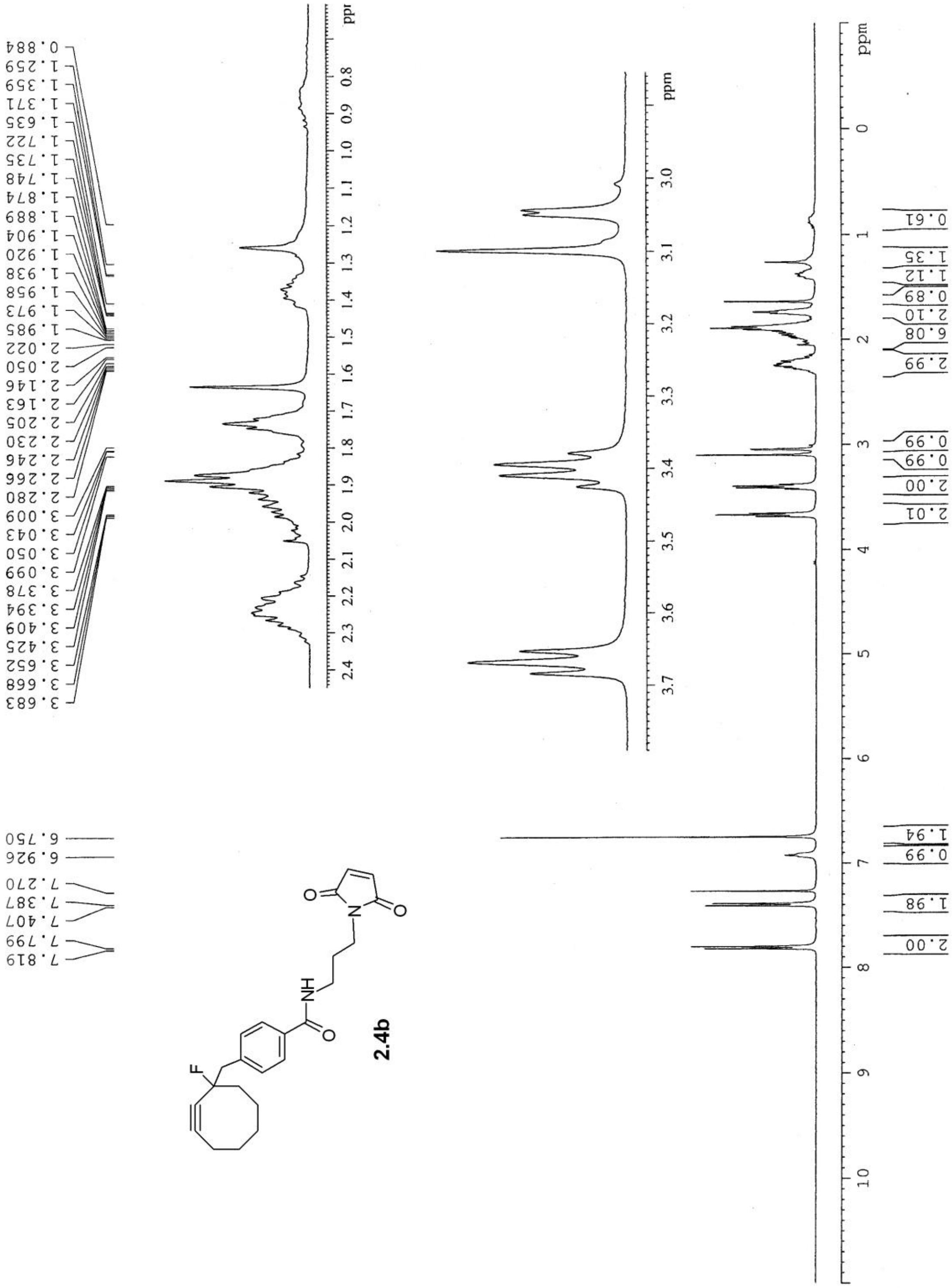
0.884
1.259
1.359
1.371
1.635
1.722
1.735
1.748
1.874
1.889
1.904
1.920
1.938
1.958
1.973
1.985
2.022
2.050
2.146
2.163
2.205
2.230
2.246
2.266
2.280
3.009
3.043
3.050
3.099
3.378
3.394
3.409
3.425
3.652
3.668
3.683
6.750
6.926
7.270
7.387
7.407
7.799
7.819
0.61
1.35
1.12
0.89
2.10
6.08
2.99
0.99
0.99
2.00
2.01
1.94
0.99
1.98
2.00
ppm
F
NH
N
O

2.4b

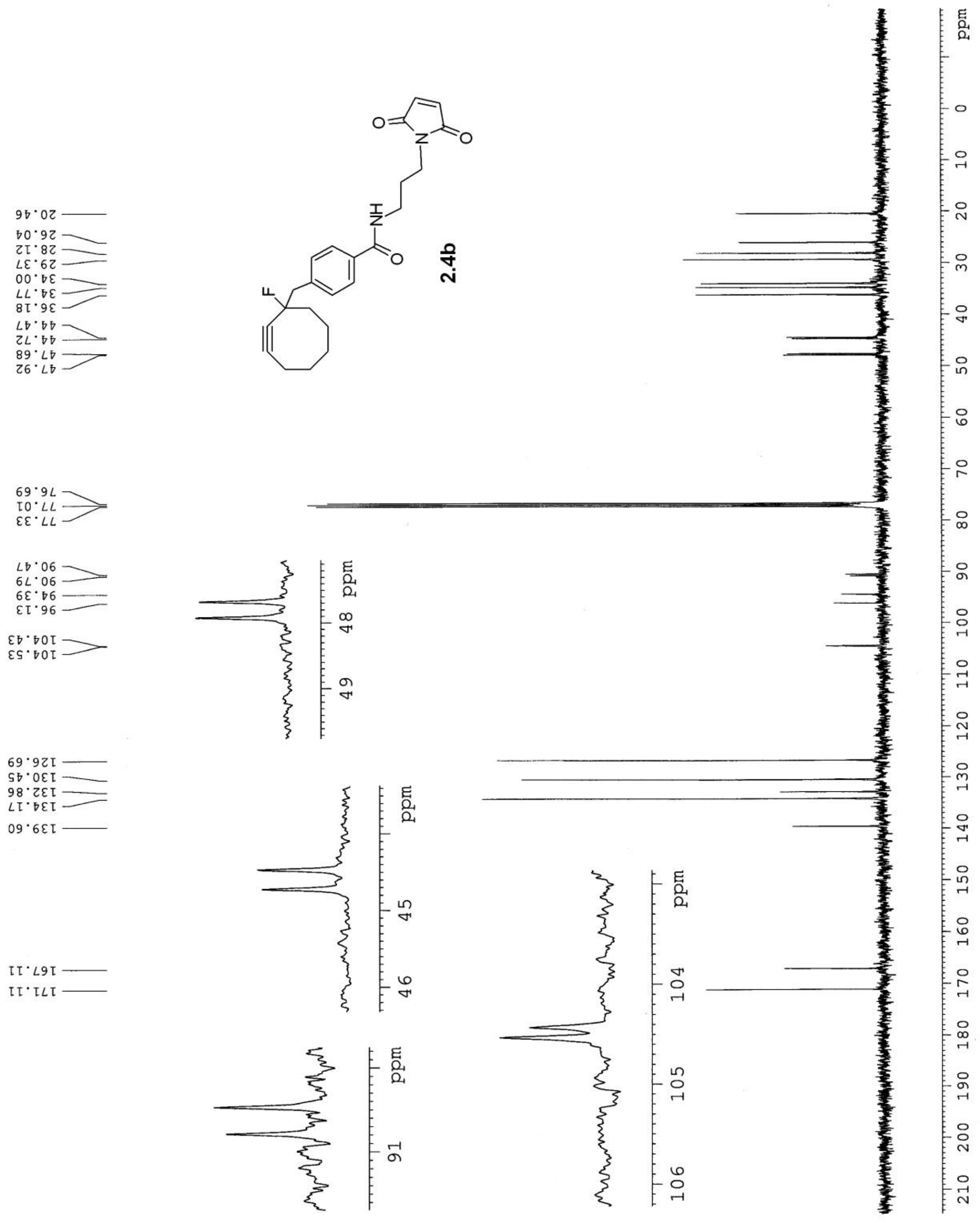

20.46
26.04
28.12
29.37
34.00
34.77
36.18
44.47
44.72
47.68
47.92
76.69
77.01
77.33
90.47
90.79
94.39
96.13
104.43
104.53
126.69
130.45
132.86
134.17
139.60
167.11
171.11
F
O
NH
N
O
O
48
49
ppm
45
46
ppm
91
ppm
104
105
106
ppm
210
200
190
180
170
160
150
140
130
120
110
100
90
80
70
60
50
40
30
20
10
0
ppm

2.4b

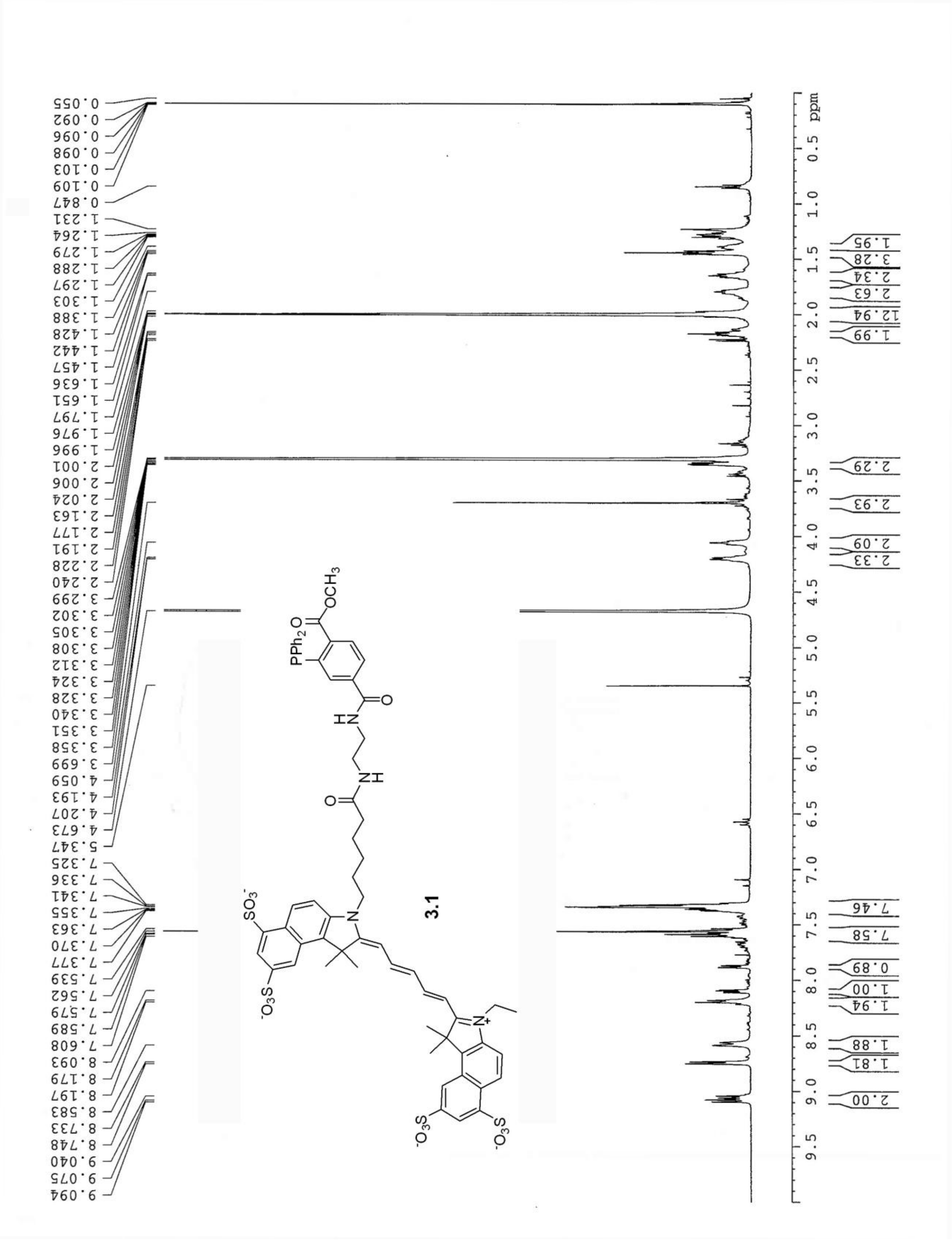
0.055
0.092
0.096
0.098
0.103
0.109
0.847
1.231
1.264
1.279
1.288
1.297
1.303
1.388
1.428
1.442
1.457
1.636
1.651
1.797
1.976
1.996
2.001
2.006
2.024
2.163
2.177
2.191
2.228
2.240
3.299
3.302
3.305
3.308
3.312
3.324
3.328
3.340
3.351
3.358
3.699
4.059
4.193
4.207
4.673
5.347
7.325
7.336
7.341
7.355
7.363
7.370
7.377
7.539
7.562
7.579
7.589
7.608
8.093
8.179
8.197
8.583
8.733
8.748
9.040
9.075
9.094
1.95
3.28
2.34
2.63
12.94
1.99
2.29
2.93
2.09
2.33
7.46
7.58
0.89
1.00
1.94
1.88
1.81
2.00
ppm
0.5
1.0
1.5
2.0
2.5
3.0
3.5
4.0
4.5
5.0
5.5
6.0
6.5
7.0
7.5
8.0
8.5
9.0
9.5
PPh$_2$
O
OCH$_3$
HN
O
NH
O
SO$_3^-$
$^-$O$_3$S
N
N$^+$
$^-$O$_3$S
$^-$O$_3$S

3.1

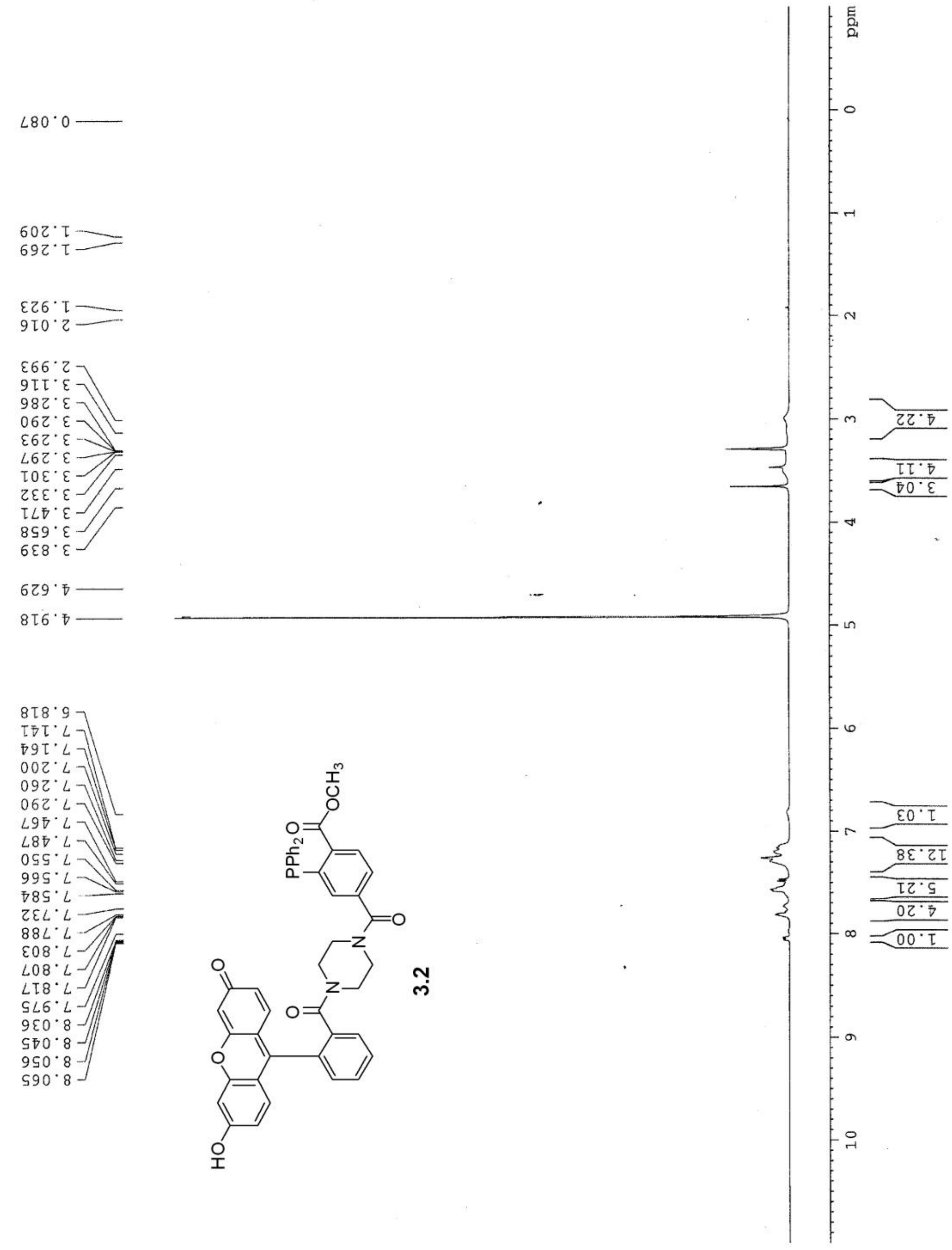
0.087
1.209
1.269
1.923
2.016
2.993
3.116
3.286
3.290
3.293
3.297
3.301
3.332
3.471
3.658
3.839
4.629
4.918
6.818
7.141
7.164
7.200
7.260
7.290
7.467
7.487
7.550
7.566
7.584
7.732
7.788
7.803
7.807
7.817
7.975
8.036
8.045
8.056
8.065
4.22
4.11
3.04
1.03
12.38
5.21
4.20
1.00
ppm
0
1
2
3
4
5
6
7
8
9
10
HO
O
O
O
N
N
O
PPh2O
OCH3

3.2

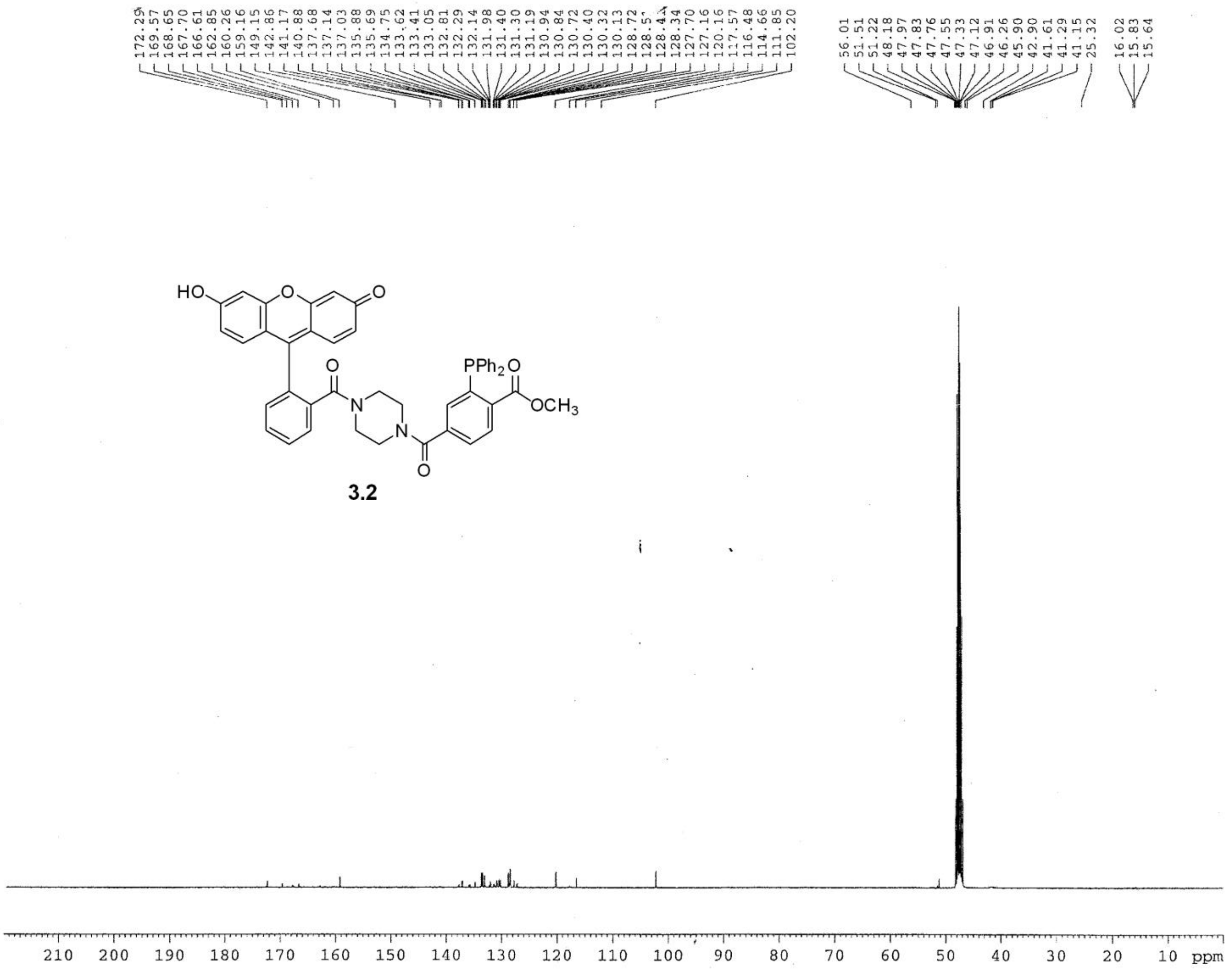
172.29
169.57
168.65
167.70
166.61
162.85
160.26
159.16
149.15
142.86
141.17
140.88
137.68
137.14
137.03
135.88
135.69
134.75
133.62
133.41
133.05
132.81
132.29
132.14
131.98
131.40
131.30
131.19
130.94
130.84
130.72
130.40
130.32
130.13
128.72
128.5
128.44
128.34
127.70
127.16
120.16
117.57
116.48
114.66
111.85
102.20
56.01
51.51
51.22
48.18
47.97
47.83
47.76
47.55
47.33
47.12
46.91
46.26
45.90
42.90
41.61
41.29
41.15
25.32
16.02
15.83
15.64
HO
O
O
O
N
N
O
PPh$_2$
O
OCH$_3$
210
200
190
180
170
160
150
140
130
120
110
100
90
80
70
60
50
40
30
20
10
ppm

3.2

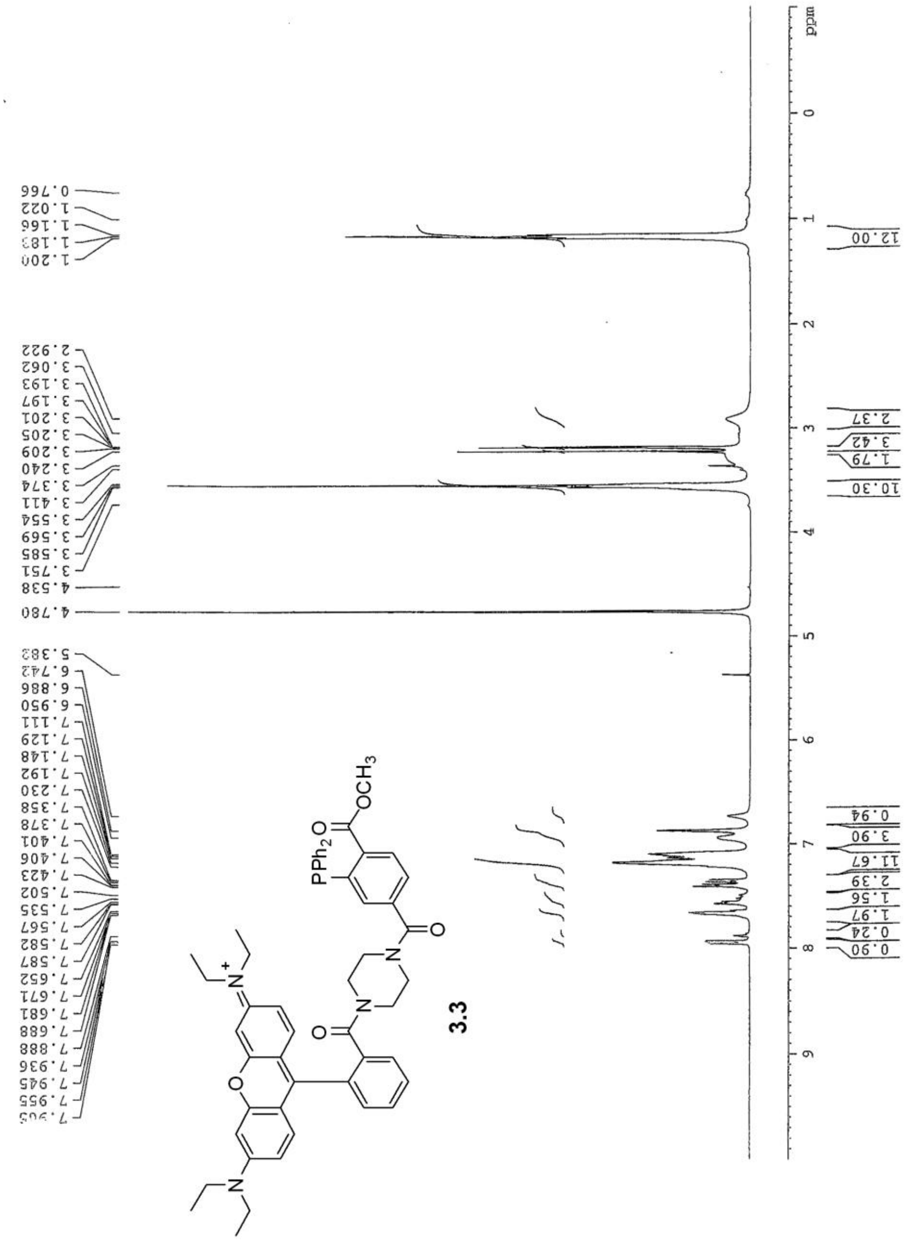
0.766
1.022
1.166
1.183
1.200
2.922
3.062
3.193
3.197
3.201
3.205
3.209
3.240
3.374
3.411
3.554
3.569
3.585
3.751
4.538
4.780
5.383
6.742
6.886
6.950
7.111
7.129
7.148
7.192
7.230
7.358
7.378
7.401
7.406
7.423
7.502
7.535
7.567
7.582
7.587
7.652
7.671
7.681
7.688
7.888
7.936
7.945
7.955
7.965
12.00
2.37
3.42
1.79
10.30
0.94
3.90
11.67
2.39
1.56
1.97
0.24
0.90
ppm
0
1
2
3
4
5
6
7
8
9
PPh2O
OCH3
O
N
N+

3.3

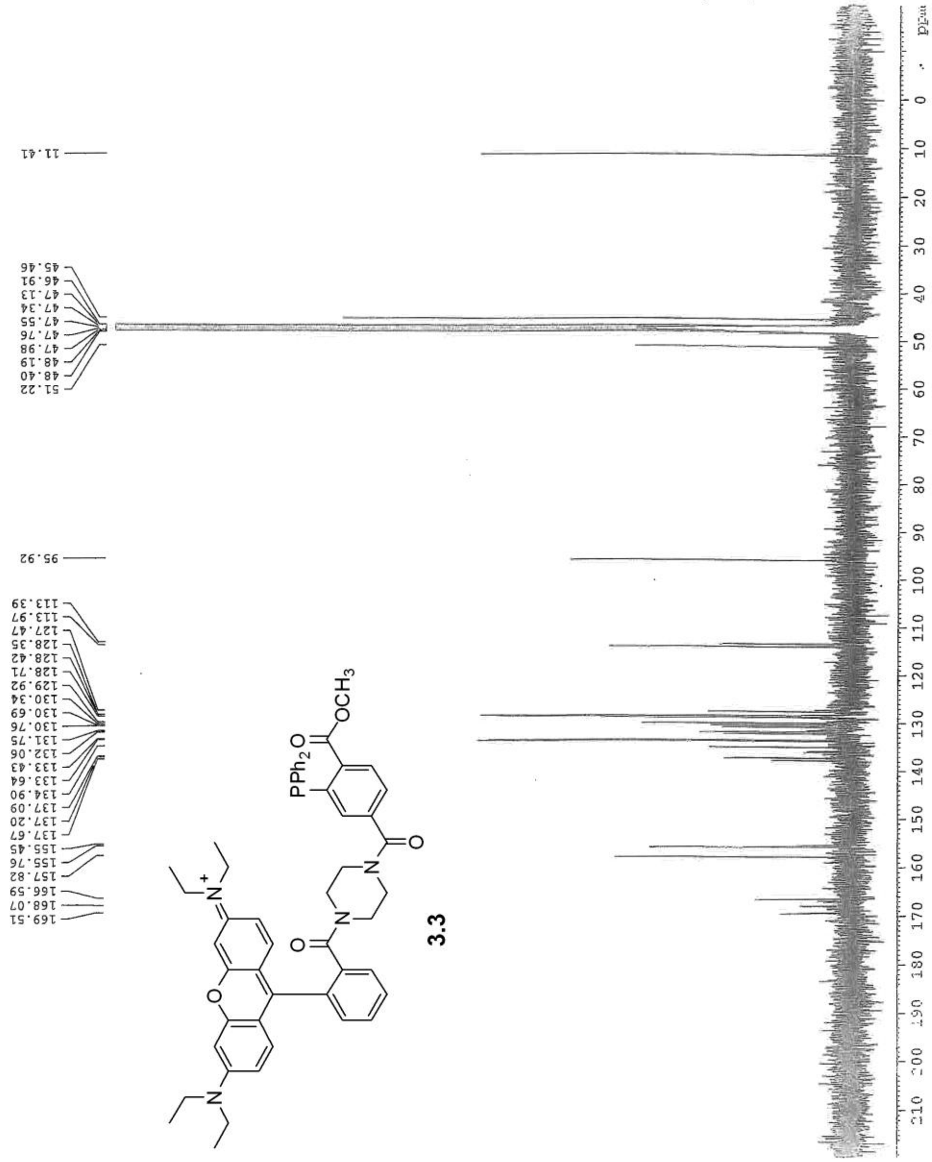
11.41
45.46
46.91
47.13
47.34
47.55
47.76
47.98
48.19
48.40
51.22
95.92
113.39
113.97
127.47
128.35
128.42
128.71
129.92
130.34
130.69
130.76
131.75
132.06
133.43
133.64
134.90
137.09
137.20
137.67
155.45
155.76
157.82
166.59
168.07
169.51
N
O
N
N
PPh2O
OCH3
ppm
0
10
20
30
40
50
60
70
80
90
100
110
120
130
140
150
160
170
180
190
200
210

3.3

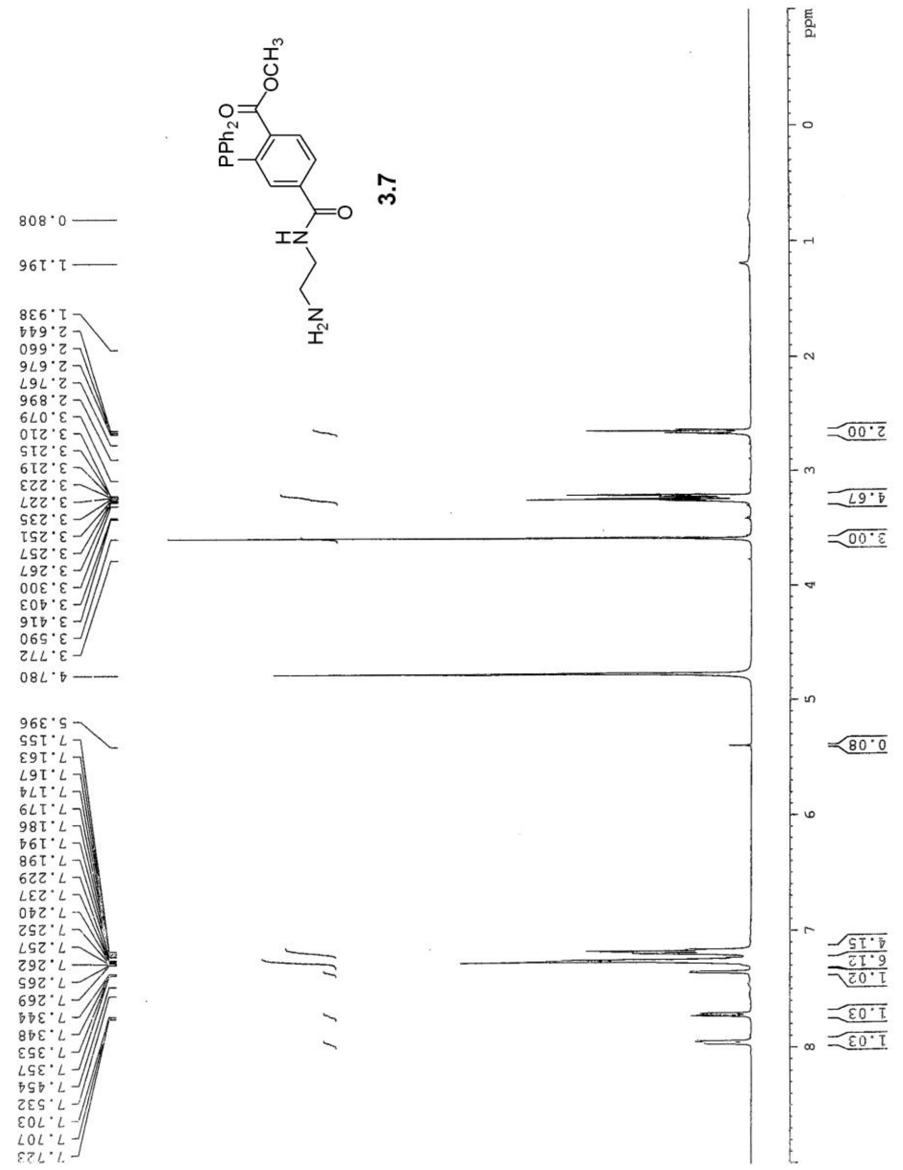

3.7

PPh$_2$O
OCH$_3$
H
N
H$_2$N
O
0.808
1.196
1.938
2.644
2.660
2.676
2.767
2.896
3.079
3.210
3.215
3.219
3.223
3.227
3.235
3.251
3.257
3.267
3.300
3.403
3.416
3.590
3.772
4.780
5.396
7.155
7.163
7.167
7.174
7.179
7.186
7.194
7.198
7.229
7.237
7.240
7.252
7.257
7.262
7.265
7.269
7.344
7.348
7.353
7.357
7.454
7.532
7.703
7.707
7.723
2.00
4.67
3.00
0.08
4.15
6.12
1.02
1.03
1.03
ppm
0
1
2
3
4
5
6
7
8

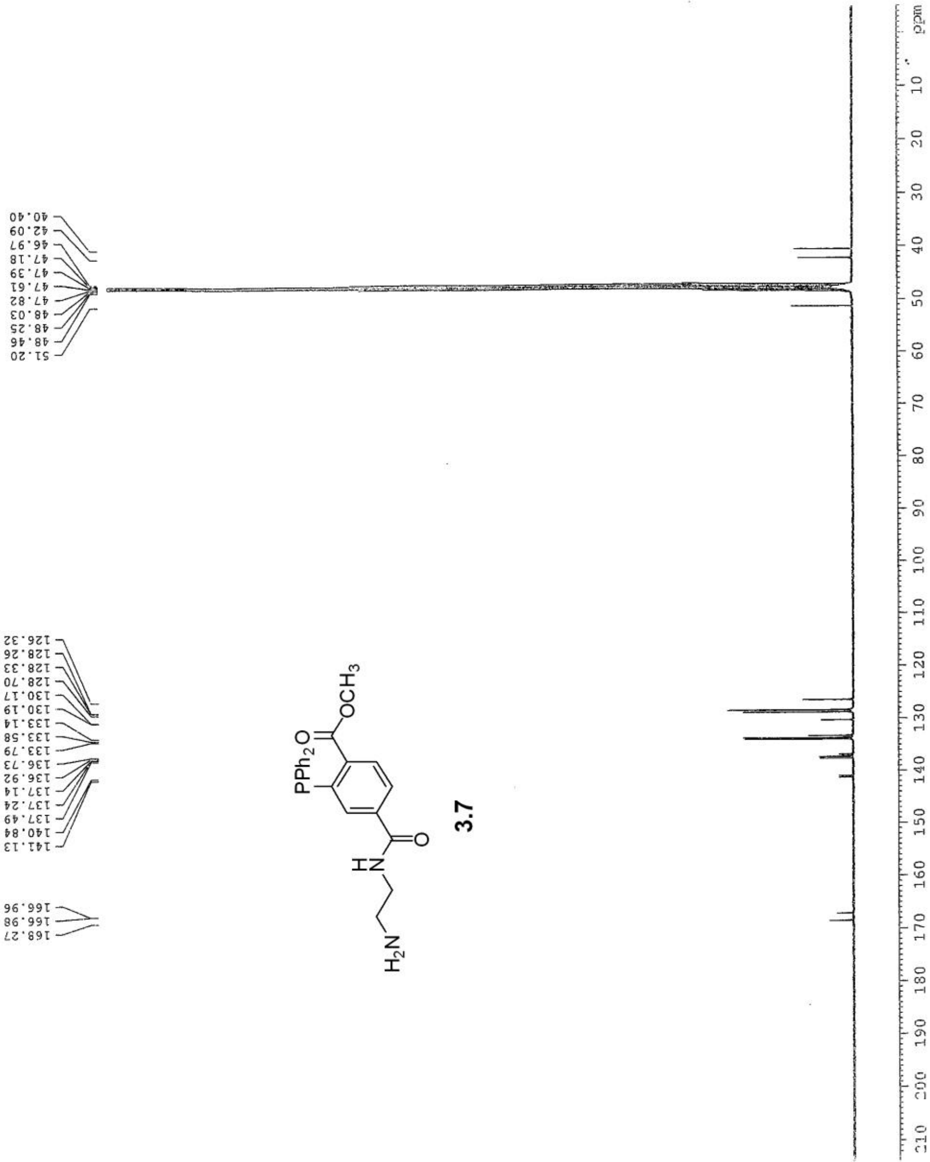
40.40
42.09
46.97
47.18
47.39
47.61
47.82
48.03
48.25
48.46
51.20
126.32
128.26
128.33
128.70
130.17
130.19
133.14
133.58
133.79
136.73
136.92
137.14
137.24
137.49
140.84
141.13
166.96
166.98
168.27
PPh2
O
OCH3
H
N
H2N
O
ppm
10
20
30
40
50
60
70
80
90
100
110
120
130
140
150
160
170
180
190
200
210

3.7

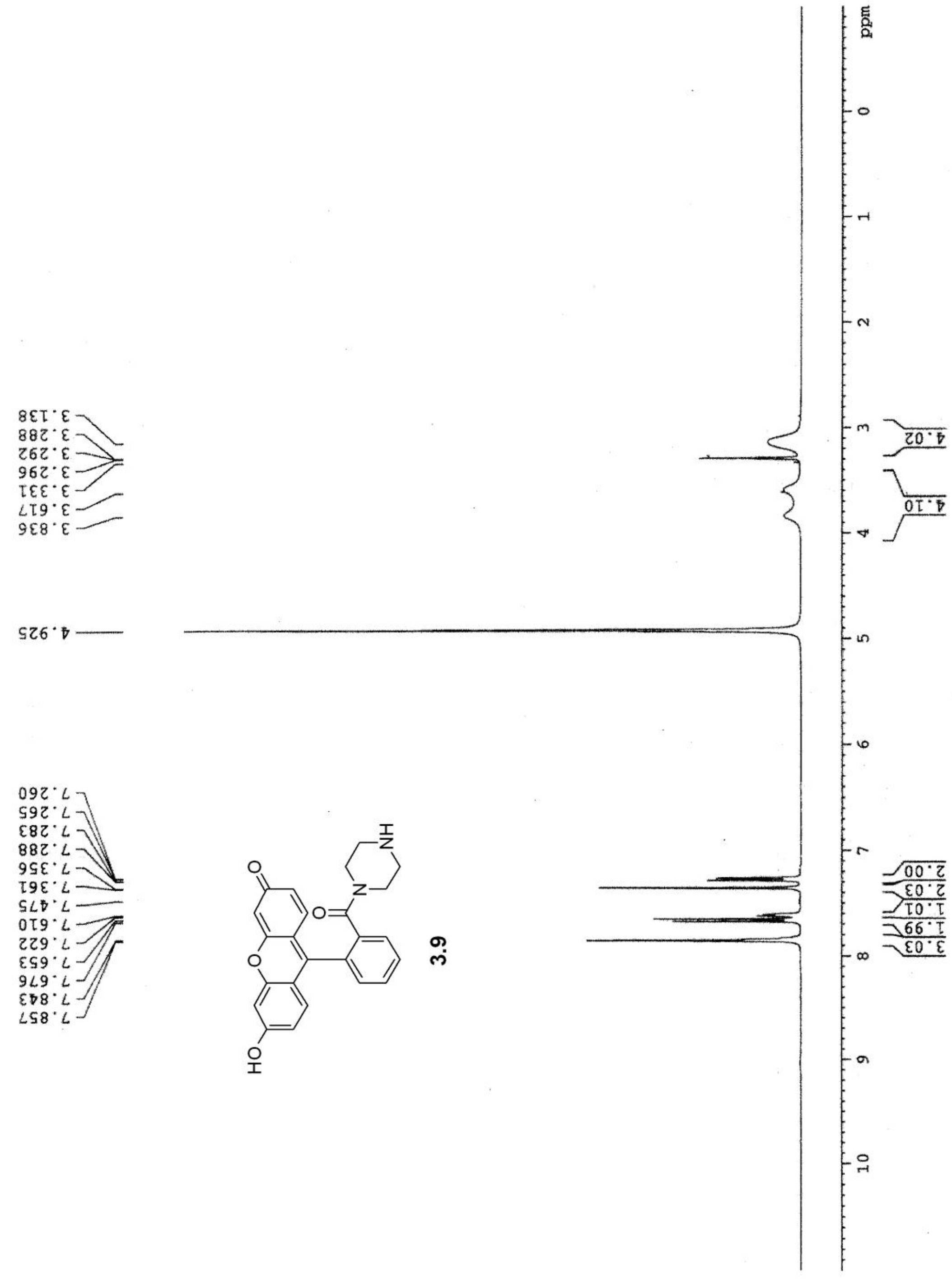
3.138
3.288
3.292
3.296
3.331
3.617
3.836
4.925
7.260
7.265
7.283
7.288
7.356
7.361
7.475
7.610
7.622
7.653
7.676
7.843
7.857
HO
O
O
N
NH
O
4.02
4.10
2.00
2.03
1.01
1.99
3.03
ppm
0
1
2
3
4
5
6
7
8
9
10

3.9

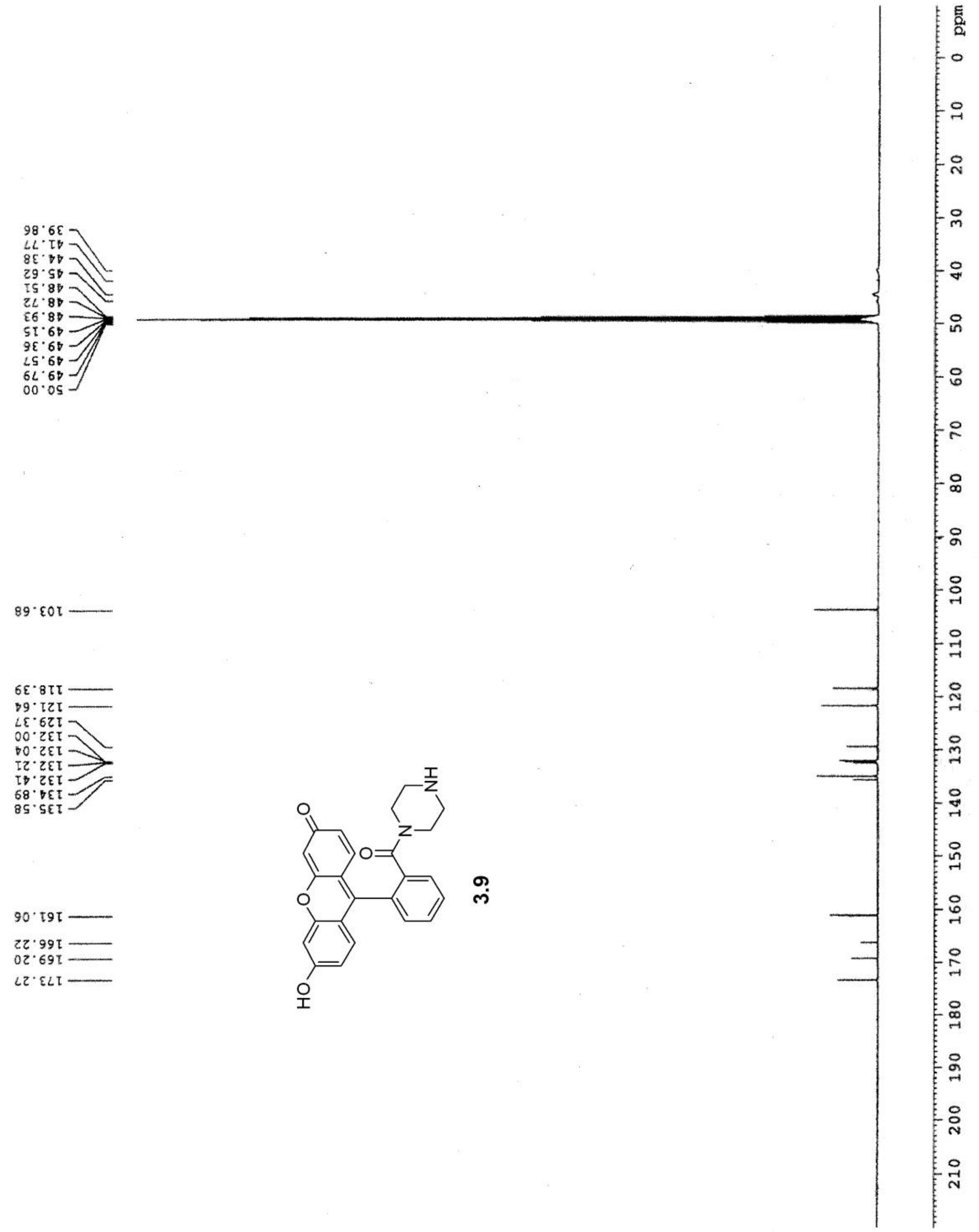
39.86
41.77
44.38
45.62
48.51
48.72
48.93
49.15
49.36
49.57
49.79
50.00
103.68
118.39
121.64
129.37
132.00
132.04
132.21
132.41
134.89
135.58
161.06
166.22
169.20
173.27
O
O
HO
O
N
NH
ppm
0
10
20
30
40
50
60
70
80
90
100
110
120
130
140
150
160
170
180
190
200
210

3.9

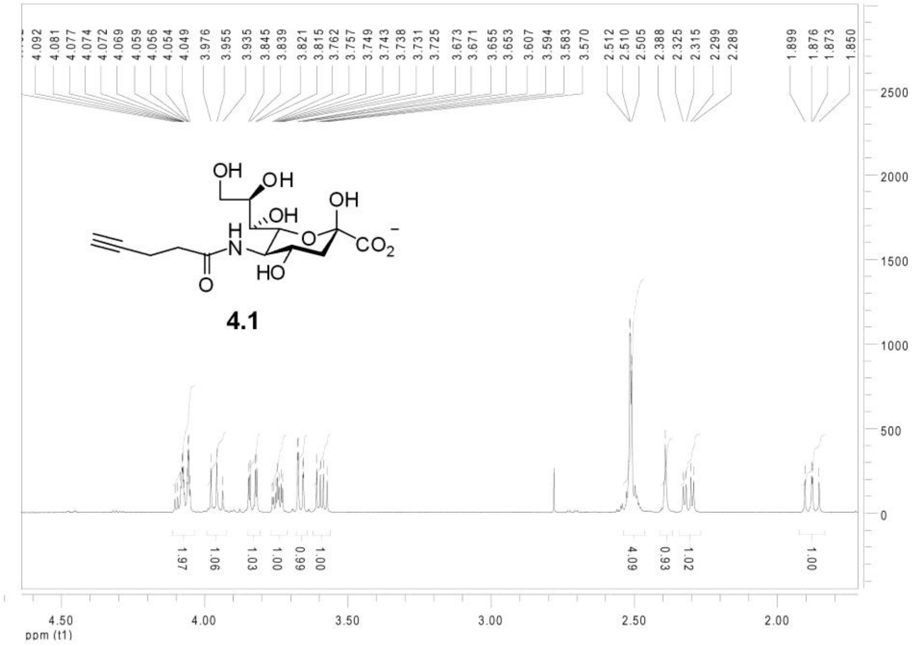
4.092
4.081
4.077
4.074
4.072
4.069
4.059
4.056
4.054
4.049
3.976
3.955
3.935
3.845
3.839
3.821
3.815
3.762
3.757
3.749
3.743
3.738
3.731
3.725
3.673
3.671
3.655
3.653
3.607
3.594
3.583
3.570
2.512
2.510
2.505
2.388
2.325
2.315
2.299
2.289
1.899
1.876
1.873
1.850
2500
2000
1500
1000
500
0
1.97
1.06
1.03
1.00
0.99
1.00
4.09
0.93
1.02
1.00
4.50
4.00
3.50
3.00
2.50
2.00
ppm (t1)
OH
OH
OH
OH
H
N
O
O
CO_2^-
HO

4.1

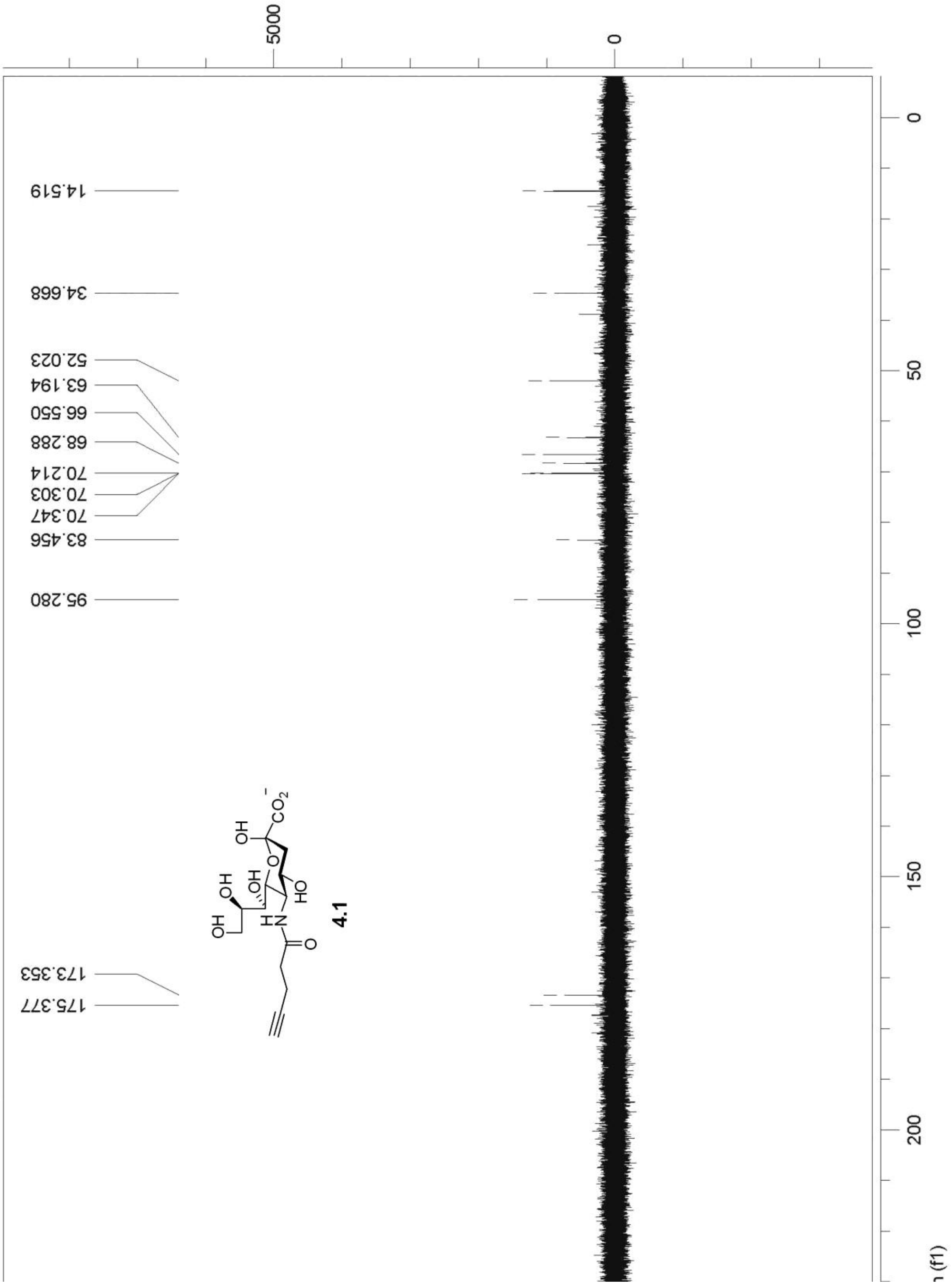
14.519
34.668
52.023
63.194
66.550
68.288
70.214
70.303
70.347
83.456
95.280
173.353
175.377
4.1
5000
0
0
50
100
150
200
n (f1)

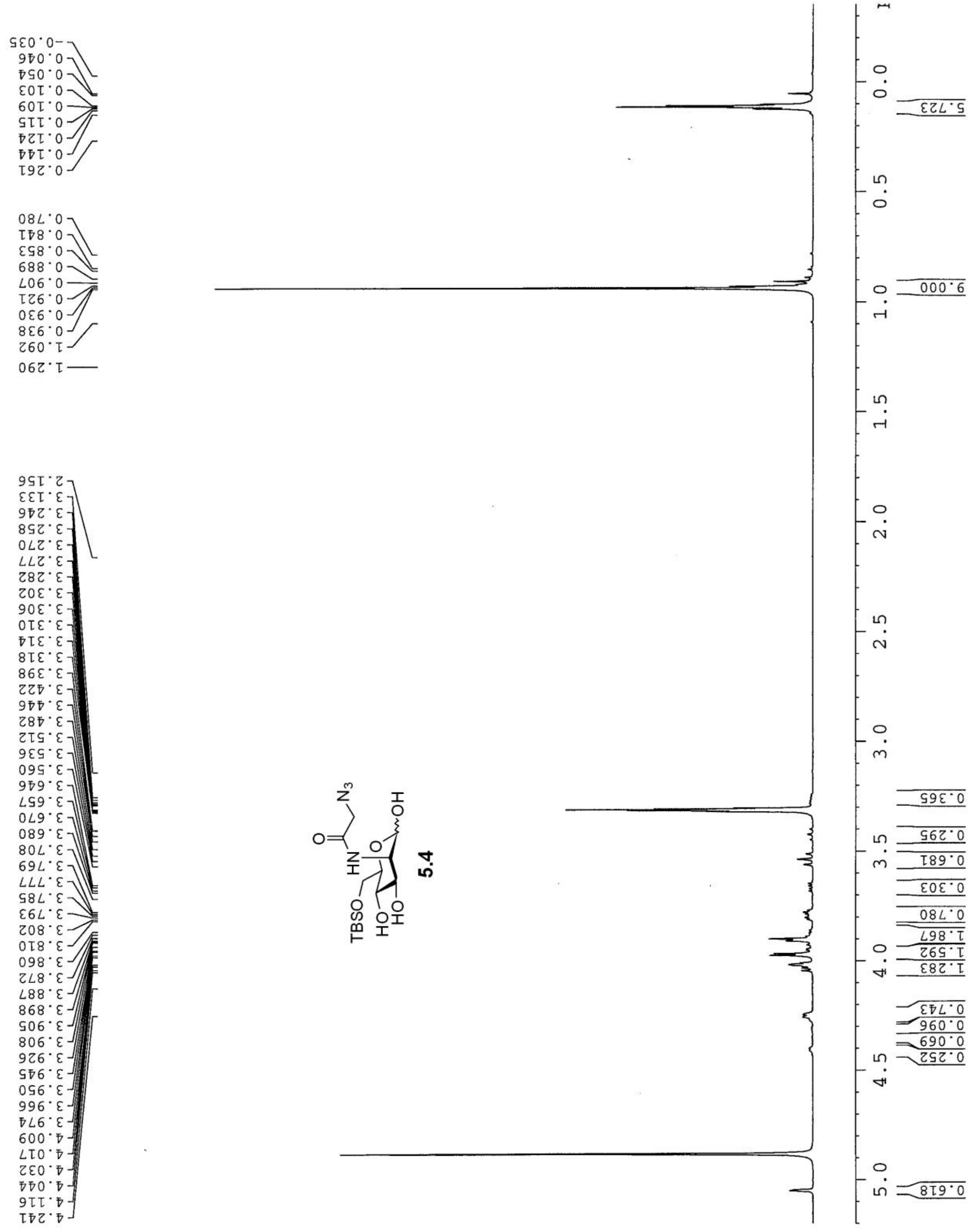
-0.035
0.046
0.054
0.103
0.109
0.115
0.124
0.144
0.261
0.780
0.841
0.853
0.889
0.907
0.921
0.930
0.938
1.092
1.290
2.156
3.133
3.246
3.258
3.270
3.277
3.282
3.302
3.306
3.310
3.314
3.318
3.398
3.422
3.446
3.482
3.512
3.536
3.560
3.646
3.657
3.670
3.680
3.708
3.769
3.777
3.785
3.793
3.802
3.810
3.860
3.872
3.887
3.898
3.905
3.908
3.926
3.945
3.950
3.966
3.974
4.009
4.017
4.032
4.044
4.116
4.241
0.0
0.5
1.0
1.5
2.0
2.5
3.0
3.5
4.0
4.5
5.0
5.723
9.000
0.365
0.295
0.681
0.303
0.780
1.867
1.592
1.283
0.743
0.096
0.069
0.252
0.618
N_3
O
HN
O
OH
TBSO
HO
HO

5.4

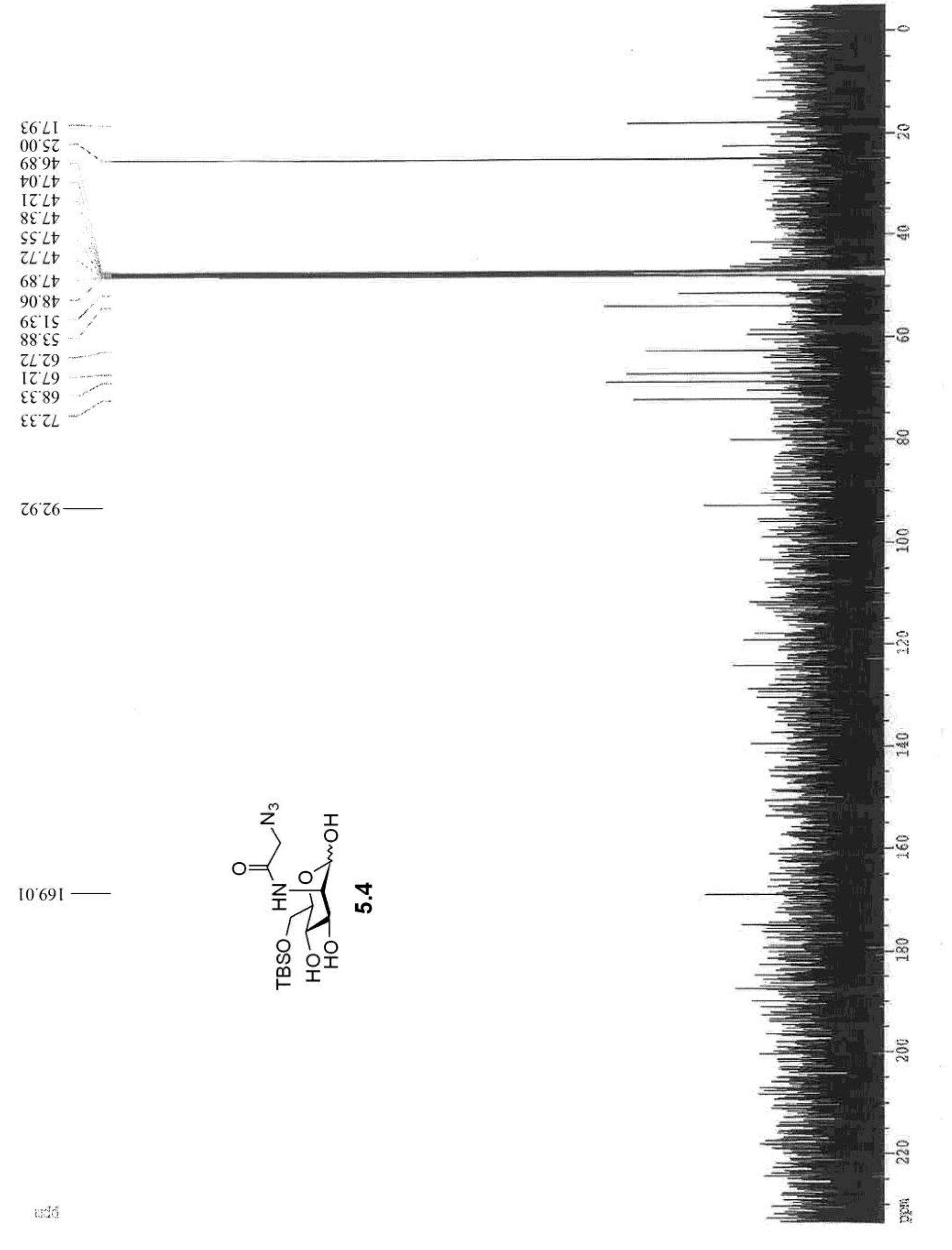
17.93
25.00
46.89
47.04
47.21
47.38
47.55
47.72
47.89
48.06
51.39
53.88
62.72
67.21
68.33
72.33
92.92
169.01
ppm
TBSO
HO
HO
HN
O
N3
OH
5.4
0
20
40
60
80
100
120
140
160
180
200
220
ppm

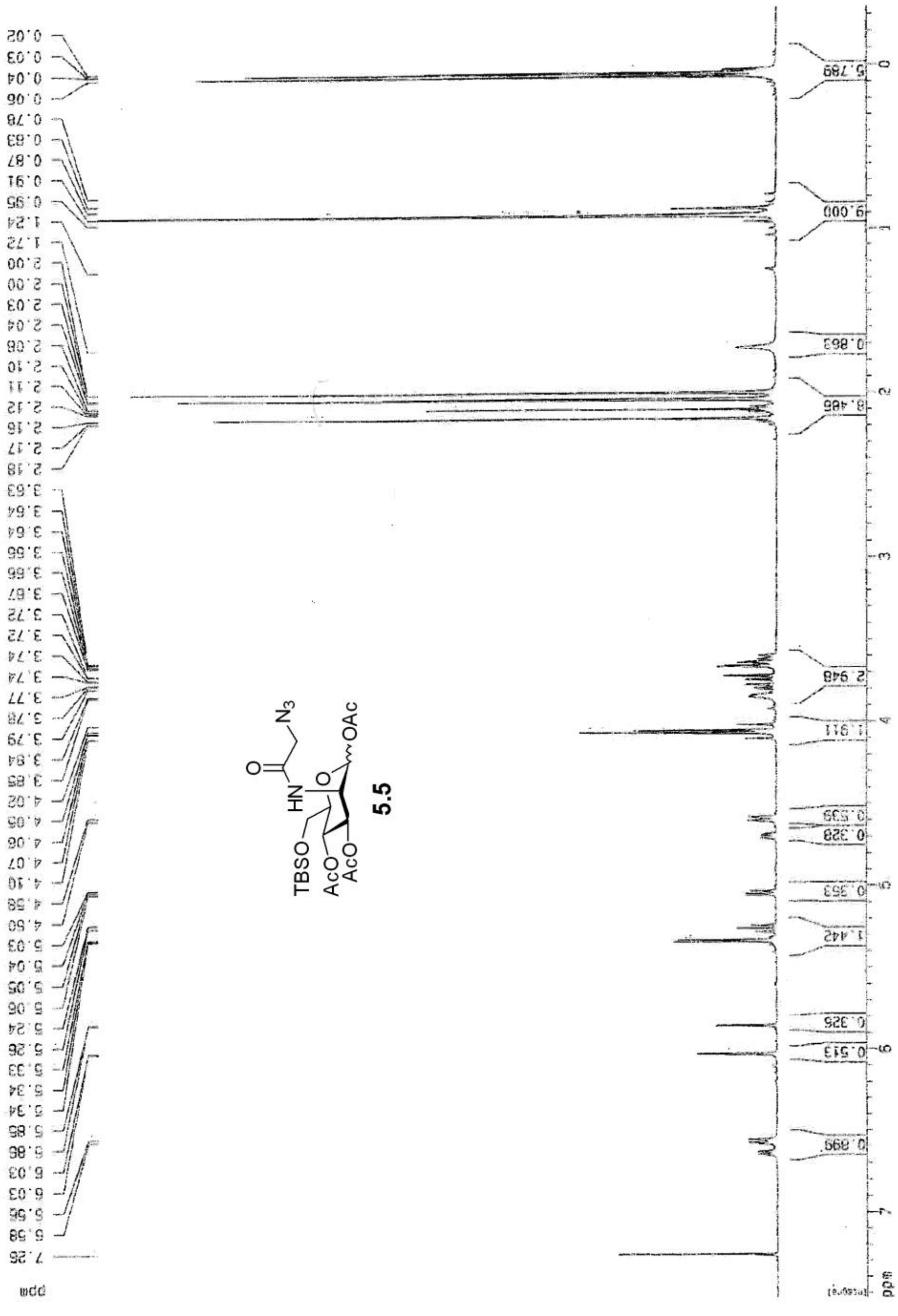
0.02
0.03
0.04
0.06
0.78
0.83
0.87
0.91
0.95
1.24
1.72
2.00
2.00
2.03
2.04
2.06
2.10
2.11
2.12
2.16
2.17
2.18
3.63
3.64
3.64
3.66
3.66
3.67
3.72
3.72
3.74
3.74
3.77
3.78
3.79
3.84
3.85
4.02
4.06
4.06
4.07
4.10
4.58
4.60
5.03
5.04
5.05
5.06
5.24
5.26
5.33
5.34
5.34
5.85
5.86
6.03
6.03
6.56
6.58
7.26
ppm
5.789
9.000
0.863
8.486
2.948
1.911
0.535
0.328
0.353
1.442
0.325
0.513
0.899
0
1
2
3
4
5
6
7
ppm
TBSO
AcO
AcO
HN
O
O
N3
OAc
5.5

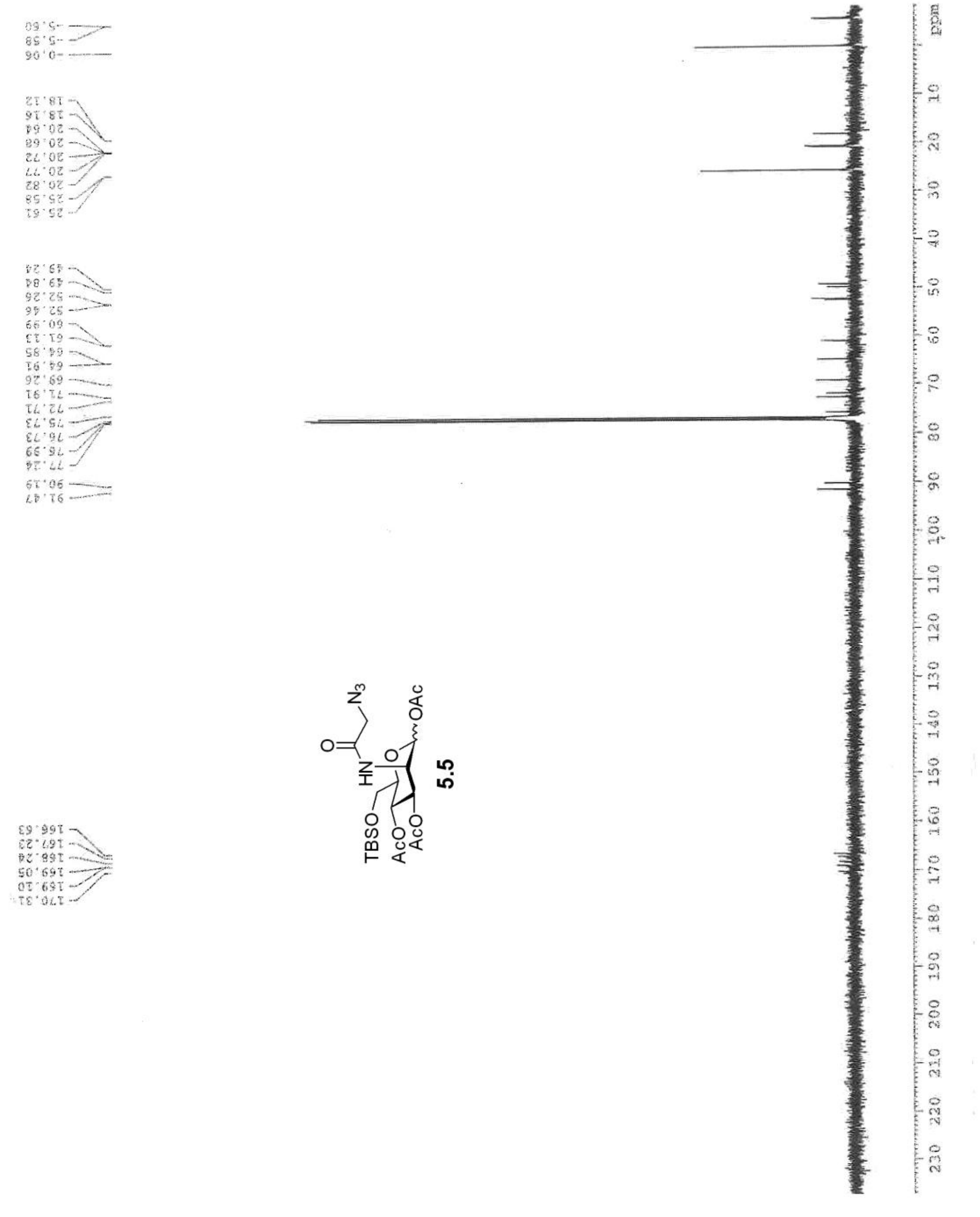

-5.60
-5.58
-0.06
18.12
18.16
20.64
20.68
20.72
20.77
20.82
25.58
25.61
49.24
49.84
52.26
52.46
60.99
61.13
64.85
64.91
69.26
71.91
72.71
75.73
76.73
76.99
77.24
90.19
91.47
166.63
167.23
168.24
169.05
169.10
170.31
N3
O
HN
O
OAc
TBSO
AcO
AcO
ppm
10
20
30
40
50
60
70
80
90
100
110
120
130
140
150
160
170
180
190
200
210
220
230

5.5

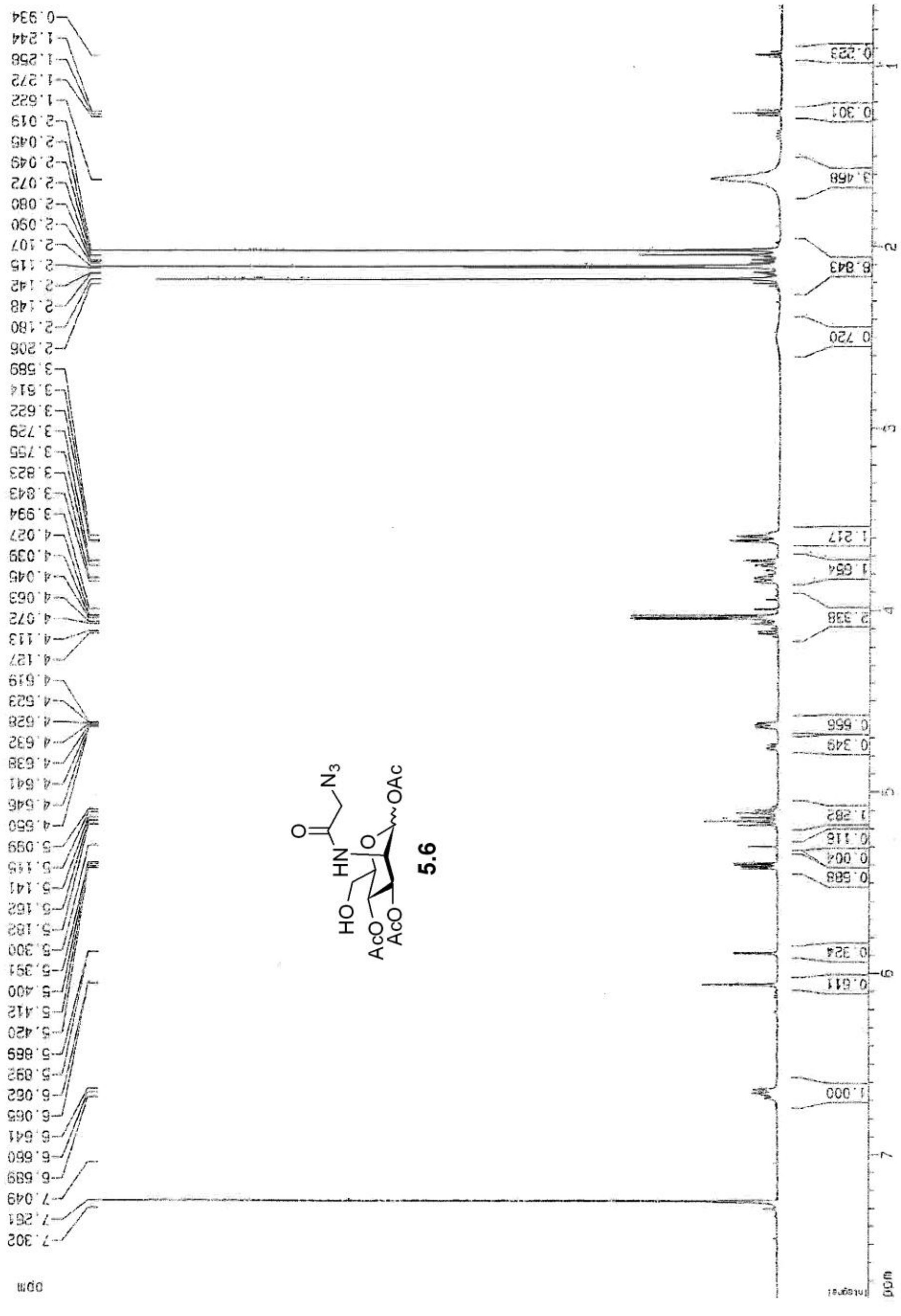ppm
0.934
1.244
1.258
1.272
1.622
2.019
2.045
2.049
2.072
2.080
2.090
2.107
2.115
2.142
2.148
2.180
2.206
3.589
3.614
3.622
3.729
3.755
3.823
3.843
3.994
4.027
4.039
4.045
4.063
4.072
4.113
4.127
4.619
4.623
4.628
4.632
4.638
4.641
4.646
4.650
5.099
5.115
5.141
5.162
5.183
5.300
5.351
5.400
5.412
5.420
5.869
5.892
6.062
6.065
6.641
6.660
6.689
7.049
7.261
7.302
0.223
0.301
3.468
6.843
0.720
1.217
1.054
2.338
0.666
0.349
1.282
0.116
0.004
0.688
0.324
0.611
1.000
1
2
3
4
5
6
7
Integral
ppm
HO
AcO
AcO
HN
O
O
N3
OAc
5.6

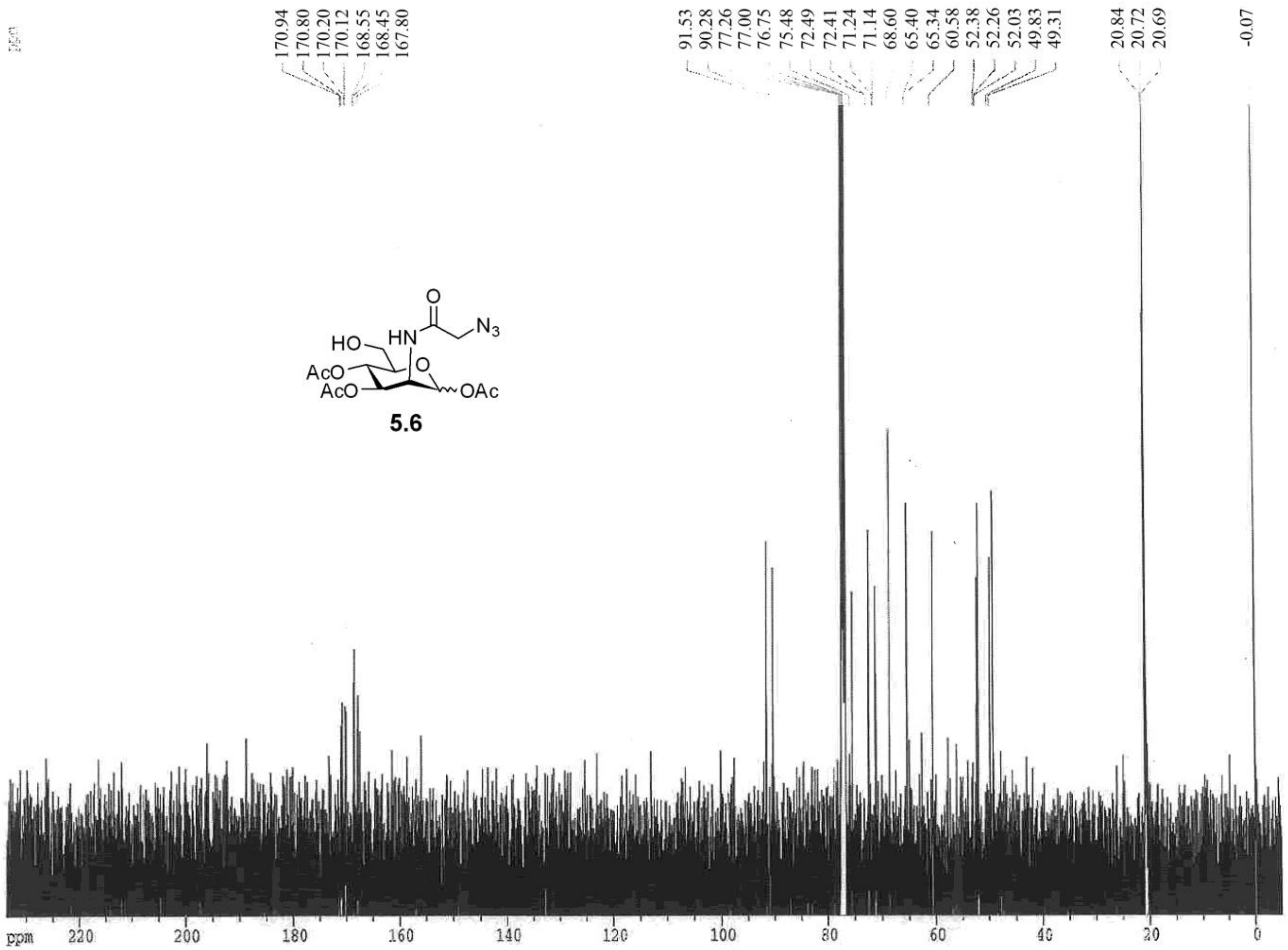
170.94
170.80
170.20
170.12
168.55
168.45
167.80
91.53
90.28
77.26
77.00
76.75
75.48
72.49
72.41
71.24
71.14
68.60
65.40
65.34
60.58
52.38
52.26
52.03
49.83
49.31
20.84
20.72
20.69
-0.07
HO
HN
O
N3
AcO
AcO
O
OAc
ppm
220
200
180
160
140
120
100
80
60
40
20
0

5.6

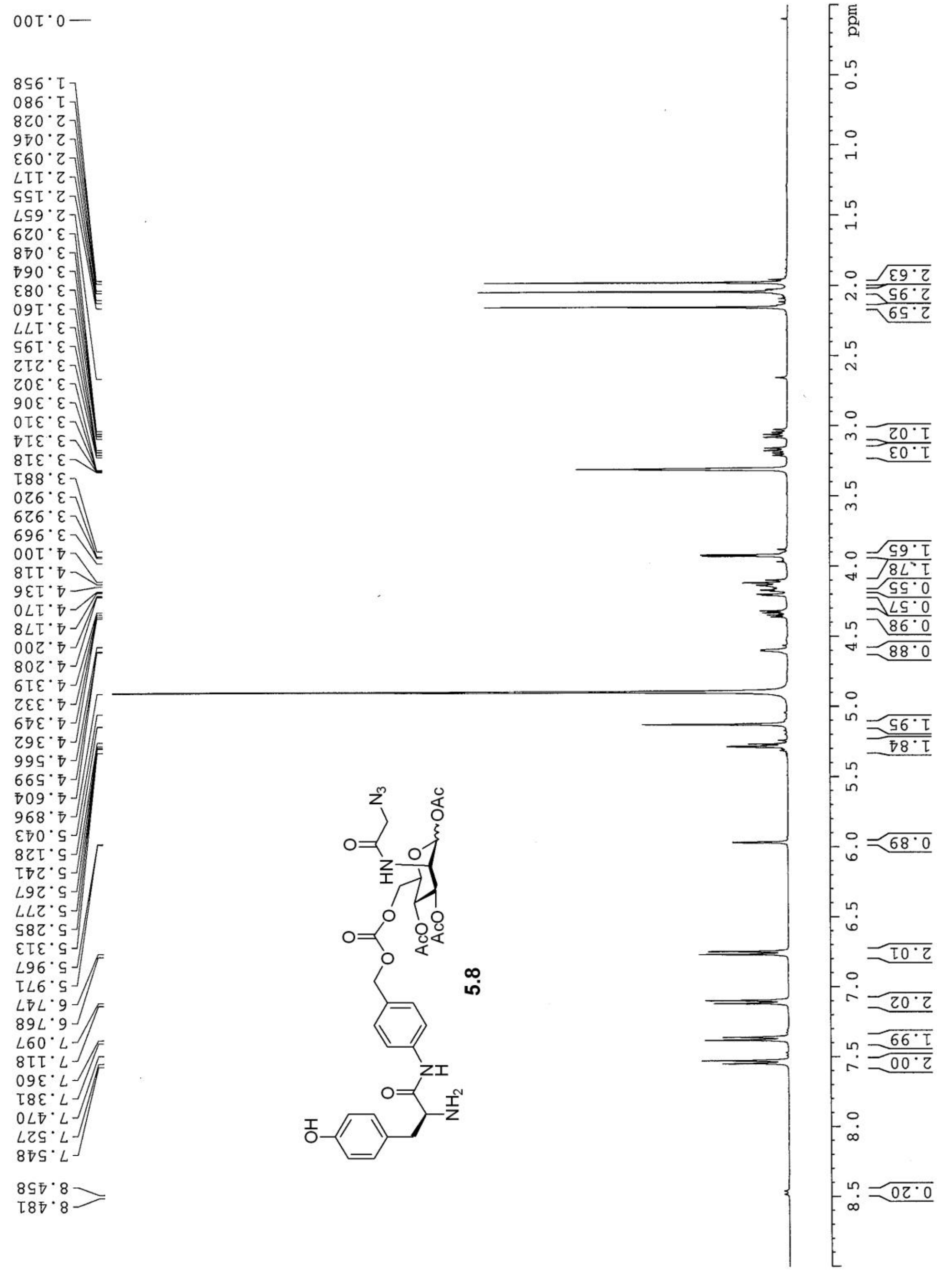
0.100
1.958
1.980
2.028
2.046
2.093
2.117
2.155
2.657
3.029
3.048
3.064
3.083
3.160
3.177
3.195
3.212
3.302
3.306
3.310
3.314
3.318
3.881
3.920
3.929
3.969
4.100
4.118
4.136
4.170
4.178
4.200
4.208
4.319
4.332
4.349
4.362
4.566
4.599
4.604
4.896
5.043
5.128
5.241
5.267
5.277
5.285
5.313
5.967
5.971
6.747
6.768
7.097
7.118
7.360
7.381
7.470
7.527
7.548
8.458
8.481
2.63
2.95
2.59
1.02
1.03
1.65
1.78
0.55
0.57
0.98
0.88
1.95
1.84
0.89
2.01
2.02
1.99
2.00
0.20
ppm
0.5
1.0
1.5
2.0
2.5
3.0
3.5
4.0
4.5
5.0
5.5
6.0
6.5
7.0
7.5
8.0
8.5
N3
O
HN
O
OAc
AcO
AcO
O
O
O
NH
O
NH2
OH

5.8

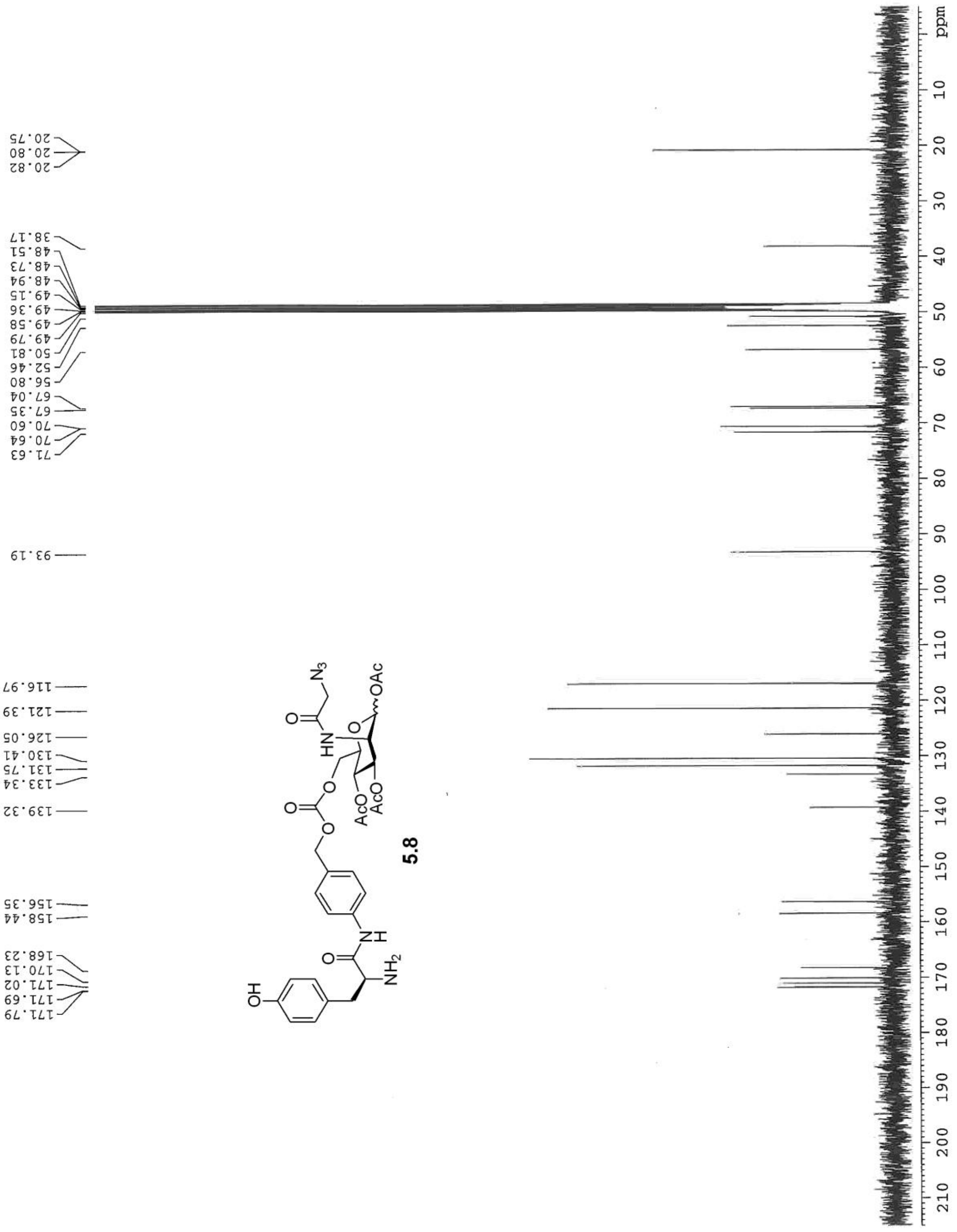

20.75
20.80
20.82
38.17
48.51
48.73
48.94
49.15
49.36
49.58
49.79
50.81
52.46
56.80
67.04
67.35
70.60
70.64
71.63
93.19
116.97
121.39
126.05
130.41
131.75
133.34
139.32
156.35
158.44
168.23
170.13
171.02
171.69
171.79
N3
O
HN
O
OAc
O
O
O
AcO
AcO
OH
O
N
H
NH2
ppm
10
20
30
40
50
60
70
80
90
100
110
120
130
140
150
160
170
180
190
200
210

5.8

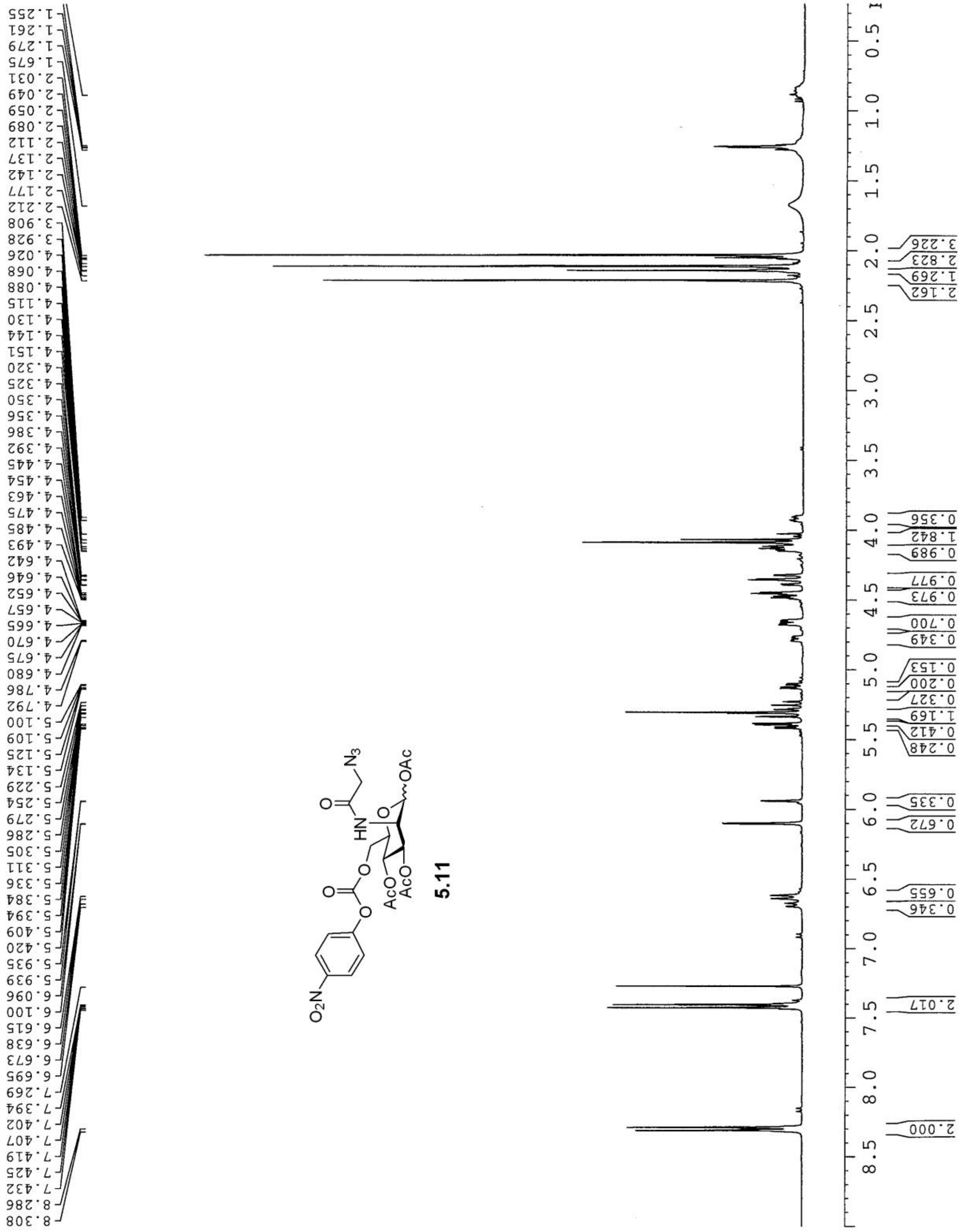
1.255
1.261
1.279
1.675
2.031
2.049
2.059
2.089
2.112
2.137
2.142
2.177
2.212
3.908
3.928
4.026
4.068
4.088
4.115
4.130
4.144
4.151
4.320
4.325
4.350
4.356
4.386
4.392
4.445
4.454
4.463
4.475
4.485
4.493
4.642
4.646
4.652
4.657
4.665
4.670
4.675
4.680
4.786
4.792
5.100
5.109
5.125
5.134
5.229
5.254
5.279
5.286
5.305
5.311
5.336
5.384
5.394
5.409
5.420
5.935
5.939
6.096
6.100
6.615
6.638
6.673
6.695
7.269
7.394
7.402
7.407
7.419
7.425
7.432
8.286
8.308
O2N
O
O
O
AcO
AcO
O
HN
O
N3
OAc
0.5
1.0
1.5
2.0
2.5
3.0
3.5
4.0
4.5
5.0
5.5
6.0
6.5
7.0
7.5
8.0
8.5
3.226
2.823
1.269
2.162
0.356
1.842
0.989
0.977
0.973
0.700
0.349
0.153
0.200
0.327
1.169
0.412
0.248
0.335
0.672
0.655
0.346
2.017
2.000

5.11

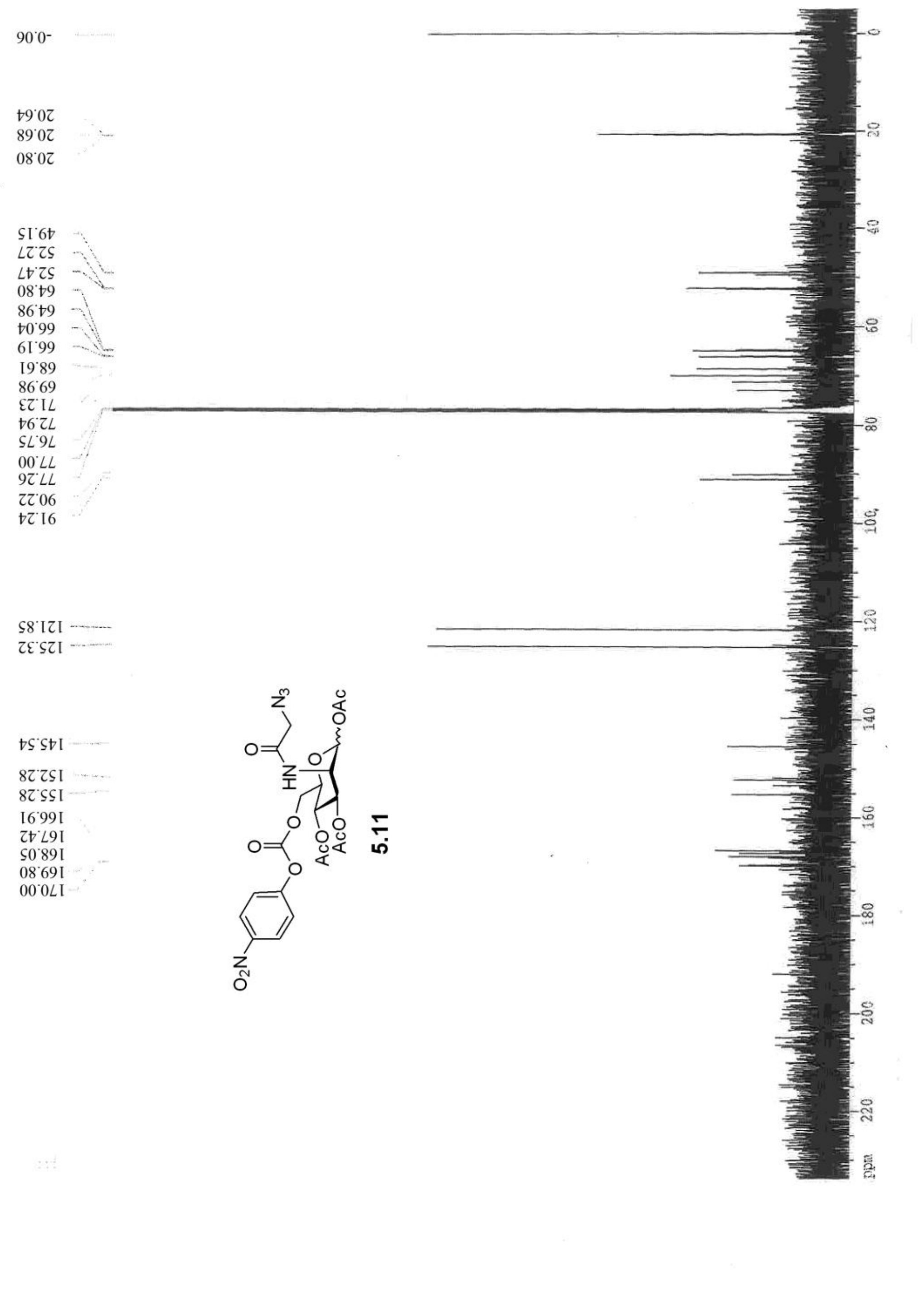
-0.06
20.64
20.68
20.80
49.15
52.27
52.47
64.80
64.98
66.04
66.19
68.61
69.98
71.23
72.94
76.75
77.00
77.26
90.22
91.24
121.85
125.32
145.54
152.28
155.28
166.91
167.42
168.05
169.80
170.00
N3
O
HN
O
OAc
O
O
O
AcO
AcO
O2N
0
20
40
60
80
100
120
140
160
180
200
220
ppm

5.11

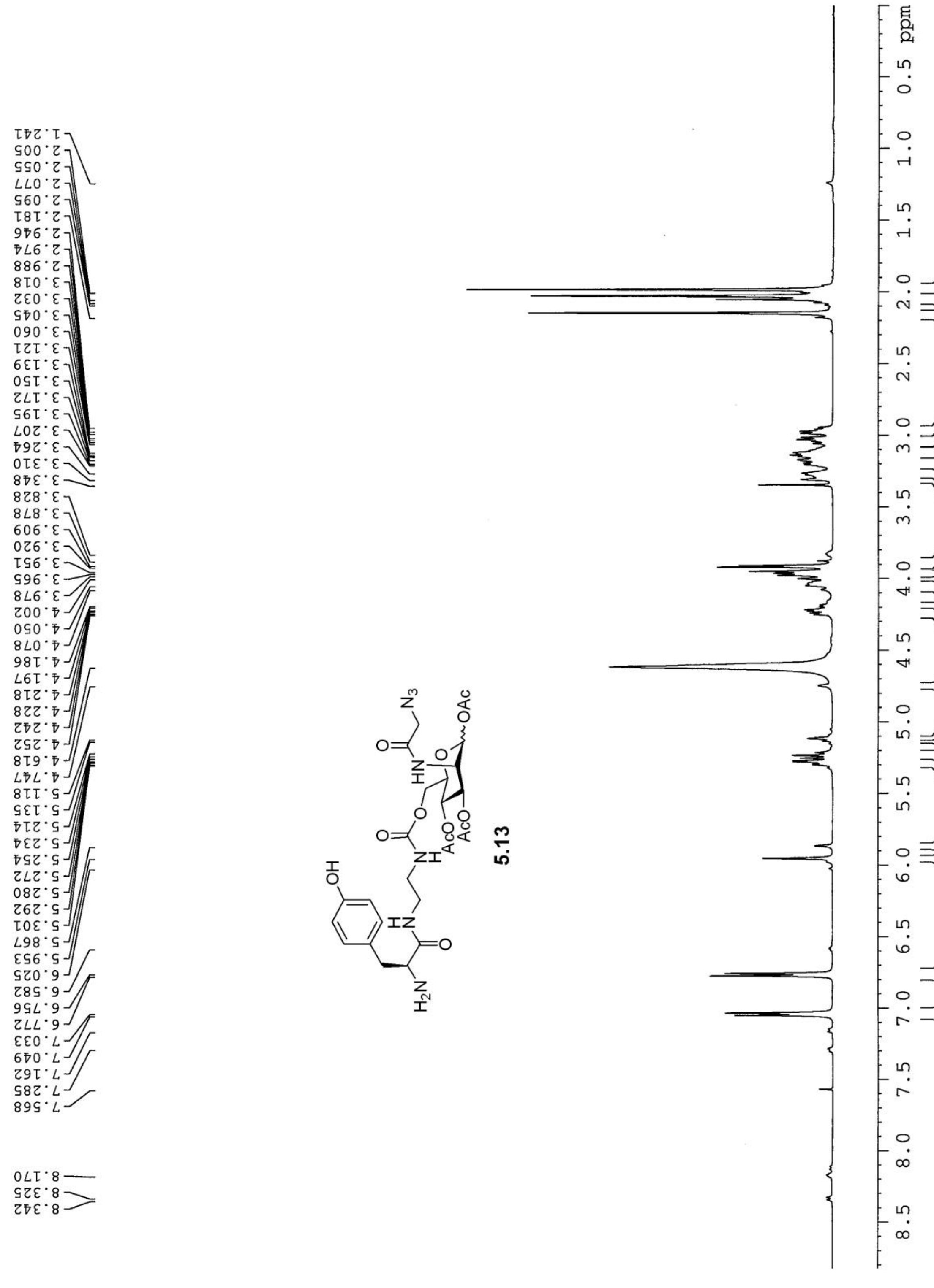
1.241
2.005
2.055
2.077
2.095
2.181
2.946
2.974
2.988
3.018
3.032
3.045
3.060
3.121
3.139
3.150
3.172
3.195
3.207
3.264
3.310
3.348
3.828
3.878
3.909
3.920
3.951
3.965
3.978
4.002
4.050
4.078
4.186
4.197
4.218
4.228
4.242
4.252
4.618
4.747
5.118
5.135
5.214
5.234
5.254
5.272
5.280
5.292
5.301
5.867
5.953
6.025
6.582
6.756
6.772
7.033
7.049
7.162
7.285
7.568
8.170
8.325
8.342
3.427
4.063
2.546
1.003
1.135
1.777
1.388
1.018
0.471
1.621
1.981
0.487
1.110
0.338
0.834
0.311
0.315
0.096
0.793
0.856
0.201
0.746
1.995
2.000
ppm
0.5
1.0
1.5
2.0
2.5
3.0
3.5
4.0
4.5
5.0
5.5
6.0
6.5
7.0
7.5
8.0
8.5
N3
O
HN
O
OAc
AcO
AcO
O
O
N
H
HN
O
OH
H2N

5.13

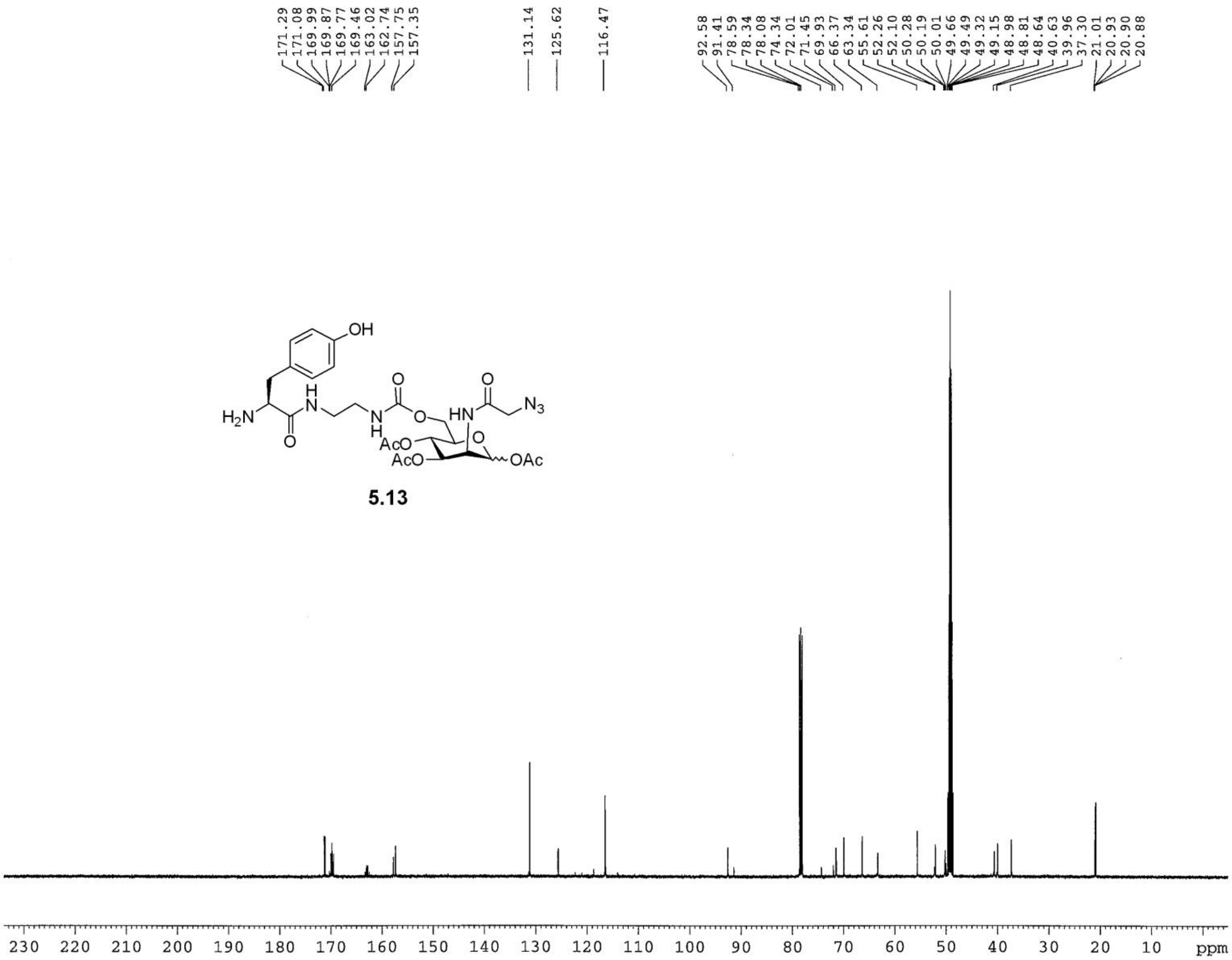
171.29
171.08
169.99
169.87
169.77
169.46
163.02
162.74
157.75
157.35
131.14
125.62
116.47
92.58
91.41
78.59
78.34
78.08
74.34
72.01
71.45
69.93
66.37
63.34
55.61
52.26
52.10
50.28
50.19
50.01
49.66
49.49
49.32
49.15
48.98
48.81
48.64
40.63
39.96
37.30
21.01
20.93
20.90
20.88
OH
H
N
O
H$_2$N
O
N
H
O
HN
O
N$_3$
AcO
AcO
O
OAc
230
220
210
200
190
180
170
160
150
140
130
120
110
100
90
80
70
60
50
40
30
20
10
ppm

5.13